ELECTRIC FIELD INDUCED DROPLET MANIPULATION

IMAN FROZANPOOR

How to cite:

FROZANPOOR, IMAN (2022) ELECTRIC FIELD INDUCED DROPLET MANIPULATION. Doctoral thesis, Durham University.

ELECTRIC FIELD INDUCED DROPLET MANIPULATION

Iman Frozanpoor

Department of Engineering

Durham University

This dissertation is submitted for the degree of

Doctor of Philosophy

2022

I Would Like To Dedicate This Thesis To My loving Mom & Dad AND To My Nephews: **Arian & Yuna**!

Iman (2022)

Declaration of Authorship

The research in this thesis is based on experiments and characterisation carried out in the Department of Engineering in Durham University. I hereby declare that the contents of this dissertation are original and have not been submitted for consideration to any other degree or qualification. Furthermore, the work in this thesis is the result of my own work and includes nothing which is the outcome of work done in collaboration.

Iman Frozanpoor

Acknowledgements

First and foremost, I would like to express my sincere gratitude to project supervisors: Dr Claudio Balocco, Prof Andrew Gallant, Dr Michael Cooke, and Dr Vibin Ambukan for their invaluable help, support, advice, and inspiration. Special thanks and recognition is also owed to former project supervisors: Prof David Wood, Dr Zoltan Racz, and Mr Ian Bossons for their valuable support and insightful contributions.

I especially appreciate Dr Jidong Jin for his valuable discussions and for sharing his insight into microfabrication in the cleanroom. I would also like to thank Dr Chris Pearson, Mr Neil Clarey, Ms Amy Tate, Dr Diana Alvarez-ruiz, Ms Sahar Nasirian, Dr Alejandro Galan-Gonzalez, and Mr Ian Hutchinson for technical assistance and discussions. The ZnO nanowires presented in this work were prepared by Dr Alejandro Galan-Gonzalez. The characterization with scanning electron microscopy was carried out by Dr Alejandro Galan-Gonzalez and Dr Diana Alvarez-ruiz.

I want to thank Mr Kieran Killough and Mr Daniel Williams for their contribution and legal assistance in publishing patent documents. I am also profoundly grateful for technical assistance and supervision support from managers at Jaguar Land Rover, including Dr Adrian Gaylard, Mr Kevin Davitt, and Mr Richard Latimer. Lastly, I am thankful for the financial support provided by Jaguar Land Rover and the Engineering and Physical Sciences Research Council UK., through the Industrial Case Award EP/P510476/1.

Grey College, Durham ♥♥ *Gradibus Ascendimus*

List of publications

Filed Patent Applications:

I. Frozanpoor, "Device for Manipulating a Substance, Vehicle and Assembly Comprising the Same, and Method of Using the Device," (in English), United Kingdom Patent Appl. WO/2020/245275, 2020. [Online]. Available: https://patentscope.wipo.int/search/en/detail.jsf?docId=WO2020245275&tab=PCTBIBLIO&_cid=P12-KOY9ZY-64123-1

I. Frozanpoor, "Device for manipulating a substance," (in English), United Kingdom Patent 2587459 Patent Appl. 202008391, 2020. [Online]. Available: https://patentscope.wipo.int/search/en/detail.jsf?docId=GB321213149&_cid=P11-KW88LV-16684-1

I. Frozanpoor, "Device for manipulating a substance," (in English), United Kingdom Patent 2587061 Patent Appl. 202008392, 2020. [Online]. Available: https://patentscope.wipo.int/search/en/detail.jsf?docId=GB320239574&_cid=P11-KW88LV-16684-1

I. Frozanpoor, "CONTROLLER AND CONTROL," (in English), United Kingdom Patent 2584465 Patent Appl. 201907986, 2019. [Online]. Available: https://patentscope.wipo.int/search/en/detail.jsf?docId=GB313068653&_cid=P11-KW88LV-16684-1

I. Frozanpoor, "Device for manipulating a substance," (in English), United Kingdom Patent 2584466 Patent Appl. 201907987, 2019. [Online]. Available: https://patentscope.wipo.int/search/en/detail.jsf?docId=GB313068654&_cid=P11-KW88LV-16684-1

Journal Publications:

Frozanpoor, I.; Cooke, M.; Racz, Z.; Bossons, I.; Ambukan, V.; Wood, D.; Gallant, J., A.; Balocco, C., Programmable Droplet Actuating Platform Using Liquid-Dielectrophoresis. **J Micromech Microeng** 2021, 31, 055014.

Frozanpoor, I.; Cooke, M.; Ambukan, V.; Gallant, J., A.; Balocco, C., Continuous Droplet-Actuating Platforms via an Electric Field Gradient: Electrowetting and Liquid Dielectrophoresis. **Langmuir** 2021, 37 (21), 6414-6422.

Frozanpoor, I.; Cooke, M.; Ambukan, V.; Alvarez-Ruiz, D.; Gallant, J., A.; Balocco, C., Tilting Micromirror Platform Based on Liquid Dielectrophoresis, **Sens. Actuators, A** 2021, 113177.

Thesis Abstract

In this thesis, we explore several droplet manipulation concepts on different length scales for a surface cleaning application. The design evolution to transfer these techniques from laboratory conditions to a chaotic environment, such as on the road, is an evolving engineering challenge where reliability and performance are equally important. Electrowetting and liquid dielectrophoresis are techniques by which an electromechanical response from an applied electric field enables precise droplet manipulation. This thesis presents several contributions to these technologies, focusing primarily on scalability, simplicity, and reliability.

The control of surface wettability using the electric methods attracts much attention due to their fast response (milliseconds), exceptional durability (hundreds of thousands of switching cycles) and low energy consumption (hundreds of microwatts). Furthermore, their superior performance and reliable nature have prompted a vast amount of literature to expand their application. They are widely used in several scientific and industrial fields, including microfluidics, optical devices, inject printing, energy harvesting, display technologies, and microfabrication.

Droplet actuation using electric methods has been a long-standing interest in microfluidics, and most often, it is limited by high operating voltages. The first actuation method explored in this thesis is based on interdigitated electrodes to generate a dielectrophoretic response. In order to apply an effective electrostatic force for droplet manipulation, the geometry of the electrodes must be optimised, which similarly leads to a lower operating voltage (as low as 30 V). Furthermore, microscale electrodes can be iteratively combined to realise larger arrays to move larger droplets. The iterative approach was developed for a large-scale device to manipulate droplets of varying size while keeping the actuation process simple.

In the second actuation method, a pair of microelectrodes separated by a variable gap distance generated an electrostatic gradient to produce a continuous droplet motion along the length of the electrode pad. The novel actuation method transported droplets of different size without active control. The droplet actuation was demonstrated on a larger scale using several platforms, including radial-symmetric, linear, and bilateral-symmetric droplet motion. An automated self-cleaning platform was tested in laboratory conditions and on the road. The technology has significant potential in the automotive sector to clean body parts, camera covers, and scanning sensors.

The electrostatic force applied across the droplet was calculated by placing a continuously moving droplet on a tilted platform and measuring the critical angle at which the droplet's gravity overcomes the opposing applied electric force. Several electrode designs were also considered to evaluate the effect of electrode geometry on the actuation force. The droplet actuation was also modelled using an analytical approach to estimate the critical signal frequency, maximum electrostatic energy, and maximum electrostatic force.

Lastly, a tilting micromirror platform investigated the dielectrophoretic response without measuring the droplet contact angle. The mirror platform is also suitable for other optical applications as it provides three axes movement for beam steering. The tilting platform enabled an angular coverage up to 0.9° (± 0.02°), with a maximum displacement of 120 μm. We also explored the feasibility of using a microhydraulic actuator based on liquid dielectrophoresis for a microfluidic application. The actuation method opens new possibilities for positioning and manipulating particles and components. These could be hazardous medical materials or even radioactive substances, where direct contact should be avoided.

Contents

Chapter 1
Introduction

1.1 Motivation & relevance

The conventional windscreen wiper was initially developed by Mary Anderson in the year 1903, to which the US. Pat. No. 743,801 was awarded in 1905 (see Figure 1).[9] The device used manual power to push a wiper mechanism to clear rain droplets on the windscreen. At least three other inventors patented a similar invention in the same year, including Captain Gladstone Adams of Whitley Bay, in northern England. Since then, the technology has been steadily improving, but the fundamental concept of mechanically removing droplets remained consistent with minor design changes.

The technological advances in sensor cleaning platforms pave the way for new autonomous driving vehicles. Sensor systems deliver pivotal data to autonomous cars, enabling automated functionalities. However, the deposition of surface contaminants such as rainwater, mud, sand, snow, which obscure the sensors, may cause a grave hindrance to vehicle safety systems. Currently, smart vehicles disable their active safety systems when the data from the sensors become unreliable. Hence, the engineering challenge is to clean the sensors in the most effective and timeliest manner to improve reliability for complete automated control.

The conventional cleaning platforms in the automotive industry are systems that remove surface contaminants by propelling abrasive materials through any of these methods: mechanical wipers, compressed air, and liquid blast nozzle systems. The significance of a self-cleaning platform will continue to increase as the industry moves towards higher levels of automation. Therefore, this thesis focuses on the development a new cleaning approach using electric fields to remove surface contaminants.

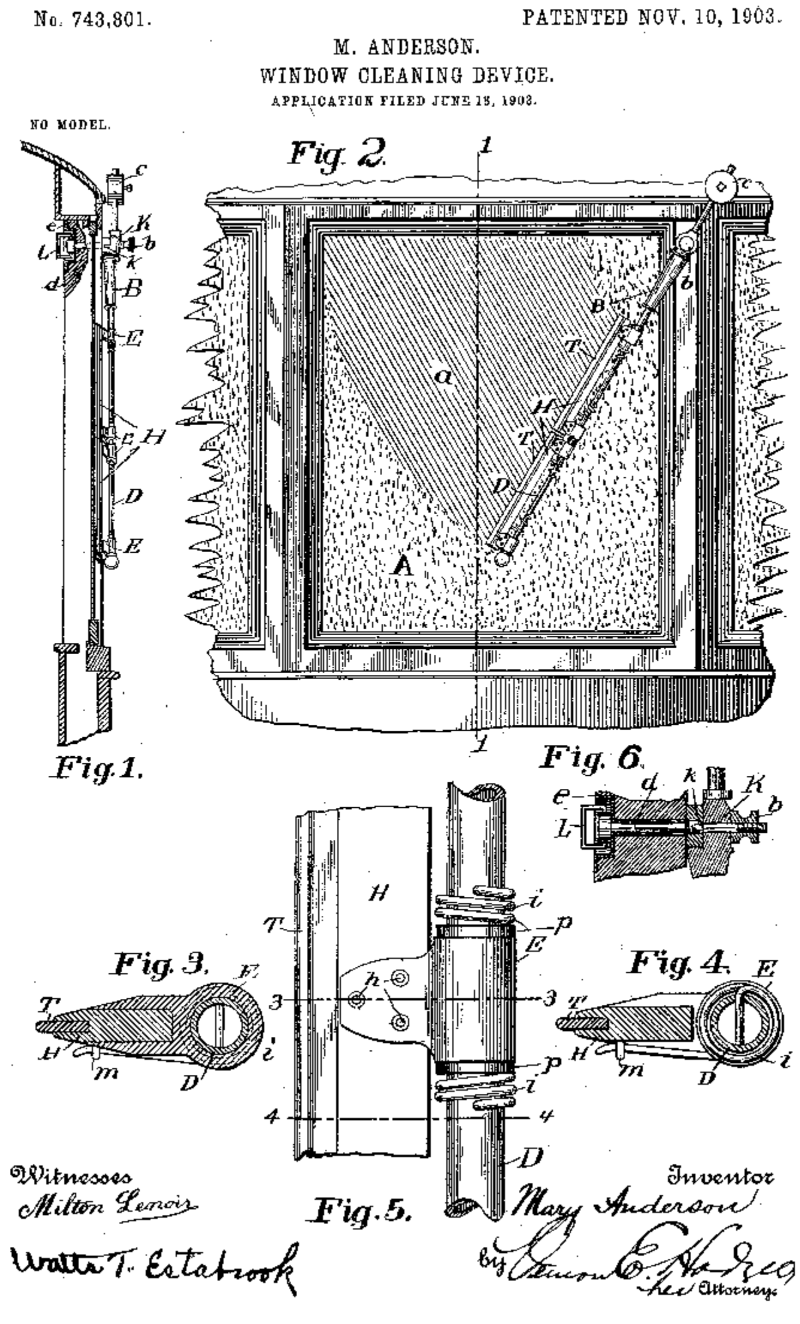

Figure 1 The general engineering drawing by M. Anderson for an invention of a window cleaning device using mechanical blades with several moving parts, US. Pat. No. 743,01.

The mechanical technologies have several drawbacks including, physical deterioration of wiper blades, aerodynamic noise, and mechanical damage to the glass. An electric cleaning platform without a moving part is appealing for automotive manufactures. They could precisely move rain and other contaminants to clean different body parts, e.g., windscreen, rear window, body parts, headlights, door mirrors, cameras, and scanning sensors. Moreover, a self-cleaning platform has several other applications. For example, in microfluidics, biomedical devices, optical cameras, and solar panels. In addition to other domestic products such as cleaning helmet visors and glasses.

Electrocapillarity was first studied in 1875 by Gabriel Lippmann, where he revealed that the capillary depression of an electrolyte solution could be changed by applying a voltage to it. The latest developments were re-established by Berge,[10] where he used a thin insulating layer and separated the liquid from the electrode, also known as electrowetting-on-dielectric (EWOD).[11] The insulating layer enabled higher operating voltages and prevented the chemical process of electrolysis.[12] The concept of using dielectric body forces to move dielectric droplets was first introduced by Batchelder in the 1980s.[13] This concept was later expanded to liquid-dielectrophoresis (L-DEP), actuating various dielectric liquids. This thesis focuses on developing different methods based on these technologies to clean surfaces.

An experimental approach by WCH Technologies Corporation in 2012,[14] presented an electronic wiper surface consisting of thousands of rectangular electrodes embedded across the windscreen. They claimed that the electric forces actuated water droplets at very high speeds (up to ten metres per second). However, the operating voltages were as high as 10 kV.

The work presented in this thesis aims to expand on the electric-driven droplet actuation techniques to explore new methods to reshape this technology with simpler control requirements for the automotive sector. Furthermore, the cleaning platform has to address several environmental and operational variables. For instance, producing a low-voltage continuous droplet actuation without a control system, independent of the droplet size, property, or position. Furthermore, the developments will likewise have other applications, such as droplet-based sensors, microfluidics, and optical communications.

1.2 Thesis structure

Chapter 1 - Introduction

The introduction chapter presents the research goals, physical phenomena, and reported current technologies. Furthermore, the research scope is discussed, highlighting the motivation and relevance of developing a new cleaning platform for the automotive industry.

Chapter 2 - Theoretical Background & Relevant Applications

This chapter reviews the fundamental theory of wettability, electrowetting, and liquid dielectrophoresis. Here, the different droplet actuation methods and their application are discussed. The concept of wettability and droplet contact angle is introduced to explain the balance of surface tension forces acting on a sessile droplet. Next, we evaluate the relationship between electrowetting and L-DEP via different approaches, reviewing their behaviour as a function of applied electric field and signal frequency.

Chapter 3 - Methodology & Materials

This chapter addresses the step-by-step device microfabrication process. Furthermore, it presents the experimental methods, testing liquids, and characterisation methods used in this thesis. Additionally, a testing stage and a modular electronic control system with a relay module are all described here. The simulation software packages are also presented with their key working function.

Chapter 4 - Droplet Actuation Methods

Three droplet actuation methods are presented here; the sequential activation of standard interdigitated electrodes (IDEs), continuous actuation of droplets using variable interdigitated electrodes (VIDEs), and hydrophobic coatings to remove droplets without any applied voltage. Furthermore, the working function of each actuation method is discussed here, highlighting the main strengths and weaknesses.

Chapter 5 - Electrokinetic Forces

In this chapter, we study the generated electrostatic forces by the VIDEs using an analytical and experimental approach. COMSOL Multiphysics simulated the electric field distribution and penetration across the VIDEs with different electrode geometries. The equivalent RC circuit network models estimated the critical signal frequency as a function of electrode geometry and droplet position. Additionally, the maximum electrostatic energy and force was estimated as a function of applied voltage and signal frequency. Lastly, a new experimental approach investigated the applied electric forces by considering a frictionless macro-size droplet situated on a tilted substrate.

Chapter 6 - Large-Scale Droplet Actuation

The main focus of this chapter is to examine the scalability of the proposed actuation methods. Large-scale droplet manipulation is critical in surface cleaning applications. Several devices are presented to simplify the actuation process and to reduce costs and complexity while improving reliability.

7.0 - Applications

This chapter explores several applications of droplet manipulation via electric fields. However, the emphasis of this work is dedicated to the droplet actuation for a cleaning platform. The proposed cleaning platform was tested in controlled conditions in a cleanroom, and on the road by mounting it to a car camera. An alternative application is also considered based on a tilting micromirror platform sensor. We presented a new optical device based on the L-DEP for beam steering. Furthermore, the device is also suitable for studying and characterising L-DEP without considering the droplet contact angle. Lastly, we propose a microhydraulic actuator for a microfluidic application based on the VIDEs configuration.

8.0 - Conclusion & Future Work

This chapter presents an overall summary of the findings and reflects back to the research goals. The final chapter evaluates the performance of each actuation method and provides several suggestions for improvement. Furthermore, this chapter includes several recommendations for a future study based on some preliminary experimental results.

Chapter 2

Theoretical Background & Relevant Applications

Various droplet actuation methods are investigated here, underlining their strength and limitations. This chapter reviews the relevant application and basic theory of wettability, electrowetting, and liquid dielectrophoresis. The concept of wettability and droplet contact angle is introduced to explain the balance of surface tension forces of a sessile droplet. The relationship between electrowetting and L-DEP is discussed using different approaches to study the electrokinetic response as a function of applied voltage, contact angle, electric field, and signal frequency.

2.1 Methods of droplet actuation

Developing new and improved droplet actuating methods is a fundamental concern, particularly in microfluidics.[15, 16] Various droplet-based applications can be realised when droplets are transported, mixed, and sorted.[17] The primary focus of research in microfluidics has been to scale down conventional systems and improve their power efficiency for new applications.[18] Digital microfluidics, an essential branch of droplet-based microfluidics, deals with the actuation of discrete droplets, such as electrowetting and magnetic actuation.[19] The recent developments in these technologies present an opportunity for a larger-scale application, i.e., to clean surfaces in the automotive sector. Different droplet actuation methods are addressed here, highlighting several limitations and possible ways to improve them.

This chapter discusses six droplet actuation methods suitable for a cleaning platform, including magnetic, electric, mechanical, acoustic, hydrophobic coatings, and thermal-based systems. Self-propelled droplet motion is possible via mechanical vibration of the substrate.[20] However, a conventional mechanical system with many moving parts (i.e., wiper blades) is the most reliable and mature technology supported with over 100 years of research and development. However, they are prone to a variety of problems, such as mechanical deterioration, aerodynamic noise, and physical damage to the substrate.[21, 22] Foremost, their age is a commercial disadvantage for a manufacturer trying to promote new technologies. For instance, developing new smart technologies for autonomous vehicles is essential in their business marketing strategy.

Acoustic-based droplet control is an attractive technology with good biocompatibility and low power consumption in several MEMS platforms.[23, 24] Furthermore, a British automotive manufacturer, McLaren Automotive, has also adopted an acoustic method (ultrasonic waves) to clean windscreens.[25] In their recent design, acoustic waves are generated using a piezoelectric actuator.[26] There are two main acoustic wave modes, surface acoustic wave and bulk acoustic wave.[15] Either of these, or a combination, has been used in many other microfluidic applications.[27] Recent developments in this field demonstrated a de-icing processes activated by surface acoustic wave (SAW).[28] Several factors regulate the actuation performance, including liquid volume/flow and properties, power, and electrode design. Generally, acoustic-based designs are sensitive to defects with a poor lifecycle and a basic requirement for a complex control system. Furthermore, the acoustic waves could accelerate the growth of micro-cracks found on the windscreen.

Droplet manipulation using magnetic fields is another common method with several biological and chemical applications.[29-31] Interestingly, water is diamagnetic and can be levitated in a very high magnetic field of 10 T (in comparison, the earth's magnetic field is 50 μT).[32] The gas/liquid interface can also be macroscopically deformed using a strong magnetic field by a phenomenon known as the Moses effect.[33] Magnetic fields have also been used in other innovative applications, such as controlling water droplets in a bulk ferrofluid and transporting them on a magnetic fluid/nanoarray interface so that the droplets follow the motion of the gradient interface using the magnetic fields.[34] The magnetic-based platforms require microfabrication with magnetic materials, which depending on the application can be expensive and problematic.

Microscale thermocapillary effect is a thermal-based droplet actuation method using either resistive heating or a directed laser beam.[35, 36] The micro-scale patterns require accurate alignments, and they are prone to many mechanical defects due to the thermal stress in the resistive heating technique. Alternatively, the laser beam method is more flexible with better control, assuming that the position is identified using a feedback control system, which can be expensive.[37]

Furthermore, a low friction droplet motion is possible with a selective leidenfrost effect.[38] Such a platform is unsuitable for a microfluidic or surface cleaning application because of high temperatures (hundreds of degrees) with significant power consumption. The American electric vehicle and clean energy company, Tesla motors, recently filed a US patent based on a thermal technology for cleaning surfaces using pulsed lasers.[39] However, the practicality of this new technology is widely debated because of high energy consumption, costs, and an operational requirement for a complex control system.

The electric-based technologies can be classified into two categories, electrowetting and dielectrowetting systems.[40] In recent years, droplet motion by electric means has gained more attention than other methods such as acoustic, magnetic, pneumatic, and thermal actuation. This is because of the excellent response time, reliability, and accuracy of the droplet actuation. However, the technology is limited by the dependence on the droplet chemical properties, size, and position. In addition to high fabrication and experimental setup costs.[41] Furthermore, hydrophobic coatings are similarly a sub-branch of the electric-based system. An extensive analysis of this technology is also discussed in the next section.

The primary objective of this thesis is to propose new methods to overcome the key limitations of the electric based systems. Thus, making the technology relevant and applicable in a surface cleaning application. The new design should employ lower operating voltages (at least 100 V or less). There is also a significant emphasis on simplicity to produce droplet actuation independent of the droplet size, position, and chemcial properties. Therefore, the optimum design should rely on a self-cleaning mechanism without active control. Furthermore, the cleaning platform should be scalable, from a few millilitres to clean miniaturise electronic sensors, up to several inches to clean large body parts.

2.2 Wettability and hydrophobic coatings

The wetting phenomena are some of the most significant concepts in hydro-physics with numerous practical applications.[42, 43] For example, making the rain droplets bead up on a freshly waxed car so that it is protected from rust. The different wetting behaviours are shown in Figure 2, demonstrating the droplet's profile as a function of surface energy.

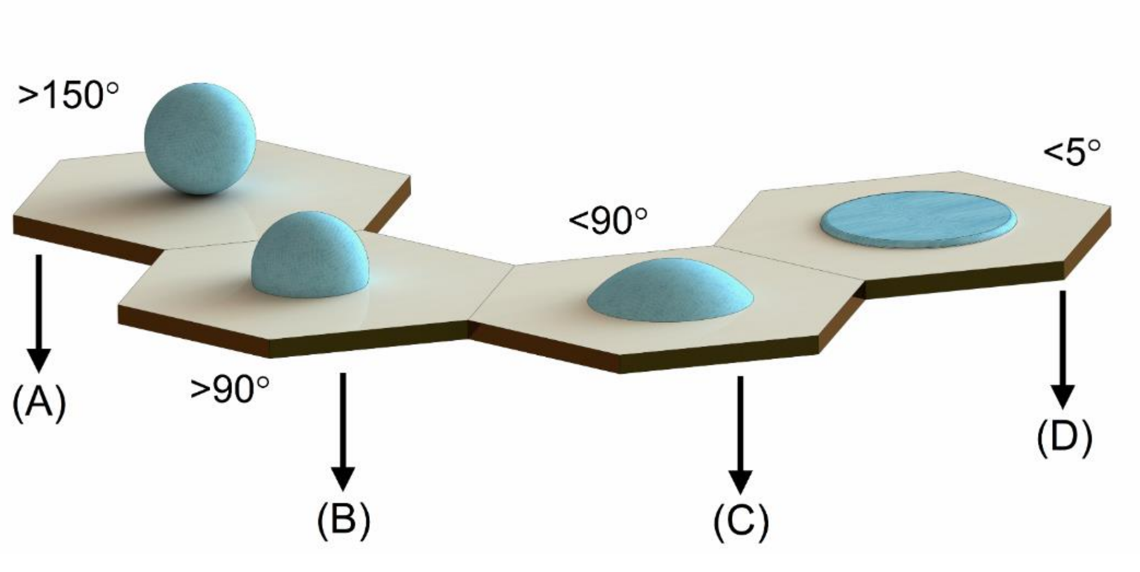

Figure 2 Schematic drawing showing the three main wetting behaviours. The droplet contact angle is the physical angle between the liquid and gas interface. (A) Superhydrophobic surface. (B) Hydrophobic surface. (C) Hydrophilic surface. (D) Superhydrophilic surface.

The definition of wettability can be simplified to the preference of a solid surface to be in contact with one liquid rather than another.[44] The term “preference” describes the equilibrium balance between the droplet’s solid, liquid, and gas interfacial forces near the droplet contact line. The spreading parameter (S) distinguishes the two opposite regimes of wetting. It is the difference between the surface energy of the substrate when it is wet and dry.

$$\mathrm{S} = \gamma_{\mathrm{SG}} - \gamma - \gamma_{\mathrm{SL}} \tag{1}$$

where γ_{SG}, γ, and γ_{SL} are the solid/gas, liquid/gas and solid/liquid interfacial tensions, respectively.[45] The spreading parameter should be negative to achieve partial wetting ($S < 0$), forming a hemispherical cap with an equilibrium contact angle, θ. This will translate into many fluidic behaviours with various applications.[44, 46] Droplets with a contact angle higher than 90° are classified as hydrophobic, and contact angles greater than 150° are considered superhydrophobic (see Figure 2 A, B). Any droplet impacting these surfaces will roll off or rebound like an elastic ball.[47] This behaviour is due to the reduced contact area between the droplet and the hydrophobic surface. In nature, lotus leaves have a unique self-cleaning ability to roll off any droplets, and thus, removing any dust particles on the leaves. This self-cleaning phenomenon is known as the “lotus effect” (see Figure 3).

On the other hand, to achieve total wetting, the spreading parameter must be positive, ($S > 0$), and the droplet will spread into a complete film to reduce its surface energy. Typical examples are when a high energy surface like glass or silicon substrates are in contact with liquids with low surface tension, such as ethanol or toluene. The system is considered hydrophilic when the contact angle is less than 90°, and supperhydrophilic if the angles are lower than 5° (see Figure 2 C, D). Hydrophilic properties is one of the central surface properties which play an essential role in several practical applications, including water treatment, oil in water separation, various fluid operations in biomedical devices, and pervaporation.[48]

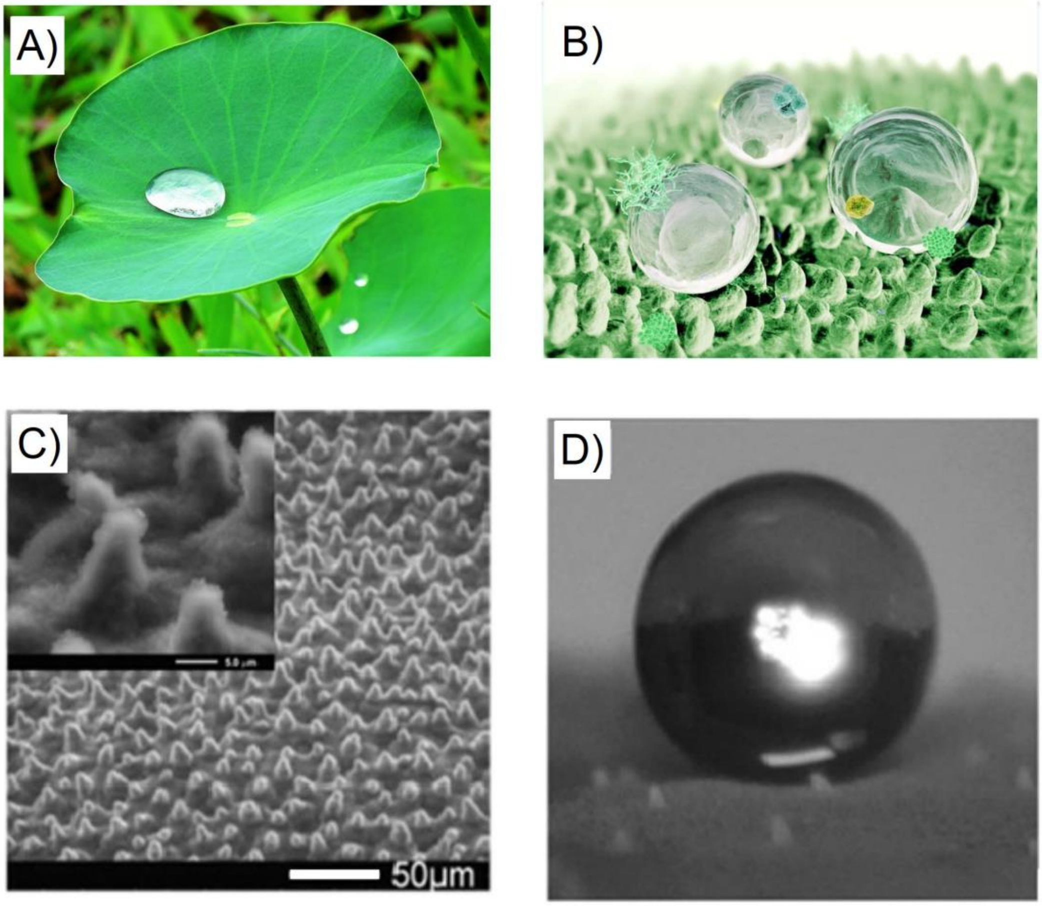

Figure 3 Phenomenon known as the “lotus effect”. (A) Droplets with a high contact angle formed on the leaf. (B) Schematic model showing the micro and nano scale features on the lotus leaf. (C) Scanning electron microscope images showing the pillars of a natural lotus leaf. (D) High contact angle (greater than 150°) of a water droplet on a lotus leaf. [6, 7]

The free energy of a resting droplet is the total sum of areas of the interfaces between the solid, liquid and gas phases.[49] Young’s equation elaborates on this relationship, which relates contact angle to the interfacial forces between the gas, liquid, and solid phases (see Figure 4 A). Young’s equation (Eq. 2), is derived by balancing the horizontal forces acting on the droplet’s three-phase contact line.[49] This equation is also the fundamental basis for the Lippman equation that predicts the dielectrowetting and electrowetting behaviours as a function of contact angle.

$$\cos\theta = \frac{\gamma_{SG} - \gamma_{lS}}{\gamma_{lG}} \tag{2}$$

Furthermore, recent experiments revealed that Young's equation show a limited scope of the problem with minor details missing. The fundamental theory was reviewed from a thermodynamic point of view by employing energy minimisation and variational approach.[50] The derivations offer a deeper understanding of droplet contact angle.[50] The new approach likewise provides a theoretical basis for rough or chemically heterogeneous surfaces.

The theory of surface tension states that there are fewer molecules near the surface of a droplet than in the bulk, and that it is always moving towards equilibrium to reduce the total surface area.[51] The Bond number expresses the importance of gravity to the surface tension force acting on a droplet,[52] $B_o = \Delta\rho g R^2/\sigma_{LG}$ where $\Delta\rho$ is the density difference between the surrounding medium and the droplet, R is the droplet's radius of curvature, g is the acceleration generated from gravity, and σ_{LG} is the liquid-gas surface tension. Majority of electrowetting studies use a Bond number less than unity to disregard the effect of gravity.[52] Many insects and arachnids in nature have evolved numerous micro/nanoscale morphological adaptations to rest or move on liquid surfaces.[53]

According to Young's law, there is only one stable contact angle, whereas a droplet resting on a tilted substrate can have multiple static contact angles.[54] The definition of contact angle hysteresis is the tendency of a droplet to roll off a surface. It is calculated by subtracting the advancing contact angle away from the receding contact angle.[55] The standard method to calculate the contact angle hysteresis is using the "tilting cradle method" which is the difference between the contact angles at the back and front edge of the droplet when it is moving on a tilted surface (see Figure 4 B).[56] An alternative method is the "volume changing method".[57] In this method, the liquid is steadily injected and extracted from a droplet resting on a static substrate. The highest contact angle before the droplet starts to move is known as the advancing angle, whereas the smallest angle is the receding angle.

The droplet sliding angle, is a characterisation method to measure the droplet mobility on a substrate (see Figure 4 B).[55] High droplet mobility requires a low adhesion between the substrate and the droplet, such that the droplet can slide off the substrate at a small inclination angle. On the other hand, hydrophilic surfaces with significant surface adhesion have a high sliding angle.

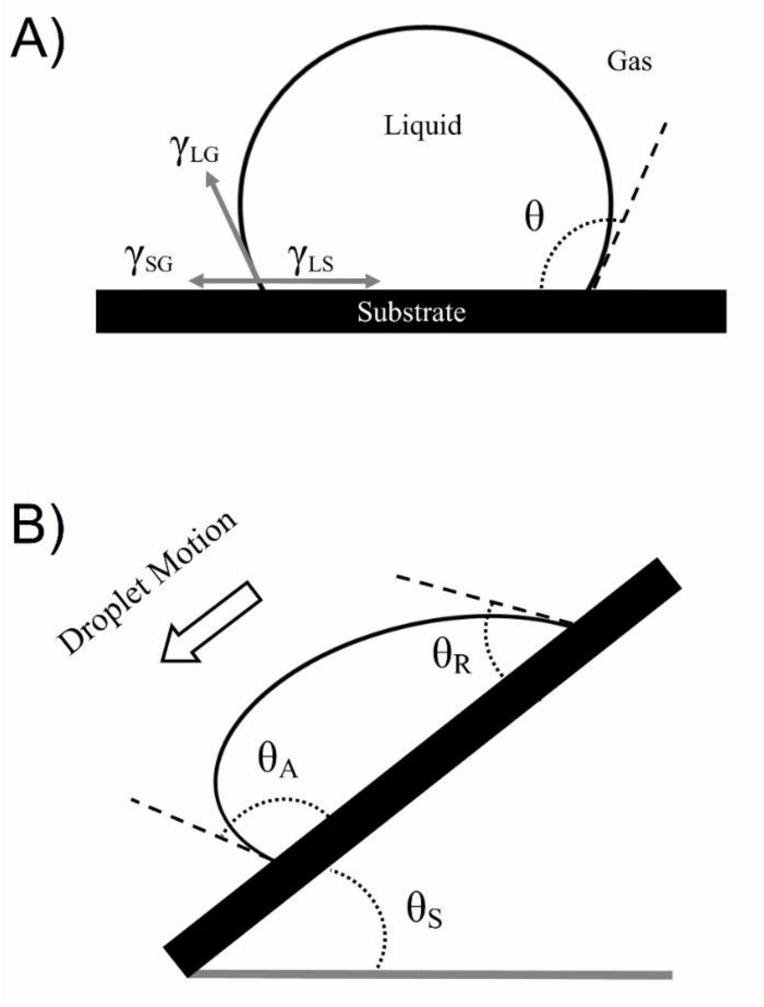

Figure 4 (A) Schematic showing three main interfacial energy phases (γ) of a resting droplet on a surface surrounded by gas. The contact angle (θ) is the angle between the liquid/gas and liquid/solid interfaces. (B) Side view schematic showing a droplet on a tilted surface with a sliding angle (θ_S), advancing angle (θ_A), and receding angle (θ_R).

It is also essential to consider the effect of surface roughness on the contact angle.[58] There are three fundamental models that describe the effect of surface roughness. In Cassie-Baxter's model, the droplet can rest on the peaks of a rough surface. Therefore, reducing the total surface contact area (see Figure 5 A).[59] In Wenzel's model,[60] the droplet is in contact with the entire surface, and consequently increasing the total interfacial contact area (see Figure 5 B). Finally, the surface roughness can be modified with a slippery liquid-infused porous surfaces (SLIPS) to minimise the contact line pinning and contact angle hysteresis,[61] (see Figure 5 C).

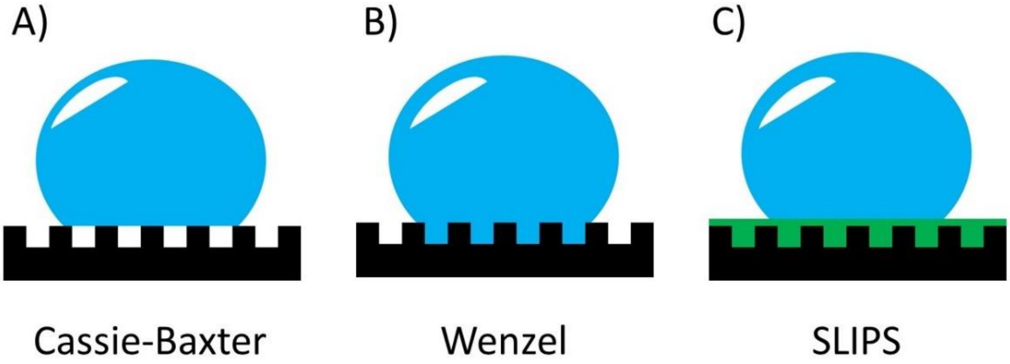

Figure 5 Schematic drawing showing different contact angle scenarios. Water droplet in (A) Cassie-Baxter state, (B) Wenzel state, and (C) on a SLIPS.

Typically, the contact angle hysteresis rises for a Wenzel case and decreases for a Cassie-Baxter case.[59] Rough features in the Wenzel case can pin the droplet at a point when they are in contact with the corners of a rough surface. This concept is even more complex in a 3D scenario, as the droplet is in contact with a combination of pillars and holes in different locations.[62] Naturally occurring surfaces have a complex topography.[63] In reality, a combination of both Cassie-Baxter and Wenzel models can be used to describe these surfaces.

Surfaces with complex topographies are more beneficial at generating high contact angles with low contact angle hysteresis. Note that this relies on the droplet remaining in the Cassie-Baxter state. There are several fabrication methods to create hydrophobic coatings. several good examples are textiles and fibers, etching patterns, particles, crystal growth, templating, phase separation, lithography, and diffusion-limited growth.[64] To produce a superhydrophobic surface, the surface chemistry needs to be hydrophobic with a roughness on a scale smaller than the liquid capillary length to reduce the total surface contact area.[65]

Hydrophobic coatings have applications in various fields such as anti-corrosion, anti-icing, self-cleaning, medical equipment, textiles, and all sorts of industrial surfaces.[66] Although commercially available cheap hydrophobic coatings such as Rain-X are appealing, they are similarly susceptible to chemical degradation.[67] Furthermore, a fast-moving vehicle cannot use a coated windscreen with a windscreen wiper because of the “Latitude problem”. This is when the wiper pulls the rain droplets back across the windscreen to the driver’s viewing area, and it can be very distractive and dangerous.

The continuous droplet motion without any applied external forces has applications in microfluidics for various chemistry and bioassay studies.[68] The latest developments in the literature are based on a surface tension gradient from hydrophobic to hydrophilic, to produce a self-propelled droplet motion.[69, 70] The droplet movement requires surface modification via either topography or chemical variations to create an energy imbalance across the droplet.

The large-scale droplet motion demands a sufficiently high wetting gradient with a small contact angle hysteresis. Superhydrophobic coatings are the preferred choice to produce a maximum wetting gradient with a low contact angle hysteresis.[71] However, these surfaces are prone to morphological defects (from abrasion or vibration) with a small lifespan and limited application outside of any controlled environment. Despite extensive progress, majority of the effective surface modifications eliminate the device transparency, such as fabricating nano-wires or micro/nano-pillars.[72] There are also new methods based on the wettability gradient to transport microscopic liquid layers using a unique topological structure.[73] The topological fluid diode enabled long-distance directional liquid transport.

2.3 Electric-driven actuations

The main disadvantage of using hydrophobic coatings by topographical patterns or chemical deposition is their static nature, which limits their application. They are similarly prone to declining performance over time because of degeneration, contaminants, and defects. In contrast, electric-driven droplet actuation allows repetitive change of contact angle with many unique advantages such as reliability, accuracy, active control, and repeatability.[74]

There are two primary electric-based methods to modify the surface wetting, and they are dielectrowetting, and electrowetting.[75, 76] They are both an electrohydrodynamic response of the liquid to an applied electric field. The main distinction between them is that dielectrowetting is governed by liquid-dielectrophoresis, which is a bulk force generated by polarising the dipoles in the liquid using a non-uniform electric field.[77] While electrowetting occurs from the movement of free charges in a conductive medium.[78] In principle, the electric field penetrating the droplet contact line attracts both the polarised dipoles and the free charges within the medium. Therefore, for a complex liquid such as rainwater, the dielectrowetting and electrowetting effects are the high- and low-frequency responses to an applied electric field in the same system.[79]

2.3.1 Electrowetting

One of the most widely used methods for manipulating droplets is electrowetting. The roots of electrowetting started with the electrocapillary phenomenon, first described in 1875 by Gabriel Lippmann. His study concluded that the capillary depression of mercury in contact with an electrolyte solution could be modified by applying a voltage difference between the electrolyte and mercury. Since then, the phenomenon has been widely studied and adapted to remain relevant for various applications by a steadily growing community of researchers.[80]

The most critical variation of electrowetting is based on employing an insulating layer over the electrodes to provide electrical, chemical, and physical protection. This configuration is also known as electrowetting on dielectric.[81] Prominently, the insulating layer in the EWOD configuration prevents the chemical process of electrolysis, in which ionic substances are broken down into simpler substances by an electric current.[82] This is a major barrier in many applications of electrowetting, particularly manipulating droplets for chemical or biomedical analysis.

The droplet manipulation using electrowetting is achieved using different electrode designs (see Figure 6). The two predominant configurations are a planar electrode design,[83] also known as an open design, and a sandwich structure,[84] where the droplet is grounded using a top-plate and an array of electrodes situated under the droplet. Electrowetting has also been demonstrated on curved surfaces (convex or concave curvatures) using flexible substrates.[85] Flexible substrates have several advantages, such as cheap production, ease of processing, mechanical flexibility, lightweight, etc.[86] Furthermore, transparent devices have been demonstrated in several studies using graphene or indium tin oxide (ITO).[87, 88]

In contrast to hydrophobic coatings, EWOD has proven successful in many respects, particularly a large contact angle variation (tens of degrees).[89] Furthermore, the use of an insulating layer in EWOD further extends the limitations of contact angle saturation due to higher input voltages (several hundred volts).[90] EWOD enables high switching speeds up to the droplet hydrodynamic response (approximately 300 milliseconds), in addition to long term stability after thousands of switching cycles without noticeable changes.[91] Other advantages of EWOD include device miniaturisation, easy operation, low power consumption, and reversibility.

Continuous electrowetting is a suitable candidate for large-scale applications for reasons of simplicity without size limitations.[92] The initial concept of the continuous actuation was achieved using liquid metals in a closed channel.[93] The electrowetting technique relied on a voltage difference drop across a thin layer of aqueous electrolyte to produce droplet motion. The introduction of nonlinear circuit elements enabled a continuous droplet motion. Embedded diodes achieved continuous droplet motion using induced electro-osmotic and electrowetting effects.[94-96] Note that continuous electrowetting using embedded diodes require a conductive testing liquid and a safety enclosure to prevent electrical shock.

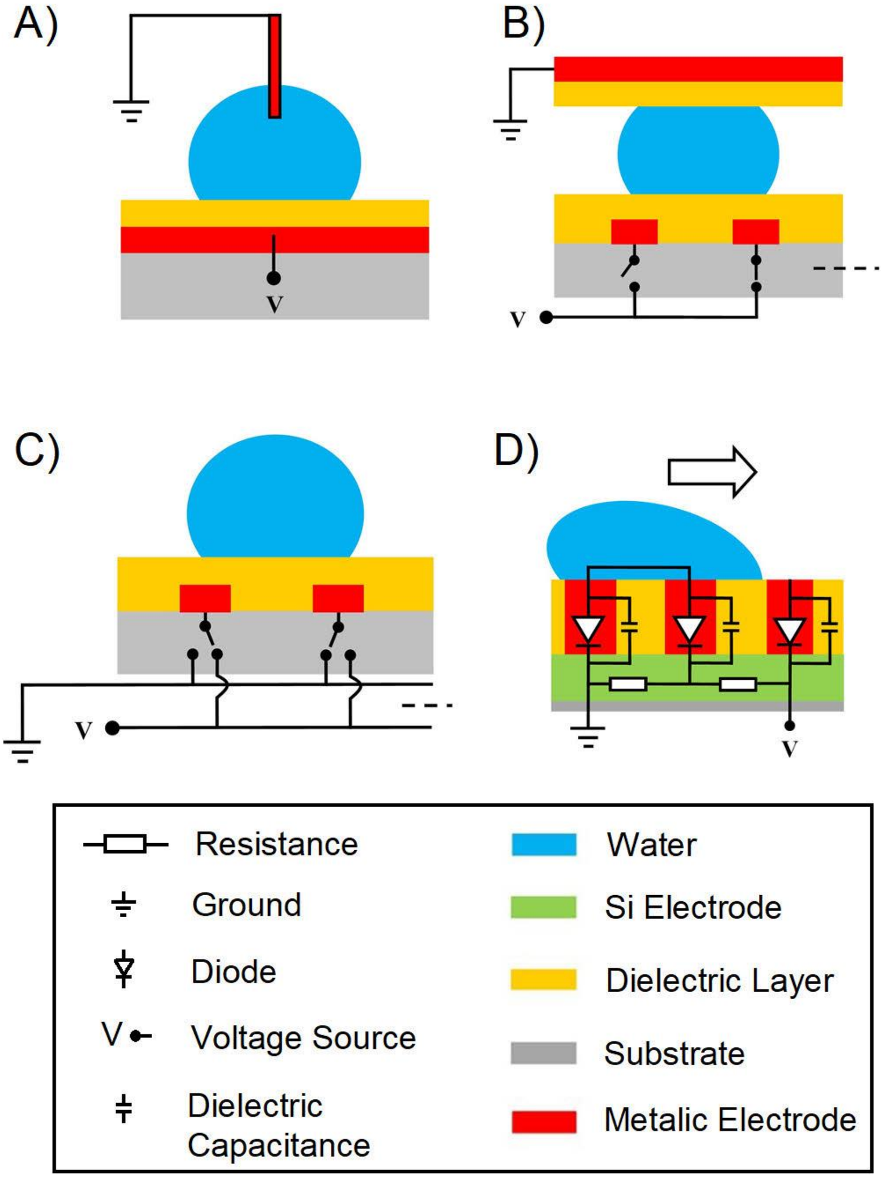

Figure 6 Schematic drawing showing different electrowetting electrode configurations. (A) Droplet on a surface with a voltage source connected from above using a conductive rod. (B) EWOD sandwich structure when the droplet is placed between two parallel plates. (C) Open structure electrode configuration where the voltage and ground signals are connected via a single layer. (D) Continuous electrowetting device with diodes. The actuation direction is shown by an arrow.

Electrowetting has not only been a critical scientific phenomenon, but it is also a viable technology for several applications, such as electronic displays, energy harvesting, and microfluidic systems.[97-99] The variable-focus lens is another applications of electrowetting, in which the liquid movement changes the focal length of the lens.[100] Furthermore, digital filters with electrowetting functionality has been reported for separating oil-water mixtures and cleaning oil spills.[101]

There are several reported programmable droplet actuating platforms, delivering precise control on different surfaces.[52, 102] The primary application emerging from this technology is digital microfluidics (DMF).[103] A typical DMF device consists of an array of electrodes, in which droplets containing samples (i.e., reagents) are dispensed from a reservoir, transported, combined, or even split into smaller droplets for analysis.[104] These are critical operations for a typical lab-on-a-chip device.[105] Additionally, microfluidic chips based on EWOD have also been demonstrated for medical diagnostics with combined droplet generation and manipulation functions.[106] There are reported EWOD studies focusing on biomedical technologies,[107] and a control mechanism in a channel-based microfluidic system.[108]

Moreover, there are reported electrowetting-based display panels with applications in electronic paper.[109] The principle of operation is an oil-based droplet with a dissolved dye that is confined to a square pixel. Likewise, the electrowetting displays can produce arbitrary colours by dividing each pixel into subpixels and arranging multiple oil layers with a variety of dye colours.[110] Furthermore, the reported reflectivity of these electrowetting-based displays is at least four times stronger than a typical liquid crystal display which also needs polarisers, and so is inherently less reflective than an electrowetting based display.[99]

Other recent developments have also demonstrated micro-scale electrowetting-based hydraulic actuators (linear and rotational microhydraulic actuators), presenting a novel method to convert electrical power to mechanical power.[111] Electrowetting is similarly applicable to mechanical-to-electrical energy conversion.[112] The energy conversion method is based on the reverse electrowetting, in which electrical energy is generated using an array of moving droplets. Furthermore, an electrowetting battery is also reported consisting of an electrode having a nanostructured surface.[113]

Electrowetting is also applicable in optical communications demonstrated by an electrowetting based optical switch with an adjustable aperture.[114] The principle of operation for the optical switch is based on creating an aperture through which light can pass by replacing a water droplet with a non-transparent oil film. Additionally, an adaptive optical beam steering has also been reported based on an electrowetting driven fluidic rotor.[115] The study verified the actuation of a macro-size structure with a water droplet.

Electrowetting creates an electric double layer by applying an electric field between the liquid-solid interface to reduce the droplet contact angle.[52] The electric double layer is an electrostatic structure that forms on the surface when an electric field is applied across a conductive liquid.[116] Therefore, a cloud of charged molecules will accumulate near the liquid-solid interface, [117] as depicted in Figure 7.

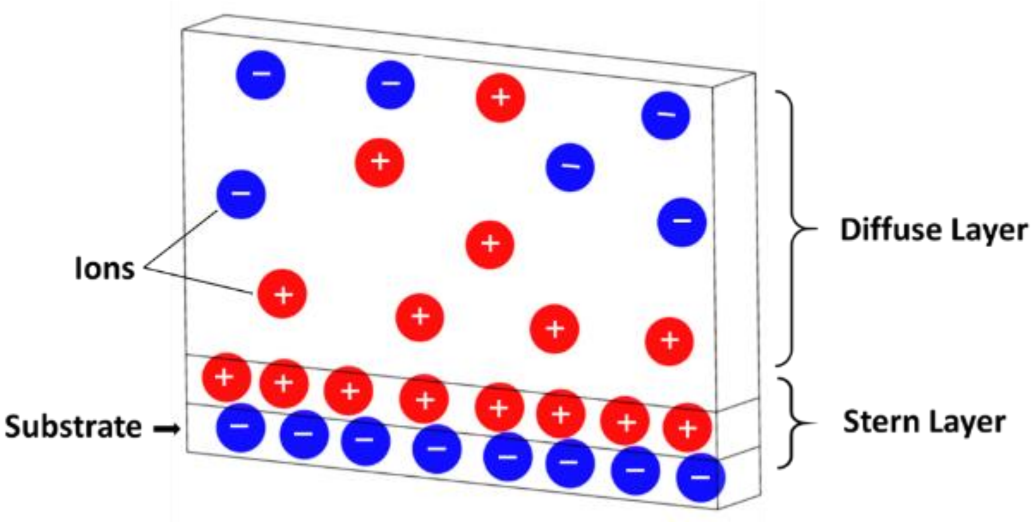

Figure 7 The electric double layer near the liquid-solid interface due to adsorption of the charged ions with two combined layers: a diffuse layer and a stern layer. The electric double layer can also be illustrated as a parallel-plate capacitors.

The electric double layer can be illustrated as a parallel-plate capacitor in series. The stern layer is a capacitive structures formed by a thin concentrated layer of oppositely charged ions to the substrate.[117] The thickness of this layer (typically, 1 to 5 angstroms) depends on the size of the ions with a much lower relative permittivity than the bulk liquid because of the orientation of the molecules.[118] The other capacitor is known as the diffuse layer with a decaying potential.[119] Furthermore, the capacitance of the double layer deviates for surfaces with different wetting properties, i.e., the hydrophobic surfaces with a smaller interface contact area.

The original Lippmann's derivation of the electrowetting equation is based on interfacial thermodynamics, that a reduction in surface tension is possible with an applied voltage. Lippmann's experimental set up was based on bare mercury exposed to an acidic electrolyte solution and the charge accumulation from the double layer reduced the surface tension. The effect is almost immediate after applying a voltage, and the effective interfacial tension, ${\sigma_{\mathrm{sl}}}^{eff}$, is defined as:

$$\mathrm{d}{\sigma_{\mathrm{sl}}}^{eff} = -\rho_{\mathrm{sl}}\mathrm{d}U \tag{3}$$

where ρ_{sl} is the surface charge density of counter-ions, and U is the electrochemical potential. The voltage dependence of ${\sigma_{\mathrm{sl}}}^{eff}$ is derived by integrating (Eq. 3). The Helmholtz model can be used to solve this equation, where the counter-ions are in a thin double layer with a distance, d_H away from the substrate. As a result, the capacitance per unit area of the double layer can be expressed as, $C_H = \frac{\varepsilon_0 \varepsilon_l}{d_H}$, where ε_l is the dielectric constant of the liquid.[120]

For a case where the metal is in contact with an electrolyte solution, the electrolytes gather on the metal interface, and the charge accumulation reduces the surface tension. Therefore, the electrolyte concentration (ρ_{sl}) on the metal interface varies with the applied potential, ($\rho_{\mathrm{sl}} = C_H U$). As a result, combining the expressions for C_H and ρ_{sl}, and integrating both sides, expresses the surface tension before and after the electric potential is applied, as it is shown in Eq. 4:[121]

$$\sigma_{\mathrm{sl}}{}^{eff}(U) = \sigma_{\mathrm{sl}} - \int_{U_{\mathrm{pzc}}}^{U} C_H U\, dU = \sigma_{\mathrm{sl}} - \frac{\varepsilon_0 \varepsilon_1}{2 d_H} (U - U_{\mathrm{pzc}})^2 \qquad (4)$$

Here, ε_1 and ε_0 are respectively the dielectric constant of the double layer and the vacuum permittivity. U_{pzc} is the potential difference of zero charge, which is the potential without the spontaneous charge accumulation. Therefore, an estimation for the change of the contact angle is obtained as a function of the applied voltage when combing Young's equation with (Eq. 4):[52]

$$\cos\theta = \cos\theta_{\mathrm{Y}} + \frac{\varepsilon_0 \varepsilon_1}{2 d_{\mathrm{H}} \sigma_{\mathrm{lv}}} (U - U_{\mathrm{pzc}})^2 \qquad (5)$$

Where θ and θ_{Y} are the contact angles after and before applying the voltage, respectively. The double layer is relatively small for classic electrowetting, 2 nm or less, demanding a low applied voltage to avoid system failure. On the other hand, depositing a dielectric layer in the EWOD configuration (see Figure 8) introduces a capacitive structure, ($C_{\mathrm{d}} = \varepsilon_0 \varepsilon_d / d$), near the insulator-liquid interface, where ε_d is the dielectric constant of the dielectric layer. Furthermore, the EWOD configuration can be modelled as two capacitors in series and the total capacitance can be simplified to just C_{d}.[122]

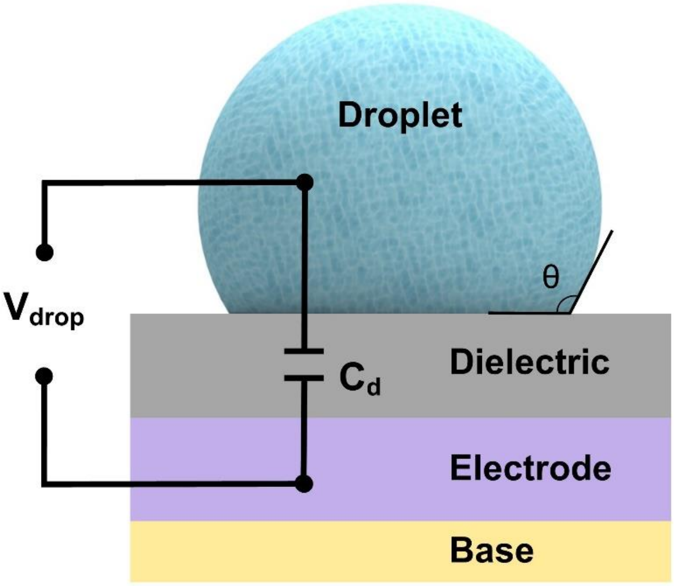

Figure 8 The capacitive structures in the EWOD configuration. The electrowetting effect changes the droplet contact angle by applying a voltage difference between the electrode and a droplet.

The penetration of electric field can be neglected under the assumption that the liquid is a perfect conductor. Therefore, the voltage drop occurs within the insulating layer, and by assuming U_{pzc} is zero, (Eq. 4) can be modified into:

$$\sigma_{\text{sl}}{}^{\text{eff}}(U) = \sigma_{\text{sl}} - \frac{\varepsilon_0 \varepsilon_d}{2d}(U)^2 \tag{6}$$

The length of the double layer is longer in the EWOD configuration (typically up to 1 μm), and the EWOD equation is derived when combining (Eq. 6) with (Eq. 2).[122] The dimensionless electrowetting number (η) is introduced in this equation to define the strength of electrostatic energy with respect to the surface tension. Furthermore, it is dependent on the material properties of the insulating layer.

$$\cos\theta = \cos\theta_{\text{Y}} + \frac{\varepsilon_0 \varepsilon_d}{2d\sigma_{\text{lv}}}(U)^2 = \cos\theta_{\text{Y}} + \eta \tag{7}$$

The close observation of (Eq. 7) summarises three main points for achieving the largest EWOD effect. Firstly, the initial contact angle should be as large as possible. Furthermore, the dielectric permittivity of the dielectric layer and its thickness play a major role. Lastly, a higher applied voltage should be employed to generate larger changes in the contact angle. However, the EWOD effect has two main limitations. Firstly, the applied voltage will no longer decrease the contact angle pass a certain limit, known as the contact angle saturation.[90] Secondly, high voltages could produce irreversible damage to the dielectric layer, resulting in a dielectric breakdown.[123, 124]

2.3.2 Dielectrophoretic actuation

Dielectrowetting is based on dielectrophoresis (DEP) which refers to the electromechanical force generated when polarising a medium using non-uniform electric fields.[76] Liquid dielectrophoresis (L-DEP) was initially performed by Pellat in the 18th century. The phenomenon was somewhat unexplored until Jones developed a pump mechanism by applying a potential difference (over 19 kV) between two parallel plates.[125] It was later verified that miniaturising the electrodes (two co-planar electrodes) created a "wall-less" electrode to actuate an oil stream against gravity using a few hundred volts.[4] In principle, the lower applied voltage stems from the scaling of the L-DEP force, which is related to the applied electric field ($F_{L\text{-}DEP} \propto E^2$).[77]

Following this, several other groups explored the phenomenon and confirmed that the change of contact angle using L-DEP followed a [$\cos(\theta) \propto V^2$] relationship, similar to electrowetting.[126] L-DEP behaviour was investigated using liquid crystals to create a liquid lens.[127] Later, L-DEP gained additional attention for overcoming the limitation of contact angle saturation.[128] The hemispherical droplet achieved complete wetting using high voltages (i.e., 300 V).[129] This work later established the interface localised L-DEP to control the liquid/air surface curvature for optical applications, such as programmable diffraction grating.[130]

Microfluidics is the control and handling of liquid samples on a small scale. It is divided into two categories, digital microfluidics and continuous microfluidics.[76] L-DEP manipulation has attracted a great deal of research interest, notably in the fields of lab-on-a-chip microfluidics.[131] The L-DEP based microfluidic devices demonstrated the ability to dispense and manipulate droplets down to the order of picolitres. The actuation of deionised (DI) water and other dielectric solutions in a microfluidic system has also been demonstrated using L-DEP forces.[132] The actuation of larger droplets using dielectrowetting was presented using interdigitated electrodes.[132] The study verified the splitting, joining, and moving of dielectric droplets in a discrete manner, operating in excess of 340 V. This study was followed by investigating anti-biofouling performance with a slippery lubricant infused surface using electric fields.[133]

Additionally, dielectrowetting is suitable for a variety of optofluidic devices.[134] Other studies have also explored the application of dielectrowetting in creating optical switches, for example, to block laser beams or generating single pixel colour arrays.[135, 136] Moreover, dielectrowetting can also control the liquid's solidification process when exposed to ultra-violet (UV) light or heat to determine the profile of the cured solid.[137] This technique removes the requirement for a photolithographic mask in the microfabrication process.

The induced drift motion of charged particles suspended in polar solutions under the influence of an electric field is the basic definition of electrophoresis.[138] The particle size and charge can increase the actuation velocity, but it is also limited by the balance between the electrostatic and viscous drag forces.[139] Figure 9 shows a polarisable particle inside a uniform (electrophoresis) and non-uniform (dielectrophoresis) electric field.[3] Unlike electrophoresis, the polarisation contour shows that there is no force acting on the particle when the electric field is uniform. However, when a particle is placed inside a non-uniform field, a dielectrophoretic effect is realised (see Figure 9 B). The force acting on one end of the dipole is unequal to the force acting on the other end, and a dielectrophoretic net force arises along the gradient of the field.[140]

$$\mathbf{F}_{Dipole} = (\mathbf{p}.\nabla)E \tag{8}$$

The bold letters here are referred to as a vector quantity. Here, $\mathbf{p}$ is the dipole moment, and E is the magnitude of electric field. Note that Eq. 8 shows that the net force is zero when the electric field is uniform. The electric field around the sphere in figure 9 (A) is not uniform, but is instead distorted by the presence of the sphere. Thus, this does not result in a net force on the particle due to symmetry.

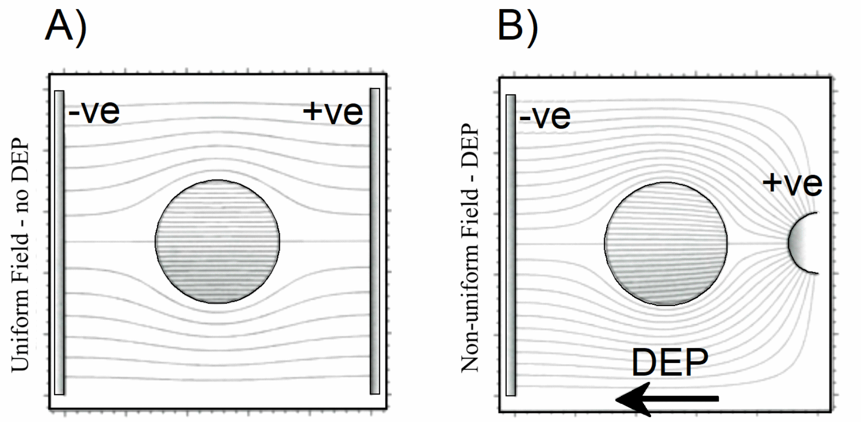

Figure 9 Schematic showing the polarisation of a particle suspended within a uniform and non-uniform electric field. (A) The uniform electric field induces polarization (no DEP), and (B) non-uniform electric field inducing a DEP force. The DEP force generated in the non-uniform electric field because of the gradient of the electric field.[3]

The primary testing liquid in this thesis was water. Relative permittivity of water varies from 87.9 to 69.8 when increasing the temperature from 0 °C to 50 °C, respectively.[141] From a practical perspective, water (rainwater) consists of many dissolved molecules and ions. In most cases, the electrical conductivity of water is affected by dissolved impurities. The process of ion hydration is when the water molecules (dipoles) are attracted to dissolved ions, i.e., surrounding them. Hence, the ionic charges move to minimise the electric field in the bulk of the liquid water. Consequently, employing an A.C. signal frequency enables the manipulations of various conductive and dielectric liquids.

The DEP effect (see Figure 9) is based on the actuation of particles suspended in a liquid medium. Therefore, the theoretical approach is no longer valid when considering a macroscopic droplets on a solid substrate. The calculations are based on the basic assumption that the particle is minutely small. Therefore, the gradient of the electric field does not change at the length scale of the particle diameter. Hence, the problem is simplified to a single dipole moment vector, but this assumption is misleading for a large droplet. This is particularly important for electrode fingers in the micro-scale, and therefore, the droplet cannot be treated as a single dipole moment vector. Consequently, the actuation of a liquid droplet using a non-uniform electric field is defined as the liquid dielectrophoresis phenomenon. In the case of L-DEP, the liquid does not require physical contact with any specific surface for the actuation of a droplet.[126] The L-DEP effect is independent of the electrode and liquid polarity, but the bulk force continues to deviate towards the region of highest electric field.

Contrary to the EWOD, the Joule heating effect in L-DEP can be significantly high, notably for water.[142] Moreover, this effect is also dependent on how much electric current flows. Joule heating refers to the process where the electric energy from the electric fields is converted into heat within the liquid. In a perfectly dielectric liquid, this effect is local within the electric field’s penetration depth. Nevertheless, this effect should be considered for some applications where it is a design limitation, such as MEMS devices, or rather beneficial in automotive applications, i.e., to melt ice layers.

We considered three theoretical models to study L-DEP. Firstly, the interface localised theorem, then the electrostatic forces, and lastly, Pellat's experiment with two parallel plates. There is also a recent development providing a numerical simulating based on the Lattice-Boltzmann method to study the L-DEP force within a multiphase dielectric liquids.[143] The L-DEP and electrowetting effects overlap in some scenarios, and it is the signal frequency, electrode geometry, and liquid properties that differentiate the two actuation methods. L-DEP actuation is possible for many dielectric liquids, and it is influenced by the ratio between the permittivity and liquid surface tension, as depicted in Table 1 for different liquids.

Table 1 Material properties for different testing liquids, collected from a referenced source.[144] The surrounding fluid is air. Note that the value of liquid permittivity is tested in the kilohertz signal frequency spectrum at room temperature.

Testing liquids	$\boldsymbol{\varepsilon_l/\varepsilon_0}$	$\boldsymbol{\sigma_{\mathrm{lv}}}$ (mN/m)
Propylene carbonate	66.1	40.9
Propylene glycol	27.5	35.5
DI Water	80.0	72.0
Mineral oil	2.1	29.3
Hexadecane	2.05	27.1
Isopropyl alcohol	19.92	22.0
Hexane	1.88	18.4

2.4 Interface localised L-DEP

The magnitude of L-DEP depends on the permittivity of the liquid and surrounding fluid, in addition to the applied electric field. The L-DEP effect is strictly localised, and it is the strongest at the three-phase contact lines, and rapidly diminishes along with the liquid-gas interface. The droplet spreading behaviour can be explained by combining the L-DEP theory with the fundamentals of wettability. To relate dielectrophoresis within the context of wettability, it is first assumed that a thin layer of dielectric liquid with a depth h, is having an electric potential that decays exponentially, $U(z) = U_0 \exp(-2z/\delta)$.[129, 145] The electric field can be determined using $\boldsymbol{E} = -\nabla U$, and the electrostatic energy per unit contact area, w_E, stored in the liquid is then given by integrating the dielectric energy density, and can be simplified into the following equation:[146]

$$w_E = -\frac{\varepsilon_0 \varepsilon_l {U_0}^2}{2\delta}\left[e^{-\frac{4h}{\delta}} - 1\right] \tag{9}$$

Furthermore, the droplet size is much larger than the penetration depth of the electric field. As a result, Eq. 9 can be simplified into, $w_E = -\varepsilon_0 \varepsilon_l {U_0}^2/2\delta$. The penetration depth of the electric field δ, localises the effective changes in the energy to the vicinity of the liquid-solid interface. Thus, a localised potential with an exponentially decaying profile is appropriate in this model. The extent of the wetting for a droplet is described by the balance between interfacial tension forces of solid, liquid, and gas interfaces to satisfy the conditions for minimum energy.

In a scenario where the droplet is spreading, the effect of increasing the droplet contact area by a small area ΔA, is better defined by substituting the γ_{SG} interface by the γ_{SL} interface. Therefore, the change in the free surface energy ΔF, can be defined as, $(\gamma_{\mathrm{SL}} - \gamma_{\mathrm{SG}})\, \Delta A$. Also, the liquid creates an additional liquid-vapour surface area as it moves along the surface, and the surface free energy increases by the following expression, $\gamma_{\mathrm{LG}} \Delta A \cos\theta$. Moreover, assuming that there is an electric field penetrating the liquid, the L-DEP energy in the newly expanded region changes from its surrounding value in the gas to that in the liquid, defined by the following expression, $-\varepsilon_0(\varepsilon_l-\varepsilon_V){U_0}^2\Delta A/2\delta$. Therefore, Young's law can be modified based on the L-DEP principle to describe the new equilibrium contact angle,[146]

$$\cos\theta(U)=\cos\theta_{\mathrm{Y}}+\frac{\varepsilon_0(\varepsilon_l-\varepsilon_V)}{2\gamma_{\mathrm{LG}}\delta}(U)^2 \qquad (10)$$

As was previously discussed for electrowetting, capacitance is the ratio of capacitive energy per unit area to the liquid-gas interfacial energy per unit area. There is an effective capacitance of the electrodes under a liquid, and an effective capacitance for the electrodes under air. In this approach, the difference of approximations of the two capacitances is used.

2.5 Electrostatic forces

The theories mentioned so far consider the change in the contact angle as a function of applied voltage, but they fail to define the actuation forces exerted on the liquid. The problem can also be simplified to a fluidic flow resulting from electromagnetic forces. The magnetic fields are ignored because the dynamic currents in the microscale systems is minute.[52] Therefore, electrostatic is the only governing principle. Technically speaking, a persistent body force is always acting on a droplet located in an electric field. Aside from the mechanical forces, i.e., pressure and shear stress, a Coulombic force is exerted from the interactions between the free charges in the liquid, thus generating an electrostatic force.

There are two ways to describe the actuation force in the electrostatic field. The first method is the Thomson's theorem, in which the total energy of the electrostatic field is kept at a minimum by modifying the geometry of the system and thus inducing a mechanical force.[147] The second method is based on a theory coupling the electromagnetic fields to the mechanical forces, also acknowledged as the Lorentz force law, ($\mathbf{f}^b=\rho_{\mathrm{f}}\boldsymbol{E}$).[148] The force density, $\mathbf{f}^b$ per unit volume is valid in a stationary electrostatic field, where ρ_f is the charge density per unit volume, $\boldsymbol{E}$ is the electric field intensity, and the bold letters are vector quantities.

However, apart from the response of the free electric charge density, there is also another term for the polarisation density in the presence of the electric field gradient. The most frequently used formulation is the Korteweg-Helmholtz body force density for simple liquids:[149]

$$\mathbf{f}^b = \rho_\mathrm{f}\boldsymbol{E} - \frac{1}{2}E^2\nabla\varepsilon + \nabla\left(\frac{1}{2}\boldsymbol{E}\cdot\boldsymbol{E}\frac{\partial\varepsilon}{\partial\rho}\right) \tag{11}$$

where ρ and ε is the mass density and permittivity of the fluid, respectively. The electrostriction in the electric force (third term) can be neglected when the liquid is incompressible and homogeneous. Hence, the body force density in the electrowetting actuation can be written as, ($\mathbf{f}^b = \rho_\mathrm{f}\boldsymbol{E} - 0.5\,E^2\nabla\varepsilon$).[149] In contrast, in the case of dielectric liquids ($\rho_\mathrm{f} = 0$), the force generated by the free charges is also neglected, and the L-DEP force (ponderomotive force density), is deducted to, ($\mathbf{f}^b$= $0.5\,E^2\nabla\varepsilon$). Note that the magnitude of the electric field should be as high as possible either by increasing the applied voltage or modifying the electrode geometries to generate the largest dielectrophoretic response.

The electrostatic pressure on the body's surface is proportional to the electric field intensity. Consequently, there is a body force towards the largest electric field intensity, which is also the very definition of dielectrophoresis. The body force density equations can also be written as the divergence of a stress tensor, also referred to as the Maxwell stress tensor.[150]

2.6 Parallel plates experiment

Pellat's experimental set-up in 1895 consisted of an applied voltage difference between two parallel plates (see Figure 10). The experimental approach is unique since the calculations are based on the rise of the liquid between two parallel plates.[18] Therefore, this approach is commonly used for the frequency-dependent analysis of electrowetting and L-DEP. In the original set-up (see Figure 10 A), the dielectric liquid rises against the pull of gravity using a dielectrophoretic body force.[151, 152]

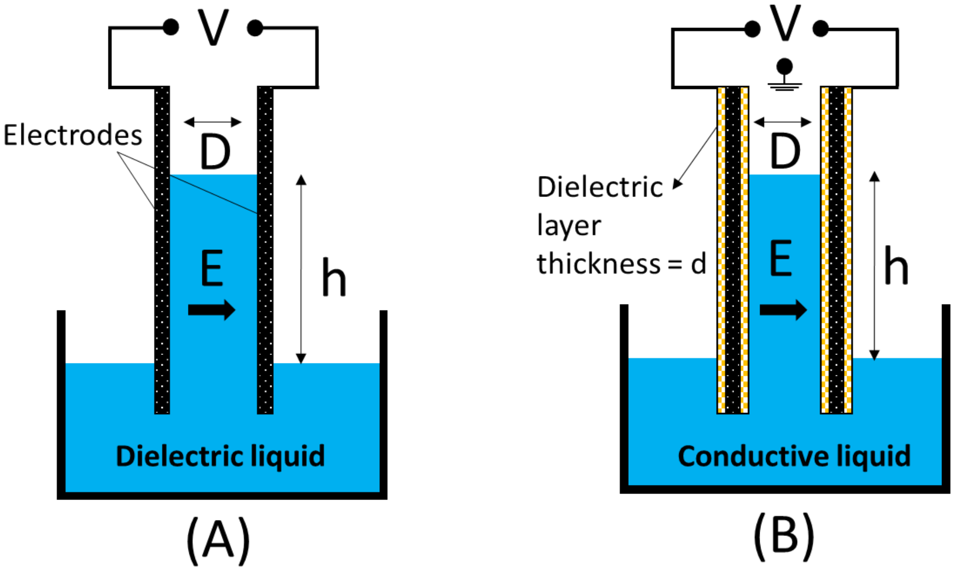

Figure 10 (A) The original Pellat's experiment showing the electromechanical response of a dielectric liquid between two electrodes. (B) The modified Pellat's experiment showing the rise of conductive liquid between two electrodes.

The modified Pellat's experiment by T. B. Jones demonstrated liquid actuation up the parallel plates using conductive liquids by coating the electrodes with an insulating protective layer (see Figure 10 B). The distance between the two electrodes D, is much greater than the thickness of the insulating layer d, ($D \gg d$). Jones approach considered the influence of capillarity on the hydrostatic equilibrium. Hence, the liquid rise h is expressed by the rise in the normal capillary effect h_{cap}, and then an additional rise from the applied voltage h_{EWOD}. The EWOD effect is determined using a free body diagram balancing the surface tension force at the contact line against the gravitational force. Therefore, the liquid rise against gravity is in principle a voltage-induced decrease of the liquid contact angle.[152] Note that the electric field in a parallel configuration is not uniform across the entire length of the electrode (closer to the end), which is a contributing factor in the actuatiuon process.

2.7 Frequency dependent actuation

The actuation behaviour depends on the time average voltage (RMS) for electrowetting responses with a signal frequency exceeding the hydrodynamic response time. This is only true if the liquid is a perfect conductor, and the basic assumptions in the Lippmann equation are not violated. However, this notion breaks down upon increasing the signal frequency.[79]

At moderate frequencies, the ions in the liquid follow the electric field and as a consequence, screens the electric field from penetrating the inner bulk of the liquid. This is only valid up to a critical frequency ω_c, where the liquid is a perfect conductor at values far below ω_c, (electrowetting is dominant).[5, 153] On the other hand, at a much higher frequency $\omega >> \omega_c$, the electric field penetrates the liquid interface, and generates a bulk L-DEP force. Furthermore, the critical frequency depends on other factors such as the geometric and electric properties of the dielectric layer.[52]

The frequency-dependent transition from a conductive to a dielectric behaviour for various salt concentrations has already been reported.[154] The basic modelling in these experiments was based on the assumption that the liquid layer is acting like a capacitor in parallel with an ohmic resistor (see Figure 11 A). Furthermore, there was a frequency-dependent analysis of the electric force moving the liquid upwards against the force of gravity. Their study presented an expression based on the balance of these forces that, $h = K(\omega)U^2$, with an analytical function $K(\omega)$, highlighting the low- and high-frequency limits.[154] All material parameters and the frequency dependence are contained in the coefficient.

Figure 11 B illustrates the values for the analytical function $K(\omega)$ derived from the experimental data by measuring the rise of the height of the liquid layer versus voltage curves. Note that the DI water curve changes after 1 kHz, whereas the KCl solution changes well beyond the 100 kHz limit.

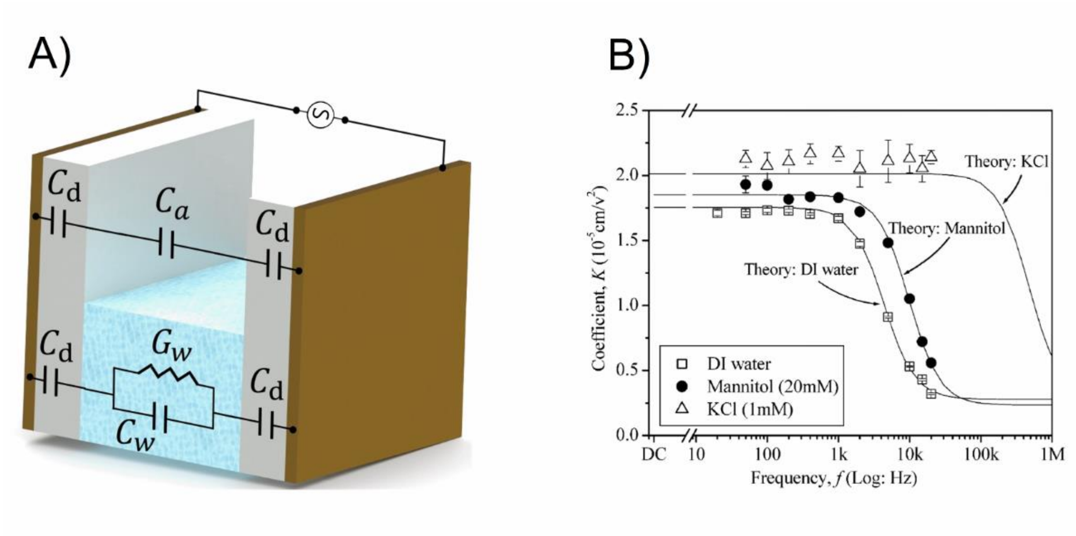

Figure 11 (A) Recreated schematic diagram showing the equivalent RC circuit model of a parallel plate experiment. (B) Graphical data showing values for the analytical function K(ω), derived from experimental data.[5]

Electrowetting is a robust phenomenon with some dependence on liquid properties. Even though DI water exhibits some electrowetting characteristics at low frequency (less than 1 kHz), it is more common to use liquids with higher conductivity, such as aqueous salt solution.[5] In contrast, the properties of the dielectric layer are far more important with regards to the signal frequency. The optimisation of this layer can improve the overall performance by reducing the operating voltages.

In principle, publications by Jones reported some clarity on the driving actuation mechanism as a function of signal frequency for a range of dielectric and conductive liquids.[40, 79] Figure 12 A demonstrates a cross-section of the tip for a dielectrophoretically driven water strip by an applied AC voltage using a planar electrode configuration. The equivalent resistor–capacitor circuit (RC circuit) network model demonstrates this relationship as a function of capacitance in the dielectric layer C_d, capacitance in the liquid C_w (dielectric nature), and the liquid conductance G_w (conductive nature). They reported that a dielectrophoretic response was possible using strong electric fields with an appropriate signal frequency to generate a strip of liquid injected from a larger droplet. The estimated critical frequency separating the low- and high-frequency is expressed as:[4]

$$\omega_c = \frac{G_w}{(C_d/2+C_w)} \tag{12}$$

Similar to the previous configurations, the frequency-dependent actuation at a much higher frequency $\omega \gg \omega_c$, the electric field penetrates the liquid interface, generating a bulk L-DEP force pulling a stream of liquid away from the mother droplet (see Figure 12 B).

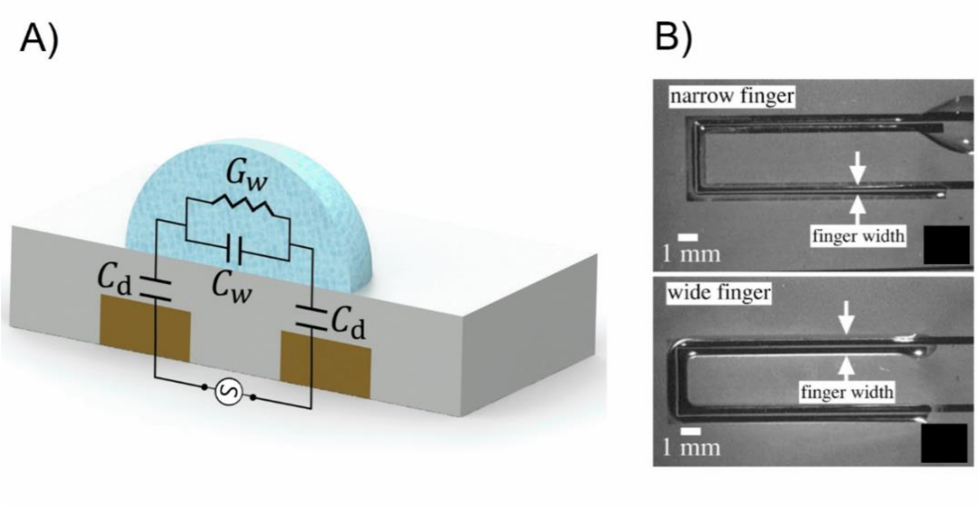

Figure 12 (A) The equivalent RC circuit network model and a cross-section of a droplet resting on two electrodes covered by a dielectric layer. (B) The top view of experimental data showing the liquid layer getting pulled away from a mother droplet at a signal frequency of 100 kHz with an applied voltage of 700 V. [4]

2.8 Summary

This chapter demonstrated an overview of the relevant fundamental theories. Firstly, the theory underlying the wettability and droplet contact angle was discussed. Additionally, we studied the electric double layer, from which the basic electrowetting equation is derived. The theory reviewed the relationship between contact angle and applied voltages. The dielectrophoretic actuation based on L-DEP was considered using a bulk force and an interface localised approach. This was followed by a comprehensive breakdown of electrostatic forces and the impact of signal frequency on the actuation principle.

Chapter 3
Methodology & Materials

This chapter addresses the device fabrication process, including film deposition and photolithography. The characterisation methods are explained, covering two main areas: surface topography scans and droplet characterisation. Furthermore, the testing set-ups are presented, highlighting the testing stage, a modular electronic control system and a relay module. This chapter also presents additional information about the simulation software packages and various testing liquids used in the experiments.

3.1 Fabrication methods

3.1.1 Metal deposition

One of the fundamental steps in fabrication of any electronic device is thin-film deposition. Several different techniques can be used to deposit thin films. Electron beam evaporation,[155] also known as E-Beam evaporation, is a vapour deposition technique in which a source material is bombarded with an electron beam from a charged tungsten filament to evaporate the material for film deposition. Figure 13 A shows a Moorfield Minilab E-beam evaporator (part of a cluster system with sputter coater chambers). Figure 13 B shows a schematic of the working function, and key components of the evaporator, including a chamber, vacuum pump, adjustable holder with samples, a hot cathode, a crucible with the source material, electron beam, and a magnetic beam deflector.[156]

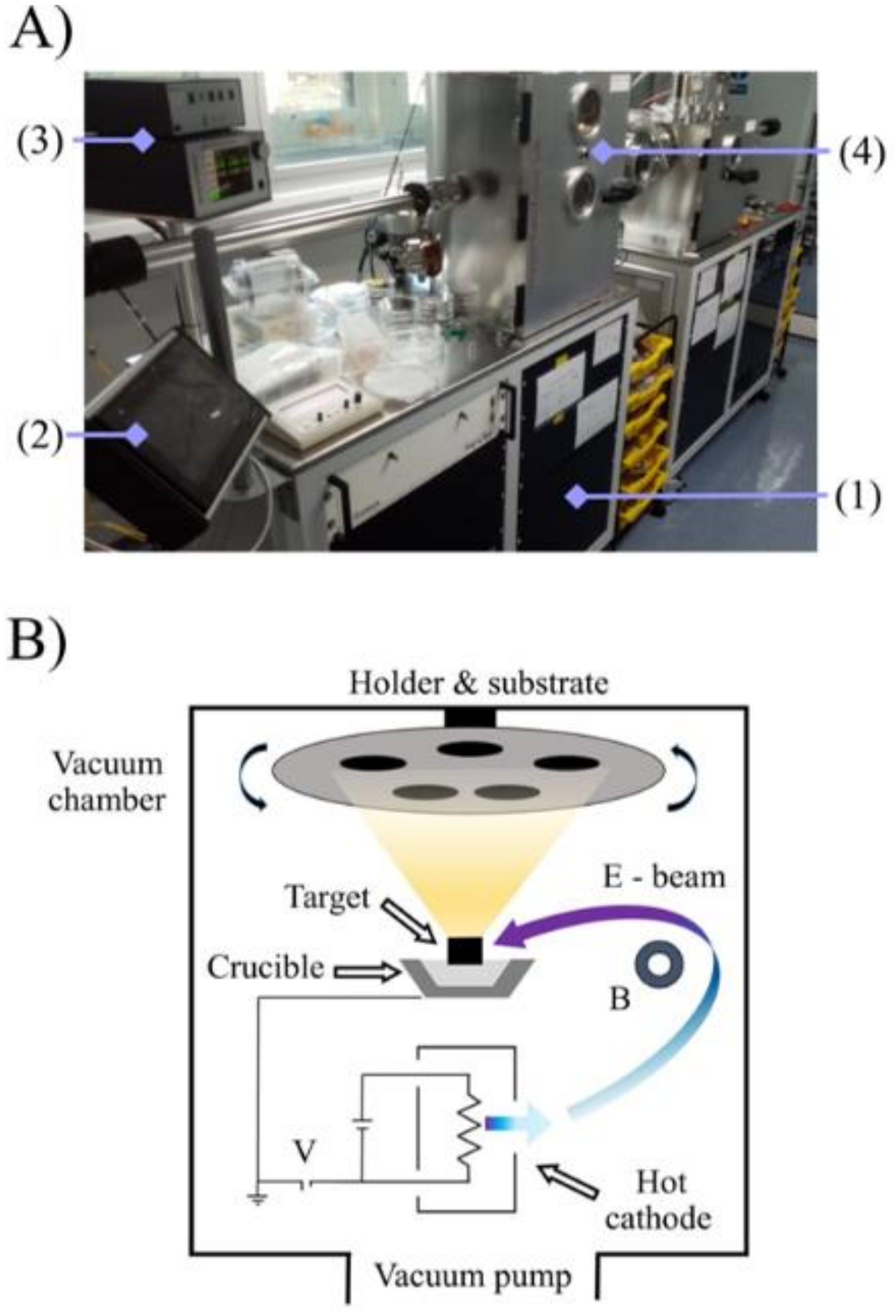

Figure 13 (A) Moorfield minilab electron-beam evaporator, (1) electrical control unit, (2) LCD pad to control the evaporator, (3) quartz crystal deposition control display, (4) chamber. (B) Schematic showing the working function and key components of the E-beam evaporator. The deposition is carried out in a vacuumed chamber. A high voltage is applied to the filament, accelerating the electrons towards the crucible containing the source material. The crucible was water cooled. A strong magnetic field is employed to direct the electrons to the ingot location. The evaporated material coats the substrates placed inside a spinning holder. There is also a shutter to stop the evaporation and a crystal film to measure the deposition thickness.

A high voltage source (kilovolts) accelerates the beam towards the source material via a magnetic field. The heated electrons lose their energy rapidly when they contact the source material, and their kinetic energy is converted into thermal energy to heat the source surface. When the bulk temperature is sufficiently high enough, the vapour will be produced to coat the substrates in the chamber. Furthermore, a portion of the incident electron energy is lost from the discharge of secondary electron emissions and x-rays.

Initially, the substrates are cleaned thoroughly and fastened to the substrate holder without introducing any contamination. Furthermore, the holder is set to a spin-mode, where the holder is spinning during the deposition to aid uniformity. The deposition process requires a high vacuum chamber (in the orders of 10^{-7} Torr). The vacuum chamber was necessary to reduce the collisions of the source atoms with the atoms of the background and, similarly, to reduce contamination for a high-quality deposition. The deposition rate, chamber pressure, and other settings are monitored using a touch LCD panel. Furthermore, the power control rate and the system had a feedback loop to maintain a range.

A range of different metals was deposited using this technique, including aluminium, copper, and gold. The selection of a crucible material depends on the source material, and how it will interact with the crucible and the required thermal load requirement to melt it. The thickness and deposition rate can be monitored using a quartz crystal. The quartz crystal was frequently changed after multiple depositions, and regular checks were also made using atomic force microscopy (AFM) to ensure the deposition thickness was accurate. The physical movement of the crystal and thermal stress failures were sometimes responsible for deposition thickness variations.

Before starting the deposition process, the shutter was opened to reset the thickness meter to zero. Additionally, the deposition rate was set to the desired value and then opened the shutter in the chamber. After the deposition process, the electron beam and rotation of the holder was switched off for 30 minutes to allow the chamber to cool down. Subsequently, opening the vent valve enabled the pressure in the chamber to reach the atmospheric level to open the safety door. The samples were removed carefully using a tweezer and placed in a sample holder for further treatment.

E-Beam evaporation is reliable, robust, and commonly used in many industries, particularly in aerospace and thin-film solar applications.[156] The main advantage of using this deposition technique is the low level of impurities in the thin film with adequate control of the deposition rate.

3.1.2 Spin coating

The spin coating technique is widely used in microfabrication to deposit uniform thin films onto the substrates.[157, 158] The machine used for spin coating is called a spin coater. The centrifugal force from the rotation is sustained while the fluid comes off the substrate until the desired thickness is achieved. The solvents used in the photoresist are typically volatile and simultaneously evaporate. Generally speaking, thinner films are fabricated by employing a higher angular speed of spinning, or alternatively increasing the spinning time. Additionally, the film thickness is also dependent on the concentration of the solvents in the solution.[159]

The corrosion-proof Laurell WS-650-23NPP spin coater was suitable for coating different photoresist layers. The processor controller unit can store up to fifty custom programs suited for multi-stage processes. The spinner consists of a standard chuck (50 mm to 150 mm) with a maximum spin speed of 6000 RPM. The coating technique is essential in the photolithography process and the fabrication of insulating layers for high-voltage applications.[160, 161]

Initially, the photoresist bottles were left to reach room temperature to ensure consistent uniform layers. The process entails applying a small amount of coating material across the substrate using a clean micropipette. The material is then spread across the surface uniformly by the centrifugal force at low speeds (typically less than 500 RPM), followed by a high-speed spin (up to a few thousand RPM). The typical fabrication recipes are found on data sheets provided by the manufacturers.

Strict cleaning protocols were followed to prevent fabrication defects from contamination. For instance, surface contamination on insulating films such as dust acted similar to a large pinhole, which reduced the thin-film integrity and voltage breakdown limit.

3.1.3 Cleaning process

The initial steps in the fabrication process were cleaning the samples, and upholding strict protocols to limit the number of fabrication defects in the final device. The main substrate in the fabrication process was borosilicate glass, but other materials were also explored, including soda-lime glass, laminated glass, polyethene terephthalate (PET), and paper.

The glass substrates were cleaned in a piranha solution (3:1 mix of sulfuric acid: hydrogen peroxide) for 20 minutes to remove any debris and inorganic contaminants on the surface. After cleaning, the samples were washed thoroughly (30 minutes) using DI water multiple times inside an ultrasonic bath. Finally, the substrates were dried at room temperature using a filtered nitrogen to ensure they have no residual water. The PET flexible substrates were cleaned by isopropanol alcohol (IPA) inside the ultrasonic bath for 30 minutes and subsequently blow-dried with nitrogen to remove contaminants.

The fabrication process was carried out immediately after the cleaning process to minimise random defects. After the cleaning process, the effect of dust and other contaminants depositing on the samples were critical. Furthermore, the cleaned samples were kept in the fume hood and transported inside a sealed container. The cleaning process of the photomask was also critical. Note that random defects (stains) on the photomask resulted in systematic defects on the fabricated samples.

There are several ways defects on the photomask can damage the sample. Primarily, the deposition of dust and other particles is the common cause for failure. Substrates contaminated with dust and organic impurities were cleaned using acetone in an ultrasonic bath and then rinsed with IPA. The second important factor was the deposition of photoresist residual during the exposure process. The photomask was dipped inside a solution of 1165 remover and rinsed thoroughly with DI water to remove any residual photoresist. Lastly, hard physical contacts produced permanent physical defects on the photomask, i.e., scratches.

Other sanitising protocols safeguarded the fabrication process. These included wearing new nitrile gloves, cleaning the beakers after use, separating the beakers by the chemical process, regular cleaning of the tweezers and other fabrication tools, labelling all of the samples and beakers, good handling of the chemicals to avoid cross contamination, and lastly, avoid breathing over the samples.

3.1.4 Photolithography

Photolithography, also referred to as ultraviolet (UV) lithography, is a microfabrication process to pattern features on a substrate or thin film.[162] Figure 14 shows the EVG 620 photolithography system with a schematic showing the principle working function: UV light source, photomask, and a substrate with a resist layer. The fabrication process uses UV light to transfer a geometric pattern from a photomask to a photosensitive chemical (also known as a photoresist). A range of chemical treatments can either etch the exposed sections or enable deposition of new layers for a lift-off process, where the photoresist layer underneath the undesired pattern is removed via a photoresist stripper. A variety of lithography and nanolithography techniques have been developed in recent years, such as X-ray lithography, electron beam lithography, ion projection lithography, and extreme ultraviolet lithography.[163-165] This technique is instrumental in the electronics industry to fabricate various products in the semiconductor sector, a $400 Billion industry worldwide.

The cleaning process before the photolithography was essential for a successful fabrication as any contaminants on the surface block the light photons. Thus, producing large defects (a few hundred micrometres). The substrate was initially heated to drive off any moisture (unless the sample was already dry). Depending on the material, this heating process can be up to 150 °C for ten minutes and then allowed to reach room temperature.

A photomask is an opaque layer with transparencies that allow UV light to travel through a defined pattern. The masks were initially designed on the computer using the CleWin software package. The design of the photomask was dependent on the size of the chuck and the substrate. Other design considerations included allowing extra space for alignment marks and adequate spacing between each device. The digital designs were then outsourced to a third-party company (Micro Lithography Services limited) to transfer them into a high-resolution film photomask. The film layers were then transferred onto a glass photomask (with chrome patterns) for long term use.

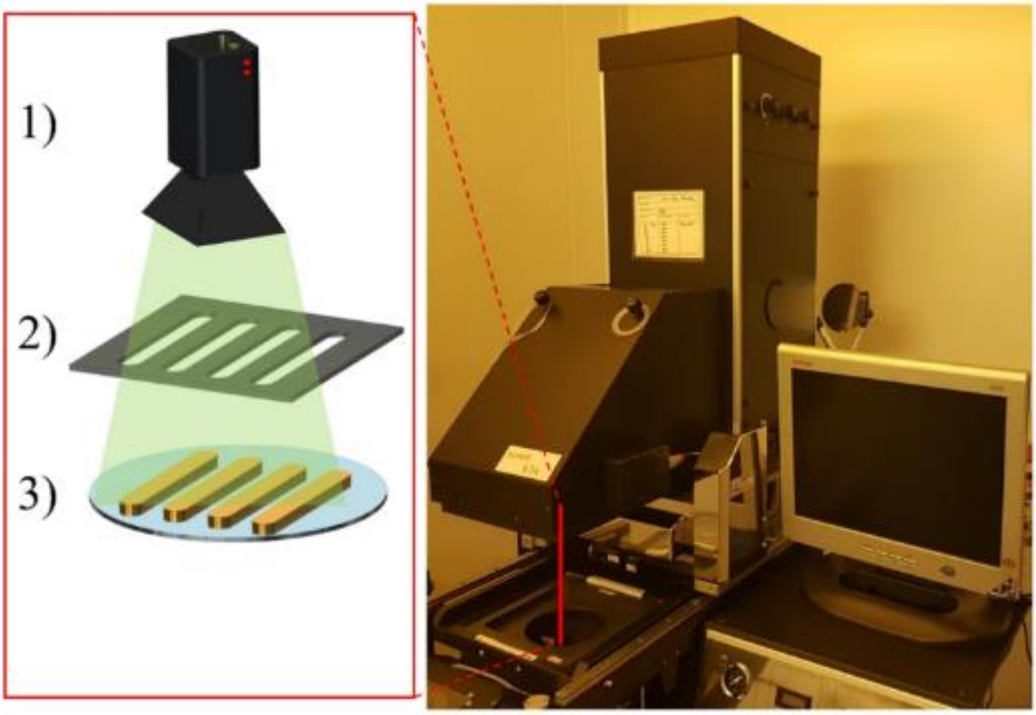

Figure 14 EVG 620 photolithography manual mask aligner system. The work function can be simplified as: (1) an apparatus for shining UV light with a controlled intensity via an optical lens, (2) a photomask that functions similar to an optical mould to fabricate features, and (3) a sample substrate coated with a photoresist layer.

Standard photolithography was used to fabricate the electrodes (see Figure 15 for the general overview of the process). 70 nm of aluminium was deposited using E-beam evaporation on a cleaned glass substrate. The aluminium layer introduced issues due to oxidation of the surface and rapid application of an insulating layer (e.g., SU-8) mostly mitigated this problem. The samples were spin-coated (500 RPM for 30 seconds, followed by 3600 RPM for 2 minutes) with a positive photoresist (S-1813) and soft-baked at 95 °C for 3 min. It was critical to have no bubbles in the resist layer before the spinning process. The bubbles can produce nonuniformity in the resist layer, leading to surface defects.

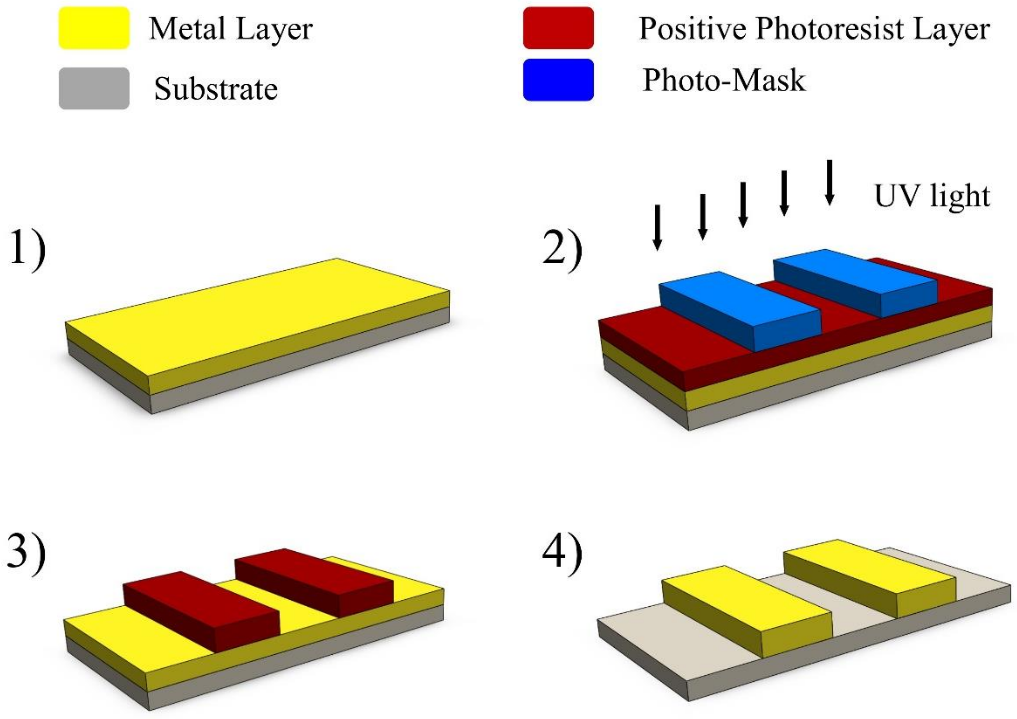

Figure 15 Simplified illustration of a photolithography process to create an electrode pattern using a positive photoresist. (1) Base substrate with a metal layer, (2) spin-coating a photoresist layer, and exposing it to a UV light using a photomask to pattern the resist, (3) developing the resits to fabricate a pattern, and (4) removal of the exposed metal surface using a wet-etch process, and removing the remaining photoresist.

The photoresist layer was then exposed to UV-light (constant energy configuration 80 mJ/cm^2) using the mask aligner. The high-intensity UV-light made chemical changes in the positive photoresist layer allowing some patterns to be removed by a photographic developer (MF-319). A post-exposure bake (95 °C for 2 min) is performed before the developing process. The samples were also baked at 115 °C for an additional 3 min.

The electrodes were patterned using a wet etch process (aluminium etchant). The aluminium etchant solution consisted of 10 % DI water, 6% Nitric acid, and 84% Phosphoric acid. The etching time for 70 nm of aluminium was 45 seconds at room temperature. The hard bake process solidified the remaining photoresist to make a durable protecting layer for chemical wet etching. Lastly, the etched samples were dipped inside a remover (1165), and thoroughly cleaned using DI water and dried using nitrogen gas.

Transparent devices were also fabricated to demonstrate a range of applications for this technology. A particular interest is utilising the cleaning platform on a flexible substrate allowing the device to be mounted onto the curved surface. The fabricated transparent device was ITO on a PET flexible substrate and ITO-coated glass sheets.[166] At first, the protective film was removed, and the flexible substrates were cleaned in ultrasound using IPA for 5 min, and then dried using filtered nitrogen gas. The samples were spin-coated with a positive photoresist, soft-baked at 95 °C for 3 min, exposed to a UV-light (80 mJ/cm^2), soft-baked at 95 °C for another 1 min, and then followed by a typical developing process (MF-319). The electrodes were patterned using a wet etch process using an ITO etchant.

The standard ITO etchant solution (ITO Etch LCE 10) was purchased from A-GAS Electronic Materials. The solution consisted of hydrochloric acid and nitric acid. The etching time for 100 nm of ITO was 45 seconds at a temperature of 45 °C. Lastly, the resist was removed and cleaned with DI water. The ITO on glass samples were also fabricated in a similar manner. However, the etch time varied with the flexible samples because the thickness of the ITO film was different, 100 nm and 70 nm on the glass and flexible substrate, respectively. The flexible substrates were attached to a flat surface to avoid non-recovery effects due to micro-cracking. Furthermore, the electrical resistance of the ITO film at different curvatures of a flexible surface may vary. In a future study, a greater in-depth analysis is needed to better optimise the application of this material.

After patterning the samples, the electrodes were tested with a probe station to ensure the films were electrically conductive without physical defects (e.g., shorted or open circuit). The electrodes were then coated with an insulating thin-film (SU-8) to provide electrical, chemical, and physical protection during use. SU-8 is a commonly used epoxy-based negative photoresist with superior properties.[159] These negative tone, epoxy-based resists exhibit excellent chemical resistance (e.g. solvents and acids), high thermal resistance (a few hundred degrees), large surface adhesion, high breakdown voltage, good optical transparency, and superior mechanical properties. Generally speaking, the SU-8 2000 series is best suited for permanent applications where, after it is fully crosslinked, the layer is left on the device. SU-8 is mainly used in the fabrication of MEMS, microfluidics, and electronic devices.[167] SU-8 is primarily used in soft lithography, but it is also suitable for other imprinting techniques such as nanoimprint lithography.[168] Furthermore, SU-8 is proven to be biocompatible,[169] and is often used in Bio-MEMS devices.[170]

The long molecular chains cross-linked in the SU-8 layer after exposure to UV light causes polymerisation of the thin film. The SU-8 series photoresists use cyclopentanone gamma-butyrolactone as the primary solvent. The thickness of the photoresist can be a few millimetres (for viscous solutions), and down to tens of nanometers (when diluted). Additionally, the film thickness varies after the expiry date due to the evaporation of the solvent. Furthermore, some cracks in the thin film were detected because of internal stress due to insufficient exposure dosage. Insufficient exposure was possible when the UV bulb in the EVG system was about to break down.

A photolithography process was needed to remove regions over the electrodes to allow physical contact with a probe. The positive photoresist is the most common type that becomes soluble in the developer when exposed. However, with the negative photoresist, the unexposed areas are soluble in the developer solution. This is an important consideration when designing the photomask, as the polarity of the opaque layer is significant.

SU-8 2000.5 series was spin-coated (4000 rpm) on the electrodes, followed by a heating process at 60 °C for 1 min, and soft-baked at 95 °C for 1 min for a thickness of 500 nm. The layer was then exposed with a dose of 65 mJ/cm^2 (constant energy), followed by another soft bake process at 95 °C for 1 min. The device was developed for 1 min in ethylene carbonate (EC) solvent. Finally, the layer was rinsed with IPA and dried with filtered nitrogen gas. The final step was to hard bake the film at 155 °C for 30 min to ensure the layer is fully cross-linked. Reducing the spinning speed would increase the film thickness. Note that the film thickness versus spinning speed is provided by the manufactures and verified experimentally using a profilometer.

SU-8 was cross-linked after exposing and developing the layer, and then hard-baked at a high temperature for better stability. However, film stresses may arise due to rapid temperature changes during the baking process, leading to micro-sized cracks. This is primarily because the layers in a multilayer device have different coefficients of thermal expansion. To prevent this, the temperature was gradually changed.

Furthermore, regulating the temperature during the baking process can reduce stress formation (leading to cracks) as the solvent evaporates. Surface contamination or fabrication defect is another common cause of cracks in the SU-8 layer. The thin-film cracks behave similar to a pin-hole under high voltages, leading to dielectric breakdown of the insulating layer. This is particularly important when depositing a thin insulating layer (e.g., 500 nm), and less relevant for thicker layers (more than a micrometer). The fully crosslinked SU-8 film tends to generate some contaminants after the developing process (white patches). This is a common fabrication defect, and to prevent this, the layer was rinsed with IPA solvent.

3.1.5 Self-assembly hydrophobic coating

The SU-8 layer was functionalised with a hydrophobic self-assembled monolayer (SAM), octadecyltrichlorosilane (OTS), to obtain a hydrophobic top-layer for better performance. OTS is an organosilicon chemical used in the semiconductor industry to form monolayer thin films on different substrates.[171] The chemical formula is $CH_3\ (CH_2)_{17}\ SiCl_3$.[172] It is an amphiphilic molecule containing a long-chain alkyl group and a polar head group that forms SAMs on various substrates, including the SU-8.[173] The schematic in Figure 16 shows the step by step preparation for the SAM OTS coating. The deposition of high-quality SAM OTS was only possible when following strict cleaning protocols to reduce contamination.

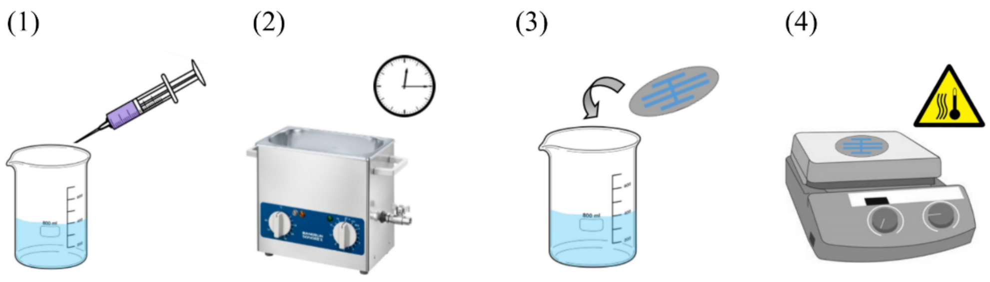

(1) OTS + hexane

(2) Sonicating solution

(3) Self assembly coating

(4) Polymerisation process

Figure 16 The fabrication steps to coat a layer of SAM OTS. (1) OTS was added to the solvent, (2) sonicating the solution to aid uniformity, (3) placing the sample inside the solution for several hours, and (4) removing the sample, cleaning it using a fresh solvent solution, followed by a soft-bake to complete the polymerisation process.

The base solvent for the solutions was hexane (99.8% purity). Initially, the solution of hexane/OTS (1 part of OTS in 500 parts of hexane by volume) was prepared in a pre-cleaned glass beaker using a glass syringe. It was vital not to use a plastic syringe, as OTS can interact with polymers, contaminating the solution. The sample was covered with a lid and sonicated for 10 min. The water in the ultrasound was changed before the sonication process, since the deposition process was thermo-sensitive. The devices were then immersed in the OTS/hexane solution for 7 hours with no agitation inside a fume hood.

The samples were immediately dipped inside a new hexane solution after the self-assembly process to remove any residuals. The samples were then taken out of the hexane solution and dried with filtered nitrogen. The final step was to soft bake the samples for 15 min at 95 °C to complete the OTS polymerisation process, and to eliminate any hexane residuals. Figure 17 shows a device with a SAM OTS hydrophobic coating with a side view image of a droplet on the OTS surface. The apparent contact angle was measured using a contact angle goniometer under ambient temperature (25 °C), and relative humidity (48 %), using a DI water droplet (6 mL). The contact angle was measured several times across the sample surface using a sessile drop method (110° ± 4°). Please note that the presence of the functional methyl group (CH_3) makes the surface hydrophobic.

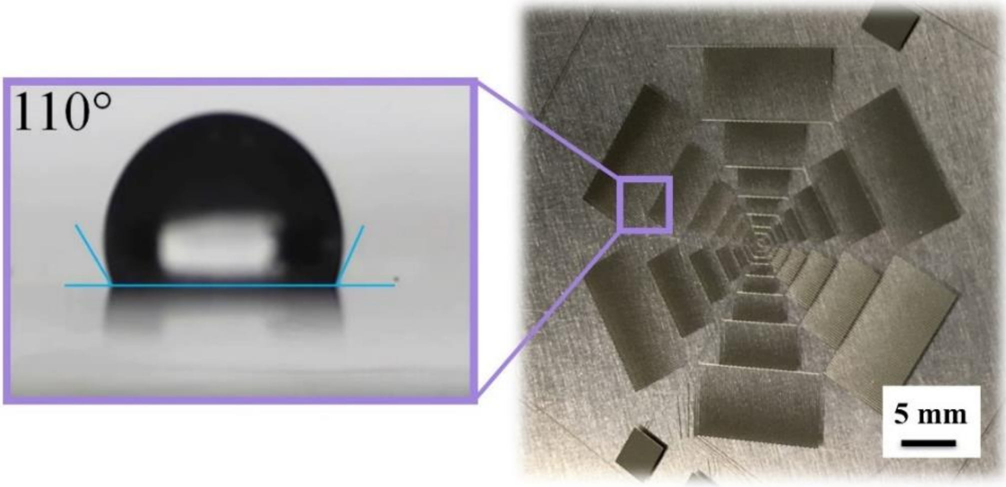

Figure 17 Top view of a device with SAM OTS hydrophobic coating functionalised with an SU-8 layer. The side view image shows a droplet with a contact angle of 110°.

3.2 Characterisation methods

3.2.1 Droplet actuation speed

The droplet actuation speed is a method to characterise the device performance. The droplet speed was measured by determining the time (measuring the number of frames), and total distance travelled across the activated electrode. The experimental setup required a high-resolution camera pointing perpendicular to the droplet (top view) with external illumination (see section 3.3.3 for more detail). The measured time was accurate up to 30 milliseconds, and the distance travelled along the electrode could be measured down to several micrometres. Note that the actuation speed was the most suitable and practical characterisation method for a droplet actuating platform.

3.2.2 Contact angle measurement

The ever-growing interest in understanding the physical interaction between droplets and surfaces has led to the development of several experimental methods to study their relationship. The contact angle goniometer, also known as a tensiometer, is a reliable characterisation instrument for measuring the droplet static contact angle, in addition to the advancing and receding contact angles.[174, 175]

The instrument consists of a backlight LCD panel (Dazzne D50) with adjustable brightness, a high-resolution camera with a variable zoom (up to 100× magnification), adjustable testing stage (two-axis movement), and a computer software to capture and analyses the drop shape (see Figure 18).

The photos and videos were recorded using the VLC media player, and the droplet's shape was analysed using pyDSA (Python package).[176] The software identified the droplet baseline, detects the droplet edge, fit the edges, and computes the contact angles. Additionally, the static contact angle can be manually measured using the ImageJ software. Sufficient illumination was essential for high-quality images. Furthermore, a filtered diffuser in front of the LCD backlight panel improved the image quality. The droplets were inserted onto the substrates using a micropipette with a volume accuracy of up to ± 0.1 μL.

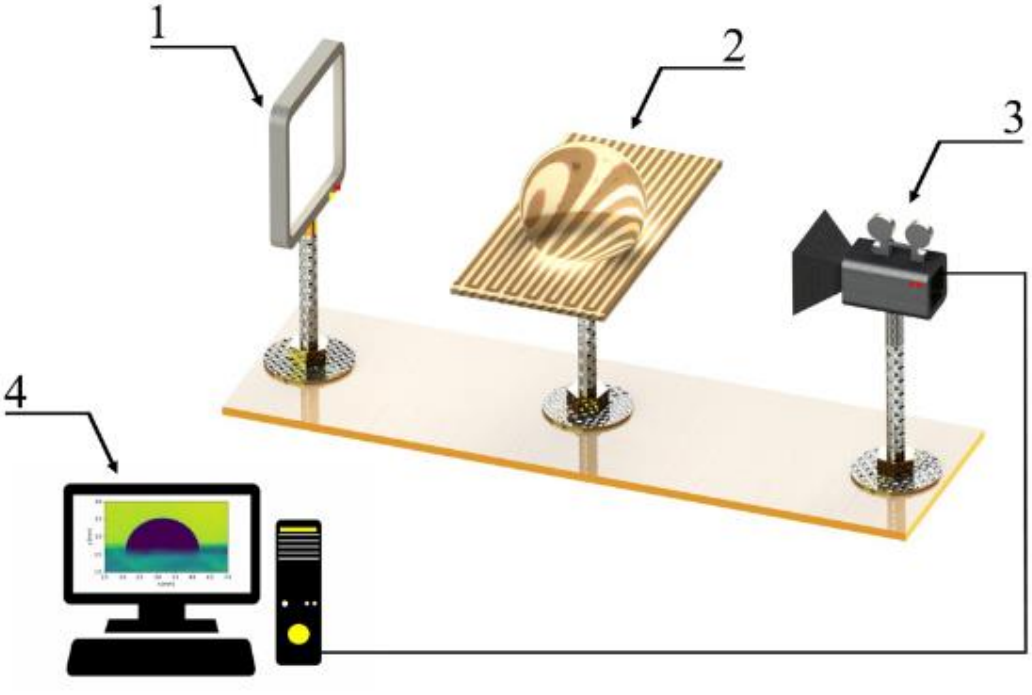

Figure 18 Schematic showing the setup of a typical contact angle goniometer to measure contact angles. (1) LED backlight panel with adjustable brightness and a filtered diffuser front panel. (2) The testing stage with adjustable two-axis movement. (3) The recording camera. (4) The camera is connected to a computer via a USB to store and analyse the droplet profile.

3.2.3 Profilometer

A profilometer is a measuring instrument to characterise the surface profile. There are two types of profilometers: contact and non-contact configurations. A contact profilometer (Bruker Dektak XT) was used in this work as a general instrument to rapidly measure the thickness of certain coatings before proceeding with the fabrication process. For a typical scan, a diamond stylus is moved across in contact with the surface for a specified distance and contact force.

3.3 Electronic control system

The electronic control system consisted of a control circuit board (low voltages), a relay module (high voltage), and a testing stage. The control system can offer high-speed switching of up to 128 electrodes using reed relays. The printed circuit board (PCB) design was carried out on KiCad, a free open-source software suitable for electronic design. Moreover, several design factors were considered including, board shape and size, number of layers, manufacturing processes, voltage levels, material and component, and costs.

3.3.1 Control circuit boards

The control circuit board is connected to a relay module board. The primary objective of this unit is to control the switching algorithm of the electrodes. Furthermore, multiple control circuit boards can be stacked on top of each other and operated in parallel with a single microcontroller to increase the number of output signals. The benefits of the controller unit are hardware customisability, low costs, and accessibility.

The control circuit board was based on an mbed NXP LPC1768 development board. This is a powerful yet user-friendly development board. It consists of 32-bit ARM CortexM3 core hardware with a 512 kB on-chip flash program memory. The controller can be operated locally via a host PC by a drag-and-drop programming method using a USB 2.0 drive. There is no requirement to install additional software apart from a standard web browser. The online compiler is based on the C/C++ package provided by the ARM mbed facilitated the programmed algorithms.

The control circuit board is powered by a 5.0 V power supply module (MB102) connected via a power adapter to the main cable or a USB 2.0. The module is low-cost, reliable, and provides power to the board when testing outside the laboratory (i.e., testing on the road). The module has a compact design (4 cm × 3 cm), and it was mounted directly to the boards. Furthermore, the output voltages of 3.3 V and 5.0 V can be selected by a jumper cap. The control circuit board consists of the following main parts (see Figure 19 for more detail):

1. Microcontroller
2. Demultiplexer
3. An array of toggle flip-flops
4. Voltage translators
5. Buffer drivers

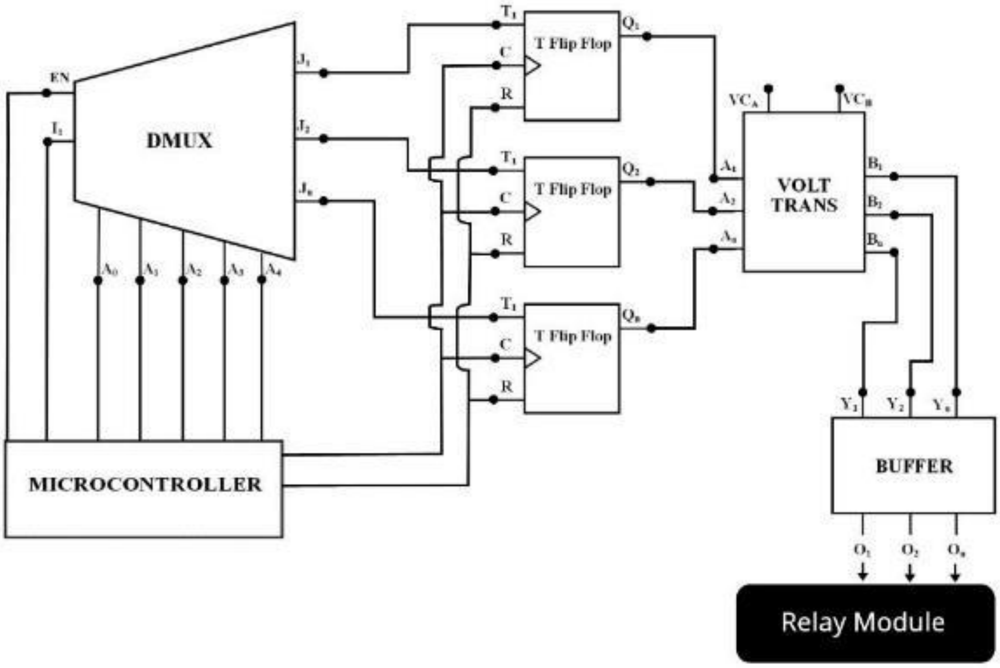

Figure 19 Functional block diagram showing the electronic design of a control circuit board. The board is controlled via an mbed NXP LPC1768 development board, controlling a 32-channel analogue multiplexer, an array of T flip-flops, a voltage translator from 3.3 V to 5.0 V, and buffer drivers.

An example of the control circuit board (PCBs) is shown in Figure 20, using both a singular and parallel configurations.

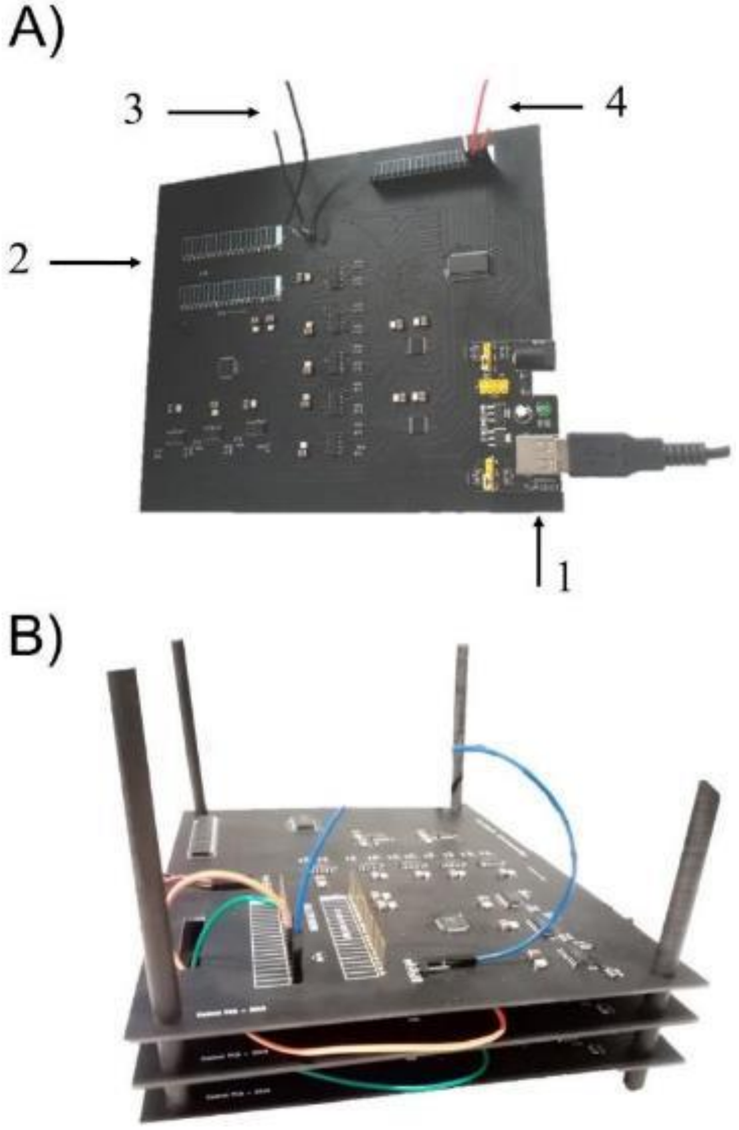

Figure 20 PCB images showing the control circuit boards. (A) Singular configuration with 32 output signals. The key features are: (1) mounted power supply module, (2) mbed development board, (3) external wire for the enable pins (EN) to activate the boards separately in a parallel configuration, (4) output signals to the relay module. (B) Image showing the boards in a parallel configuration.

A demultiplexer, also called a data distributor (or DMUX), generates a set of digital output from binary inputs. Therefore, DMUX can be used to implement a general-purpose logic. Essentially, to maximise the number of output signals using only one microcontroller. DMUX is suitable for many applications, such as communication systems, arithmetic logic units, and computer memory.

The microcontroller is connected to a 32-channel analogue multiplexer (ADG732) to switch 32 digital outputs determined from 5-bit binary address lines A_0, A_1, A_2, A_3, and A_4. The component has an enable chip (EN) that can individually select the boards (i.e., when disabled, all channels are switched off). Therefore, multiple boards can be controlled via a single microcontroller, enabling switching of up to 128 relays. They operate from a single voltage supply of 3.3 V, making them ideally suited to be powered by a microcontroller.

The electronic design consists of a series of dual J-K flip-flops with a reset configuration (MC74HC73A). The J-K flip-flops extend the SR flip-flop behaviours (K: reset and J: set) by interpreting the $K = J = 1$ condition as a toggle command. Furthermore, the J-K flip-flop can consequently be a universal flip-flop by setting the J condition equal to the K condition to synthesize a T flip-flop. When the joint J-K input (T) is set at high, the flip-flop changes the state whenever the clock input (from the microcontroller) is strobed. Correspondingly, when the input signal is set to low, the previous state remains valid. Therefore, the state of the component at an applied trigger pulse is determined only when the previous state is known.

The flip flops employ two decoupling capacitors connected to their power supply pin to reduce the signal noise. A bypass capacitor is a common practice in electronic designs to avoid voltage spikes or ground bounces. Two capacitors are typically employed (one large and one small capacitor) to smooth out the voltage signal (100 pF and 1 μF). The bypass capacitors are similarly used in other components, including the DMUX. The bypass capacitors were placed as close as possible to the voltage supply pins and the common GND. Additionally, a pull-down resistor (10 kΩ) was connected to the T input of the flip flops to a common ground (GND) to ensure a known state for a signal and prevent a floating signal.

A level shifter, also known as a voltage level translation, is a circuit used to translate voltage signals from one logic level to another, enabling compatibility between ICs with different drive voltage requirements. The relay module had a voltage requirement of 5.0 V from 3.3 V, thus requiring a level shifter. We added a series of 8-bit non-inverting directionless level translators (TXS0108E) to the output signals of the flip-flops. The component is designed explicitly for translating logic voltage levels and uses two separate configurable power-supply rails, a 3.3 V port-A (VC_A) and a 5.0 V port-B (VC_B).

Since the output signal is transferred from one board to another, a buffer/driver (SN54ABT16244) is added to the design. These are integrated circuit devices that isolate the inputs from the outputs. Therefore, the load is reduced by the input circuit enabling the signal to be sent onto another PCB via cables over longer distances. Additionally, it also provides additional protection by boosting the current/voltage level. SN54ABT16244 is a 16-bit buffer driver to explicitly improve the signal quality.

3.3.2 Relay module

The relay module is a hardware for remote device switching with high operating voltages. The working function of the module can be used to sense external (ON/OFF) conditions. The PC interface connection is made through the control system module to regulate the switching mechanisms. Figure 21 shows the schematic of the electronic design.

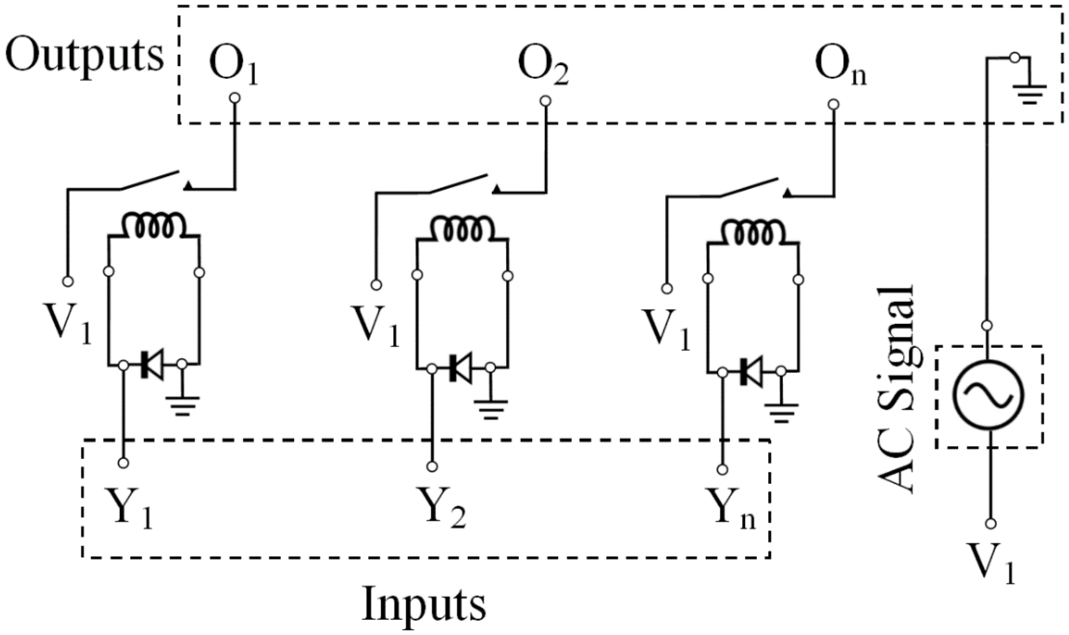

Figure 21 Functional block diagram showing the electronic design of a relay module. High voltage input signal (V_1) is supplied from a signal amplifier. The schematic drawing also shows the digital signals from the control circuit board (Y_n) and high voltage output signals (O_n) to the electrodes.

Figure 22 shows a relay module PCB. Each module consists of 32 reed relays to electromagnetically switch high voltages. The key features of the reed relays were compact size, a maximum switching voltage of 1 kV (DC or peak AC), a maximum switching current of 1 A (DC or peak AC), and a release time of 0.1 ms (measured without coil suppression).[177] Additionally, it has an operating time of 1 ms, shock and vibration resistance up to 50 g (10 Hz to 2000 Hz), and an operating temperature between - 40 °C to 105 °C.[177] The life test assessment provided by the manufacturers shows that the typical number of operations (load at 100 V and 10 mA) is approximately fifty million operations without any failures.[177] Additionally, a flyback diode with reverse polarity from the power supply and in parallel to the relay's inductance coil prevented voltage spikes from the power supply when it was disconnected.

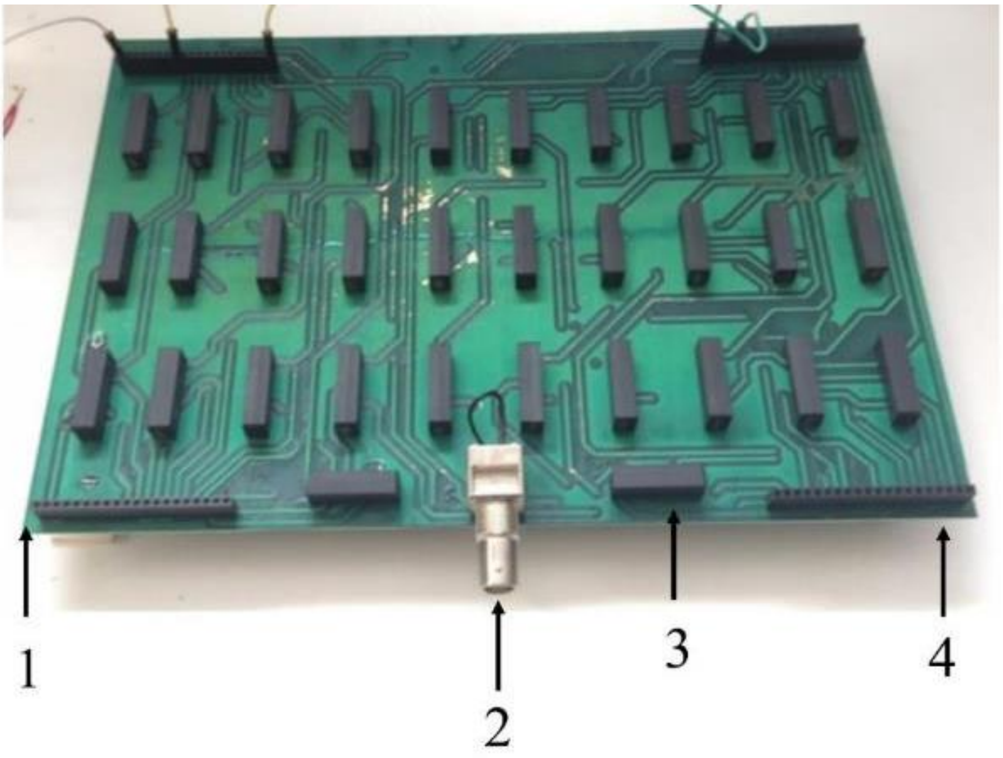

Figure 22 Relay module with 32 reed relays to regulate high voltage signals. (1) Mounting racket for assembly, (2) BNC connection for high voltage input signals, (3) reed relays, (4) input and output rackets.

The signal generator via a signal amplifier powered the relay module using a BNC connection. The Keysight 33210A function waveform generator created a sine wave signal with inherently low distortion. The function generator can generate a variable period, pulse width and amplitude (up to 5 MHz) for various electronic applications. The Falco Systems WMA-300 is a high voltage (300 V_{pp}) signal amplifier with a DC to 5 MHz signal bandwidth and a 300 mA current limit. The signal amplifier was intended for high voltage demanding applications with a wide bandwidth. Additionally, the signal amplifier was designed to withstand short-circuit conditions. Lastly, the high voltage signals (frequency, noise, and amplitude) were monitored using a digital oscilloscope.

3.3.3 Modular electronic design

A modular electronic control system (Board-A) with a relay module (Board-B) was custom-designed, allowing the control of individual high-speed reed relays by simple commands from a host PC. Figure 23 shows the logic block diagram of a modular electronic kit.

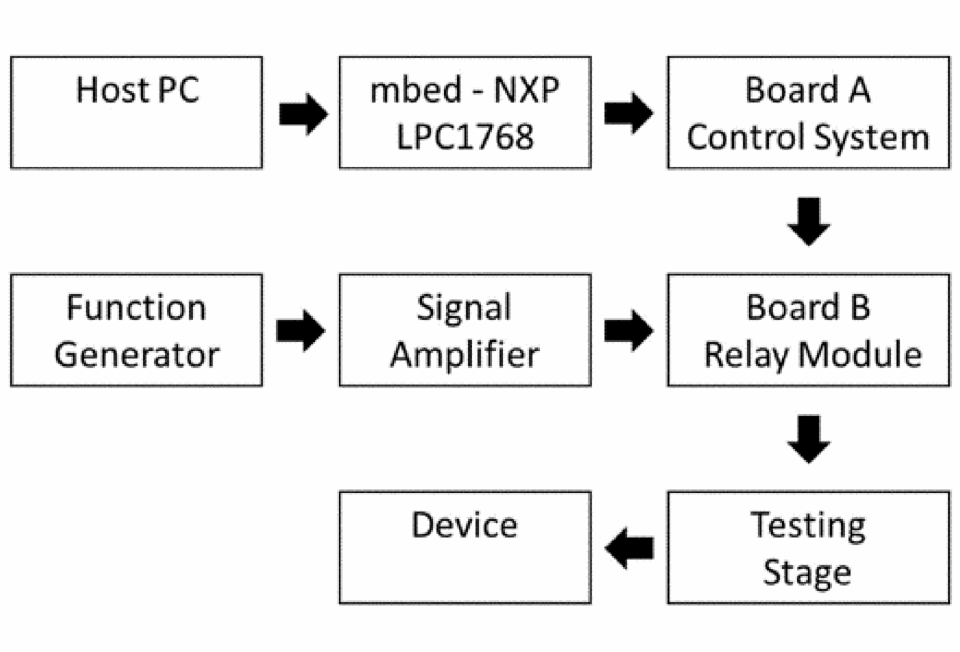

Figure 23 The host PC is connected to a microcontroller to switch output signals from the control system (Board-A) to the relay module (Board-B). Function generator facilitated the AC signal waveforms over a wide range of frequencies and then amplified with a signal amplifier. The high voltage signals were connected to the device via the testing stage with an array of spring pogo pins.

The electronic boards were mounted inside an inaccessible enclosure for safety. The enclosure provided electrical isolation and mechanical protection against physical damage. An internal racket held the relay modules (up to 4 boards) with adequate distance. The Board-A was screwed to a stand located in the case. Figure 24 shows the modular electronic kit with the main features.

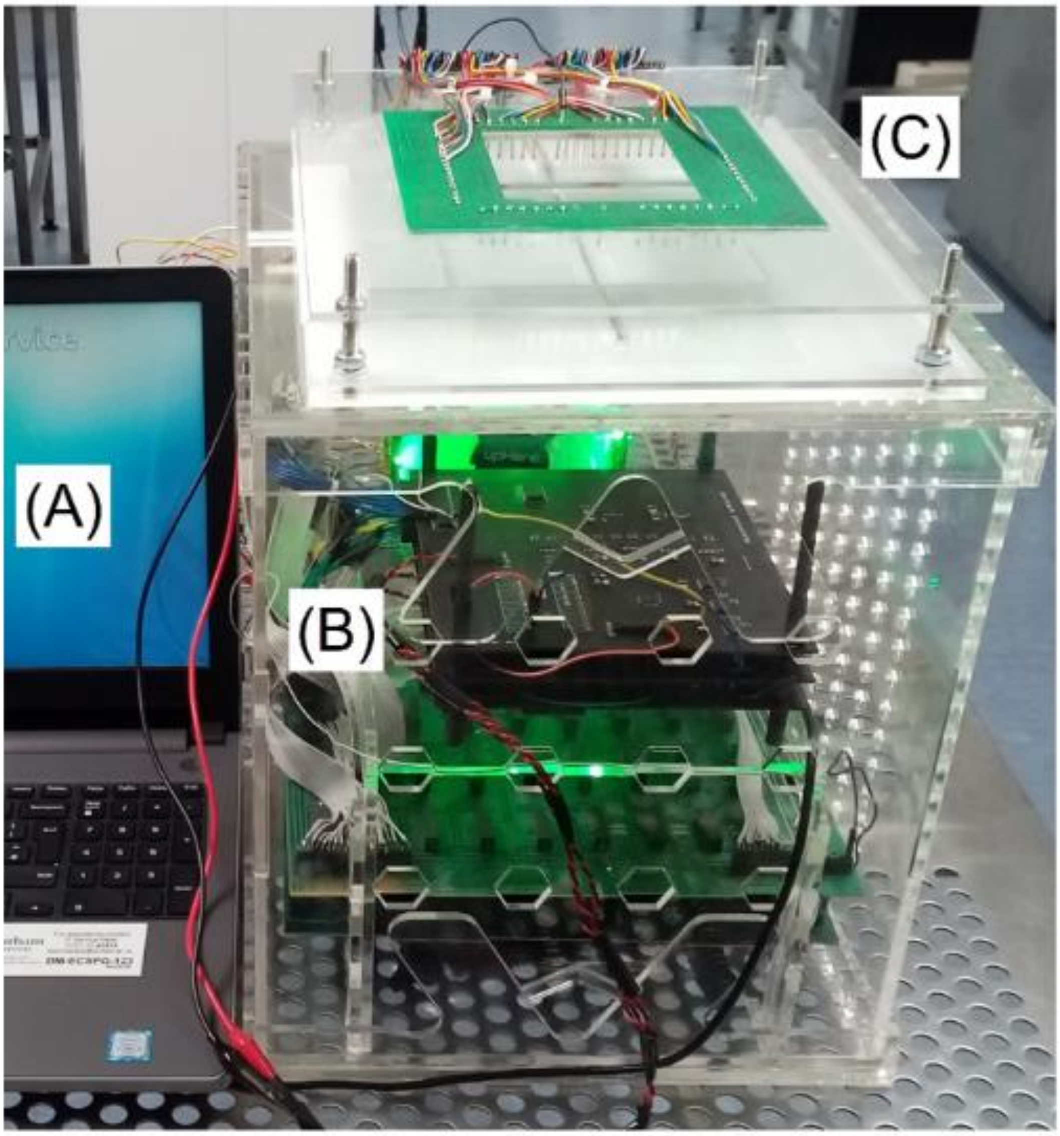

Figure 24 Image showing the modular electronic test kit with key features including, (A) host PC, (B) safety case that consists of a microcontroller, Board-A in a parallel configuration, high voltage Board-B, 64 outputs, LED board for displaying the switching pattern of the relays, and (C) the testing stage with spring pogo-pins.

The module kit with 128 channels was relatively cheap, with a total cost of approximately £150. It is also cheaper than the commercially available counterpart (64 channel module for £375).[178] Each relay module board had a separate BNC connection to have up to four high voltage output signals from different amplifiers. Furthermore, an array of LEDs was added to the back of the case to show the switching sequence patterns.

Figure 25 shows a typical testing set up with the key features including, a high-resolution camera, external illumination, probe station for electrical analysis, and a testing stage with an array of spring pogo-pins for electrical contacts. Furthermore, spring pogo-pins were attached to the stage using a through-hole connection from a PCB.

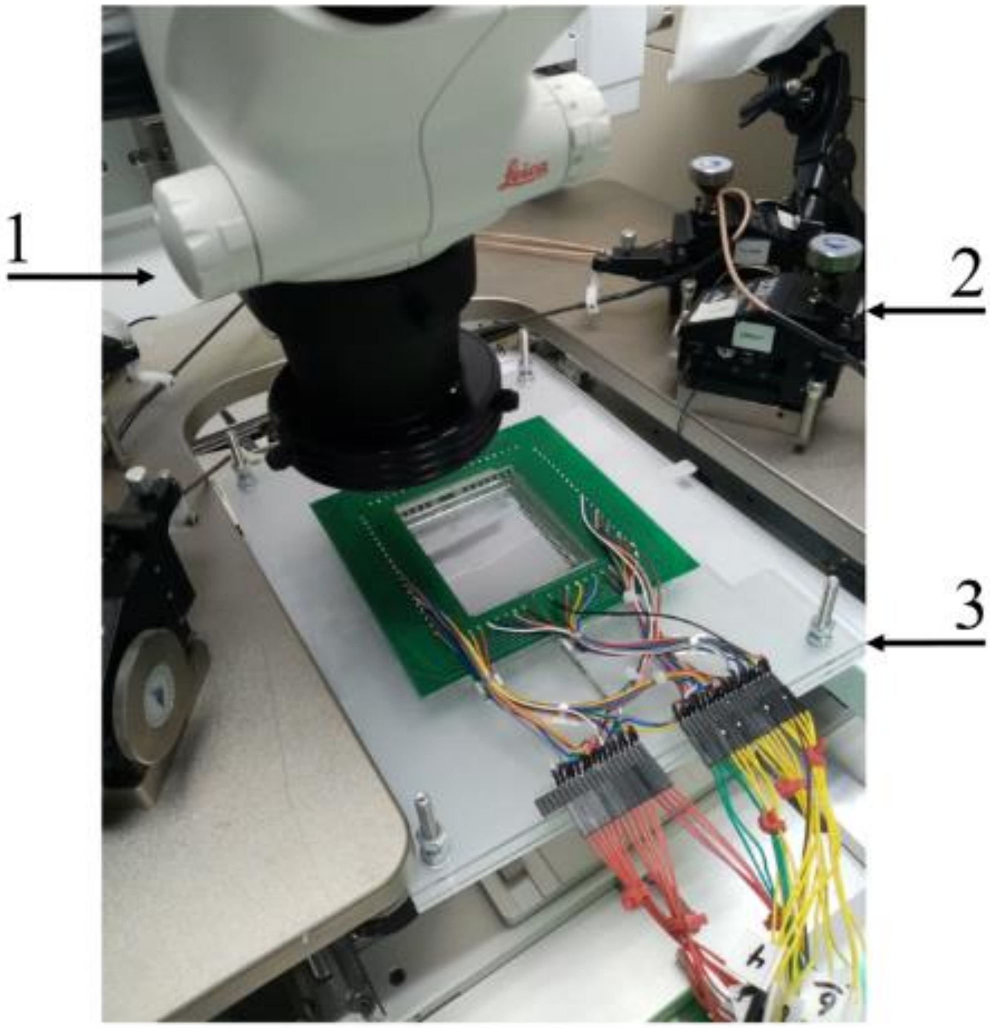

Figure 25 The testing set up with key features including; (1) high-resolution camera, (2) probe station for electrical analysis, and (3) the main testing stage with an array of spring pogo-pins for contacts to the main device. Please note that the top layer of the testing stage was screwed to the main device for better rigidity.

3.4 Simulation software packages

The cross-platform software package COMSOL Multiphysics is a multi-physics simulation and solver.[179] The software allows conventional physics-based modelling including, a numerical technique to simulate electric field distribution using the finite element method (see section 4.1.1, 5.1.1, 7.1, and 8.2.1). The electric field simulations are significant in the design and fabrication of the devices. MATLAB,[180] Also known as matrix laboratory, is a proprietary multi-paradigm programming software and numerical computing environment. The software is used in this work to solve equations and generate mathematical models (see section 5.1.2).

The simulation models is the first step towards generating a description of the physical process to predict their response. The simulations are based on the finite element method (FEM),[181] a widely popular numerical method for solving engineering problems in two/three space variables. To solve a typical problem, the FEM splits a complex system into smaller, simpler domains, referred to as finite elements. Each element contains the information (e.g., material property) needed to determine the element's status connected to the surrounding elements. Furthermore, mathematical models are needed (also known as governing equations) to solve the physical problems numerically. However, this is not sufficient to describe the system behaviour. We also need to provide additional boundary conditions to solve the equations. In general, studying any engineering phenomenon with the FEM is often categorised as finite element analysis (FEA).

COMSOL Multiphysics models are split into three stages: (pre-processing, solution, post-processing). Pre-processing includes creating the model geometry, establishing a domain, and setting the solution data. Generating and refining the mesh was a vital process. For example, The mesh density near the electrodes was increased to better conform to the electrode shape.[182] A triangular mesh model was used with a maximum element size of 500 nm and a minimum element size of 5 nm. Sharp geometries were also avoided to produce smoother results.

The Poisson's equation used in COMSOL Multiphysics (electrostatics) is the classical PDE of elliptic type that describes electrostatics with a space charge density.[183] The relationship for electric potential is derived assuming static conditions, $\mathbf{E} = -\nabla V$. Combining the electric potential equation with the constitutive relationship, $\mathbf{D} = \varepsilon_0\mathbf{E} + \mathbf{p}$, between the electric field **E**, and electric displacement **D**, COMSOL represents Gauss' law as the following equation:[183]

$$-\nabla.(\varepsilon_0\nabla \mathrm{V} - \mathbf{p}) = \rho \tag{13}$$

The physical constant ε_0 is the permittivity of vacuum, **p** is the electric polarisation, and ρ is a space charge density. This equation which is pre-programmed in COMSOL Multiphysics describes the electrostatic field in the materials. Further details and the governing partial differential equations (PDE's) are provided in COMSOL AC/DC module user's guide on the main website.[183]

A series of assumptions were considered to define the boundary conditions. For two-dimension (2D) models, the individual electrodes were sufficiently long such that the fringe effects at the ends are insignificant. The ohmic heating from the applied voltage was insufficient to produce any physical constant changes. Impurities and particles on the device or in the fluid were ignored. Additionally, geometrical defects from the microfabrication were neglected. The relative dielectric constant for the SU-8 layer was estimated to be approximately 3.2. The OTS thickness was on the nanoscale (less than 5 nm), and it is substantially smaller than the SU-8 thickness, thus neglected. The effective DC voltage was between 20 V to 140 V.

The system parameters were two electrodes (control and ground), with a given electrode gap distance. Due to symmetry, only one set of electrodes was modelled, and the two boundaries to the right and the left were modelled as electrically symmetric. In the electrostatic module, COMSOL automatically selects the conservation of charge condition for the boundaries between the domains. This includes equations for charge conservation according to Gauss' law for the electric displacement field. A zero-charge boundary was also selected at exterior boundaries. This boundary condition is similarly valid at the symmetry boundaries.

3.5 Testing liquids

The primary testing liquid for an automotive application is rainwater, and various samples were collected using a liquid collector container. The electrical conductivity of rain can be similar to DI water, but the typical rain droplets can be slightly conductive. However, the concentrations of interfering ions (such as sodium, potassium, calcium, chloride, etc.) remain relatively low.[184]

The chemical properties of rain droplets collected from various locations in the UK show a consistent pattern.[185] The concentration of interfering ions is highly related to the geological position of the rainfalls. For example, the concentration levels are higher near the coast than over the land.[186] The chemical and physical properties of rainwater can vary, and in special cases such as rain dust or acidic rain,[187] the droplets can be more conductive than usual.

Appendices include a list of testing liquids, highlighting the relevant chemical, physical, and electrical properties that are important for L-DEP and electrowetting. The higher surface tension was important in both EWOD and L-DEP actuation. However, the higher permittivity was crucial in L-DEP actuation, whereas the larger electrical conductivity was more dominant in EWOD actuation up to the saturation limit.

3.6 Summary

The fabrication process and various characterisation methods were discussed in this chapter, including cleaning protocols, deposition techniques, patterning (photolithography) via a wet-etching or a lift-off process, and self-assembly hydrophobic coating. The chapter also discussed the necessary consumable materials for photolithography included various photoresists, developers, and strip removers. SU-8 was the insulating layer, and it was functionalised with SAM OTS.

The consumable materials are commonly used in the industry for large-scale manufacturing at a low price. The primary fabrication equipment was a photolithography system plus the spinners. They are also commonly used in large-scale manufacturing. Thermal evaporators are commonly used to deposit different layers. Industrial-scale thermal evaporators or sputter systems with a large chamber can significantly reduce fabrication costs.

This chapter demonstrated the electronic design and the setup of the testing stage. An electronic module generated digital signals to control multiple high voltage outputs. The electronic system consisted of a control circuit board (Board A - low voltage), a relay module (Board B - high voltage), and a testing stage. The control system could offer high-speed switching (few milliseconds) of up to 128 electrodes using reed relays. Additionally, the working function and set up of the COMSOL Multiphysics simulations models and the testing liquids were discussed.

Chapter 4
Droplet Actuation Methods

Droplet manipulation by electric means has gained significant attention for providing automated droplet handling for various applications. However, the operational capabilities in the current format are restricted to the laboratory testing conditions. Here, we explore three droplet actuation methods that are intended for a cleaning application. Furthermore, we demonstrate the manipulation of different droplets across a wide range of geometries and surfaces.

The sequential activation of electrodes is a method to produce discrete droplet actuation, which is also a critical droplet handling operation in many microfluidic platforms. We modified the existing standard interdigitated electrodes (IDEs) design,[126] for a cleaning application. The proposed concept reduced the complexity of previous designs and provided new operational capabilities.

An additional novel electrode design is also introduced here, focusing on the continuous actuation of droplets using variable interdigitated electrodes (VIDEs) to move different volumes of droplets. The technological advancement emerging from this work enables lower operating voltages, eliminates actuation size limitations, and reduces complexity of the control system requirements.

The significance of the signal frequency and applied voltages on the actuation performance is thoroughly investigated to highlight the optimum design parameters. This chapter similarly investigates different hydrophobic coatings, from hydrophobic to superhydrophobic. Furthermore, a hydrophobic coating with a wettability gradient is presented here for transporting droplets. The wettability gradient based on SAM OTS produced droplet motion without any input energy.

4.1 Interdigitated electrodes

IDEs produced a dielectrophoretic force near the droplet’s liquid-solid interface, causing it to spread. This technique was established initially for small-scale applications, such as microfluidics. However, our approach expands on an already existing design to achieve new droplet actuation operations. For instance, a larger active area, actuation of droplets with varying volume, and a lower operating voltage.

4.1.1 Numerical simulations of IDEs

COMSOL Multiphysics numerically simulated the relationship between the electrode gap distance and penetration depth of the electric field. Since the electric field has dimensions of (Vm^{-1}), thus scaling down the gap distance subsequently increases the magnitude of electric field to generate an adequate L-DEP force at lower voltages. However, the size of the system is limited by the fabrication method and the associated costs and fabrication defects.

The material properties and thickness of the insulating layer were crucial factors to achieve a reliable and high-performance operation. The high voltages applied across a thin layer can reduce the device lifespan or result in a dielectric breakdown. Likewise, the performance of a thick dielectric layer is similarly compromised because of the lower penetration of electric field.

The primary objective was to provide a set of design recommendations. This is particularly important since the fabrication and testing of many devices is both expensive and time-consuming. The mesh density near the important boundary layers was finer (see Figure 26 A). The effective voltage was 100 V and no electrical conductivity was assigned to the water layer. The system parameters were two sets of aluminium electrodes (control and ground signals), with an SU-8 insulating layer, and a thick layer of DI water (see Figure 26 A).

Initially, the electric potential across the electrodes was simulated (see Figure 26 B). Figure 26 C shows the surface polarisation, highlighting that the polarisation happens at the boundary of the liquid/solid interface (less than 5 µm). This could be important when introducing new layers, such as SLIP or micro pillars with a thickness larger than several micrometers. Figure 26 D shows the electric field fringing lines. The electrical fields are described as an absolute value (norm) to define the amplitude of the electric fields.

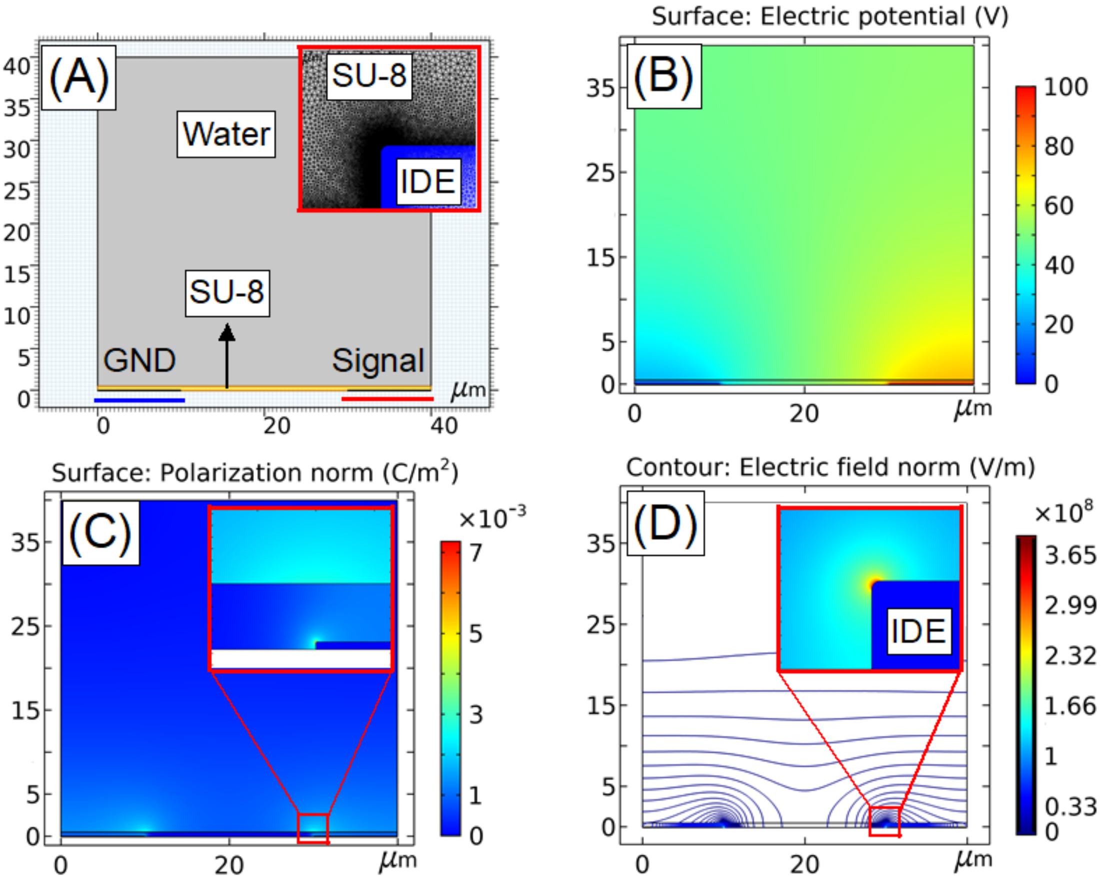

Figure 26 COMSOL Multiphysics simulation results. (A) The system parameters for a device with two electrodes (signal and ground), with a gap distance of 20 µm, insulating SU-8 layer, and a covering DI water layer. The subfigure shows a high density mesh near the electrode boundary. (B) Surface contour showing the electric potential difference at 100 V. (C) The norm polarisation contour, with a zoomed-in image to show the local polarisation near the water-insulating interface. (D) The line contour demonstrating the propagation of the electric field. The zoomed-in image shows the local electric field near the electrode boundary

The propagation of the electric field for different electrode gaps (20 µm, 40 µm, and 80 µm) is simulated to study two main effects. Firstly, the maximum local electric field within an insulating material was estimated to fabricate a device with appropriate protection. Secondly, the penetration depth of the electric fields into a liquid film is also investigated. The electric field's decay in the vertical axis above the electrodes is important for generating an appropriate bulk force.

Figure 27 A shows the relationship between the electrode gap distance and penetrating electric fields up to 0.5 µm, and Figure 27 B shows further penetration up to 5 µm in the liquid layer. The simulation results confirmed that IDEs with a smaller gap distance generated a higher electric field. Additionally, IDEs with a gap distance of 20 µm generated an equivalent electric field value at lower voltages to previously reported studies using higher voltages (200 V or more) with a gap distance between 80 µm to 120 µm.[132, 137]

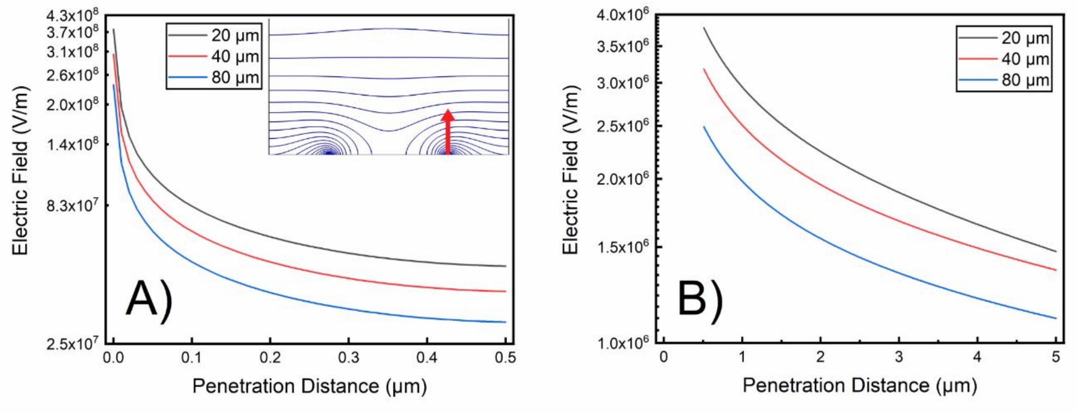

Figure 27 COMSOL Multiphysics simulation results showing the decay of modulus of electric field away from the IDEs into the liquid layer. (A) The electric field penetration up to 0.5 µm. (B) The electric field penetration from 0.5 µm up to 5 µm.

Figure 28 A shows that the maximum local electric field for different applied voltages (20 V to 140 V), with a fixed electrode gap distance of 20 µm, and an insulating layer with thickness of 0.5 µm. The results confirmed that the higher applied voltages generated a stronger electric field. Figure 28 B shows the maximum local electric field for different SU-8 thicknesses (0.25 µm, 0.5 µm, 1 µm, 2 µm, and 5 µm), and a fixed electrode gap distance of 20 µm, with an applied voltage of 100 V. The results showed that the thinner layers generated a higher electric field value with a greater penetration distance. Please note that this will depend on whether there is air or liquid above the coated electrodes.

Additionally, the maximum electric field for layers thinner than 0.5 µm was lower than the breakdown voltage limit. The reported range is between 200 to 440 MV/m for SU-8 with a thickness of 50 µm to 2 µm, respectively. Note that these estimations are from a parallel plate capacitor configuration.[188] Furthermore, Figure 28 C shows the results for different electrode gap distance (5 µm, 10 µm, 20 µm, and 40 µm) and a fixed applied voltage (100 V), with an insulating layer thickness of 0.5 µm.

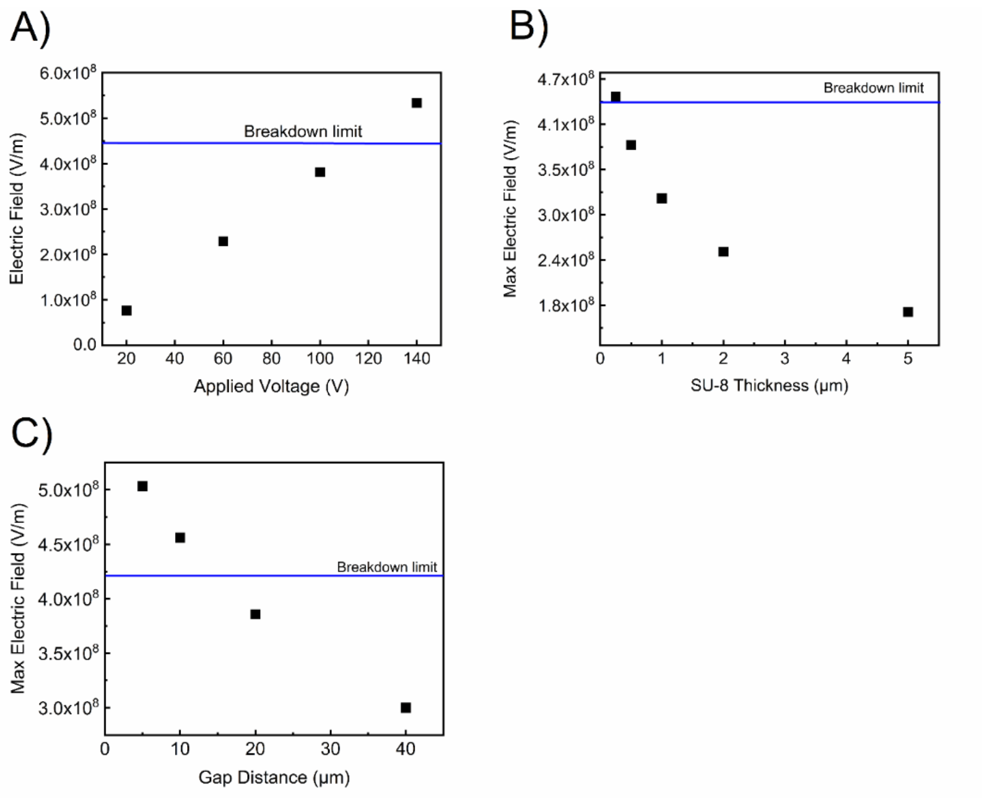

Figure 28 Simulation results showing the maximum local electric field for different conditions. (A) Applied voltage from 20 V to 140 V. The insulating thickness was 0.5 µm and the electrode gap distance was 20 µm. (B) Investigating different thicknesses of SU-8 (at 100 V) with an electrode gap distance of 20 µm. (C) The change of maximum electric field for different electrode gap distance. The thickness of the SU-8 layer was 0.5 µm and the applied voltage was 100 V.

The study confirmed that fabricating electrodes with a gap distance of 10 μm or smaller would result in a dielectric breakdown (at 100 V or more). Furthermore, the simulations were also experimentally verified testing the IDEs with a gap distance of 10 μm.

Although the exact bulk force was not calculated here, these results emphasise the significance of reducing the gap distance and minimising the insulating and hydrophobic thicknesses. Therefore, the new geometry produces a strong L-DEP force for a fixed applied voltage. The experimental results also validated this concept because the thicker covering top layers produced smaller changes in contact angle and physical traces of dielectric breakdown for some specific testing parameters. Several examples were a thinner insulating layer than 0.5 μm, or increasing the applied voltages above 100 V.

4.1.2 Device fabrication

The conceptual design of a device with four separate layers is presented in Figure 29. The aluminium IDEs are patterned using standard lithography process on a clean glass substrate. The primary objective of the sample preparation was to minimise the thickness of the covering dielectric and hydrophobic layers to maximise the device performance. A common photosensitive epoxy resin (SU-8 2000.5) with a thickness of 0.5 μm to 1 μm was used as a dielectric material on the electrodes to electrically, chemically, and mechanically shield them during testing. Furthermore, testing SU-8 layers thinner than 0.5 μm would result in a dielectric breakdown (i.e., 350 nm). Several critical factors had a significant impact on the performance of the insulating layer. For example, surface defects, impurities before spinning the SU-8 layer during the fabrication process, uniformity of the SU-8 layer, and the electrode defects such as edge walls.

The effect of hydrophobicity was significant on the droplet movement. The dynamic motion across a surface with a high contact angle and low sliding angle require smaller changes in the contact angle. Therefore, producing a higher actuation speed or reducing the demand for higher voltages. Note that the untreated SU-8 layer had poor hydrophobic properties (70°). Figure 29 C shows the side view image of a droplet on the OTS layer with a mean contact angle of 110° (± 4°), confirming the hydrophobic enhancement of the SU-8 layer. SAM OTS layer was nanoscopic (1.5 nm to 2.0 nm),[189] and therefore, the hydrophobic coating minimised the thickness of the covering layers. In comparison, previously reported studies employed a Teflon coating with a thickness of hundreds of nanometres.[126]

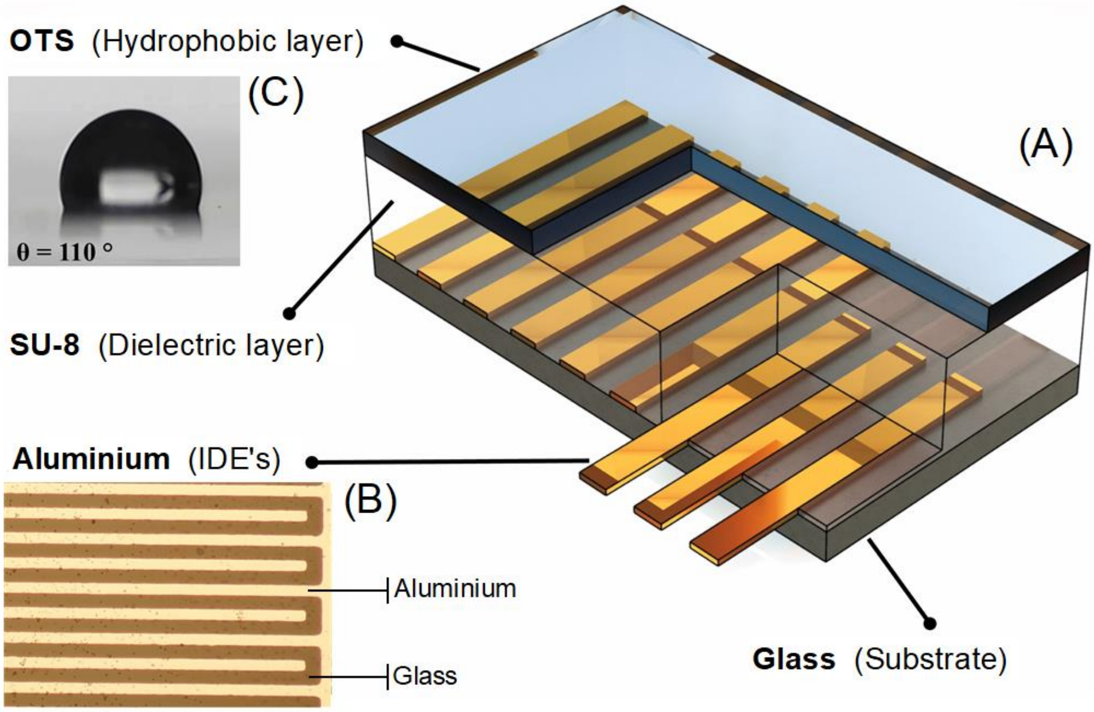

Figure 29 (A) Schematic model of a typical device with four separate layers: glass, aluminium, SU-8 and OTS. (B) The top view optical microscope image of an electrode pad (IDEs). (C) The side view image of a water droplet on a surface coated with SAM OTS.

4.1.3 Contact angle measurements

The change of contact angle in previous studies was limited by the fixed thickness of the insulating and hydrophobic layers (a few micrometres), with a higher operating voltage (250 V or more).[132] We investigated the change of contact angle as a function of electrode gap distance and operating voltage to evaluate the device performance. Furthermore, the frequency dependence of L-DEP is also studied to highlight the optimum operating parameters.

Several experiments were carried out to analyse the effect of applied voltage and electrode gap distance on the contact angle. The experiments were conducted in ambient conditions. The testing liquids were DI water and propylene carbonate. The L-DEP bulk force was frequency dependent, with an optimum crossover frequency of 20 kHz and 40 kHz for propylene carbonate and DI water, respectively.[132]

The change of contact angle as a function of electrode gap distance for a fixed applied voltage is shown in Figure 30 A. The results revealed that electrodes with a smaller gap distance produced larger changes in the contact angle. This was anticipated because the thickness of the dielectric layer and the applied voltage remained constant. Indeed, a better performance for electrodes with a larger gap distance is possible using a thicker insulating layer with a higher applied voltage, typically several hundred volts. Furthermore, Figure 30 B shows the change of contact angle as a function of applied voltage. The results verified the fundamental relationship between electrowetting and dielectrowetting that the cosine of contact angle is proportional to the applied voltage squared, similar to electrowetting.[126]

The experimental results in Figure 30 C verify a critical signal frequency for DI water when the liquid was exhibiting a dielectric response consistent with expectations of operating above a critical signal frequency. The highest dielectrophoretic response was between 30 kHz and 50 kHz. The difference was insignificant at lower frequencies (i.e., up to 5 kHz), dominated by electrowetting. The dielectrophoretic response is related to the magnitude of the electric field. Hence, the effect is visible at higher frequencies (30 kHz to 50 kHz). Note that slight variation in the electrical conductivity of the liquid will shift the critical signal frequency by tens of kilohertz.[190]

Moreover, a larger gap distance (80 µm) fails to generate an adequate L-DEP force at higher frequencies (i.e., 40 kHz). IDEs with a gap distance of 80 µm can still produce an equivalent L-DEP force, but only when employing higher voltages (200 V or more), as reported elsewhere.[132] The L-DEP and electrowetting dominate the droplet actuation in the high- and low-frequency limits, respectively. This is notably evident for the electrowetting actuation of conductive droplets using lower signal frequencies.

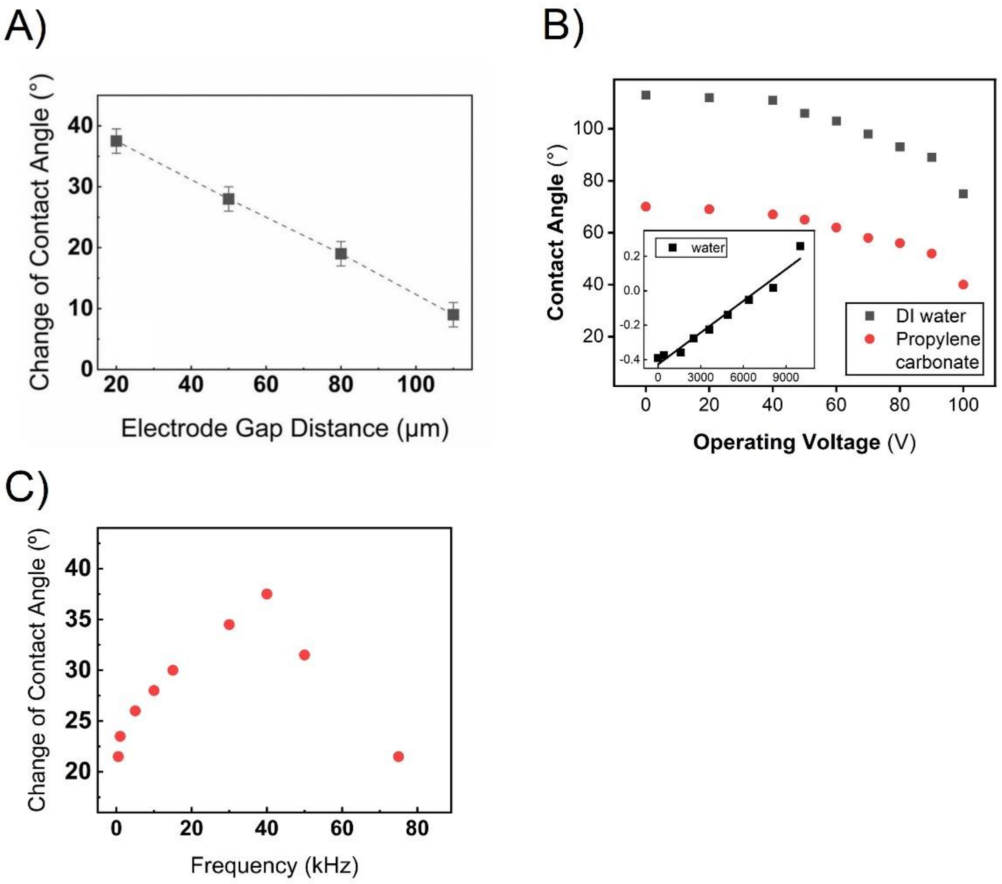

Figure 30 Experimental results from a contact angle goniometer. (A) Change of contact angle for DI water droplets at 100 V (40 kHz) for different electrode gap distances. (B) Change of contact angle for DI water (40 kHz), and propylene carbonate droplets (20 kHz), at different operating voltages with an electrode gap distance of 20 µm. The linear dependence of cos(θ) on V^2 is shown in the inset for testing of DI water. (C) Change of contact angle (DI water) versus signal frequency at 100 V for a fixed geometry (20 µm).

4.1.4 Actuation principle

The actuation mechanism was governed by L-DEP, where the activated electrodes generate a condition for a droplet to spread across a surface (see Figure 31). Suppose a sessile droplet is placed on the edge of an electrode; when activated (ON), the penetrating L-DEP force changes the contact angle on one side of the droplet, thus causing asymmetric wetting, which changes the droplet's center of mass, effectively causing motion. There was also a small overlapping region between the electrodes for a smoother actuation. Furthermore, the overlapping region reduces any actuation lag, where the droplet moves back to the previous electrode pad. An alternative method to minimise the actuation lag was by changing the size of the IDEs. The electrode surface area determines the range of droplet volume compatible with the electrode design. The droplet spreading speed was also influenced by the size of the electrode pads and the electrode activation time.

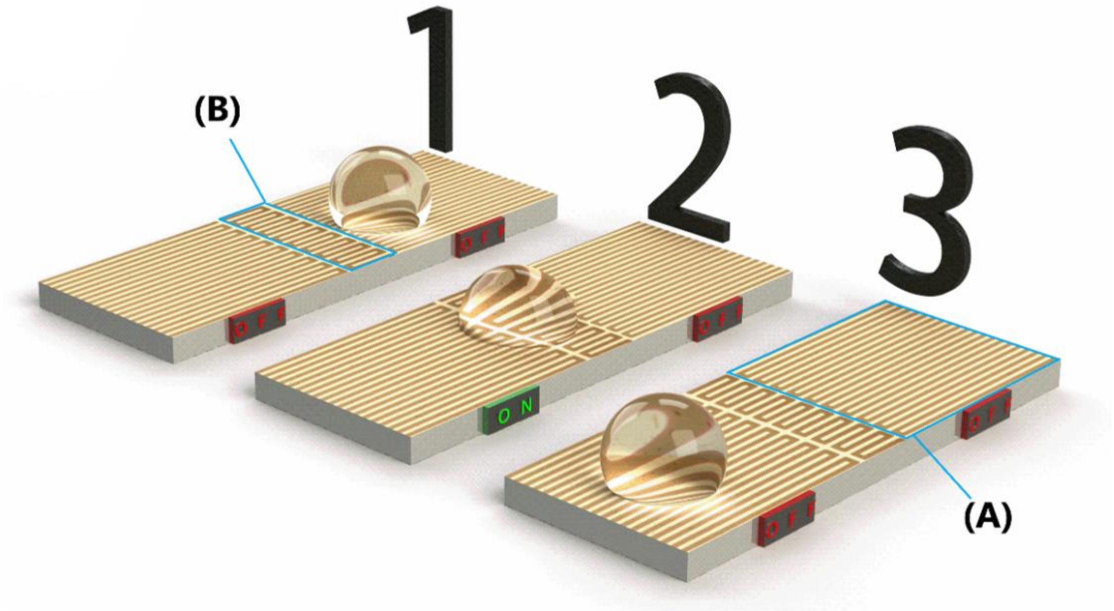

Figure 31 3D schematic of the droplet actuation process. (A) An electrode pad. (B) An overlapping region to facilitate a smoother droplet transition. The electrode pads are activated [ON] when a voltage source is applied between the ground and signal terminals to generate a non-uniform electric field that penetrates the liquid interface. Oppositely, when the circuit is open [OFF] the electrode is idle.

4.1.5 Droplet actuation

The present study deals with the actuation of droplets using a sequential switching technique. The droplet transportation mechanism follows a three actuation step principle; (1,0,0 – 0,1,0 – 0,0,1), where 1's are the activated electrodes, and 0's represent the deactivated electrodes. Figure 32 shows 36 IDEs actuating a DI water droplet on an OTS surface. However, other liquids are similarly compatible since L-DEP is frequency-dependent. For instance, using dielectric liquids (i.e., propylene carbonate) can generate even a higher L-DEP force, as they are commonly used in other dielectrowetting studies.[132]

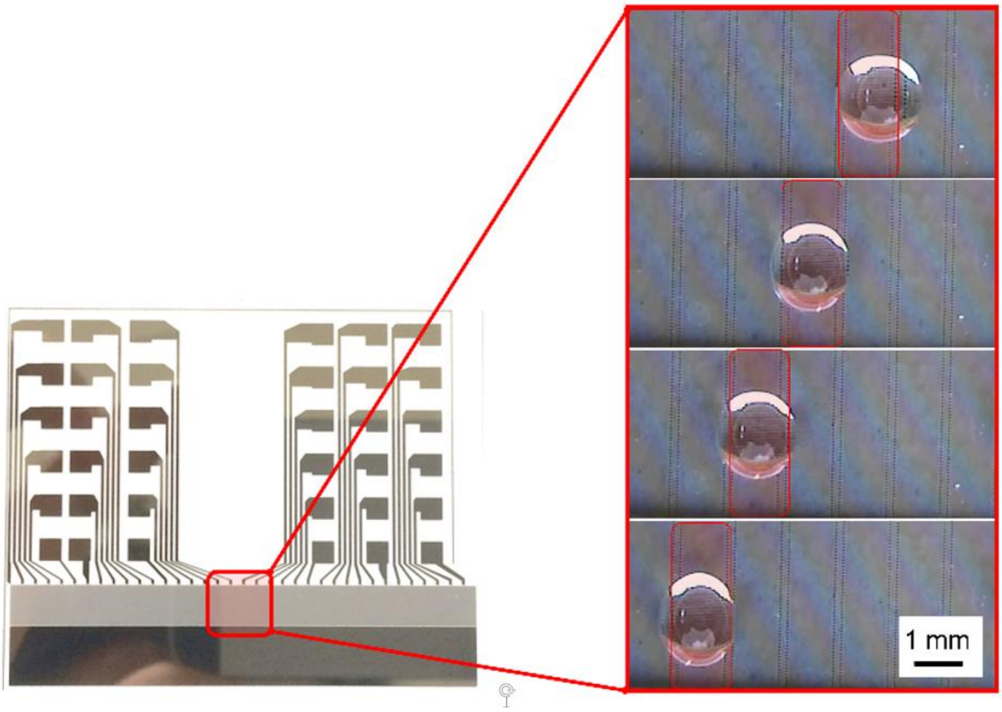

Figure 32 The top view image of a device with 36 IDEs sets (6 mm × 1 mm) to actuate a DI water droplet using 95 V with a signal frequency of 40 kHz. The activated IDEs are represented with a highlighted red colour box.

Linear droplet actuation was achieved at 105 V, with a measured speed of 20 mm/s. Unlike other studies of L-DEP or EWOD, the electrode pads had a higher length to width aspect ratio. This is particularly important for a large-scale device, providing a higher resolution to actuate smaller droplets (see Chapter 6). The minimum operating voltage on an OTS surface was 90 V.

Thus far, electric fields manipulated water droplets to wet a solid surface coated with SAM OTS. However, further refinement is feasible by improving the surface hydrophobicity. Moreover, even lower operating voltages are possible using a lubricant surface treatment. Applying an oil layer on top of the OTS surface modified the pinning forces at the droplet edge associated with the contact angle hysteresis. Indeed, previous work on electrowetting reported modification of the contact angle hysteresis to produce a reversible spreading of droplets using a thin oil layer.[191] This is an alternative method to modify the surface wettability to minimise the contact angle hysteresis,[192] and similar results are likewise attainable using an enhanced OTS surface with superhydrophobic wetting properties.[173]

The actuation of water droplets was achieved at a voltage as low as 30 V using a layer of mineral oil with an average thickness of 100 μm (see Figure 33). On the contrary, the actuation speed was severely reduced after the surface treatment to only 1.5 mm/s. This can be explained by the drop in the electrostatic energy per unit contact area in the droplet edge, determined by the applied voltage and penetration of the electric fields in the liquid layer. Furthermore, the mineral oil layer promotes contact line movements, and changes the contact angle, whilst also reducing the electric field intensity that penetrates into the water.

The thickness of the oil layer was regulated by controlling the volume of the oil-injected over a confined area and then spin-coated to aid uniformity. There are other methods to produce a lubricant impregnated surface, such as using micro-pillars.[191] However, these treatments would increase the thickness of the insulating layer, which can reduce the performance. Nevertheless, a faster droplet motion with a lower operating voltage may still be possible by reducing the lubricant thickness to generate higher forces. The application of the lubricant layer was not further pursued as it is irrelevant in the automotive sector. Furthermore, employing a superhydrophobic coating can also produce similar performances.

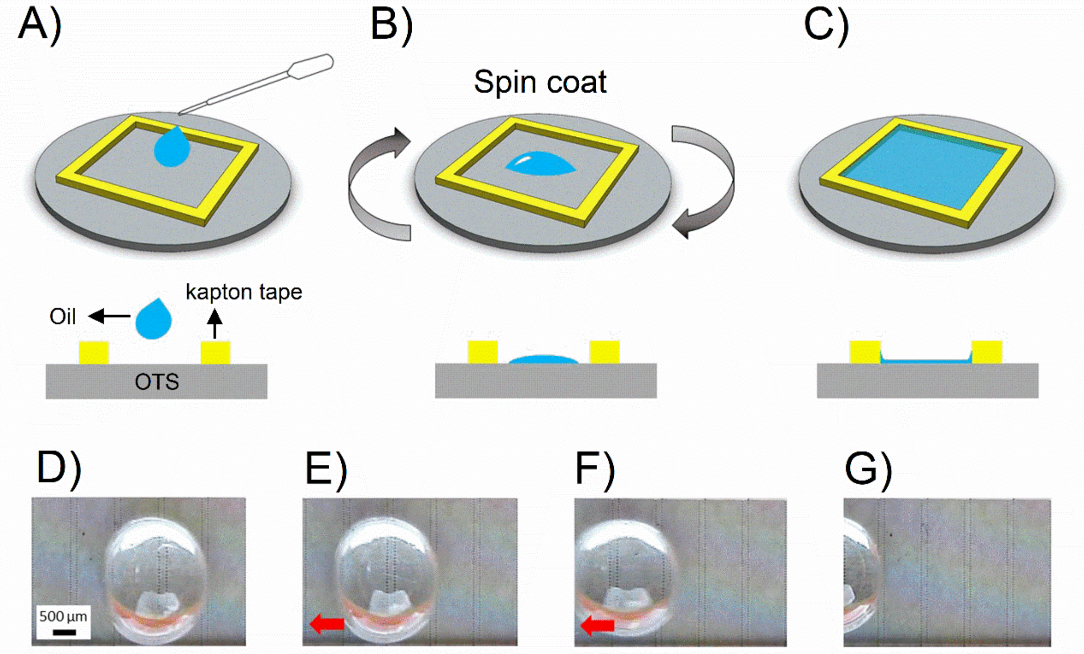

Figure 33 Experimental method showing the actuation of a droplet using lower voltages. (A - C) The thickness of the oil layer was regulated by controlling the volume of the oil injected over a confined area and then spin coated to aid uniformity. (D - G) Top view images showing the actuation of a water droplet using 30 V on a layer of mineral oil.

4.2 Wetting modification

Droplet actuation via a wetting modification is another method to produce droplet movement for a self-cleaning application. Due to the high contact angles associated with the hydrophobic surfaces, the droplets readily roll-off, compiling dirt particles along the way. This self-cleaning mechanism can either function independently or be integrated with other actuation methods (i.e., electric systems) to improve their performance.

A self-cleaning superhydrophobic coating is an appealing solution, but they have a relatively short lifecycle as their hydrophobic properties degrade over time. Furthermore, most of the effective coatings have topographical patterns that interfere with optical transparency, and are also prone to failures due to a surface mechanical damage. One of the best solutions is incorporating a suspension of hydrophobic silica nanoparticles spray-coated on a substrate.[193] Nevertheless, other superhydrophobic coatings are comparatively effective using different coating methods.[194] Various methods have been developed to prepare wettability patterns on superhydrophobic coatings. For example, plasma treatment,[195] photo-induced modification,[196] and soft-lithography.[197] The primary limitation of the coating methods for our application is the thickness of the layer.

A continuous and unidirectional droplet actuation has already been reported without any input energy using a wettability gradient.[69] Typically, by modifying the surface chemistry or otherwise adding topographical features.[70] Additionally, it is also possible to combine this approach with a microfluidic device for transporting and merging droplets. There are likewise new methods to transport microscopic liquid layers based on a unique topological structure.[73] The topological fluid diode enabled long-distance directional liquid transport.

4.2.1 Hydrophobic coating

The self-assembly of organic molecules is a spontaneous chemical process in which chains of molecules are formed on the substrate by adsorption, and are organised into a more or less large ordered domain.[198] Adsorption is a chemical process describing the adhesion of molecules from a gas or liquid to a substrate. OTS SAMs produced by adsorption is typically made by immersing a substrate into a solvent solution (typically hexane or toluene).[199] However, the self-assembly process is also possible from the vapour phase.[200] They are made by the chemisorption of the "head groups" onto a substrate, followed by a slow (several hours) organisation of the "tail group".

Generally, the SAM formation kinetics are dependent on the growth conditions and material properties of the adsorbate, substrate, and solvent. The growth temperature is critical as higher temperatures (i.e., higher than room temperature) increase the entropy of the growth leading to nonuniformities.[201] Furthermore, the concentration of adsorbate in the solution is crucial.[202] For instance, a low concentration require a longer immersion time. Other examples include the purity of the adsorbate, contamination on the substrate, level of humidity, the alkyl chain length, and mechanical vibration during the growth can all change the thin-film growth quality.

The coating of OTS via a self-assembly method was the preferred hydrophobic surface treatment because of scalability, availability, and affordability.[203] The hydrophobic coatings were sensitive to contamination, but values reproducible to better than a few degrees were obtained under controlled conditions. Additionally, the thickness of the SAM OTS coating is in the nanoscale.[189]

Hydrophobic surfaces have self-cleaning properties, and they are highly water repellent. For instance, droplets tend to roll away from the surface, carrying dirt and contaminants without any external force. This effect is amplified when other external forces are included. For example, when a tilted surface is placed in front of a wind stream, a scenario typically found in an automotive application.

Figure 34 A shows the effects of hexane-OTS solution concentration and SAM deposition time on the droplet contact angle. A higher concentration of hexane-OTS can increase the contact angle up to a saturation limit of 110°. The solution of hexane/OTS (1 part of OTS in 500 parts of hexane by volume) was the most appropriate condition with a self-assembly deposition of at least 7 hours.

Figure 34 B shows the sliding angle versus droplet volume for a surface with a contact angle of 110° (±4). Figure 34 C, D shows the side view images of a droplet with a contact angle of 110° and a sliding angle of 10°, having a contact angle hysteresis of 14°. The droplet sliding angle is a characterisation method to assess the droplet mobility. The sliding angle is between 23° and 7°, depending on the droplet volume. Moreover, the sliding angle is higher for smaller droplets because gravity is less dominant (below the capillary length).

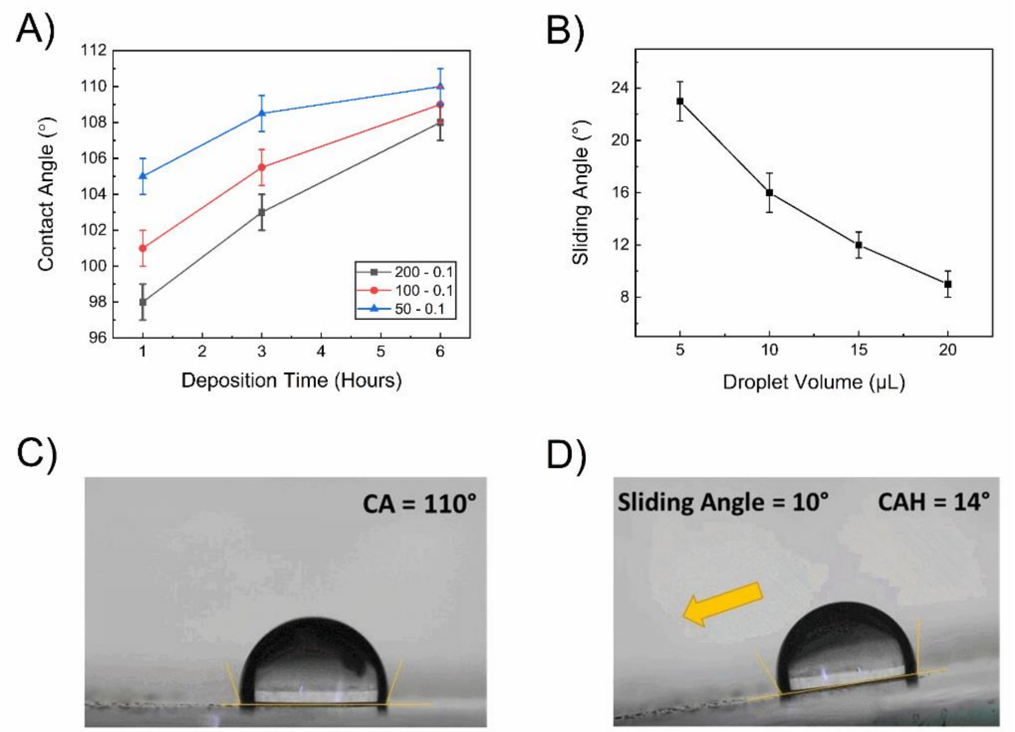

Figure 34 OTS hydrophobic coating. (A) The contact angle versus hexane-OTS solution concentration (ml). (B) Sliding angle versus droplet volume for an OTS surface with an optimum contact angle of 110°. (C - D) Side view images showing the droplet contact angle at 110°, with a sliding angle of 10°, and a corresponding contact angle hysteresis of 14°.

A closer look at the deposition time and solution concentration shows that the contact angle reaches a saturation limit at 110°. Nevertheless, reported studies showed that functionalising SAM OTS with a plasma-treated SU-8 surface significantly improved the hydrophobicity (even up to 150°).[173] However, the reported superhydrophobic properties are unstable and degrade over time. In contrast, there are other fabrication methods to obtain a superhydrophobic surface. The most popular is the modification of the surface morphology before applying the hydrophobic coating. For instance, micro-pillar arrays are commonly used to achieve superhydrophobic properties.[204] Alternatively, growing nanowires before depositing the hydrophobic coating changes the surface morphology and produces similar results.[205]

We deposited zinc oxide (ZnO) nanowires to modify the surface morphology before the SAM process to produce a superhydrophobic coating. Initially, 10 nm of silicon dioxide (SiO_2) was deposited (using an E-beam evaporator) on the SU-8 layer to improve the uniformity of the nanowires. The nanowires were grown on the surface by a seed-mediated chemical bath deposition process. The nanowire film modified the surface before the OTS self-assembly process. Figure 35 A shows multiple water droplets on a superhydrophobic surface (OTS SAM) functionalised with the ZnO nanowires.

Before and after coating the nanowires with OTS, the surface wetting properties change from superhydrophilic to superhydrophobic. Figure 35 B shows a side view image of a droplet with a contact angle of 165° from 110° when coating a non-texture surface with SAM OTS. Furthermore, the sliding angle of the superhydrophobic surface is less than 1°. Figure 35 C-E shows time-lapsed images of a water droplet moving across a surface at an inclined angle of 5°. Additionally, Figure 35 F shows an SEM image of the ZnO nanostructures-based coating. The ZnO nanostructures are cheap and easy to grow. Furthermore, they are biocompatible and ideal for microfluidic applications.[206]

ZnO nanowires are prone to mechanical damage due to their poor mechanical properties.[207] Furthermore, from an electrical perspective, ZnO is a semiconducting metal oxide. Therefore, it is an incompatible candidate for a coating material on electrowetting/L-DEP devices that require the electric field to penetrate the liquid interface. Additionally, the nanowires reduced the optical transparency (see Figure 35 A), which is also critical for some applications, particularly for a self-cleaning cover lens.

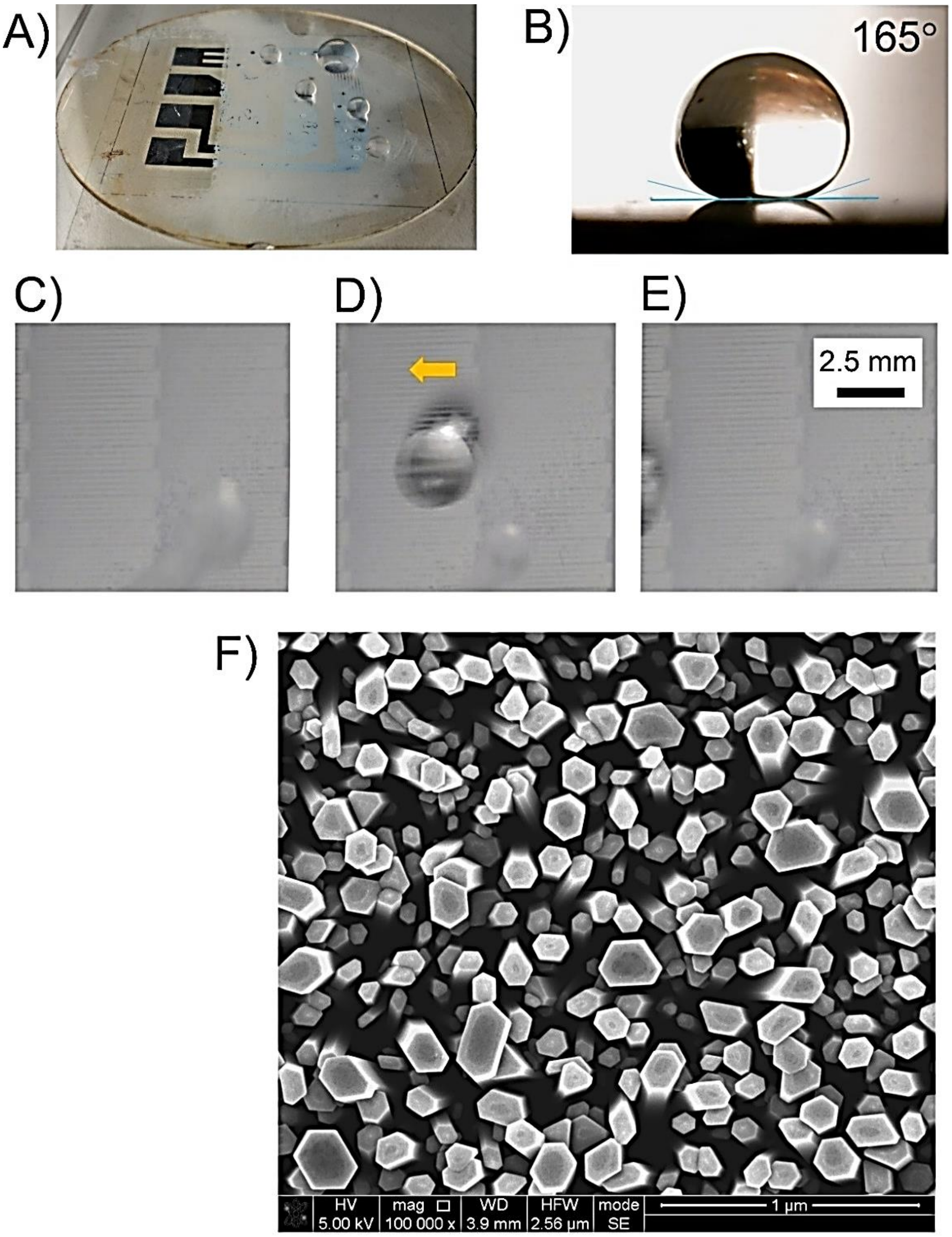

Figure 35 (A) Broad overview imagine showing multiple droplets on a superhydrophobic surface. (B) The side view image of a droplet with a contact angle of 165°. (C - E) Time-lapsed images of water droplets moving across a surface (at an inclined angle of 5°) with a superhydrophobic coating. The sliding angle of the surface is actually less than 1°, immediately rolling off any droplets that come in contact with the surface. (F) Scanning electron micrographs of ZnO nanowires. Furthermore, the height of the nanowires are 600 nm.

4.2.2 Droplet actuation by a wetting gradient

In principle, a wettability gradient is a hydrophilic/hydrophobic pattern that produces droplet motion in the direction of increasing wettability.[208] There are several reported studies investigating the wettability gradient for droplet actuation.[209-211] Nevertheless, a wettability gradient using SAM OTS coating is uncommon. Figure 36 shows the testing of a 5 mm long pad with a wettability gradient. The width of the gradient patterns change from 400 μm to 20 μm (see Figure 36 A). The patterned coatings were prepared using a photolithography process. A photoresist layer (S-1813) was spin-coated over the SU-8 layer and patterned using a photomask. The samples were then treated with a hydrophobic SAM OTS coating to enhance the surface hydrophobicity. The photoresist layer was then removed using the 1165 remover to produce a patterned OTS layer.

Figure 36 B-E shows the time-lapse images of a droplet (DI water) moving across the surface with a wettability gradient. The morphology of the patterned surface was in the nano-scale, and it was entirely transparent. For that reason, there are four red markings on the back of the glass substrate to identify the area with a wettability gradient. When a droplet was placed on the right end of the patterned strip (hydrophobic dominated area), it moves spontaneously along the direction of the wettability gradient towards the more hydrophilic region.

The droplet actuation by wettability gradient has several disadvantages. Firstly, the droplet motion is interrupted when placed over the hydrophilic area. This is problematic when several droplets are added to the surface, i.e., during rainfall to form a larger droplet. Moreover, we noticed that the effectiveness of the wetting gradient degraded over time as new impurities/contaminants were deposited over the surface over time.

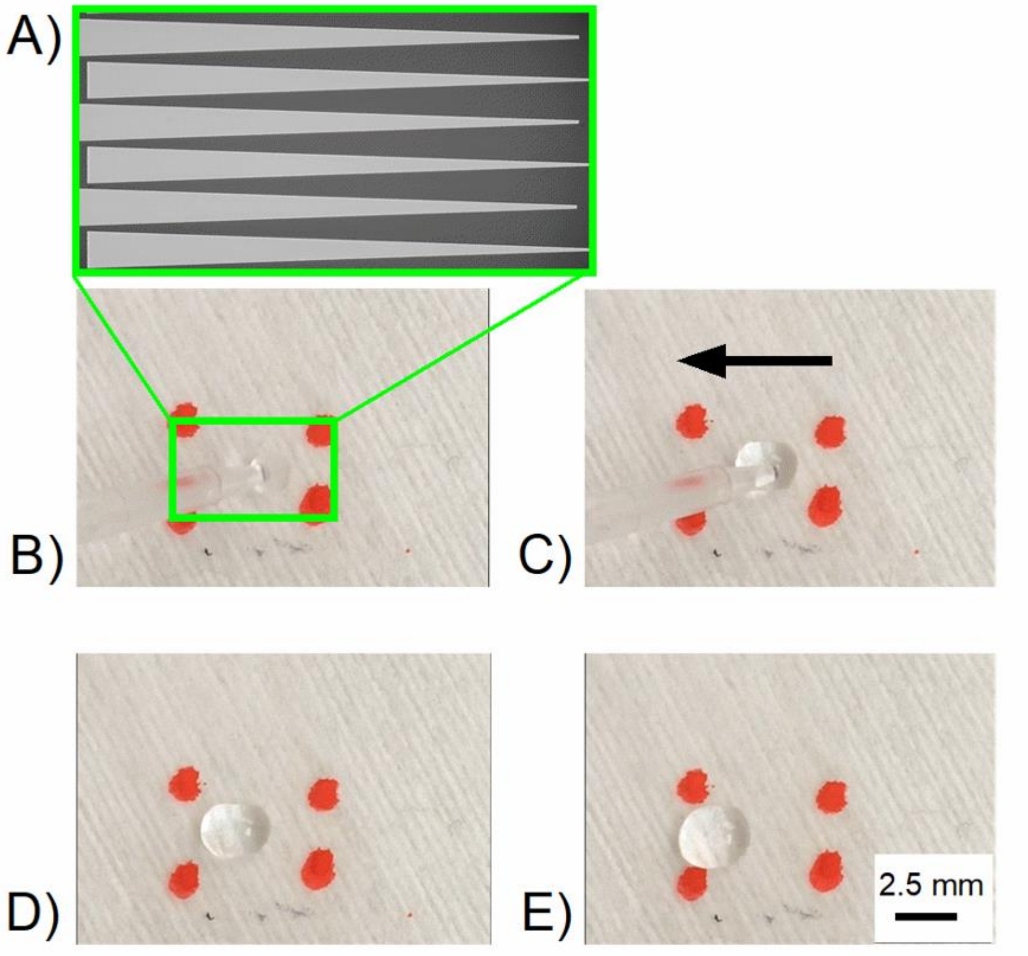

Figure 36 (A) Hydrophobic pattern showing the wettability gradient for a unidirectional droplet actuation. The dark areas are coated with SAM OTS. (B - E) Time-lapsed images of a water droplet moving across a surface with a wettability gradient. There are four red markings on the back of the glass substrate to identify the area with a wettability gradient.

The uncontrollability of the droplet motion is limited by the length of the wettability gradient and it is unsuitable for a large-scale device. Therefore, we propose a novel approach where the wettability gradient is combined with an electric system to overcome this limitation. Figure 37 shows a hypothetical device where the electric fields move the droplet from one wettability gradient pad to another and effectively increase the actuation length. However, the application of the wettability gradient is still limited by the short lifespan, making it less effective than the electric systems that can increase the applied voltage to compensate for the reduction in the hydrophobicity.

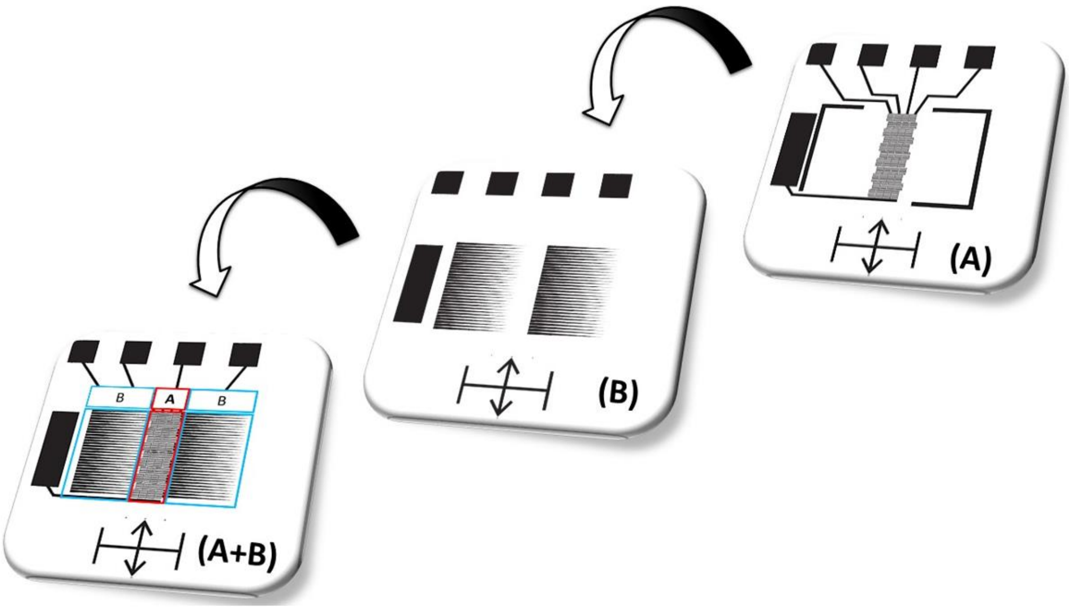

Figure 37 Schematic drawing showing a conceptual design of a combined electric-driven droplet actuation with a wettability gradient for a large-scale application. (A) The device consists of four IDEs to electrically control the droplet position. (B) Wettability gradients are fabricated over the SU-8 layer in the device-A. (A+B) The hybrid device that overcomes the limitation of the wettability gradient for a large-scale device.

4.3 Variable interdigitated electrodes

Droplet manipulation is a growing area of research with several engineering, biological, and chemical protocols in lab-on-a-chip systems.[132, 133] The work here focuses on the continuous actuation of both conductive and dielectric droplets, overcoming the main bottlenecks in competitive technologies that require high voltages and are often limited to a fixed droplet volume. Electrodes with a variable gap distance generated an asymmetric electrostatic net force, and thus, causing droplet movement.[212] Furthermore, we explored the frequency-dependent relationship between L-DEP and electrowetting. The elongation of the droplets as a function of electrode length was also considered to highlight the magnitude applied forces for various geometries of VIDEs.

4.3.1 Actuation principle

Figure 38 A shows the design of a typical VIDEs consisting of interdigitated electrode pairs with a variable gap distance (D_n) and a length (L). The droplet actuation is possible using an applied DC or AC voltage source to generate a variable non-uniform electric field along the length of the device. The electrowetting and L-DEP effect can be realised via an appropriate signal frequency to actuate various liquids with different volumes. The droplet has to be situated over at least one pair of VIDEs to be actuated. Therefore, the droplet's diameter has to be at least 500 µm. However, smaller droplets can still be actuated using an electrode design with smaller electrodes.

Figure 38 B shows the change of electric field along the VIDEs using a COMSOL Multiphysics simulation model. The droplet is continuously moved across the electrode pad towards the region with a higher electric field gradient. Unlike the sequential actuation technique (i.e., in IDEs), the droplet motion is independent of the droplet volume and position. Additionally, the actuation concept is simple, reliable, and suitable for applications with a linear droplet movement.

The fabrication process was similar to the device shown in section 4.1.2, with four separate layers. The base substrate was borosilicate glass, and then an array of VIDEs (aluminium or ITO) was fabricated using standard photolithography. The VIDEs were protected by an insulating layer (SU-8), with a thickness of 0.5 µm to 1 µm. Finally, the SU-8 layer was functionalised with SAM OTS hydrophobic coating to improve the actuation performance. Additionally, the applied voltages were further reduced using an oil lubricant layer to minimise the contact angle hysteresis associated with the pinning forces.

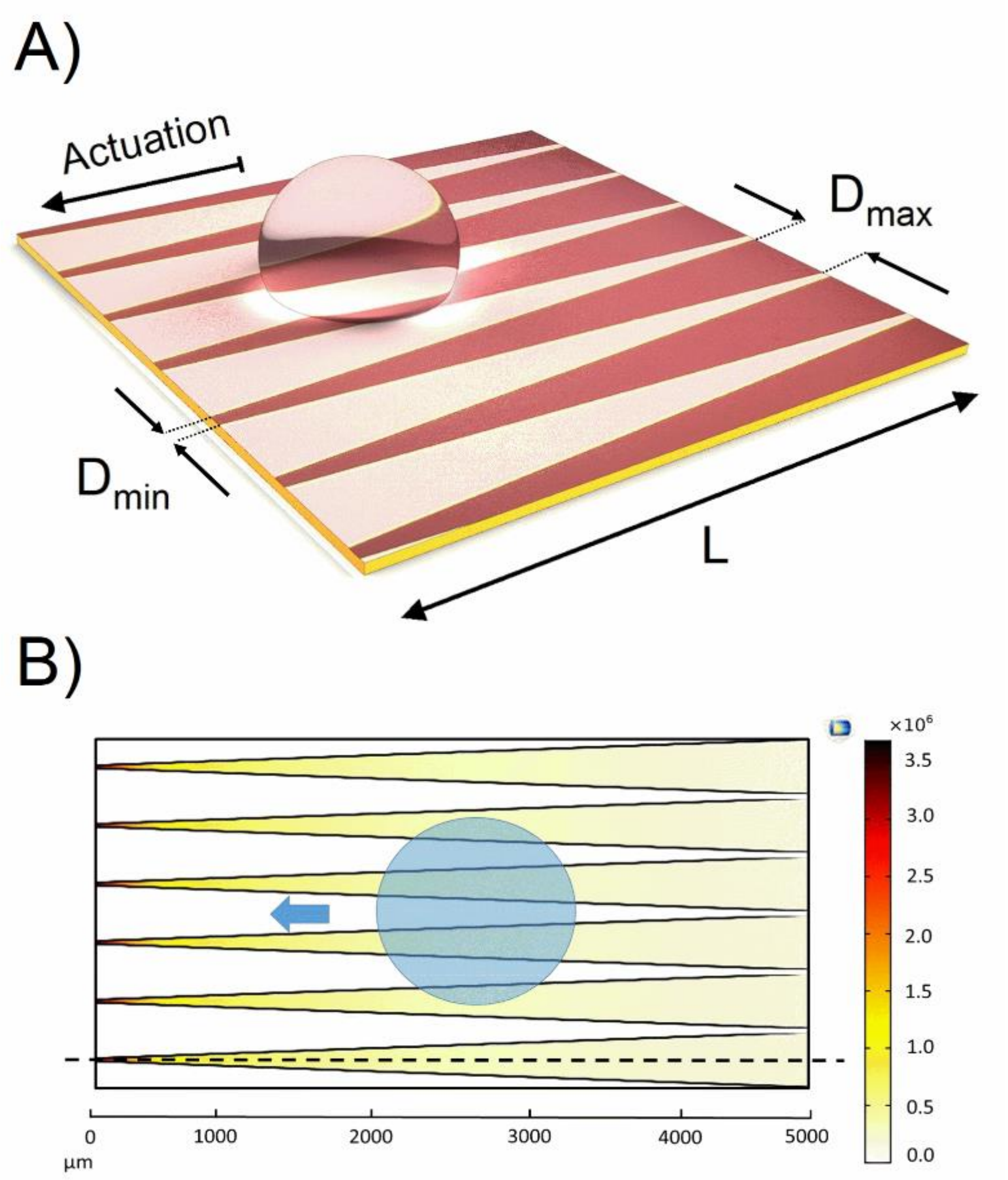

Figure 38 (A) The general overview of a device moving droplets. The device parameters are the electrode length (L), and a varying gap distance (D_n). The electrodes are connected to a voltage source to generate an electric field gradient. (B) 2D COMSOL Multiphysics simulation model to show the change of the electric field along the varying gap distance. The blue circle represent a droplet, and the actuation direction is shown with an arrow.

4.3.2 Continuous droplet actuation

The ability to manipulate droplets with different volumes is fundamental for droplet-based microfluidics, and a critical design requirement for a large-scale cleaning platform. Figure 39 shows the continuous actuation of DI water droplets with different volumes (1 µL to 9 µL) along the length of the VIDEs. Note that the continuous droplet motion is independent of its position on the electrode pad. Hence, the droplet motion is a substantial simplification compared to the conventional actuation methods, without any requirements for direct control or an active feedback control system.

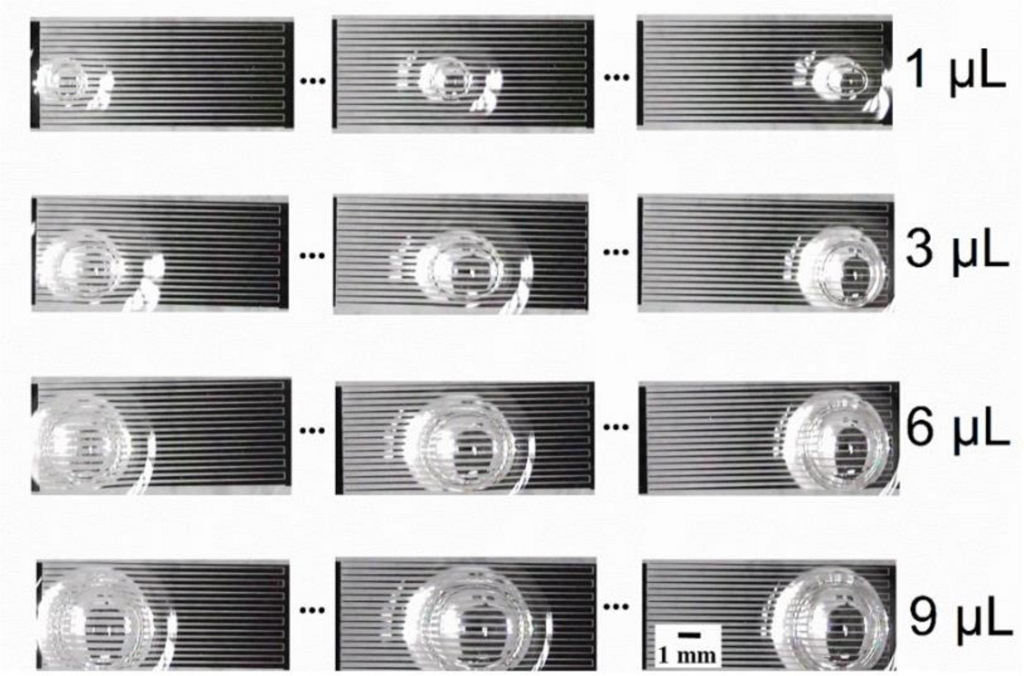

Figure 39 Experimental results showing the actuation of droplets with different volumes on a typical VIDE (L = 10 mm, and D_n = 20 µm and 200 µm). The testing liquid was DI water moving on an oil lubricant layer using 75 V with a frequency of 20 kHz. Note that there is no fixed time between the images taken in the columns.

We considered two electrode geometries with different lengths (L = 5 mm and 10 mm). Figure 40 A shows the effect of applied voltage on the actuation speed.

To calculate the actuation speed, the droplet actuation length is divided by the average time taken for the droplet to reach the edge of the electrode. The experiments verified that the performance of shorter electrodes was up to three times faster than the longer pads. The improved performance is because of sharper changes in the electrode gap distance, thus resulting in a higher effective net force. In contrast, shorter electrodes cover a smaller surface area and may require a switching method for larger platforms. Therefore, the performance is dependent on the scale of the application.

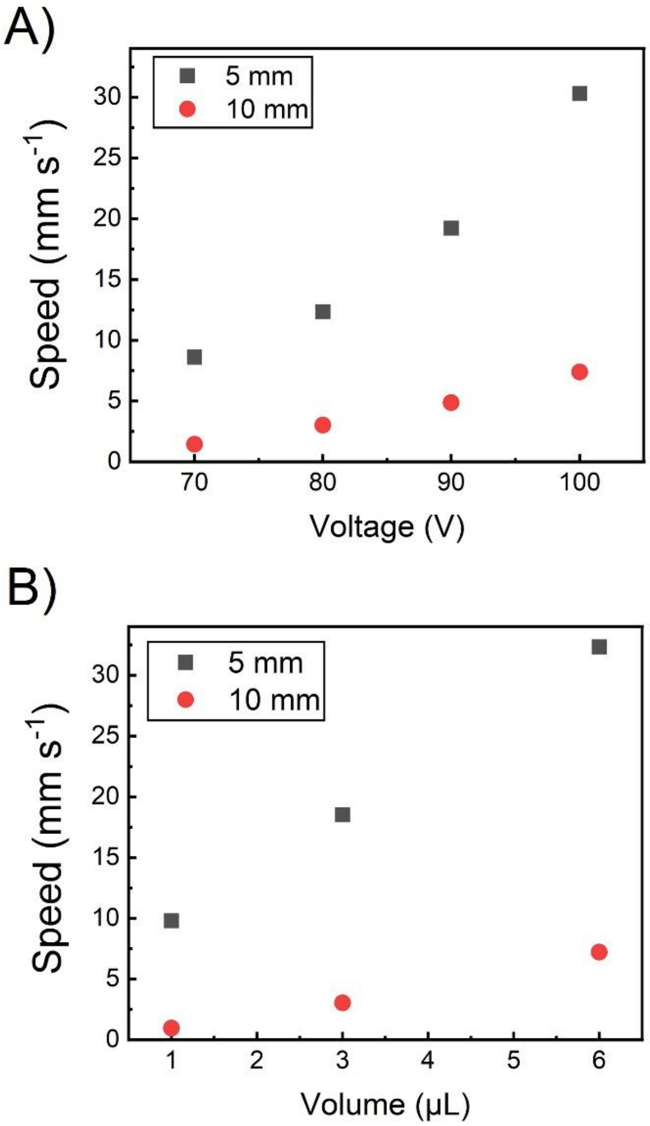

Figure 40 (A) Experimental results comparing the actuation speed at different voltages with a fixed frequency of 20 kHz. The testing liquid was DI water (6 µL), verified on two different pad size lengths. (B) Actuation speed for different volumes of droplets with a fixed voltage of 100 V at a signal frequency of 0.5 kHz.

Figure 40 B shows the actuation speed for different droplet volumes, highlighting the device performance at different scales. The droplet size has a major impact on the actuation speed. Notably, larger droplets (greater than 2.3 mm) cover a greater surface area and have a shorter distance to cover. Moreover, the larger droplets experience a greater surface friction, with gravity playing a more dominant role, which is a significant design factor for inclined surfaces. Similarly, larger droplets overlap with more electrodes, and thus the electrode size is a critical design consideration.

The experimental results provided an insight into the droplet actuation speed and similarly verified the impact of electrode geometry on the actuation performance. Additionally, other geometries with different gaps were also tested to study the effect of electrode gap distance on the actuation performance. The experiments showed that smaller changes in the gap distance (i.e., D_n = 20 µm to 40 µm) resulted in a failed actuation. The actuation speed was either too slow, or the droplets would get stretched across the surface at higher voltages. The effect of electrode gap distance on the generated electrokinetic forces is further discussed in Chapter 5.

From an application perspective, lower operating voltages are always desirable to avoid complex electronics and electromagnetic compatibility. The introduction of a lubricant layer minimised the surface adhesion, resulting in even lower operating voltages (as low as 40 V). However, the actuation on a plain OTS surface was only possible at higher voltages (100 V or more). Moreover, a lower operating voltage is feasible using a superhydrophobic coating.

Applying a modulated AC signal frequency resulted in a smoother droplet actuation on a plain OTS surface. The pulse signal keying, representing a series of logical ‘0’s and ‘1’s by switching OFF and ON the applied carrier wave signal. The simple ON/OFF binary pulse signals stimulated the droplet’s wetting properties to overcome the pinning forces at the droplet contact line. Figure 41 shows the experimental results with a pulse signal frequency of 2 Hz, and a carrier signal frequency of 500 Hz (sine-wave signal), at a voltage of 90 V RMS.

Other amplitude modulations had an adverse effect on the droplet actuation process. The utilisation of a clock signal generation where the frequency of the carrier wave is changing randomly within a range of feasible values is also practical. The proposed signal modulation is advantageous for automotive applications to reduce the electromagnetic interference (EMI) spectral density that these systems typically generate.

The technological advancements emerging from this work will enable consumer applications previously inaccessible due to the high voltages, size limitations, and control requirements. In Figure 41, the actuation time was 15 seconds. However, the pulse droplet motion using lower voltages coupled with an external force, i.e., shear wind force, can produce adequate droplet motion with practical implications.

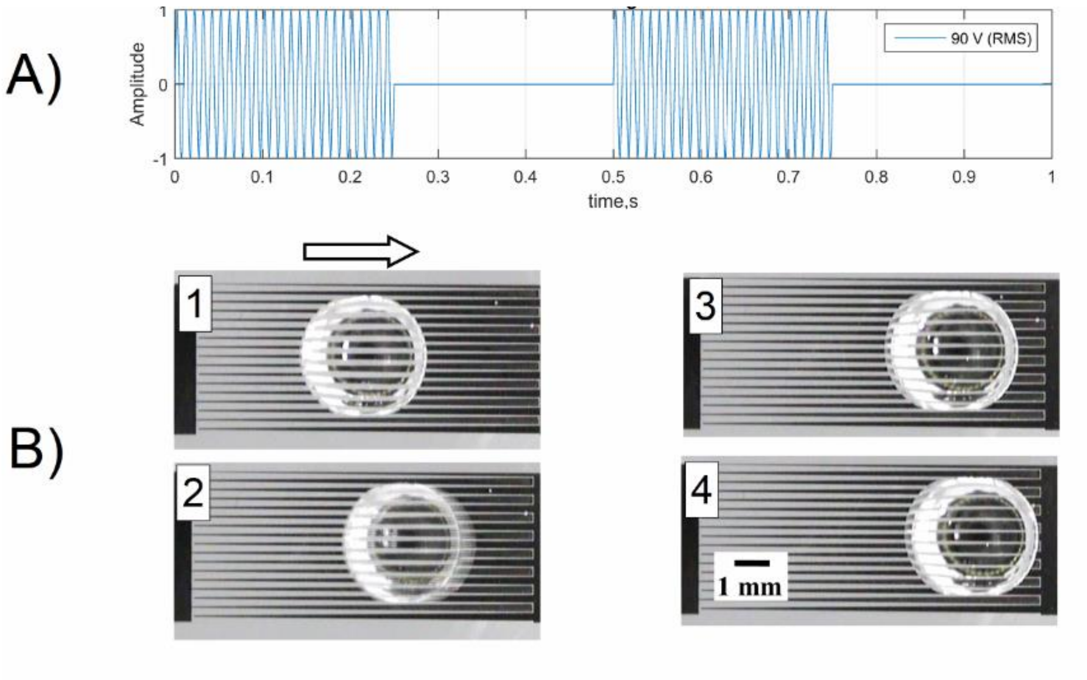

Figure 41 Top view images showing the actuation of DI water droplets using a modulated AC voltage signal (90 V RMS) on a typical VIDEs (L = 10 mm and D_n = 20 µm and 200 µm). (A) The digital modulation signal, showing a square pulse signal (2 Hz), with a carrier signal (500 Hz). (B) DI water droplet moving on an OTS surface using a modulated signal frequency at lower voltages.

4.3.3 Droplet elongation effect

The droplet deformation and elongation across the VIDEs is another method to characterise the applied electric forces. The droplet profile changes from a circular shape into an ellipsoidal geometry when approaching the D_{min}. Significant elongation occurs with a change in the droplet curvature, emphasising the magnitude and type of the electric forces applied along its longitudinal axis. This is a different characterisation criterion than the actuation speed, where the net force translates into faster droplet motion. The elongation effect is also important when estimating the applied electric force, since the droplet diameter is not constant (see Chapter 5 for more detail).

The ratio of droplet extension to the original length is the elongation factor ($\in$), and it measures the degree of deformation when it is subjected to an electric force. Figure 42 A shows the degree of deformation as a function of droplet volume for an electrode pad ($L = 10$ mm, and $D_n = 20$ µm to 200 µm), and the applied signal was 100 V. Furthermore, Figure 42 B shows the degree of deformation as a function of applied voltage for a fixed signal frequency of 10 kHz.

The higher voltages generated the largest degree of deformation. However, the most significant factor was the rate of change in the gap distance that created the largest net force. The elongation effect on the droplet volume is also related to the balance between gravity and surface tension during the deformation process. The experimental results also identified that the smaller droplets undergo the largest degree of deformation.

Figure 42 C - E, shows the droplet elongation (DI water) on a typical VIDEs. The elongation effect was significant when testing a dielectric liquid (propylene carbonate), generating strong dielectrophoretic forces at even lower voltages. When employing a signal (100 V RMS) at a signal frequency of 10 kHz, the value for $\in$ was 0.6 and 0.9 for DI water and propylene carbonate, respectively. The propylene carbonate droplets actuated across the electrode pad by initially spreading into a strip film then transported towards the highest electric field gradient. The actuation behaviour can be explained considering the high dielectric constant and low surface tension of the liquid. Furthermore, the elongation of a propylene carbonate droplet at 75 V was ∈=0.6, equivalent to the elongation factor of DI water at 100 V. Furthermore, the droplet elongation changes the droplet surface area, and it can be measured using ImageJ. This is particularly important for calculating the actuating force or carrying out other mathematical analyses.

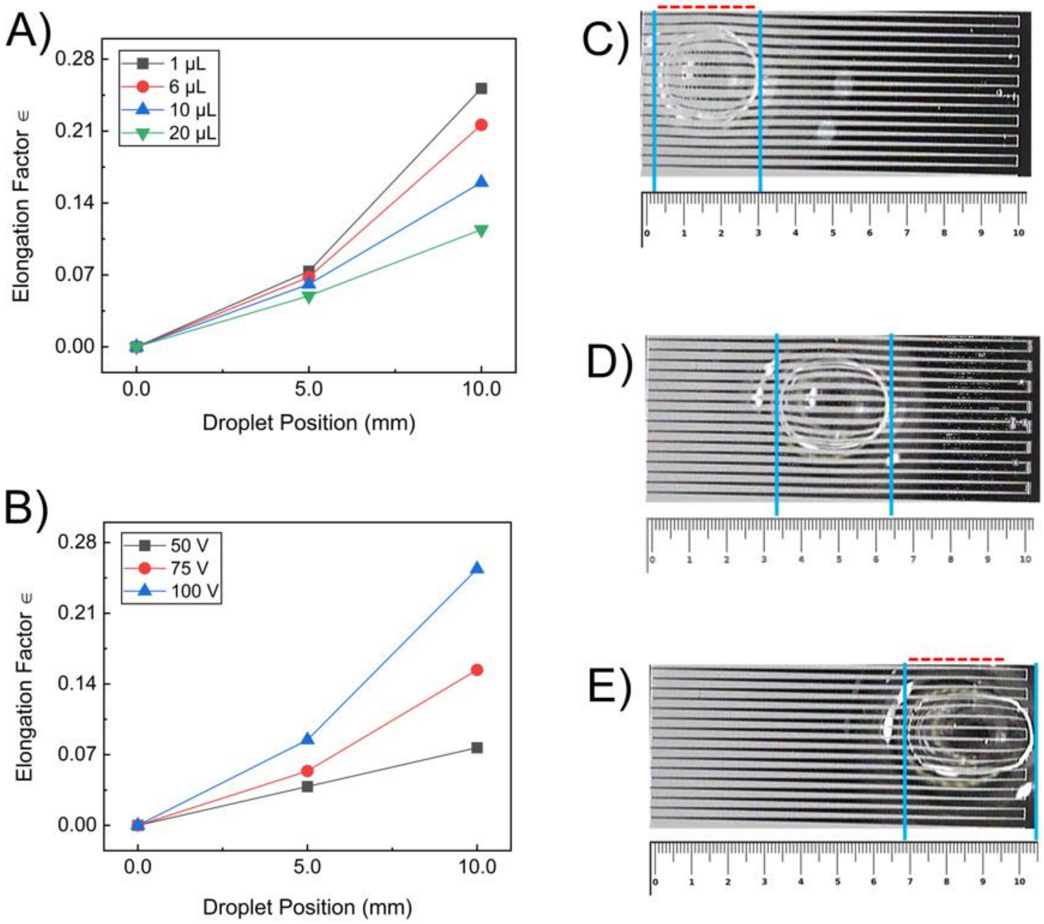

Figure 42 Experimental data showing the droplet elongation. The elongation factor (∈), is the ratio of extension to the original length. (A) For different droplet volumes (100 V at 10 kHz). (B) The different applied voltages for a fixed signal frequency of 10 kHz. (C - E) The top view images of an elongated DI water droplet at three different positions.

4.3.4 Frequency-dependent study

The electrode gap distance in the VIDEs gradually decrease, which leads to an increase in the surface area. Therefore, the electrode geometry enhances the effect of EWOD and L-DEP at different signal frequencies. The electric double layer changes across the electrode length. Additionally, there is also an electric field gradient generated across the length of the VIDEs.

The frequency-dependent behaviour can be explained considering a series capacitive coupling on a planar electrodes (see section 2.7). The RC circuit network model quantifies such dependency by considering the ohmic conductance and capacitance of the dielectric coating and liquid droplet. The liquid behaviour is dominated by electrowetting at low frequencies, where the voltage drops mainly across the dielectric layer. On the contrary, the L-DEP effect is dominant at higher frequencies, where the voltage drops mainly across the liquid. If the signal frequency exceeds the crossover frequency, the voltage drop occurs along with the liquid, which results in an electrothermal effect, and thus, eventually leads to Joule heating.[213] Typically, this is associated with high voltages (several hundred volts), applied at a high signal frequency (> 50 kHz for water).

In this section, the frequency-dependent relationship between the two mechanisms is reported. The water-based solutions were tested at room temperature using different signal frequencies (0.5 kHz to 1.5 MHz at 75 V, and a DC voltage applied at 75 V). The results are summarised in Figure 43 A for the saturated potassium chloride (KCl) solution, DI water, and a 0.006 M KCl solution, which had similar properties to rainwater. Note that any variation in the electrical conductivity of the liquid will significantly shift the crossover frequency.[190] However, detecting small changes in the actuation performance is less likely using the droplet actuation speed method. This is because the actuation speed is not very sensitive to small changes, and thus, it only measures large changes that produces droplet motion.

The higher voltages are not recommended for this study, because of the thickness of the dielectric layer. The highest actuation speed was detected for lower frequencies, where the electrowetting effect is dominant. For instance, the highest dependence on the frequency for DI water was registered between 0.5 kHz to 10 kHz. This is expected as the critical frequency for DI water is approximately 5 kHz.[4] Note that this value changes for different testing conditions. Furthermore, a dielectrophoretic response requires much higher voltages (several hundred volts).[214]

The halide salt solutions behaved differently because the conductivities are much higher than that of DI water, with an estimated critical frequency in the range of a few hundred kilohertz, as it is also experimentally reported elsewhere.[154] Employing DC voltages resulted in lowered performance, and hence was avoided. The average actuation speeds of 1 mm s^{-1} and 1.25 mm s^{-1} were registered (at 75 V) for solution concentrations of 0.006 M and 4 M, respectably. However, depending on the application, a DC voltage source is still favourable because of simpler control requirements. Note that the contact angle saturation limit is far below the 4 M KCl solution tested in this experiment.[215]

Testing results for dielectric liquids highlighted the optimum signal frequency at which they are experiencing the highest dielectrophoretic response. Figure 43 B shows the testing results for dielectric liquids (DI water and propylene carbonate). The L-DEP effect utilises the liquid properties of propylene carbonate, e.g., high surface tension and high dielectric constant, to generate a strong L-DEP force. The optimum frequency for the propylene carbonate was approximately 20 kHz. In contrast, the generated L-DEP force applied at a high frequency (i.e., 50 kHz) was not significant enough for DI water to produce high-speed droplet motion. Further refinement is feasible because L-DEP is not limited by contact angle saturation. Thus, higher voltages produce a deeper penetration with a larger electric field to generate even greater forces.

The frequency-dependent study using different liquids provided sufficient information to select a fixed signal frequency (0.5 kHz) for a surface cleaning application. Additionally, signal processing of low frequency AC signals (in the range of a few kilohertz) is preferred to high frequencies needed for L-DEP, such as in the case for IDEs. Furthermore, the fixed signal frequency reduced the control system complexity, and thus all of the associated costs.

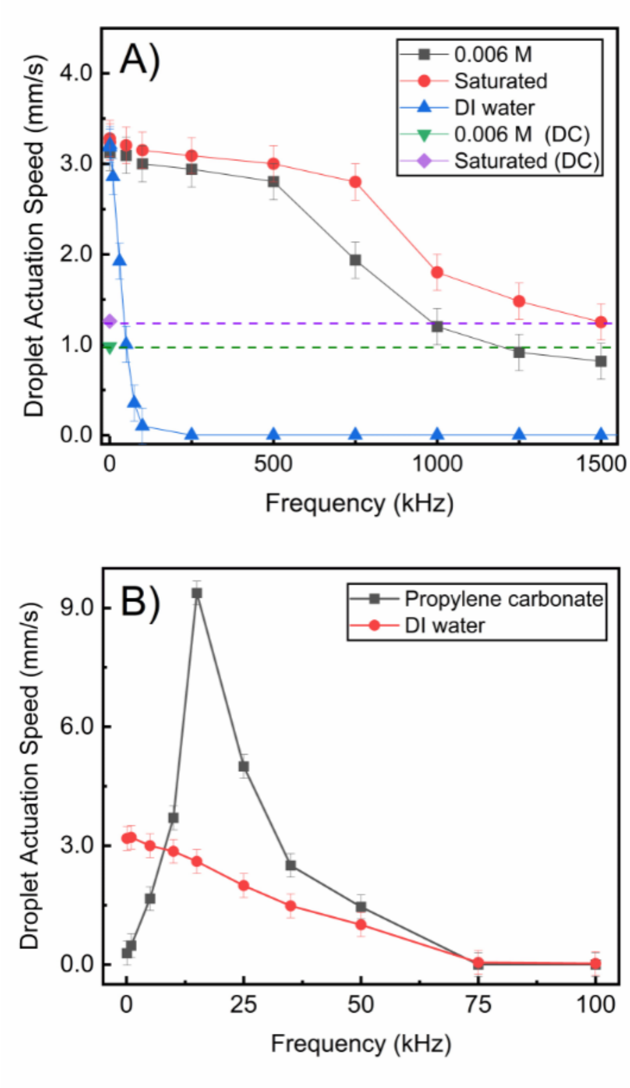

Figure 43 Experimental results that characterise the device performance using the average droplet actuation speed. (A) The frequency-dependent study for water and KCl solutions with different concentrations, tested using DC and AC signal frequencies. The fixed electrode geometry has dimensions of L = 10 mm and D_n = 20 µm to 200 µm. (B) Experimental results for dielectric liquids with an applied voltage of 75 V.

4.4 Summary

In this chapter, we explored various droplet actuation methods. Firstly, the conventional IDEs were improved by reducing the electrode gap distance and insulting thickness to achieve lower operating voltages (100 V or less) from several hundred volts in the previous studies.[132] The lower operating voltages have several advantages, such as electromagnetic compatibility and other safety concerns. Additionally, when considering these adaptations for a different application (i.e., microfluidics), the open surface structure has advantages compared to the sandwich structure, including easy droplet access with the external device. The electrokinetic force generated by the IDEs produced high actuation speeds. The high actuation speed was associated with strong electric fields generated from IDEs with a gap distance of 20 µm. Consequently, IDEs are predominantly suitable for applications where the high actuation speed is a design requirement.

This chapter also introduced a novel electrode design with a variable gap distance to generate an electrostatic gradient to continuously move droplets. The actuation principle is not limited by the droplet size or a requirement for a control system. It is significantly simpler than the conventional IDEs, and likewise, more appropriate in a self-cleaning application. On the other hand, the droplet actuation may not be suitable for some microfluidic applications that require actuation selectivity and directionality. Measuring the droplet deformation and elongation across the VIDEs characterised the applied electric forces. Moreover, the frequency-dependent electromechanics of aqueous droplets is also critical to better understand the relationship between EWOD and L-DEP. It is also possible to select a fixed signal frequency to simply the actuation process.

The study of the hydrophobic coatings showed that a higher contact angle is possible by increasing the concentration of OTS-hexane solution with a longer deposition time. Additionally, we presented a superhydrophobic coating using ZnO nanowires with several applications in microfluidics. The spontaneous droplet actuation using a wettability gradient of SAM OTS was also presented here. However, the actuation method was unsuitable for a cleaning application because of the limited length of the wetting gradient, and the gradual degradation of the hydrophobic coating. The high surface energy of less hydrophobic regions prevented the droplet from moving, which was a major design limitation for a surface cleaning platform. However, we also proposed a novel approach where the wettability gradient is combined with an electric system to overcome this limitation.

In summary, every actuation method is suitable for a specific application. However, we propose that the VIDEs are the most appropriate design for a self-cleaning platform. A notable suggestion is integrating the wettability gradient with the VIDEs design to reduce the actuation voltages. Furthermore, applying a higher voltage can compensate for the degradation of the hydrophobic coating gradient, extending the lifecycle of the cleaning platform. An alternative approach is employing an effective superhydrophobic coating to reduce the actuation voltage.

Chapter 5
Electrokinetic Forces

This chapter focuses on studying the droplet actuation physics and the electrokinetic forces generated across the VIDEs using an analytical and experimental approach. COMSOL Multiphysics simulated the distribution of electric fields generated by the VIDEs. Additionally, we explored an RC circuit network model to analyse the actuation physics of VIDEs. The analytical study estimated the values of equivalent capacitors, resistors, maximum electrostatic energy, maximum electrostatic force, and critical signal frequency. The experimental method consisted of a tilted platform that characterised the electric body forces as a function of gravity of a droplet on a frictionless surface. Furthermore, we experimentally verified the optimum actuation performance and critical signal frequency using the tilting stage method. The analysis demonstrated in this chapter provides an analytical method to improve the electrode design and maximise the droplet actuation force.

5.1 Device model and simulations

5.1.1 Electric field simulation

The electrostatic module in COMSOL Multiphysics provided the simulation models to analyse the electric field distribution. There are four different electrode geometries selected for this study with varying length and gap distance (see the details in Table.2). The electrode gap distance was kept at 20 μm to prevent a dielectric breakdown at higher voltages (up to 100 V).

Table 2 The dimensions (length and gap distance) of the electrodes (VIDEs) used in this section. The minimum electrode gap distance was kept at 20 µm.

Electrodes (VIDEs)	Length (mm)	Maximum gap distance (µm)
VIDE 1	10	400
VIDE 2	10	200
VIDE 3	5	400
VIDE 4	5	200

Referring back to Eq. 11 (section 2.5), the primary driving factor for generating the largest electric body force is the magnitude of an applied electric field. In particular, the rate of change in electric field across the length of the VIDEs. Therefore, for an electrode pad with a fixed length, the change of gap distance is an important design consideration to control the actuation forces. Figure 44 shows the simulation results for different pairs of VIDEs with an applied voltage of 75 V.

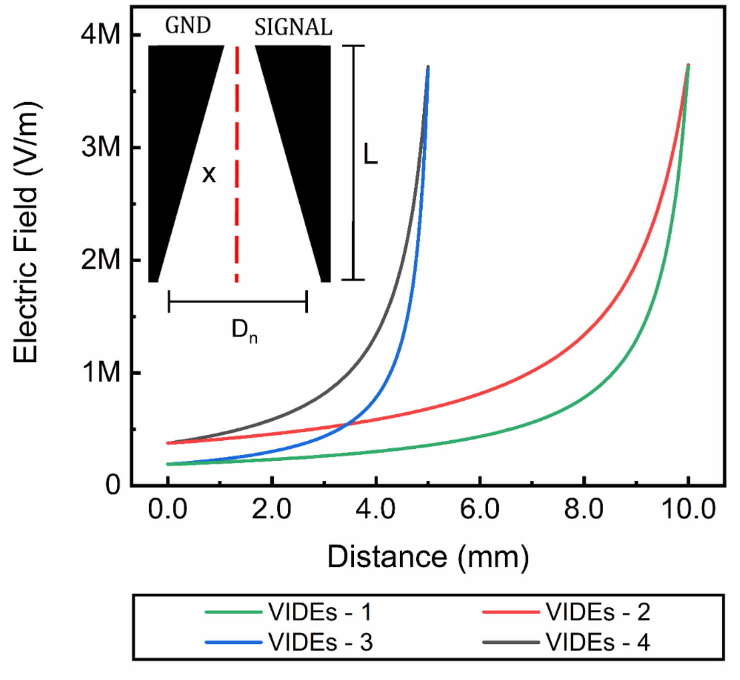

Figure 44 Line graph showing the decay of the norm electric field along the length of the VIDEs for different geometries. The subfigure shows the cut plane that the readings were taken from, labelled as "x". D_{min} was fixed at 20 µm. Please refer back to Table. 2 to see the electrode geometries.

The simulation results showed that shorter electrodes (L = 5mm), and VIDEs with a variable gap distance between 20 µm to 400 µm produced the sharpest change in the electric field. Furthermore, the density of electrode pairs (i.e., number of fingers) is similarly important. For instance, VIDEs with a maximum gap distance of 200 µm had twice the electrode density per unit area.

Although only four electrode geometries were considered here, other designs are still feasible with a longer length or a different gap distance. However, increasing the length beyond a certain limit becomes problematic because the rate of change in the electric field becomes too subtle. VIDEs with a lower electrostatic gradient produce smaller forces. Thus, requiring either a superhydrophobic surface or a larger applied voltage to produce droplet motion. A larger voltage is needed because of a wider range in the electrode gap distance to generate an equivalent actuation net force. Whereas an improved hydrophobic surface minimises the retention force of surface adhesion.

5.1.2 RC Circuit Network Analysis

To carry out the RC circuit network analysis, the circular cross-section of the droplet with a radius R, was split into sub-domains (see Figure 45). The average droplet radius was estimated experimentally using the data collected from section 4.3.3. The analytical analysis in this section considers only two finger electrodes (pair of VIDEs). The area of interest is calculated from the electrode width W_x, when considering the reference centre line distance d, and the distance Y_1 and Y_2, which are the distances along the edge of the electrode pad. There is a shared surface area between the finger electrode and droplet interface, labelled as A_1. Additionally, there are two smaller areas A_0, covering both ends of the finger electrode, which was neglected to simplify the calculations. Note that the equivalent surface area A_{eq}, which is the combined area between two finger electrodes rises linearly along the length of the VIDEs at different segments x'. There is also a corresponding horizontal intersection point x_1 and x_2 for every reference segment point of x'.

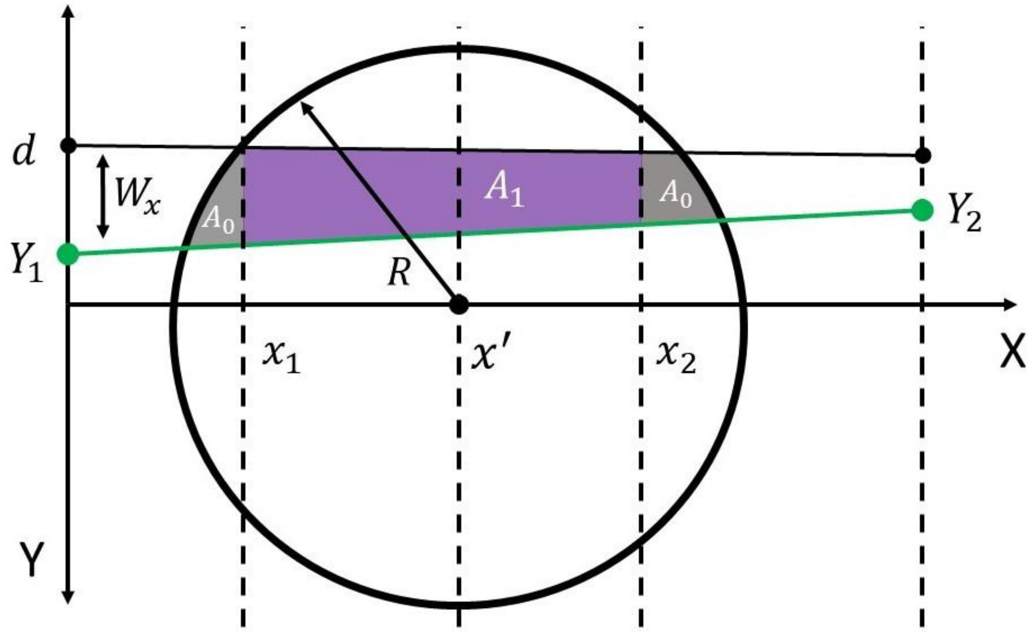

Figure 45 Schematic showing a droplet with a radius (R). The droplet is situated across the length of the electrode (L), at different segments (x'). The areas of interest (A_1 and A_0) are calculated from the electrode width (W_x), when considering a reference centre line distance (d), and (Y_1 and Y_2), which are the distances along the edge of the electrode pad.

The distance x_1 and x_2 are shown as,

$$x_1 = x' - \sqrt{R^2 - d^2} \tag{14}$$

and,

$$x_2 = x' + \sqrt{R^2 - d^2} \tag{15}$$

The electrode width is shown as,

$$W_x = (Y_1 - Y_2)\frac{x}{L} + (d - Y_1) \quad (16)$$

And the intersection area between the electrode and the droplet is expressed as,

$$A_1(x') = \int_{x_1}^{x_2} W_x \, dx = (Y_1 - Y_2)\frac{({x_2}^2 - {x_1}^2)}{2L} + (d - Y_1)(x_2 - x_1) \quad (17)$$

The equivalent RC models provided additional information about the actuation mechanism. The analysis is based on a cross-section of a droplet situated over a pair of electrodes using a planar configuration (see section 2.7). The equivalent RC model is the capacitance in the dielectric layer C_D, capacitance in the liquid C_w (dielectric nature), and the liquid resistance R_w (conductive nature), as depicted in Figure 46.

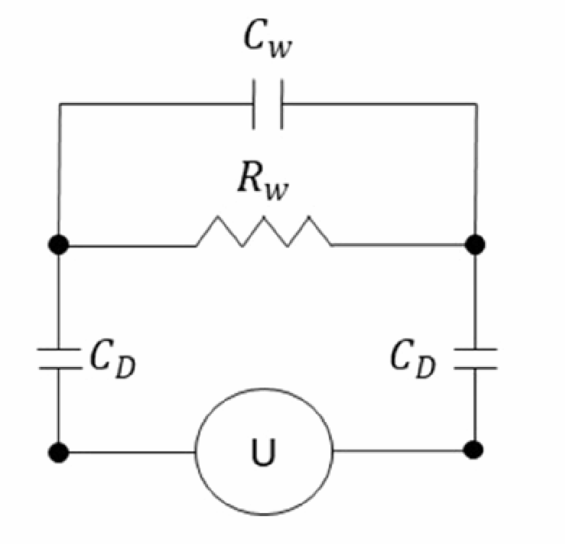

Figure 46 Schematic diagram showing the RC circuit network model of a droplet situated on a pair of electrodes (VIDEs) covered with an insulating layer.

The interface area can be substituted to estimate the equivalent parallel plate capacitor (C_D), expressed as: [4]

$$C_D \approx \frac{\varepsilon A_1}{D} \quad (18)$$

with the assumption that the droplet is separated by an insulating layer with a thickness D, a relative permittivity ε, and the thickness of the SAM OTS layer is in the nanoscale, and thus neglected. Moreover, the liquid conductance component G_w, is expressed as:[4]

$$G_w \approx \frac{\sigma_w K(1-k^2)s}{2K(k^2)} \tag{19}$$

where s is the length of an interface between the droplet and electrode pad. K is the complete elliptical integral of the first kind, $k^2 = [g/(g+w)]^2$, g is the electrode gap distance, and w is electrode width. There are consequences of the assumptions inherent in the expression for the liquid conductance. This includes having only two parallel co-planar stripes of negligible thickness, and assumes that water of finite conductivity fills the entire half space. Additionally, the electrical resistance R_w which is the inverse of the conductance.

Lastly, the capacitance in the liquid (C_w) is shown as,[4]:

$$C_w \approx \frac{G_w \varepsilon_w}{\sigma_w} \tag{20}$$

Figure 47 A - D shows the estimated values for C_D, C_w, G_w, and R_w, respectively. The electrical values are estimated for different VIDEs (see the electrode geometry in Table 2). The analytical analysis shows that the value of dielectric capacitance decreases linearly, whereas the liquid capacitance decreases nonlinearly as the electrode gap distance increases. In contrast, the estimated electrical resistance rises with an increase in the electrode gap distance. The calculations verify that electrodes with a larger gap distance (VIDE-1 and VIDE-3), and shorter length (VIDE-3 and VIDE-4) have the highest rate of change in the capacitance and resistance. The electrical values calculated analytically can estimate the critical signal frequency, maximum electrostatic energy, and maximum electrostatic actuation force.

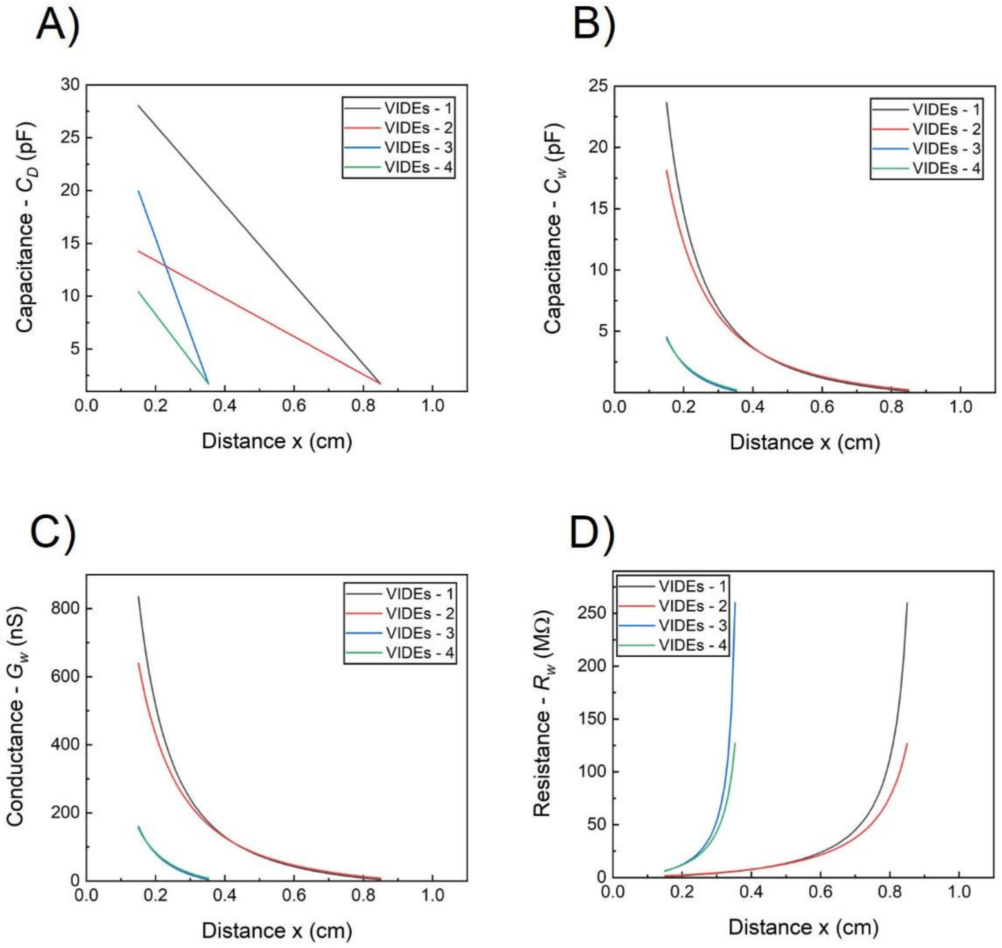

Figure 47 Analytical analysis based on the equivalent RC model to describe various electrical components within the system. The distance (x) is the length of the electrode pad. (A) Insulating layer with an equivalent parallel plate capacitor (C_D). (B) Capacitance in the liquid (C_w). (C) Liquid conductance component (G_w). (D) Electrical resistance (R_w) which is the inverse of the conductance. Please refer back to Table 2 to see the electrode geometries.

Furthermore, Eq. 12 (Section 2.7) can estimate the critical signal frequency to clarify the driving actuation mechanism (see Figure 48). Note that the conductance value is actually underestimated, but any error is always overwhelmed by the variation in the liquid conductivity, which was measured to be in the order of 10^5 µS/m. Close observation shows that the optimum signal frequency response was over an area with the smallest electrode gap distance. In this analysis, the critical signal frequency was underestimated because the system is only considering two finger electrodes. Additionally, the calculations ignore the small gaps in the ends of every finger electrode A_0 (see Figure 45).

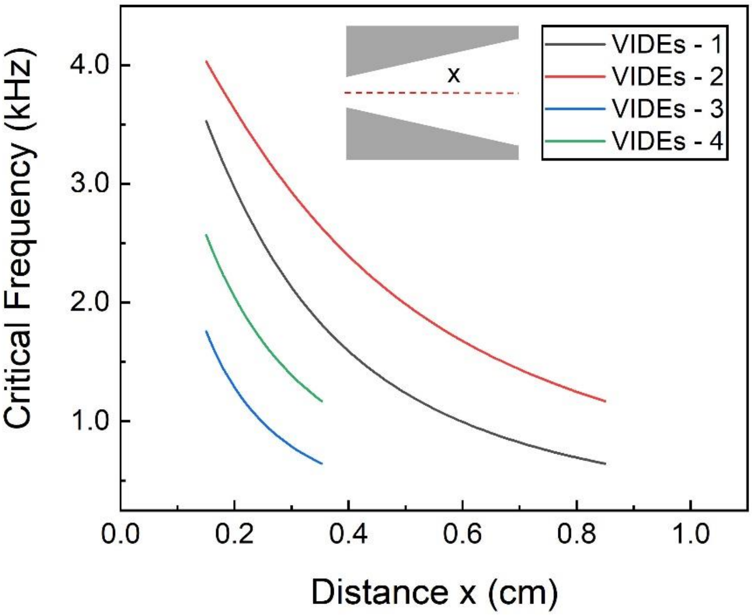

Figure 48 Critical signal frequency for different electrode geometries. There is a range in the frequency values because of the varying gap distance. Please refer back to Table 2 to see the electrode geometries.

Referring back to Figure 46, there is also an electrostatic stored energy W_e in the insulating layer and water droplet when applying a potential difference U, which can be written as:

$$w_e(x) = \frac{C_D|V_D|^2}{4} + \frac{C_w|V_w|^2}{2} \tag{21}$$

Where V_D and V_w are the voltage difference across C_D, and C_w, respectively. Please refer to the appendices for a detail breakdown of the derivations. Note that the electrostatic energy considers both the dielectrophoretic and electrowetting components. The complex amplitude of applied voltage across C_w is:

$$V_w = \frac{i\omega(C_D/2)R_w}{1+i\omega R_w(C_D/2)+i\omega R_w C_w} U \tag{22}$$

where ω=2πf, and the absolute value equals to,

$$|V_w|^2 = \frac{\omega^2 (C_D/2)^2 {R_w}^2}{1+\omega^2 {R_w}^2 (C_D/2+C_w)^2} |U|^2 \tag{23}$$

In addition, the voltage across C_D can be written as,

$$V_D = \mathrm{U} - V_w \tag{24}$$

and

$$|V_D|^2 = \frac{1+\omega^2 {C_w}^2 {R_w}^2}{1+\omega^2 {R_w}^2 (C_D/2+C_w)^2} |U|^2 \tag{25}$$

Figure 49 A shows the maximum electrostatic energy with a signal frequency sweep between 500 Hz and 35 kHz. The analysis shows that the maximum electrostatic energy decreases with an increase in the signal frequency, and the polynomial curve flattens at higher frequencies (i.e., > 10 kHz). Moreover, Figure 49 B shows the maximum electrostatic energy for varying voltages (up to 100 V). The graphic data shows that the energy levels rise nonlinearly when increasing the applied voltage.

The virtual work theorem was used to estimate the maximum actuation force, considering the first derivative of the electrostatic energy dw_e/dx', with respect to the distance (x′). Figure 49 C shows the maximum estimated electrostatic force with a frequency sweep between 500 Hz and 35 kHz. Note that this is the maximum electrostatic force along the whole electrode length, and it is not to be confused with the droplet actuation net force. Furthermore, the actuation force is nonlinear across the VIDEs because of the VIDEs geometry variations. Therefore, the actuation force is different depending on the droplet position along the length of the VIDEs. This analysis is verified experimentally by looking at the droplet elongation (see section 4.3.3). Further work is needed to estimate the droplet actuation net force experimentally. For instance, by conducting a dynamic study of the droplet actuation speed using a high-speed camera to estimate the net force.

The analysis shows that the largest actuation force was detected at a lower signal frequency spectrum (e.g., < 10 kHz). The actuation performance shows that there was a slight dip in the actuation force at the lower frequency spectrum. However, the actuation force remains fairly constant at higher frequencies (e.g., > 10 kHz). Additionally, Figure 49 D shows the maximum electrostatic force for varying voltages (up to 100 V). The study shows that the actuation force rises nonlinearly when increasing the applied voltage.

Figure 49 E shows the maximum electrostatic force of VIDEs with a different electrode gap distance (D_{max}) and a signal frequency sweep between 500 Hz and 35 kHz. The analysis shows that electrodes with a wider gap distance (D_{max}) produce larger forces. Figure 49 F shows the relationship between the electrode length and the maximum electrostatic force (500 Hz and 35 kHz). The analytical results show that shorter electrodes produce a larger force at a lower signal frequency. Moreover, the performance declines at a faster rate at higher frequencies.

The primary focus of the study was to provide an analytical approach to analyse the actuation physics. The calculations show that electrodes with a larger gap distance (VIDE-1 and VIDE-3) and a shorter length (VIDE-3 and VIDE-4) generate the highest electrostatic force, which is estimated to be in the orders of several tens of micronewton. Additionally, further work is needed to better understand the actuation mechanism as a function of electrode geometry.

The estimations considered both the conductive and dielectric components. However, the analysis neglects any changes in the physical properties of water at varying frequencies. Another assumption was that the droplet contact angle remained constant as it moved along the VIDEs. The analytical analysis also ignored the oil layer in the lubricant treatment. This effect is not so significant since the dielectric constant of oil is much lower than that of water. The water-oil interface also changes when applying an electric field but in principle, the oil layer is thicker near the droplet edge. The changes in the film thickness is visible when experimentally observing the droplet profile in motion.

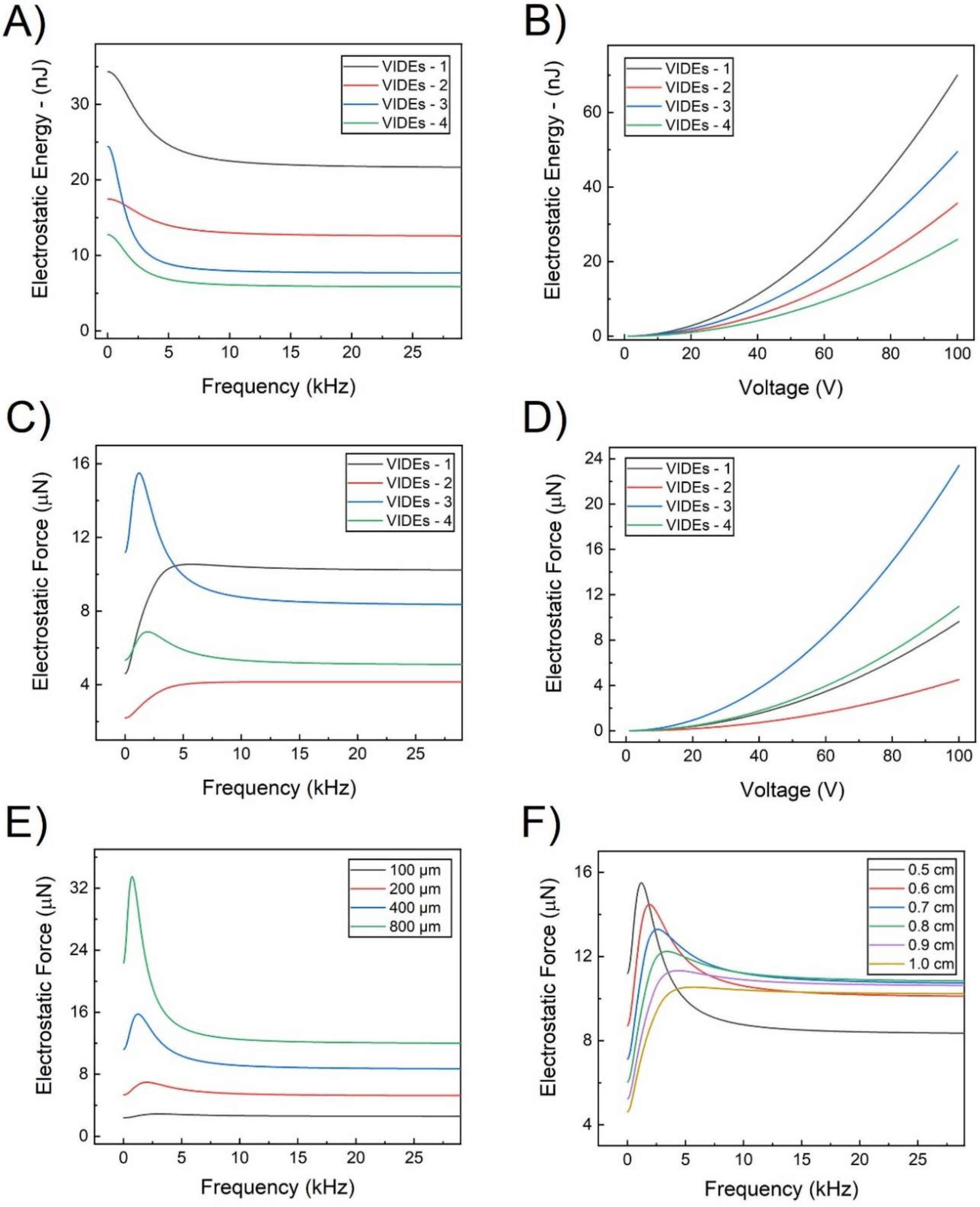

Figure 49 A) The maximum electrostatic energy versus the signal frequency. (B) The maximum electrostatic energy for varying voltages. (C) The maximum electrostatic force versus the signal frequency. (D) The maximum electrostatic force for varying voltages. (E) The maximum electrostatic force versus the signal frequency for VIDEs with a different (D_{max}). (F) The maximum electrostatic force against the applied frequency for VIDEs with a different length. Please refer to Table 2 to see the electrode geometries.

5.2 Experimental Method

Figure 50 shows the experimental set-up with a mechanically rotary control of the mount using a screw gauge adjuster (± 0.1° accuracy). The device (VIDEs) is attached to the platform and firmly secured using screws. There are several spring pogo pins for electrical contact to the device. There is also a camera mount for a Sony Exmor RS 8 MP (1080p). Recording measurements using the side view angle is not recommended due to misalignment issues. Furthermore, because the droplet sliding angle is the primary measuring parameter, only the top view perspective is sufficient to detect any droplet displacement.

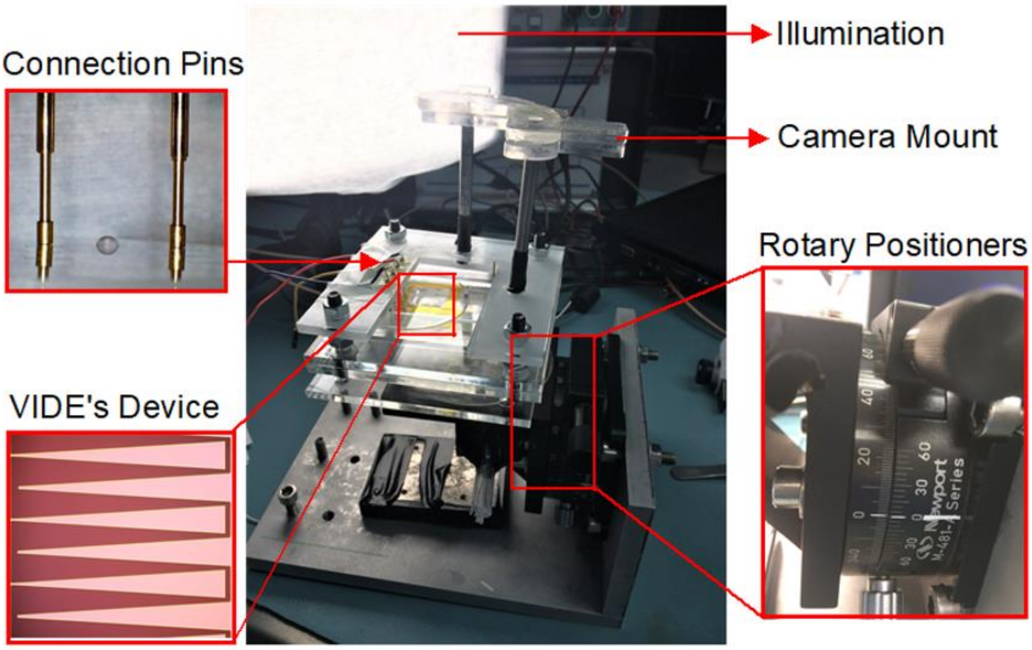

Figure 50 Testing stage with a rotary positioner, spring pogo-pins for electrical contacts, illumination, and camera mount. Firstly, the VIDEs were held in place with Kapton tapes and then mounted with screws to the stage for better rigidity. The testing was carried out on an insulating mat.

5.3 Tilting Stage Experiment

The optimum operating conditions (VIDEs) in Chapter 4 were identified based on the droplet actuation speed and elongation. The tilting stage experiment in this chapter characterises the electromechanics of a continuously moving droplet as a function of the maximum electrokinetic force. The maximum electric force acting on the droplet is identified to be an external force F_e, acting against the gravitational force of a macro-size droplet with a known weight W, resting on an inclined surface with a tilting angle α. Please refer to Figure 51 for a free body diagram of a droplet on a tilted surface.

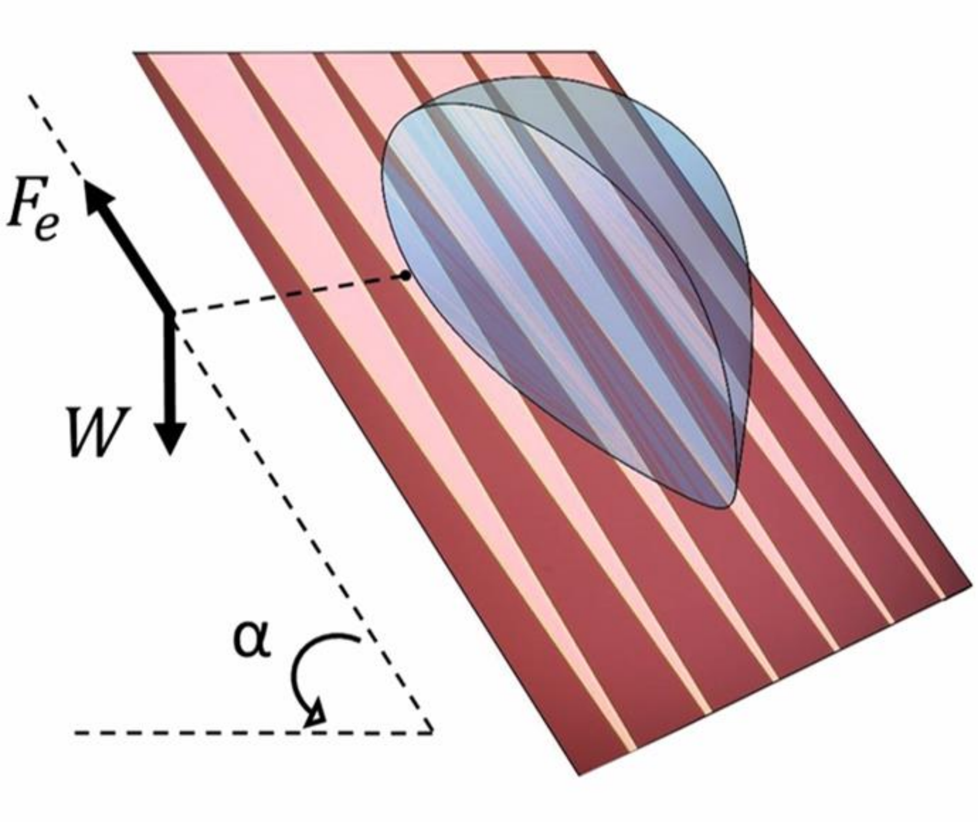

Figure 51 Free body diagram of a droplet actuating on a typical VIDEs, showing the droplet sliding angle. The two opposing forces acting on the droplet include gravitational force (W), and applied electrokinetic forces (F_e). The retention force from surface adhesion is neglected because of a small sliding angle on the lubricant surface.

The droplet sliding angle at zero volts was an approximation of the surface adhesion retention force. It underlines the opposing force that acts against the applied electrokinetic force. Therefore, the effective in plane electrokinetic force is calculated by considering the condition for a droplet remaining stuck on an inclined surface, and expressed as:

$$F_e = \rho \Omega g \left(\sin \alpha_p - \sin \alpha_s \right) \tag{26}$$

where Ω is the droplet volume, ρ is the liquid density, g is the gravity, α_s shows the droplet sliding angle in the absence of an applied voltage, and α_p is the droplet sliding angle under the influence of an applied electrokinetic force.

The testing liquid was DI water with a volume of 15 µL. The droplet volume was regulated using a micropipette with an accuracy range of up to 0.1 µL. The droplet volume should be as high as possible to minimise the effect of surface adhesion. Although 20 µL was suitable for longer VIDEs, but the droplet diameter was too large for shorter VIDEs.

Droplet actuation was feasible on an OTS surface when applying high voltages (100 V or more), but the surface adhesion is generally substantially high. Therefore, it was important to minimise the surface adhesion through an oil surface treatment. As a result, the dominant actuation mechanisms were the gravitational and the electrokinetic forces. Figure 52 A demonstrates that a lubricant surface treatment modifies the droplet sliding angle from 12° to 1°, when the droplet volume was 15 µL. To achieve this, mineral oil was spin-coated within a confined area. Kapton tapes with a thickness of 30 µm provided a confined area to contain the oil layer, approximately 100 µm thick. An alternative approach in a future study is to consider a superhydrophobic coating with a similar sliding angle. Note that such an adaptation is beneficial and would reduce any experimental errors associated with the lubricant surface treatment.

Figure 52 B shows the relationship between the maximum electrokinetic force and signal frequency between 500 Hz and 75 kHz with a fixed applied voltage of 70 V. Higher voltages were avoided to minimise the critical sliding angle, and thus, reducing experimental errors. The experimental results showed that there was a peak at the lower frequency region below the critical frequency domain, and the optimum frequency was between 500 Hz to 10 kHz.

The peak performance was higher for VIDEs with a larger D_{max}. The effective force was also higher for electrodes with a shorter length. The sharper changes in the electrode gap distance explains the better performance for some geometries. Furthermore, this is similar to the analysis based on the equivalent RC circuit network (see section 5.1.2). Note that collecting more experimental data points would significant improve the performance accuracy, particularly at the lower frequency spectrum.

The declining performance at higher signal frequencies (15 kHz or more) was lower for VIDEs with a smaller D_{max} because of a higher electrode density per unit area. Note that a higher applied voltage was needed to generate larger L-DEP forces at higher signal frequencies. The typical operating voltages in previous studies were several hundred volts. Additionally, the gradual reduction in the actuation performance at higher signal frequencies could be because of energy losses due to an increase of the liquid temperature.

Figure 52 C shows the relationship between the applied voltage (up to 100 V) and electrokinetic force at a fixed signal frequency (1 kHz). A stronger electric field was generated at higher voltages. Noticeably, the experimental results confirmed a non-linear increase in the applied electric force upon increasing the applied voltage. The actuation performance was higher for electrodes with shorter length and larger D_{max}. The actuation performance as a function of applied voltage closely matches with the theoretical analysis based on the equivalent RC network model (section 5.1.2). Note that the analysis based on the RC network model considered only a pair of VIDEs, but the experimental results include several pairs. As a result, the actuation force is proportionally larger.

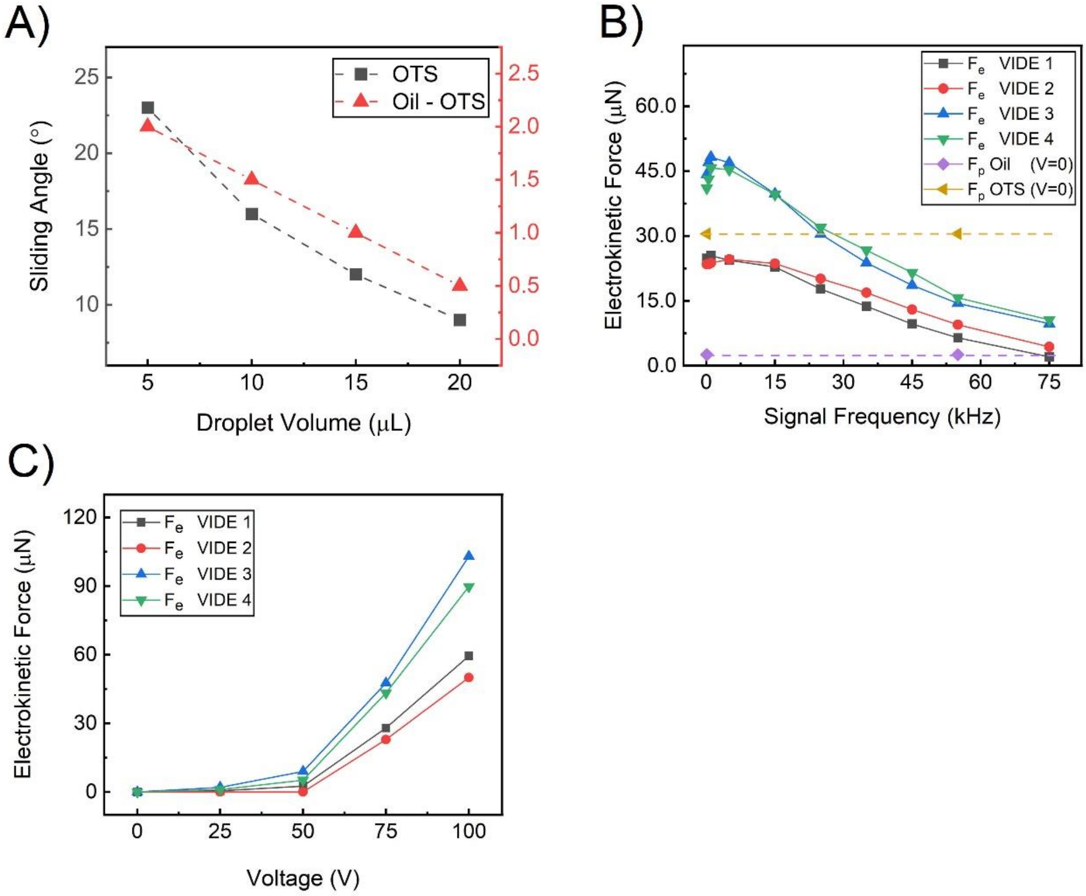

Figure 52 (A) Droplet sliding angle without an applied voltage for different droplet volume on an oil-treated and plain OTS surface. The right hand axis labelling is for an OIL-OTS surface. (B) Experimental results showing the maximum electrokinetic forces (F_e) for varying signal frequencies. (C) The electrokinetic forces (F_e) versus applied voltage at a fixed signal frequency of 1 kHz.

5.4 Summary

This chapter examined the applied electrokinetic force (EWOD and L-DEP) using an experimental and analytical approach. The actuation force was calculated for various electrode geometries. The analysis made attempts to explain the physical actuation mechanism and provided an analytical method to optimise the electrode geometries and improve the actuation performance.

The electrokinetic force depends on the magnitude and rate of change in the applied electric field. COMSOL Multiphysics simulated the propagation of the electric field. The largest electrokinetic force was associated with geometries with a sharper change in the electrode gap distance and a higher electrode density per unit area. Furthermore, the RC circuit network analysis investigated the critical frequency response and estimated the maximum electrostatic energy and maximum electrostatic force. The RC network model presented in this chapter can also include dissipative energy due to changes in the liquid properties at higher frequencies. However, including multiple parallel VIDEs in the theoretical model can significantly improve the accuracy of the calculations.

The electrostatic energy and force were shown to be strongly peaked when the droplet interface was located near the edge of electrodes (D_{min}). The analysis also demonstrated that the frequency response changes depending on the droplet position. Therefore, the droplet is always moving towards the region with the highest electrokinetic response. This effect is also coupled with rapid changes in the electric field penetration to produce a continuous droplet motion.

A new experimental approach investigated the applied electric forces by considering a frictionless macro-size droplet situated on a tilted substrate. There were two forces that acted on the droplet, a driving electric force that moves the droplet, and a resisting force of surface adhesion acting against the droplet movement. The experimental approach investigated the effect of signal frequency and applied voltage on the actuation performance. Furthermore, the frequency-dependent analysis confirmed the optimum operating conditions and estimated the critical signal frequency for different geometries (ranging between 500 Hz to 5 kHz).

In summary, there was no universal optimum design for any application. For example, a longer electrode provides droplet actuation at a longer distance. However, the actuation performance is better for shorter electrodes, but they usually require an electrode switching method for larger devices, which can increase the costs and system complexity.

Chapter 6

Large-Scale Droplet Actuation

This chapter examined the scalability of the proposed droplet actuation methods. Large-scale droplet manipulation is critical in microfluidics and surface cleaning applications. However, the large-scale operation is also accompanied by various limitations, such as a greater complexity and higher costs. This is primarily associated with the large-scale fabrication methods, signal management, and control system complexity. Multiplexing is an effective solution where a selected set of electrodes are activated simultaneously.[216] It is predominantly suitable for applications where the droplets are transported instantaneously. Nevertheless, the droplet actuation remains limited by the fixed volume of the droplets.

We tested various large-scale platforms (several inches) based on the IDEs and VIDEs electrode configuration. Moreover, the droplet actuation in our designs were independent of the droplet size or position. This chapter presents an electrode switching method suitable for a large-scale device based on the IDEs design. The iterative switching mechanism combines microelectrodes to actuate larger droplets. There is also a proposed signal management technique for the VIDEs to reduce the device complexity and costs. Additionally, there are four electrode configurations based on the large-scale VIDEs, demonstrating linear, bilateral-symmetric, and multi-symmetric droplet motion. Lastly, we recommend a new electrode design combining VIDEs and IDEs into a single large-scale device. Note that the electrode dimensions are also shown in the Appendices.

6.1 Iterative switching of the IDEs

The actuation of droplets with varying volume is essential for a self-cleaning platform, particularly in an automotive application. The manipulation of discrete droplets has been validated in the literature for a droplet sensing method within a feedback control loop; for instance, vision systems, fluorescence spectroscopy, capacitive sensing, and impedance measurements have all been demonstrated.[217-220] Nevertheless, they are not feasible for a large-scale cleaning platform due to high costs, limited design parameters, and device complexity.

There is also a connection between the electrode size and droplet volume. For instance, smaller droplets can be actuated using electrodes with a small surface area, and likewise, larger droplets require a proportionally larger electrode pad. This is less problematic if the active surface area is small and the electrodes are activated one at a time. However, this is not appropriate in an application with micro-sized IDEs with a large active area. Furthermore, other actuation methods are similarly suitable in a cleaning platform, such as a scrubbing like motion, which is also absent in the linear droplet actuation.

Microscale electrodes can be iteratively combined to effectively realise larger arrays, therefore, actuating droplets with varying volumes. An iterative fractal approach produced droplet actuation without a feedback control system. The logic matrix of the switching patterns is shown in Figure 53. The iterative fractal steps are based on the process of recursion, and they simplify the actuation process. This is primarily because the actuation is independent of the droplet size and position. Additionally, the concept is scalable as the iterative algorithm can be applied to any number of electrodes.

The Fibonacci series (shown in Figure 53) provides a wide range of operations. The Fibonacci sequence is a series in which each number is the sum of the previous two numbers, and the number at a specific position in the series can be obtained using a recursive method. It is particularly relevant when the actuated droplets join up together during the operation. The size of the droplets should always be slightly larger than the electrode surface area. For example, after the third cycle, when using three combined IDEs, the next cycle should activate at least five IDEs to actuate any newly formed droplets. However, the actuation process is also dependent on other factors such as the electrode activation time, delay time between the steps, signal frequency, and operating voltage.

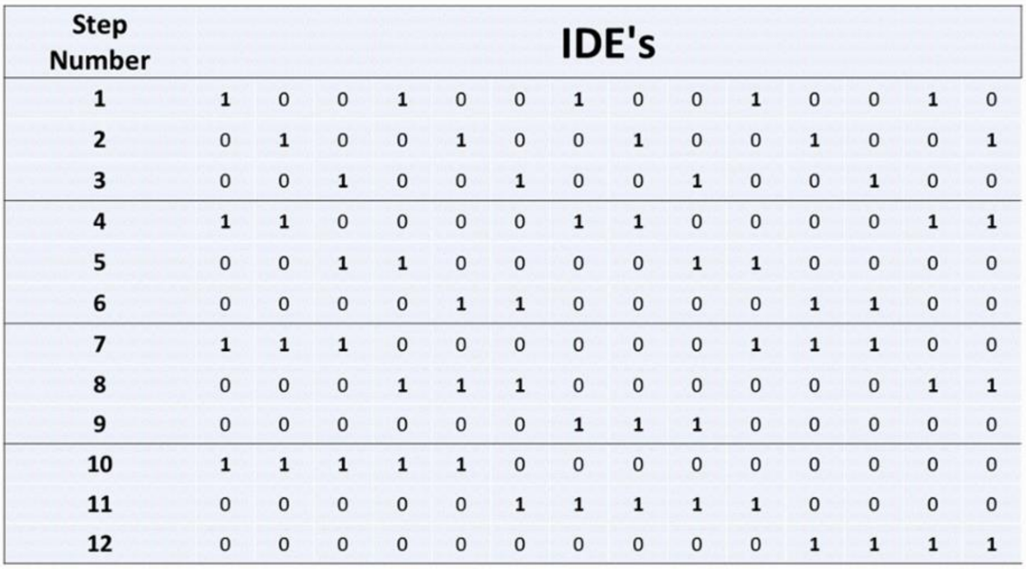

Step Number	IDE's													
1	1	0	0	1	0	0	1	0	0	1	0	0	1	0
2	0	1	0	0	1	0	0	1	0	0	1	0	0	1
3	0	0	1	0	0	1	0	0	1	0	0	1	0	0
4	1	1	0	0	0	0	1	1	0	0	0	0	1	1
5	0	0	1	1	0	0	0	0	1	1	0	0	0	0
6	0	0	0	0	1	1	0	0	0	0	1	1	0	0
7	1	1	1	0	0	0	0	0	0	1	1	1	0	0
8	0	0	0	1	1	1	0	0	0	0	0	0	1	1
9	0	0	0	0	0	0	1	1	1	0	0	0	0	0
10	1	1	1	1	1	0	0	0	0	0	0	0	0	0
11	0	0	0	0	0	1	1	1	1	1	0	0	0	0
12	0	0	0	0	0	0	0	0	0	0	1	1	1	1

Figure 53 The iterative algorithm to transport different droplet volumes. The iteration cycles for 14 IDEs are illustrated here. The activated electrodes (1) and deactivated electrodes (0) are presented in a matrix format. The cycles are repeated three times to ensure a complete transition. This concept can be applied to any number of electrodes on a large surface.

Figure 54 A - H verified the iterative switching actuation mechanism to control multiple droplets with different volumes. The iteration time between activating each electrode pad was fixed to a value higher than the spreading time of a single droplet. This was 100 ms in our system with an additional delay cycle (100 ms). The droplet actuation was carried out on a surface with lubricant treatment, and the operating voltage was 85 V with a signal frequency of 40 kHz.

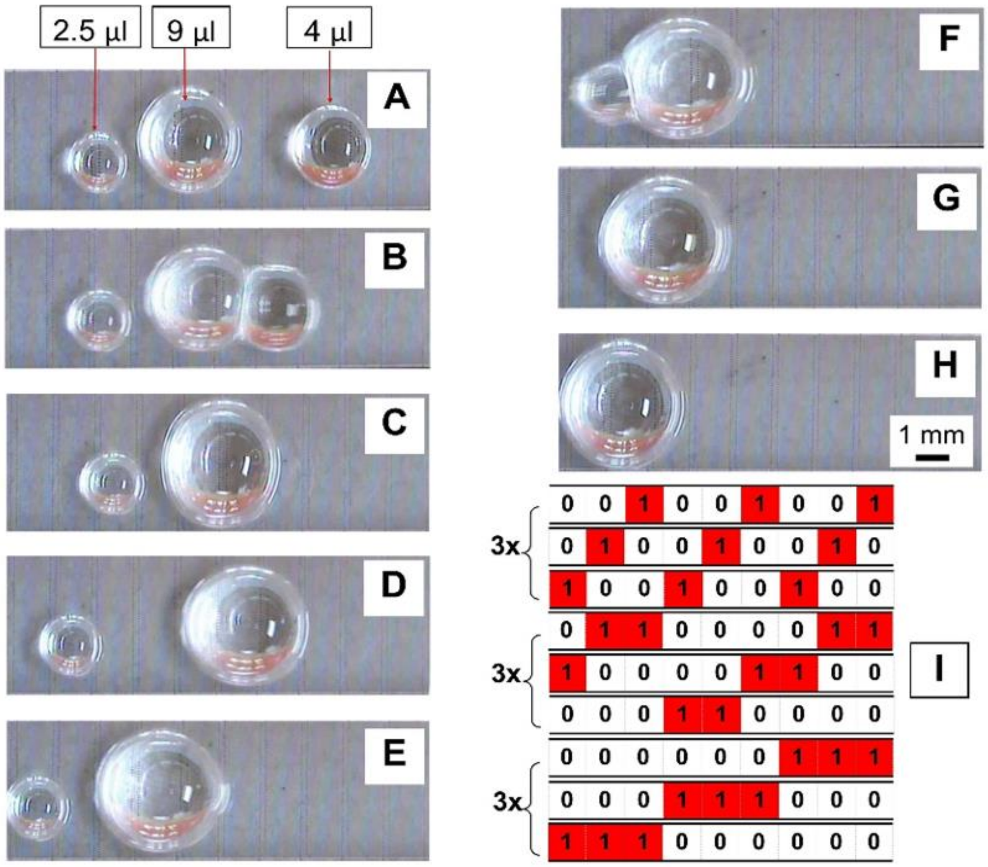

3x	0	0	1	0	0	1	0	0	1
	0	1	0	0	1	0	0	1	0
	1	0	0	1	0	0	1	0	0
3x	0	1	1	0	0	0	0	1	1
	1	0	0	0	0	1	1	0	0
	0	0	0	1	1	0	0	0	0
3x	0	0	0	0	0	0	1	1	1
	0	0	0	1	1	1	0	0	0
	1	1	1	0	0	0	0	0	0

Figure 54 Actuation of multiple droplets using an iterative switching approach. (A - H) The actuation of three DI water droplets with different volumes (2.5 µl, 4 µl, and 9 µl) using the iterative algorithm. The actuation is carried out on a thin lubricant layer and the operating voltage is 85 V at 40 kHz. (I) The switching algorithm commands. The code repeats itself every three IDEs and it is applicable to any number of IDEs on a larger device.

The actuation characteristic is directed towards a cleaning application, and it resembles a scrubbing like motion while eventually moving the droplets in one direction for disposal. The repetitive nature of this technique is ideal for a large surface, and it is also immune to the disruptive introduction of new droplets, i.e., in the case of rainfall. The initial steps in the iterative actuation use individual IDEs to move smaller droplets. However, after 1.5 seconds, the newly formed larger droplet covers a surface area of more than three electrodes (see Figure 54 C), and therefore, the actuation towards the left side of the device is delayed until a full set of iterations is completed.

The actuation of a droplet moving from one electrode to another is only possible when it is over an area that is due to be active, or else, it will move back to the previous position for the next set of iterations. Moreover, depending on the application, the back-and-forth motion may be desirable as it can remove contaminants from the surface. Otherwise, a direct linear actuation, which avoids the back and forth motion, can be realised using a longer activation time or a higher electrode resolution (i.e., smaller electrodes).

Figure 55 shows a large-scale device based on 72 IDEs (each 1 mm by 64 mm) fabricated on a 5-inch glass substrate. The large-scale device was based on an electrode design with a gap distance of 20 µm, and as a result, the device was susceptible to fabrication defects. Therefore, the fabrication process was outsourced to an external partner (Micro Lithography).

Note that this is a major disadvantage when compared to a large-scale device based on the VIDEs configuration. The probability of a device failure from a fabrication defect is lower for VIDEs because the electrode gaps are larger (several hundred micrometres). Moreover, the fabrication cost of the IDEs device shown in Figure 55 was approximately £500, whereas a large-scale VIDEs device was approximately £25. Note that the cost estimations may vary significantly when fabricating the devices in larger quantities using industrial fabrication techniques.

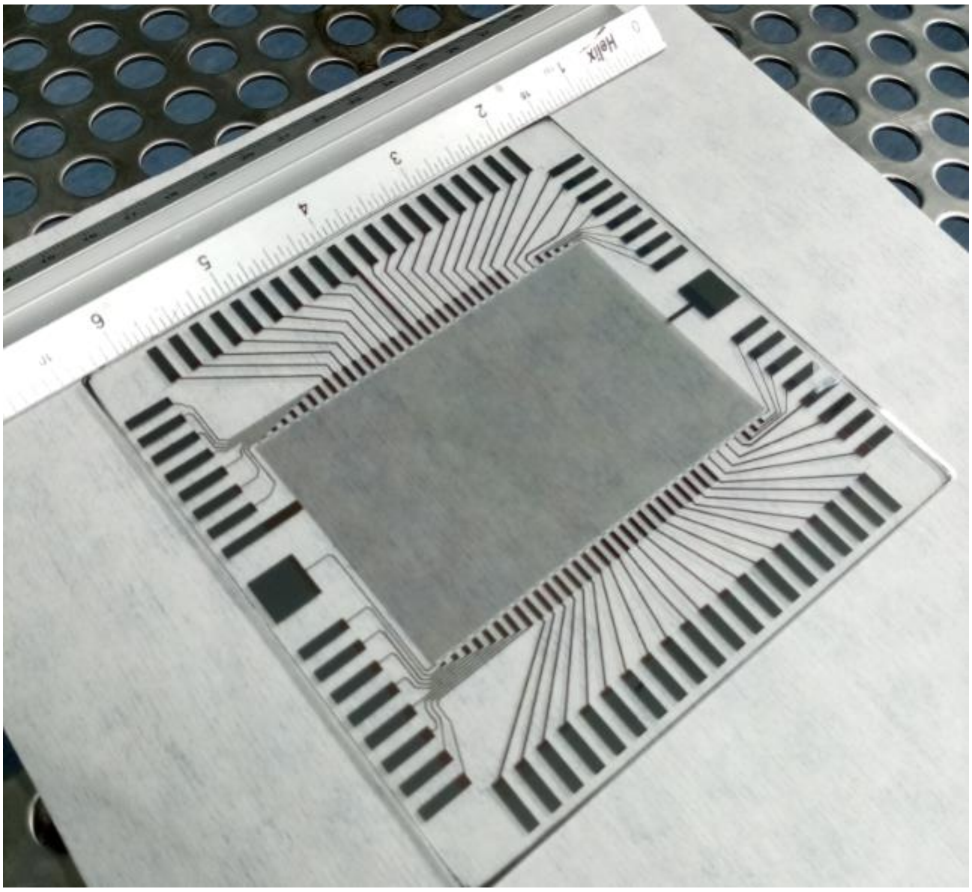

Figure 55 Top view image of a large-scale device with 72 electrodes (IDEs) fabricated on a five inch glass substrate. The device is coated with an SU-8 insulating layer and functionalised with SAM OTS for better hydrophobicity.

6.2 Large-scale platforms based on VIDEs

This section evaluates the scalability of the VIDEs for various large-scale devices (up to a few inches). The droplet actuation based on the VIDEs is versatile and reliable. The droplet manipulation is uniquely beneficial for automotive applications without a control system, where the droplet movement is independent of its size or position. The large-scale devices presented in this section have several cleaning applications, for example, to clean side door mirrors and headlights.

The droplet actuation was carried out on a lubricant treated surface to reduce the applied voltages (less than 100 V), and the testing liquid was DI water. Figure 56 shows two electrode designs based on the bilateral-symmetrical (see Figure 56 A) and linear droplet motion (see Figure 56 B). The primary focus was to demonstrate the droplet actuation behaviour and not the performance, i.e., droplet actuation speed. Therefore, higher actuation speeds and other refinements (such as a thicker insulating layer for mechanical protection) are feasible using higher voltages.

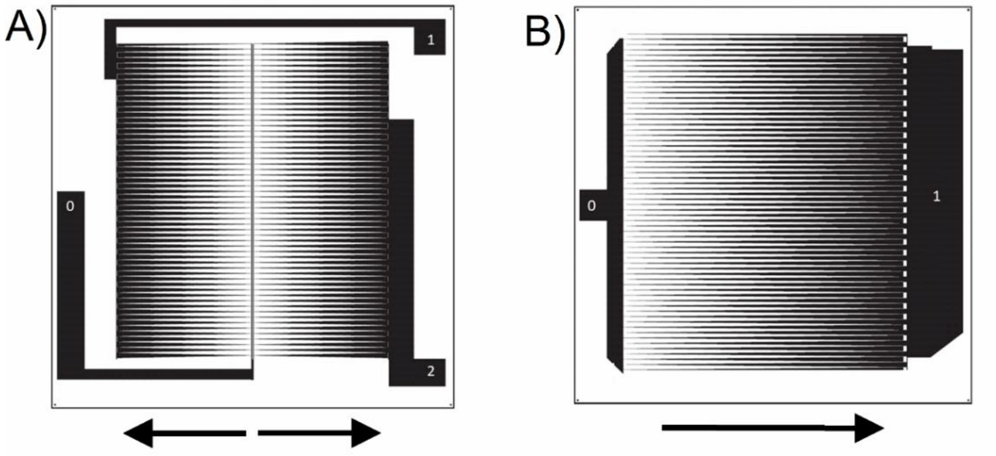

Figure 56 Electrode design for a large-scale droplet actuation without a control system. (A) The electrode design for a bilateral-symmetrical droplet motion with two signal contacts and a common ground. (B) The electrode design for a linear droplet motion with one signal contact and ground terminal. Terminal (0) is a ground signal, and terminal (1) and (2) are voltage sources.

Figure 57 shows the bilateral-symmetrical droplet motion on a 3-inch glass substrate (active area of 20 cm^2), to demonstrate the VIDEs scalability. The electrode design is suitable for applications where gravity is less important, e.g., on flat surfaces. This is particularly important for larger droplets when they are on a tilted surface.

The bilateral-symmetric droplet motion splits the active area into two sections. Thus, allowing faster droplet motion in opposite direction. However, assuming that no new droplets are introduced (i.e., rainfall), the opposing electric forces in the centre of the device (between the two VIDEs) could generate a lag in the actuation process that prevents any droplet motion. A practical solution is a basic switch mechanism to cycle between the two electrodes to eliminate the opposing forces in the centre of the device (i.e., ON-OFF, OFF-ON, ON-OFF …).

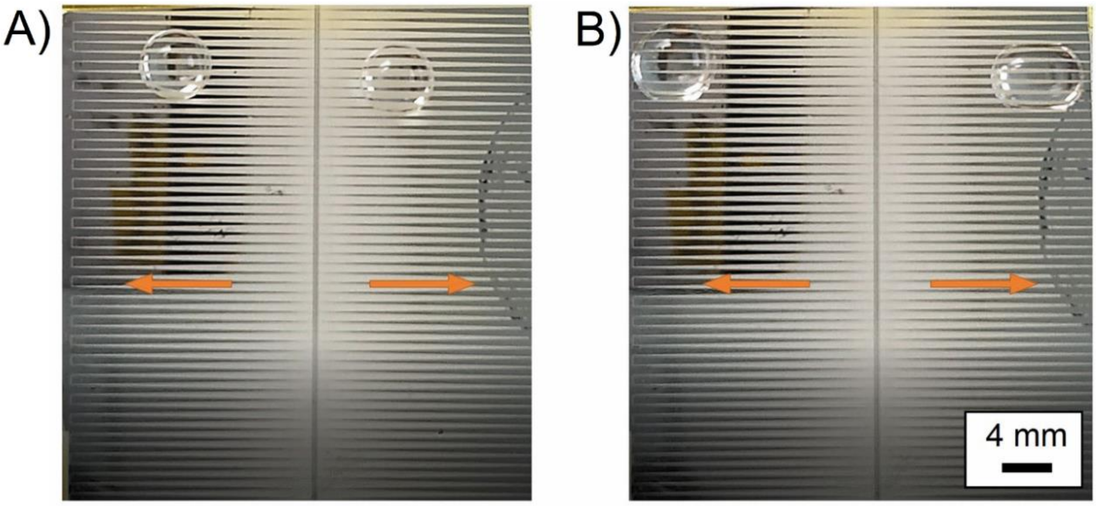

Figure 57 Bilateral-symmetrical droplet motion based on the design shown in Figure 56 A with an oil lubricant layer using 90 V at 0.5 kHz. (A) The droplets positioned on random location on the VIDE. (B) The droplets are actuated across the VIDE when applying the voltage. The spontaneous droplet motion is a critical operation that is uniquely advantageous for a large-scale cleaning platform.

Figure 58 shows the linear droplet motion on a 3-inch glass substrate to demonstrate the scalability of the VIDEs using only one electrode configuration. The actuation path is marked by a dotted yellow line with an arrow. Note that the active surface area of the device was 20 cm^2, but only a section of the device is shown here for better visual clarity.

The electrode design presented in Figure 58 is suitable when it is coupled with another assisting factor, such as, gravity, vibration, and wind. Moreover, the droplet motion without any lubricant treatment is possible using higher voltages to compensate for a surface with lower hydrophobicity. This is particularly important in the automotive application where hydrophobic coated surfaces tend to degrade over time.

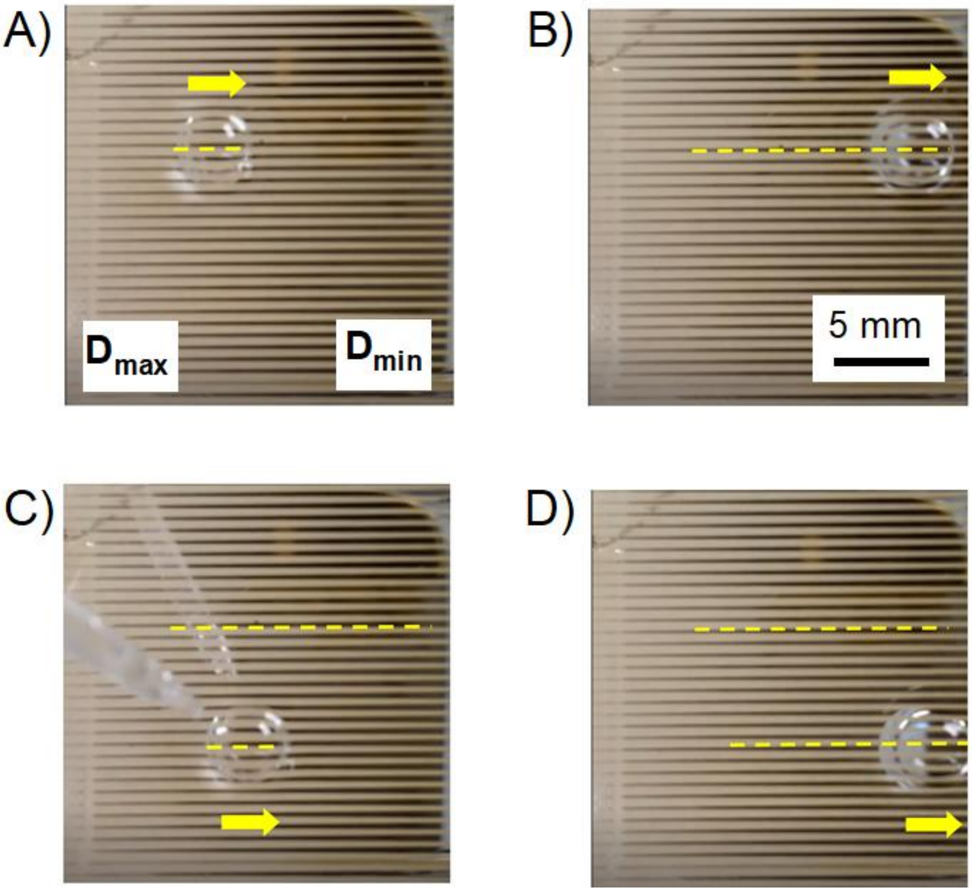

Figure 58 Experimental results showing the large-scale linear droplet motion based on the design shown in Figure 56 B. The applied voltage was 90 V at 0.5 kHz. New droplets are introduced to demonstrate a continuous operation. Note that the image is zoomed-in. The direction of actuation is highlighted with an arrow and the actuated path is shown with a dotted line.

The droplet actuation on a large-scale platform with several electrodes (VIDEs) require a multi-layer fabrication technique with additional complications, particularly signal management. The embedded signal patterns can be considered a hardwire multiplexing technique, in which the electrodes are split into three groups of electrode pairs with three signal voltage sources and a common ground (see Figure 59). The VIDEs are arranged along the longitudinal axis, such that no two adjacent pairs are from a single one of the three series. In the embodiment shown in Figure 59, the order of a series of adjacent pairs along the longitudinal axis is: [C, B, A, C, B, A, C …]. This arrangement is not suitable for the IDEs configuration when the droplet volume is not constant. Furthermore, a large number of electrodes with a longer electrode path will introduce a rise in the electrical resistance.

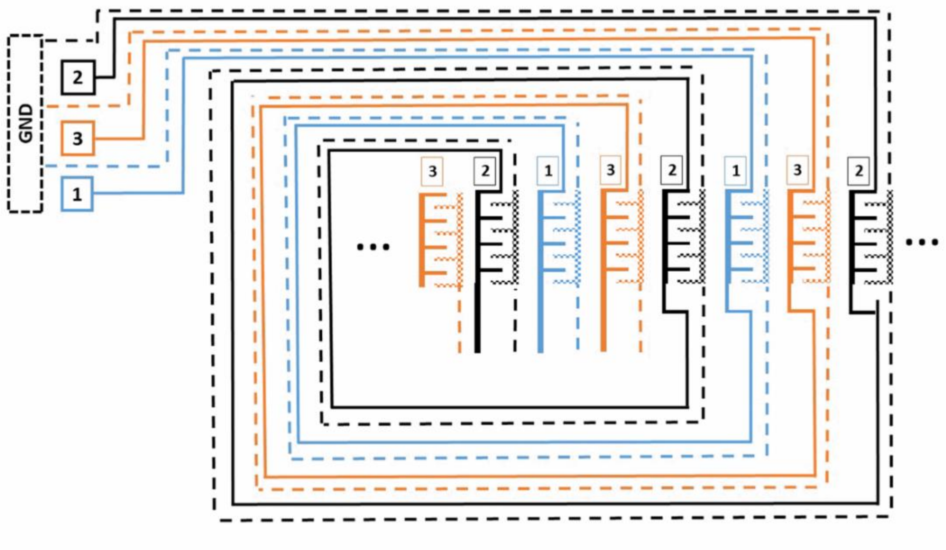

Figure 59 An arrangement of interlinked flow signals between three VIDEs. The electrode concept is similar to a labyrinth of three spiral patterns. This concept will allow the control of any number of electrodes on a large surface using only three signals. This approach requires only a single layer photolithography process.

Sequentially activating the electrodes produces a droplet motion along the longitudinal axis (e.g., C, B, A, C …). The arrangement utilises only four terminals (including a common ground, GND) for three independently controllable series, thus removing the design requirement to fabricate many electrical contact points. Such an arrangement eliminate the requirement for wire bonding and other costly or time-consuming electrical connection techniques.

Combining VIDEs using the embedded signal patterns enabled simple manipulation of parallel droplets on a large-scale without any dependence on the droplet size or position. Only three signal contacts are needed to operate a large platform with multiple VIDEs. Two electrode designs are suggested here (see Figure 60) to demonstrate the linear and radial-symmetric droplet motion.

The linear droplet motion (see Figure 60 A) makes use of an array of shorter VIDEs to move droplets. The analysis of different VIDEs in the previous chapters validated a higher performance for shorter electrodes. The linear design is suitable for a large-scale cleaning platform where linear droplet motion is appropriate, such as on a tilted surface assisted by gravity or wind. Note that even more electrodes can be fabricated for a larger device, demonstrating the device scalability.

The radial-symmetric droplet motion (see Figure 60 B) is carried out on a sun-flower VIDEs design. The length of the electrodes rises (using the Fibonacci sequence) away from the centre of the device (L = 1 mm, 2 mm, 3 mm, 5 mm, etc.). The electrode design is suitable for cleaning electronic sensors on flat or inverted surfaces where gravity is less significant. Lastly, the electrode designs (radial-symmetric and linear) are separated by an overlapping area intended to enable a smooth droplet transition between the electrode pads (see Figure 60 C).

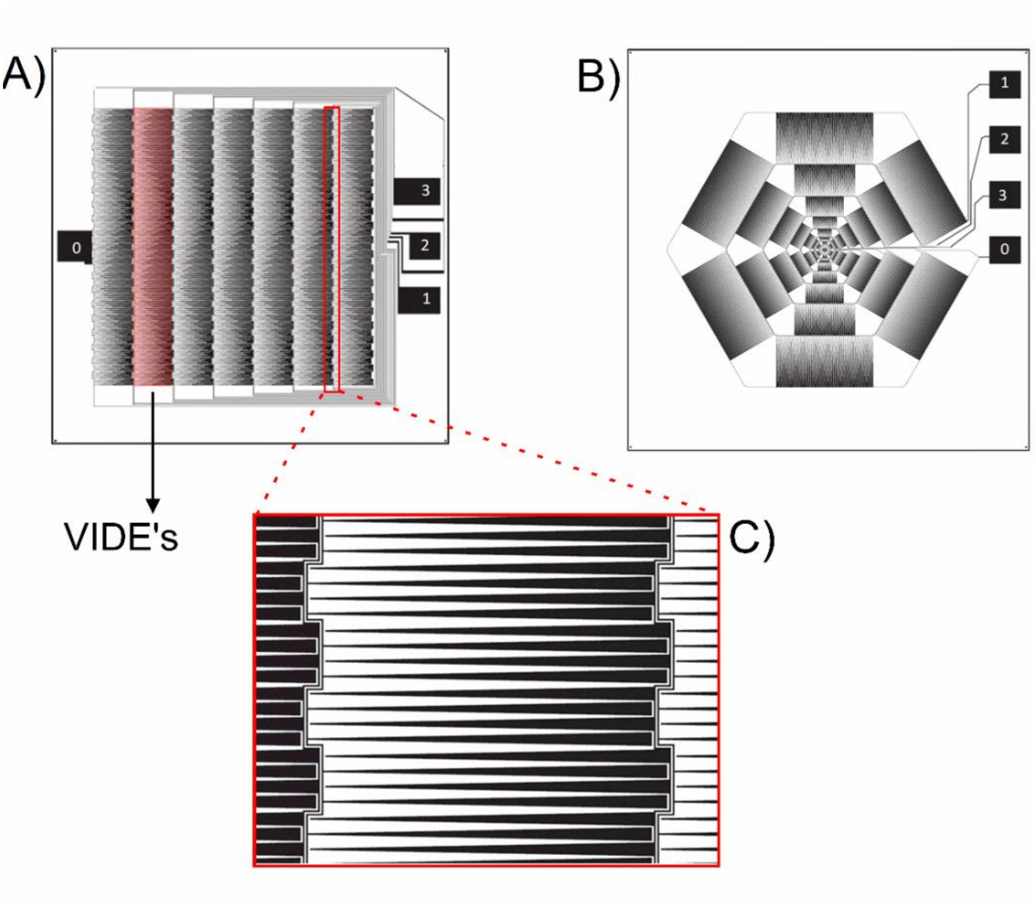

Figure 60 The proposed electrode designs based on the embedded signal patterns shown in the Figure 59. (A) The large scale linear droplet motion using seven VIDEs. The fabrication of additional VIDEs are still feasible for a larger device. (B) The radial-symmetric droplet motion. (C) The two VIDEs are separated by an overlap area to aid the smooth droplet transition between the electrode pads. The terminal (0) is a ground signal, and terminal (1, 2, and 3) are voltage sources.

Figure 61 shows the experimental results for a large-scale linear droplet motion using seven VIDEs (5 mm in length). The sequential activation of electrodes was similar to the operation of a device with several standard IDEs. However, since the VIDEs length was 5 mm, the actuation was not limited by the droplet size or position. The testing verified that the actuation of two droplets with different volumes (6 μL and 9 μL), using a 75 V sine-wave AC signal with a frequency of 0.5 kHz. Additionally, the experimental results showed that the sequential activation of the VIDEs is scalable without any signal management issues.

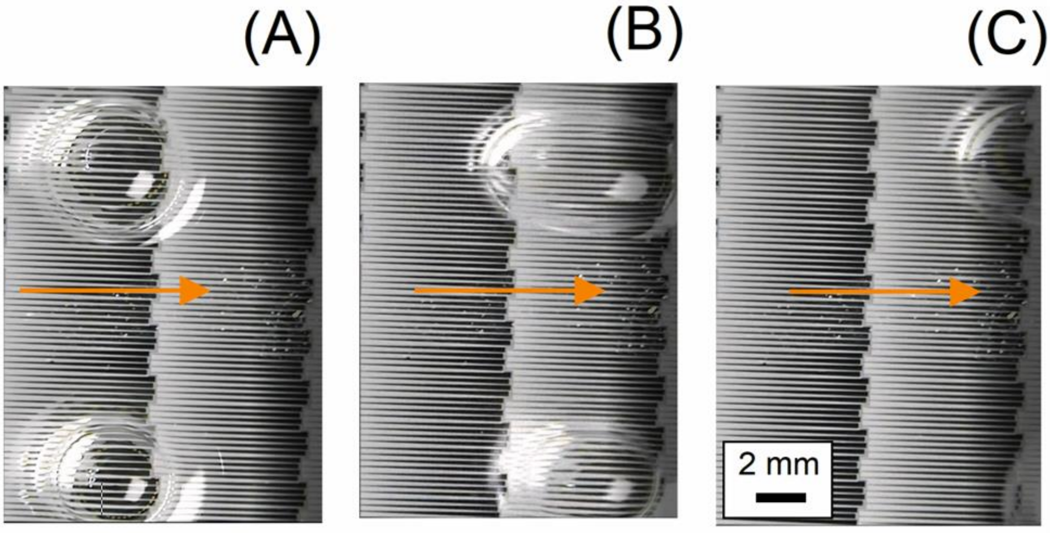

Figure 61 The experimental results showing the top view of DI water droplets moving on a surface. The linear droplet motion is based on design shown in Figure 59 A. The operating voltage was set as 75 V RMS (0.5 kHz).

Figure 62 shows the radial-symmetric droplet motion using the design shown in Figure 60 B. The droplet motion was validated by introducing random water droplets on the surface with different volumes so that the device moves them to the outer regions for disposal. The applied signal was set to 90 V, with a signal frequency of 0.5 kHz. The signals were connected to the electrodes using the interlinked embedded signals.

The surface area of blank gaps in this design increases in the outward direction. The droplets in the inner regions are continuously transported to the outer areas to form larger droplets, eliminating the impact of large gaps in the outer areas of the device. Moreover, the primary use of this device is aimed towards applications where gravity is less dominant, i.e., flat surfaces, typically found in electronic sensors.

Furthermore, reversing the position of the D_{max} and D_{min} across the VIDEs changes the direction of the actuation. Thus, some microfluidic applications can also benefit from the VIDEs electrode design to collect or continuously transport droplets on a large surface for further chemical or biological analysis.

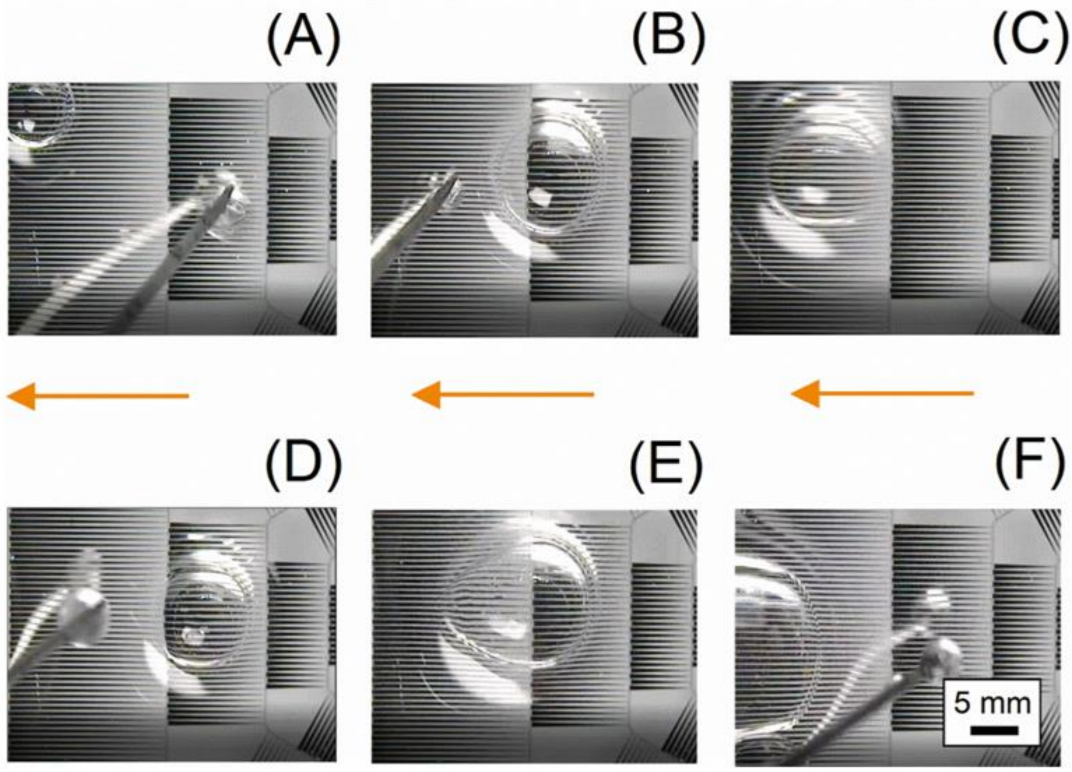

Figure 62 The experimental results showing the top view of water droplets on the device during operation. The radial-symmetric droplet motion based on the electrode design shown in Figure 60 B. The operating voltage was set as 90 V RMS (0.5 kHz).

Alternatively, the VIDEs and IDEs can be combined into a large-scale device (several inches), as depicted in Figure 63 for a hypothetical device for future studies. Furthermore, the electrodes can be selectively activated to avoid actuation lags between the VIDEs and IDEs. The electrode design shown in Figure 63 shows that the VIDEs could move and combine smaller droplets into larger ones. Then, the larger droplets can be rapidly transported across the surface in a direction using the IDEs. This is the only meaningful method to actuate large volumes of droplets with different volumes on a large-scale device, i.e., to be fabricated on the car windscreen or other body parts.

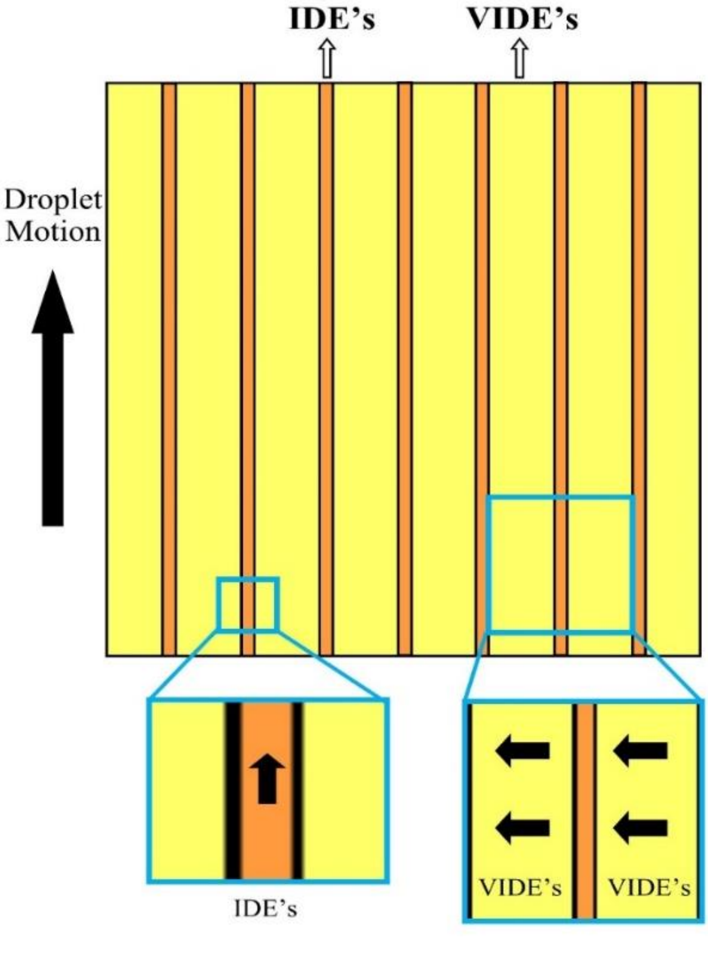

Figure 63 The proposed electrode design for combining VIDEs and IDEs into a single platform for large-scale droplet actuation. Note that the actuation direction of VIDEs is diagonal, and longitudinal for the IDEs. However, the droplet actuation is linear and it is ideal for large-scale surface cleaning, i.e., cleaning windscreen, door windows, and other body parts.

6.3 Summary

The experimental results presented in this chapter verified the scalability of the VIDEs and IDEs configurations. The large-scale device based on the IDEs produced either a linear droplet motion or a new iterative approach where smaller electrodes are combined to realise larger electrodes. The iterative switching method produced a scrubbing like motion, where droplets move back and forth while moving towards a direction for disposal. However, the behaviour can be modified by changing the activation and delay time, size of the IDEs, voltage and signal frequency. The introduction of the iterative switching method is a compelling and simple addition to minimise the device complexity and reduce costs. Nevertheless, a simple linear droplet motion (using a sequential IDEs activation) is still feasible.

The physical mechanism in electrowetting and L-DEP is different. This is notably evident for the electrowetting actuation of conductive droplets using lower signal frequencies. There are reported speeds of up to 70 mm s^{-1} (100 V at 67 Hz) using large electrode pads with a polished superhydrophobic surface treatment.[221] Furthermore, they consists of large electrode pads that generate a strong double layer effect and the surfaces are not transparent. Therefore, they are incompatible with dielectric liquids and the iterative switching approach.

This chapter introduced two categories of a large-scale platform based on the VIDEs configuration. Firstly, two designs are proposed without a control system to produce a linear and bilateral droplet motion. An embedded signal management technique was also introduced to reduce the requirement for a complex control system and minimising costs. Furthermore, this chapter presented two additional designs focusing on the linear and multi-symmetric droplet motion using three digital signals.

Table. 3 compares the performance of VIDEs and IDEs for a surface cleaning application. The study validates that a self-cleaning platform should be based on the VIDEs configuration because of the design simplicity, scalability, and reliability.

Table 3 Performance comparison between the two electric actuation methods; VIDEs and IDEs.

Comparison Criteria	Electrode Designs	
	IDEs	VIDEs
Dependence on the droplet size	There is a connection between the size of the electrode pad and the droplet size. However, a digital switching method overcomes the operational limitation.	Droplets of any size can be actuated along the length of the VIDEs without a control system.
Dependence on the droplet position	It is only the activated electrodes that can move droplets. Thus, the digital switching method is proposed to eliminate this limitation.	There were no limitations, as long as the droplet was positioned over the electrode pad when it was activated.
Dependence on the liquid properties	L-DEP actuation requires a high-frequency signal (typically 30 kHz to 40 kHz). It is suitable for both dielectric and conductive liquids.	A fixed low-frequency signal can actuate a range of different liquids, i.e., rainwater with different properties.
Operating voltages	The operating voltage was 100 V on an OTS surface. The operating voltage is reduced to as low as 30 V using a lubricant treatment.	The operating voltage was more than 100 V on an OTS surface. The operating voltage is reduced to 40 V using a lubricant treatment.
Droplet actuation speed	The actuation speed to spread across an IDEs is estimated to be as high as 20 mm s^{-1}, at 100 V.	The continuous droplet actuation speed across an electrode pad was registered to be as high as 13 mm s^{-1}, at 100 V, for a 10 mm long electrode pad.
Fabrication complications	The electrode gaps were 20 µm. The fabrication process was sensitive to fabrication defects.	The electrode patterns were between 20 µm to 400 µm, but only a small section of the design is in the 20 µm range. Therefore, there are fewer critical defects from the fabrication process (i.e., from dust contaminants).
Scalability	There were no limitations as long as the control system can manage the size of the operation.	There were no limitations. Several designs were also introduced in Chapter 6.
Complexity of the control system	There was a need for a control system to control individual electrodes separately.	There was no need for a control system. When it was necessary, a simple control system was adequate, with only three simple switches.

Chapter 7
Applications

This chapter aims to explore several applications based on the droplet actuation methods presented in the previous chapters. Firstly, a self-cleaning platform was tested in the laboratory settings. The platform was also tested on the road to assess the practicality of the technology for an automotive application. Moreover, this chapter presents a micromirror tilting platform with optical applications. The beam steering mechanism presented by the optical platform was also suitable for characterising L-DEP. Lastly, a microhydraulic actuator was presented based on the continuous droplet actuation of VIDEs to move small samples in a microfluidic application.

Self-cleaning cover lens

The newly emerging autonomous vehicles are the future of transportation. For that reason, there is a technological demand for a novel self-cleaning platform to replace conventional systems. Furthermore, the reliability and effectiveness of the onboard perception sensors in autonomous vehicles are still under evaluation. These sensors include regular cameras and LiDAR sensors (light detection and ranging).[222] LiDAR quantifies the distance between the objects by illuminating them with a laser beam and measuring the reflected light with a sensor. Thus, keeping their surface clean is a major engineering challenge.

Figure 64 A shows several examples where an active self-cleaning platform is considered beneficial. A large-scale self-cleaning platforms is particularly suitable to clean side windows, windscreen, backscreen, headlamps, and door mirrors. Various on-board sensors have to operate in challenging environments, including high winds, dust, dirt, rain, frost, and moisture. However, receiving signals can be obscured by the build-up of contaminants on the lens, resulting in the critical loss of information. The current solutions are based on a support structure, and a platform assembly, including a set of channels for high speed flows to keep the sensor clean (see Figure 64 B). However, the passive solution requires refillable cleaning fluids. Additionally, the spray nozzles can get blocked over time due to the build-up of contaminants. Hence, they typically require regular maintenance, which can increase the operational costs.

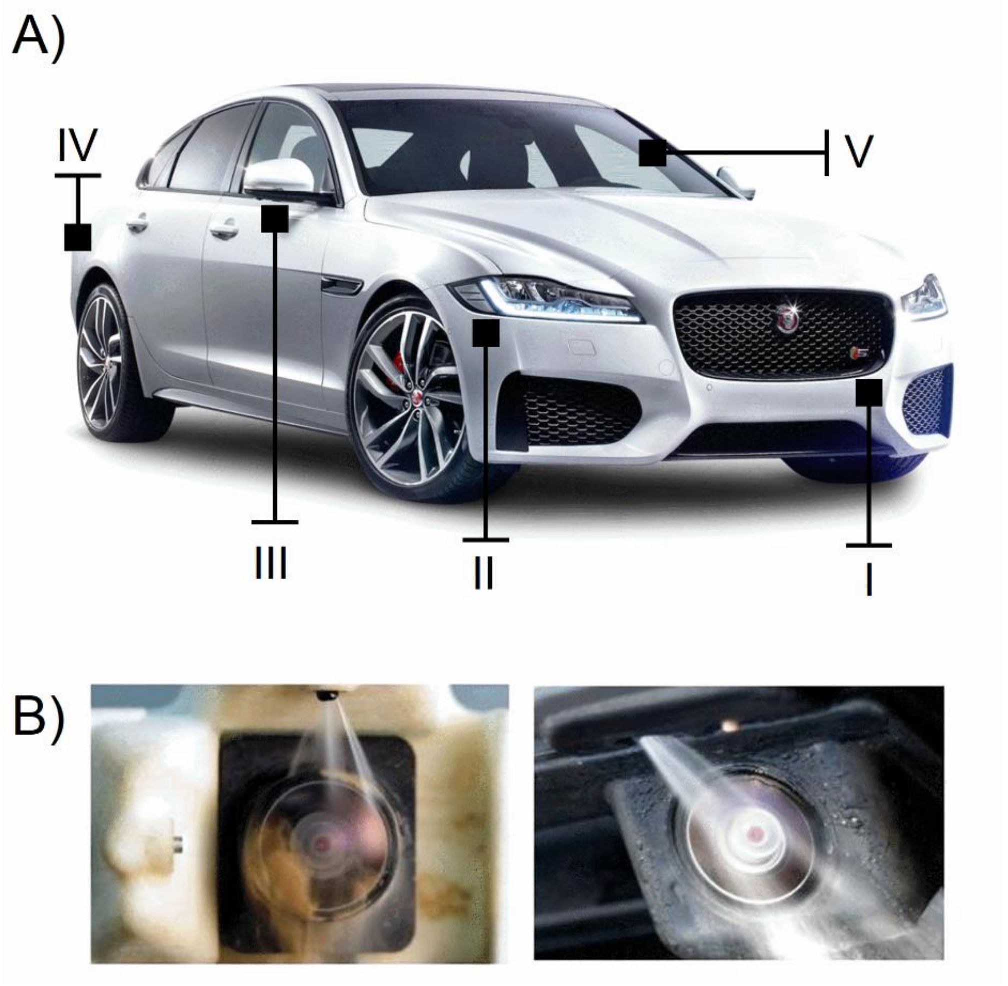

Figure 64 Application of the electric cleaning platform in a modern vehicle. (A) Several examples where the cleaning platform can be applied to are: (I) front cameras, (II) headlight lamps, (III) camera in the mirrors and side mirrors, (IV) parking cameras, and (V) windscreen and sensors in the windscreen.[2] (B) The conventional passive cleaning system (Ficosa cleaning system) based on the jet nozzles and a washer pump to clean cameras and sensors using cleaning fluids.[8]

Our solution consists of a self-cleaning cover lens to remove a variety of liquid and solid contaminants. The optimum design for our application is based on the VIDEs without a control system. Depending on the position of the sensor, a linear or a multi-symmetric electrode design is suggested. The linear system is suitable for a vertical configuration, and the circular symmetric design is suitable for both vertical and horizontal configurations. The cleaning platforms were tested in laboratory conditions and on the road by connecting the cover lens to the car battery via a power inverter, a function generator, and a signal amplifier.

Tilting micromirror

EWOD and L-DEP have several other applications, including electrowetting lens, liquid pumps, display technologies, energy harvesting, and batteries.[52, 97, 223, 224] Furthermore, we explore new applications based on this technology for optical and microfluidic uses. In this chapter we considered using L-DEP to power a miniature tilting mirror platform featuring full axis control. A reflective mirror plate was situated on top of three water droplets, and the surface orientation was regulated by changing the droplet's profile using electric fields. Furthermore, the tilting platform provided a cost-effective and accurate method to investigate L-DEP without measuring the droplet contact angle or actuation speed.

Microhydraulic actuator

Lastly, we explored the feasibility of using droplet motion (using VIDEs) to move small samples for microfluidic applications. The hydrophobic coated cover plate (carrier) can be situated on top of a droplet, and then actuated using electric fields. This is similar to the microhydraulic actuators driven by electrowetting, converting electrical power into mechanical power to transport solid objects.[111] The continuous and contactless transportation method has potential biological and chemical applications to transport dangerous materials for analysis, e.g., radioactive substances or microorganisms.

7.1 Self-cleaning cover lens

There are several parameters to consider when designing an electric-based cleaning platform. Firstly, the chemical and physical properties of rainwater may vary based on the environmental factors such as air pollution, ambient temperature, and surrounding geological formations. Developing a reliable concept was an essential design requirement. Furthermore, the ability to remove contaminants such as dirt, particles, mud rain, rain droplets, and ice were all considered necessary.

The primary goal was to make every design feature simple without sacrificing performance. Although simplicity is an ever-expanding concept in engineering design, we eventually steered towards developing a self-cleaning system. Two electrode configurations are considered here. Firstly, a linear system with a single VIDE of length 10 mm, and a variable electrode gap distance between 200 µm and 20 µm. Secondly, a circular symmetric electrode design is suggested (see Figure 65 A, B) based on three VIDEs with different lengths.

The circular symmetric electrode design spontaneously moved several droplets with varying volume without using a control system. The droplet actuation is always away from the centre of the device, where the optical sensor or camera is situated. The platform was tested in the cleanroom on a horizontal surface, and on the road by attaching it to a car camera. The self-cleaning platform presented in this thesis is easily integrated onto any surface, which is a critical design requirement for the automotive industry.

Magnitude of the applied electric field was the primary driving factor in the droplet actuation mechanism. Figure 65 C shows the COMSOL Multiphysics simulation results that demonstrated a rapid rise of electric field intensity away from the centre of the device. Note that the shorter VIDEs (e.g. VIDEs - 3) positioned near the edge of the device had the largest change in the electric field. Therefore, a net electric force continuously actuated droplets away from the centre of the device, and thus, keeping it clean.

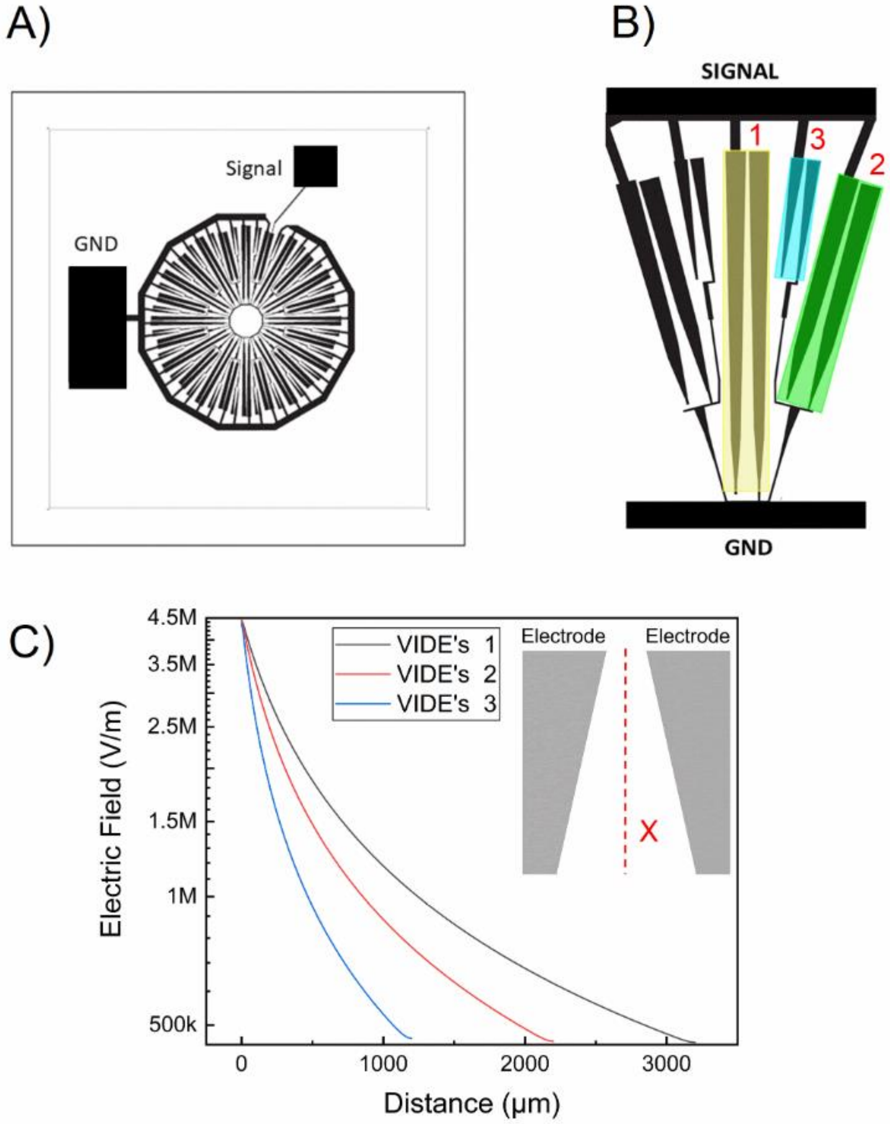

Figure 65 (A) Schematic drawing of the device for the continuous circular symmetrical droplet motion without a control system. (B) A small section of the electrode design showing three VIDEs with different lengths (1 mm, 2 mm, and 3 mm). The electrode patterns are repeated around the centre of the device. Please refer to the appendices for more information about the electrode geometries. (C) 2D COMSOL Multiphysics simulation model showing the norm electric field distribution for VIDEs with different lengths at 90 V. The graphical data shows the change of electric field along the length of the VIDEs. The data was collected from the plane (x), as it is shown in the subfigure by a dotted line.

7.1.1 Laboratory testing

The initial experiments were carried out under controlled conditions to review the actuation behaviour. The circular symmetric droplet motion was demonstrated using 90 V with a signal frequency of 0.5 kHz (see Figure 66). The testing liquid was mud-rain, but other liquids are similarly suitable, including isopropyl alcohol and DI water. Mud-rain contains a noticeable concentration of soil, sand, or dust particles. The particles in the droplet are drawn to its outer edge when evaporated, and are left behind as a ring of residue (stain).[225] Therefore, actively removing the droplets is critical to maintain the surface of a sensor/camera clean.

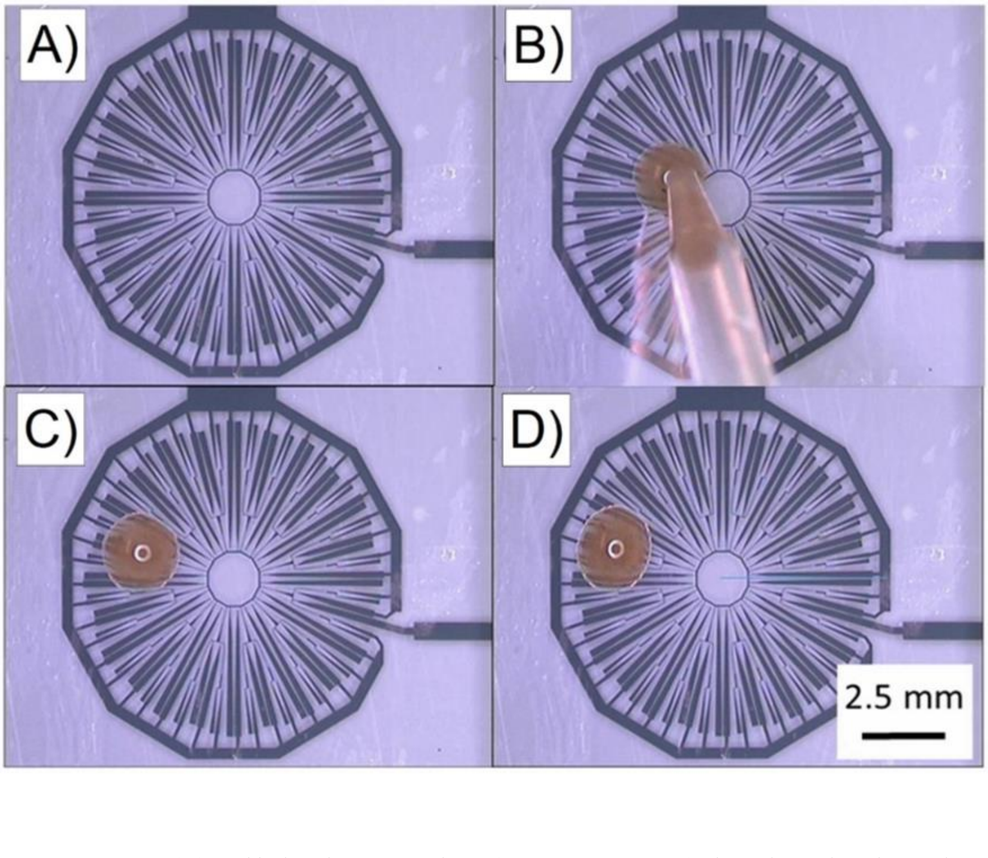

Figure 66 (A) Self-cleaning cover lens (10 mm x 10 mm), based on the electrode design shown in Figure 65. (B - D) The top view images showing the circular symmetrical droplet motion using an applied voltage of 90 V with a signal frequency of 0.5 kHz. Note that the final position does not show an evaporated droplet.

The cover-lens was mounted on a camera and tested using an inverted set up looking upwards at a rainbow panel, as presented in Figure 67 A. The testing liquid was mud-rain and the droplets were placed on top of the device using a micropipette.

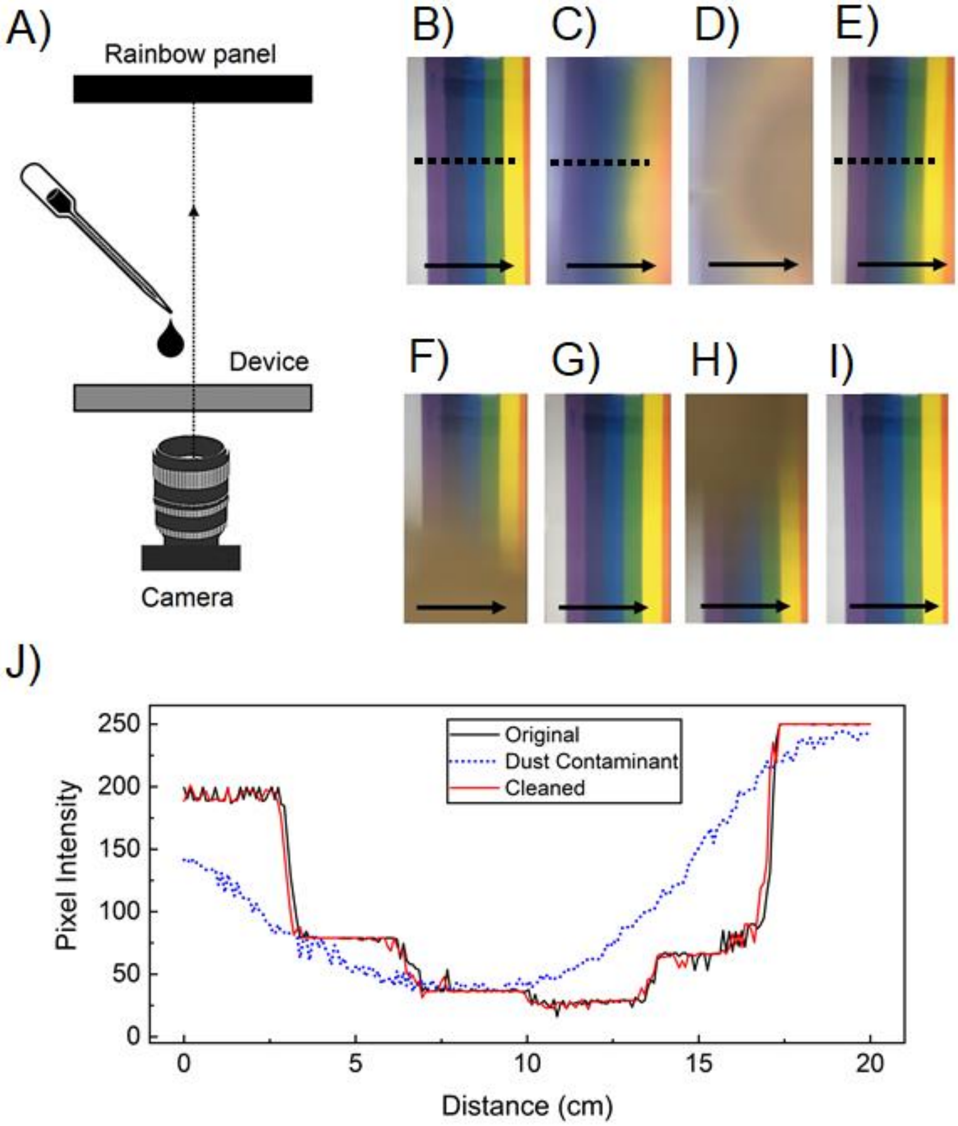

Figure 67 Test results for cleaning a camera cover lens. The black arrow shows the direction of the droplet actuation. (A) The overview of the experimental setup with a rainbow panel, device (VIDEs) mounted to the camera lens, and a camera. (B) A clean cover lens, (C) adding dust to the surface, (D) adding a droplet, (E) cleaning the cover lens, (F) adding another droplet to the surface, (G) cleaning the lens, (H) adding an additional droplet, and (I) cleaned cover lens. (J) The cleaning process is demonstrated using a 2D plot showing the grey colour pixel intensity across the rainbow pattern.

Initially, the lens was covered with standard dirt (see Figure 67 C) to obscure the image quality and then systematically cleaned using droplets to show the effectiveness of the self-cleaning cover lens (see Figure 67 D - I). Note that these operations are actually simulating the same conditions expected in a practical test outside the cleanroom. Furthermore, Figure 67 J shows the luminance across the rainbow pattern during the cleaning process (using ImageJ software). The scanned regions are also highlighted with a black dotted line.

The cleaning platform can be activated with a motion sensor to save energy. Additionally, it can remain active over long periods because of low power consumption. The typical input current was up to 300 mA, with an applied voltage less than 100 V. The cover lens can also be protected with a mechanical cover when the system is inactive, preserving the hydrophobic coating. Moreover, a higher operating voltage can always compensate for any changes in the hydrophobicity of the OTS layer. Alternatively, the cover-lens can always be replaced with a new one, as they are easily mounted to the camera and are relatively cheap to fabricate.

7.1.2 Testing on the road

Maintaining the surface of sensors and cameras clean is essential for automotive applications. The testing on the road verified the effectiveness of a self-cleaning cover-lens in a practical application with several interfering factors, such as wind, a moving vehicle, vibrations, dirt, mud, rain, etc. Figure 68 shows the experimental setup with a test bench which was mounted to the roof of the vehicle. The test bench consisted of two cameras, one fitted with a self-cleaning cover lens and another with a standard plastic cover lens. A Raspberry Pi was streaming a live video into a web page and then recording it on a laptop via a Wi-Fi link. The signal generator and signal amplifier was connected to the car battery via a power inverter, thus converting the DC voltage to an AC voltage source.

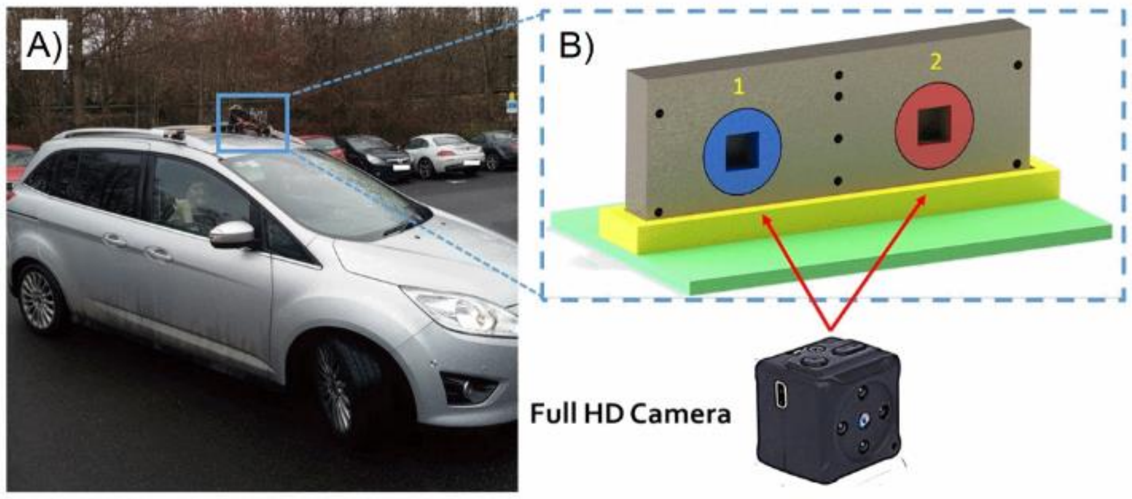

Figure 68 (A) Testing vehicle with a mounted test bench. (B) The test bench was mounted to the roof of the vehicle with two cameras. The camera on the left (2) with a self-cleaning cover lens (linear VIDEs), and the other camera had a plastic cover lens.

The platform was tested on a fast-moving vehicle travelling at 40+ mph on a rainy day to evaluate the performance of the cover lens. The initial experiment focused on the effect of wind shear forces to remove pinned droplets attached to the hydrophobic surface (see Figure 69). Furthermore, the droplet manipulation behaviour was substantially reduced for speeds slower than 40 mph. Note that there is also a small diffraction grating effect with the semi-transparent electrodes. The visual effect is easily eliminated using entirely transparent electrodes (based on ITO).

Chapter 4 demonstrated the importance of droplet size on the sliding angle. In principle, water droplets smaller than 3 μL remain attached to the hydrophobic surface, whereas larger droplets (e.g., 30 μL) slide down with the assistance of gravity. Furthermore, it is expected that the threshold voltage (voltage required to move a droplet) is lower with a rise in the inclination angle and the droplet volume. On the other hand, electric fields can consistently move water droplets of any size on an inclined surface when employing high voltages (100 V or more). In effect, the applied voltage may vary depending on the testing parameters, including the vehicle speed and precipitation rate.

Figure 69 Testing on the road experiment with a vehicle moving at 40 mph. There are two testing cameras, (left) one with a self-cleaning cover lens, and (right) the other one had a standard plastic cover lens. The wind shear force of a moving vehicle prevented any droplet sticking to the camera on the left. However, the camera on the right with a less hydrophobic surface allowed droplets to remain attached the surface (illustrated by a green circle).

The cover lens was also tested to verify the systematic removal of rain droplets of a slow-moving vehicle (less than 10 mph). Figure 70 shows the downward droplet motion assisted by the VIDEs. The applied voltage was 90 V, with a signal frequency of 0.5 kHz. The testing results verified a rapid movement of rain droplets assisted by gravity and the electric force generated by the VIDEs.

The testing results confirmed that the obscured view becomes clear through the systematic removal of droplets. This is particularly useful for an automotive application to maintain sensors and cameras clean during operation. Additionally, the proposed platform is aesthetically appealing without any mechanically moving parts. The structural integrity of the VIDEs remained intact after several hours of use, and the device was still functioning months after testing without a noticeable change in performance. Furthermore, power consumption is relatively low compared to current technologies based on hydraulic pumps and mechanical wiper blades (typically 200 W at 12.5 V and 16 A).[226] Moreover, our platform was simple and also considerably cheap because the VIDEs can be fabricated in large quantities on a flexible substrate (see section 8.2.2).

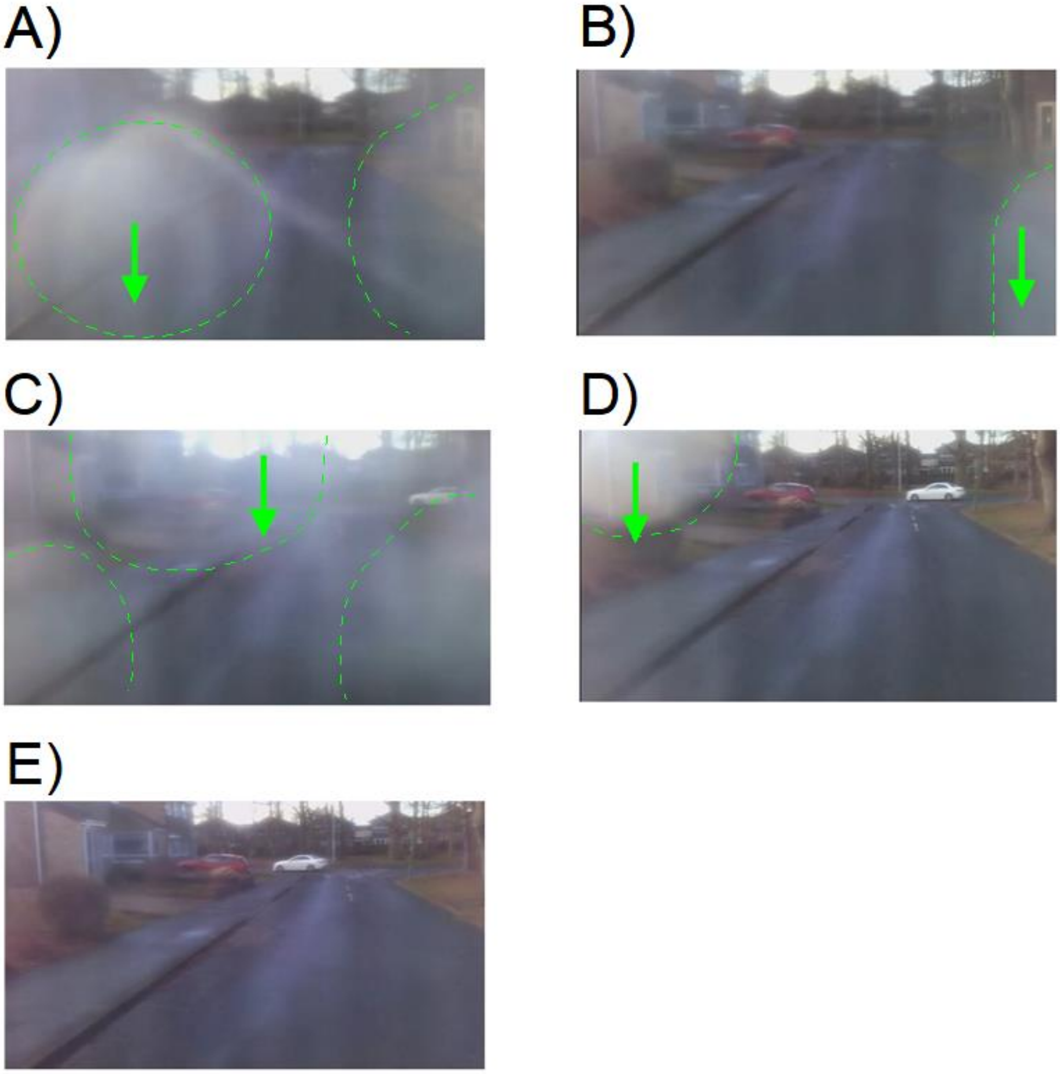

Figure 70 Testing on the road with a self-cleaning cover lens. Speed of the vehicle was 10 mph. The green arrows show the direction of actuated droplets that were obscuring the view. The testing voltage was 90 V with a signal frequency of 0.5 kHz.

There are a handful of reported investigations considering droplet motion and deformation by airflow.[227-229] The relationship was investigated using a controlled airflow, and a critical velocity (13 m/s to 7 m/s) was identified that produced droplet displacement. In effect, the externally applied electric body force reduces the critical airflow velocity that initiates droplet displacement. Therefore, it is possible to combine the actuation forces depending on the speed of a moving vehicle and the surrounding wind. However, this effect is difficult to study because of the chaotic nature of the wind streams. In principle, gravity is the dominant factor when the vehicle is stationary or travelling at a low speed (10 mph or less), whereas the wind shear forces are dominant at higher speeds (40 mph or more).

7.1.3 Surface contaminants

Rainwater is the primary liquid contaminant for a self-cleaning cover lens in an automotive application. During a light rainfall, the intensity can be as low as 2.5 mm/hour, whereas, in a heavy rainfall, the precipitation rate can be as high as 50 mm/hour.[230] The size of drops typically vary from 6 mm to 0.5 mm.[231] Furthermore, the terminal velocity of rain droplets with a diameter of 3 mm is approximately 8 m s^{-1}. The micro-size drops found on the road consist of mud and other solid contaminants generated by the vehicle's unsteady aerodynamic effect when travelling on the road.[232] As a consequence, airborne droplets typically accumulate on the vehicle.

Rain droplets are slightly conductive, with a small concentration of interfering ions such as sodium, potassium, calcium, chloride. Furthermore, geological factors highly influence the concentration of interfering ions.[233] For example, the concentration levels are higher near the seaside than over the land. There is also a low concentration of organic compounds such as alcohols and fatty acids in some rain droplets. The chemical composition can generally be simplified to a diluted aqueous solution. The variations in dissolved particles change the electrical conductivity of the solution.[234] The conductivity ranges from 10 µS cm^{-1} to 1 mS cm^{-1}, as reported in several sources.[235] [236] In some cases, the chemical properties of rainwater can considerably vary, such as rain dust or acidic rain.[237] Rain dust is alkaline, also known as mud-rain.[238] On the other hand, acidic rain has much lower pH values. They are produced when gasses such as sulphur dioxide and nitrogen oxide react with rain droplets in the atmosphere.

Figure 71 shows VIDEs cleaning a surface by transporting different contaminants typically found in an automotive application, including rain, sand, standard dirt, and mud. We verified the removal of sand and dirt contaminants with a diameter of 10 µm to 1000 µm using rainwater (see Figure 71 A, B). Figure 71 C shows the removal of a suspension liquid (mud-rain). The cleaning platform was also compatible with DI water, IPA, or rubbing alcohol. The actuation of droplets in microfluidics has extensive applications in biological applications. VIDEs actuated semi-skimmed milk droplets to demonstrate the flexibility of the platform (see Figure 71 D). Semi-skimmed milk contains fat, lactic acid, proteins and some vitamins such as A, B3, B5, and D. Other biological fluids, including blood, is also compatible with the technology, thus expanding the application for various biomedical devices.[239]

In principle, while a reliable technology may not affect customer satisfaction positively, an unreliable technology will severely affect customer satisfaction. The self-cleaning cover lens device that was tested in this chapter showed little changes in the actuation performance. The experiments demonstrated that the performance remained fairly stable after a long operation, as long as the operating voltages remain below the breakdown limit.

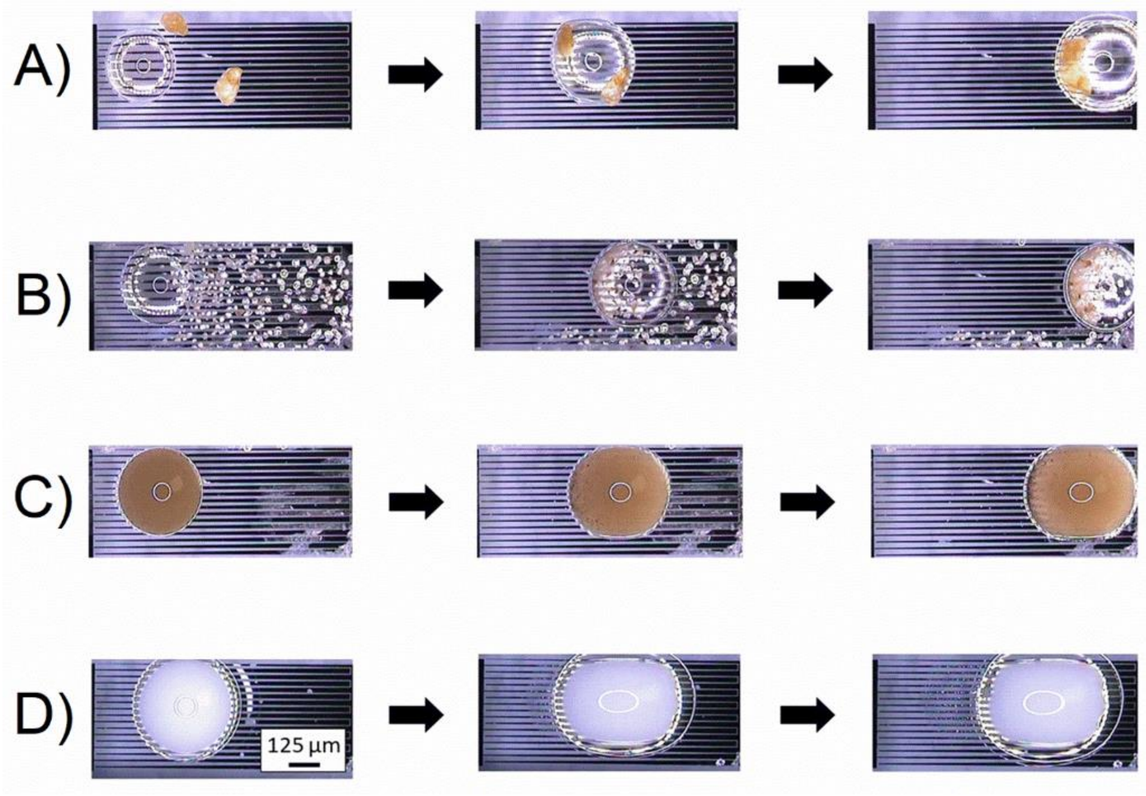

Figure 71 Summary of the test results showing the top view of various droplets moving on a surface with oil surface treatment. (A) Rain droplet moving dirt contaminants (700 µm - 100 µm), (B) rain droplet moving sand contaminants (20 µm - 150 µm), (C) actuation of suspension of a muddy water droplet, and (D) actuation of semi-skimmed milk droplet.

7.1.4 Defrosting application

Defrosters, demisters or defoggers are surface cleaning technologies found typically on the rear window, windscreen, or side windows of a car to remove frost, ice, and condensation build-up. The defogging process utilises the heat from the car engine to blow fresh air through the heater core and distribute it over the interior surface of the vehicle. The defrosters consist of resistive conductors embedded in the glass to heat the surface at the expense of relatively high power consumption. Even though the existing designs are well established in the automotive sector, a practical and novel approach is also needed to promote new technologies and improve their power efficiency.

Dielectric heating is a major design consideration when incorporating DEP in microfluidic systems to avoid excessive temperature changes.[240, 241] The applied non-uniform electric field displaces charged particles, giving rise to an induced dipole. The water molecules can also act as permanent dipoles in the medium and respond to the applied field to transfer the power from the electric field to the medium. This dissipating power produces a bulk temperature rise, and it is also influenced by the signal frequency, and the strength of the electric field.[213]

Figure 72 shows the dielectric heating effect generated by the applied electric field to melt an ice droplet (20 µL of DI water). IDEs with a gap distance of 20 µm generated a strong local electric field (at 100 V), to increase the bulk temperature. The heating effect was only possible at higher voltages (100 V or more). The ambient air temperature in the experiments was -7 °C, with a signal frequency of 100 kHz. The electric power may be dissipated in the electrodes via ohmic heating. Alternatively, it can also be dissipated in lossy dielectrics.

The heating platform can readily melt and remove snow and frost formations typically found in automotive applications. The heating effect remains local to the vicinity of the ice formation, and therefore, it is more energy-efficient than conventional systems based on resistive heating. Additionally, the design can also merge with a droplet actuating platform, similar to the one presented in Chapter 4 with multiple electrode pads. Therefore, providing a multi-purpose cleaning platform that can be embedded on the rear windscreen, windscreen, side mirrors, sensors, and cameras.

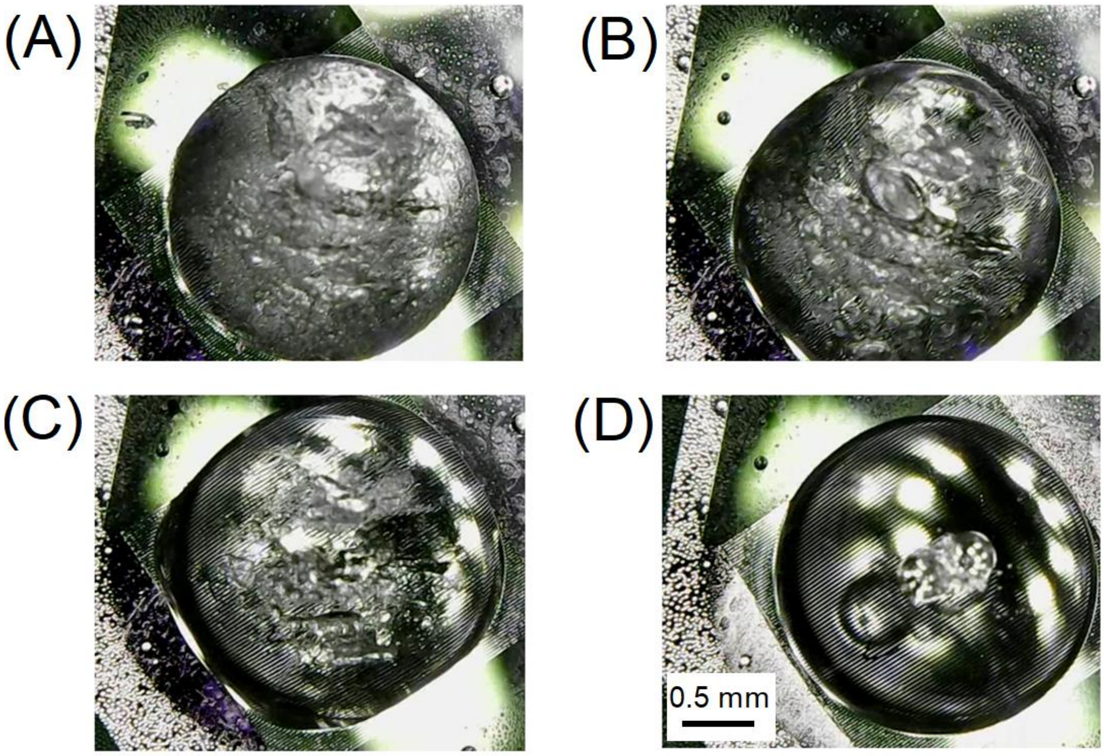

Figure 72 Top view images showing the defrosting effect using electric fields to melt ice. The applied voltage was 100 V with a signal frequency of 100 kHz. (A) Ice droplet in an ambient air temperature of -7 °C, (B) activating the device for 8 seconds, (C) semi-liquid state after 16 seconds, and (D) complete liquid state after 30 seconds. Note that there is no surface treatment in the experiments.

The magnitude of the electric field was not the only critical parameter. The defrosting time was also dependant on the applied signal frequency. Table 4 shows the relationship between the defrosting time and signal frequency. The experiments verified that the heating effect was visible only at higher signal frequencies where L-DEP was dominant.

Testing electrodes with a gap distance larger than 20 μm (at 100 V) failed to produce adequate heating. Therefore, emphasising the importance of employing a large electric field. Although it takes 30 seconds to melt the entire droplet, the semi-melted droplet becomes mobile after two seconds when it is positioned on a tilted surface. Furthermore, applying even higher electric fields can evaporate the entire droplet. Therefore, further refinement is feasible, either by employing higher voltages or changing the electrode geometries. This was verified by either reducing the electrode gap distance or using an irregular electrode geometry (see Section 8.2.0).

Table 4 Experimental results showing the defrosting time versus signal frequency. The heating effect is only possible at higher frequencies, ideally 50 kHz to 100 kHz. Note that this is the time taken to melt the entire droplet. However, the droplet becomes mobile after several seconds when it is situated over an inclined surface.

Signal Frequency (kHz)	Defrosting Time (seconds)
1	NA
5	160
10	120
50	30

7.1.5 LiDAR sensor

LiDAR is an optical sensor for determining range by targeting a surface with a laser beam and measuring the time taken for the reflected beam to return back to the receiver. LiDAR sensors can also produce digital three-dimension (3D) representations surrounding areas. LiDAR sensors are commonly used to make high-resolution 3D maps, with applications in geography, archaeology, geology, and atmospheric physics.[242-244] LiDAR sensors are similarly fundamental to the perception of the vehicle surrounding in autonomous cars.[245]

We tested a self-cleaning cover lens by placing it over a LiDAR sensor to produce a 3D scan of an office with furniture. The LiDAR scanner from an iPad pro was used to take the images. Figure 73 shows the testing results in three configurations: without a device, a transparent device with ITO electrodes, and a semi-transparent device with aluminium electrodes. The study verified that there was no loss of information in the LiDAR scans when using a transparent device coated with ITO electrodes. However, there was some loss of information when using a device with aluminium coated electrodes. Nevertheless, the self-cleaning cover lens can be integrated with LiDAR sensors, which is a critical requirement for an automotive application.

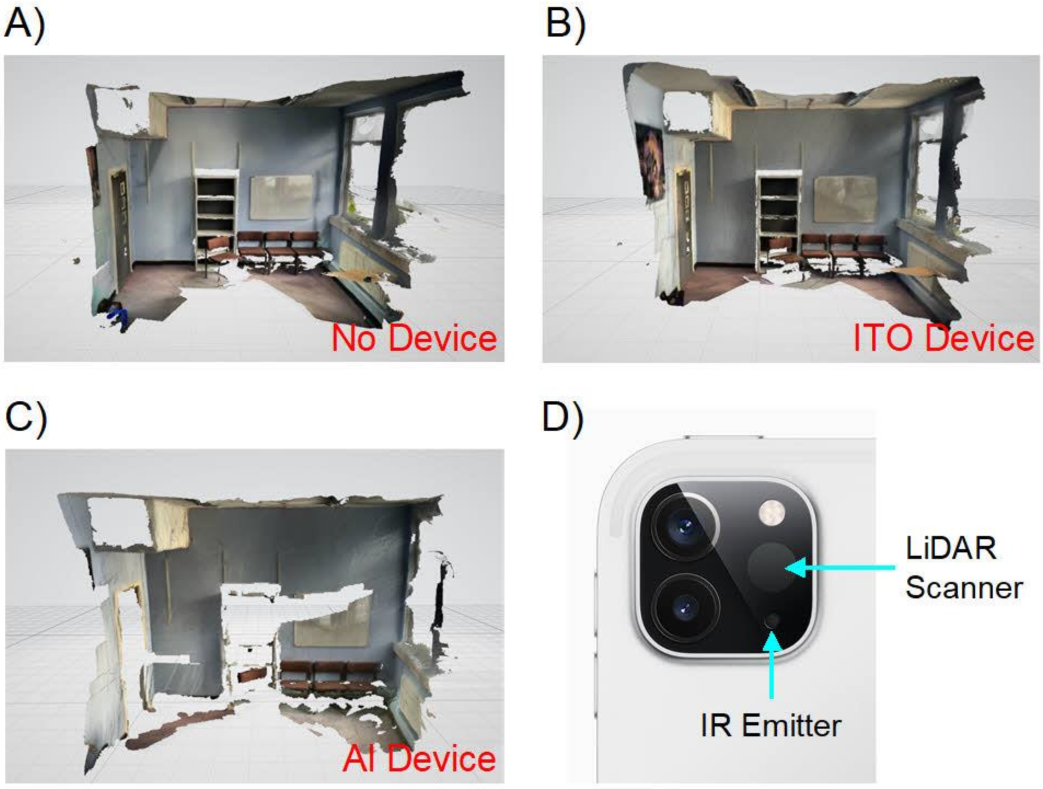

Figure 73 Summary of the test results using a LiDAR sensor to scan an office with indoor furniture. (A) When using no self-cleaning cover lens, (B) using a self-cleaning cover lens with ITO coated electrodes, (C) employing a device with aluminium coated electrodes, and (D) cut-out image showing the Apple iPad pro camera system with LiDAR sensor scanners.[1]

7.2 Tilting micromirror platform

Micromirror is an optical beam-steering device technology that appears in various industries and numerous applications, including micromachining, micropositioning, microscopy, and lithography.[41, 246] Micromirrors are typically found in optical devices,[247, 248] tuneable lasers,[249] 3D scanning using light detection and ranging (LIDAR).[250] The technology is similarly extensively used in digital projection displays and optical switches.[251, 252] They are lightweight, compact, and consequently present an ubiquitous solution for optical beam steering.[253]

The research field has been steadily growing, and the latest developments are focusing on high-speed affordable devices with a wide field of view. Micromirrors exhibit distinctive characteristics, such as a wide scanning angle, fast response, and low power consumption. Moreover, size of the electrostatic platforms are between 0.5 mm to 10 mm, with a wide range of scanning angle from 0.6° to 146°, and an operating voltage ranging between 5 V to 250 V.[251]

Micromirrors are commonly used in MEMS devices, and there are several types of platforms with different working mechanisms, including electrothermal, electrostatic, electromagnetic, and pneumatic.[254-257] This chapter presents a droplet-based micromirror platform with a three-axis tilt mechanism (see Figure 74).[258] The surface orientation is adjusted by regulating the operating voltage or signal frequency, and thus, modifying the droplet contact angle. A simple camera was used to video record the beam movement on a projection screen, which also reduced the experimental costs.

The working function of the device was based on three IDEs, situated 120° apart from each other (see Figure 74 A). Figure 74 E shows a linear beam movement by activating one of the signal electrodes. The position of the laser beam was accurate with a precision of up to (± 500 µm). Furthermore, the movement of the laser beam could exceed up to several centimetres, thus making it easy to detect using a recording camera. The working mechanism was based on L-DEP, and the testing liquid was DI water. However, the actuation is similarly compatible with many more liquids, such as oil-based solutions, tap water, liquid crystals, organic compounds, and various solvents.

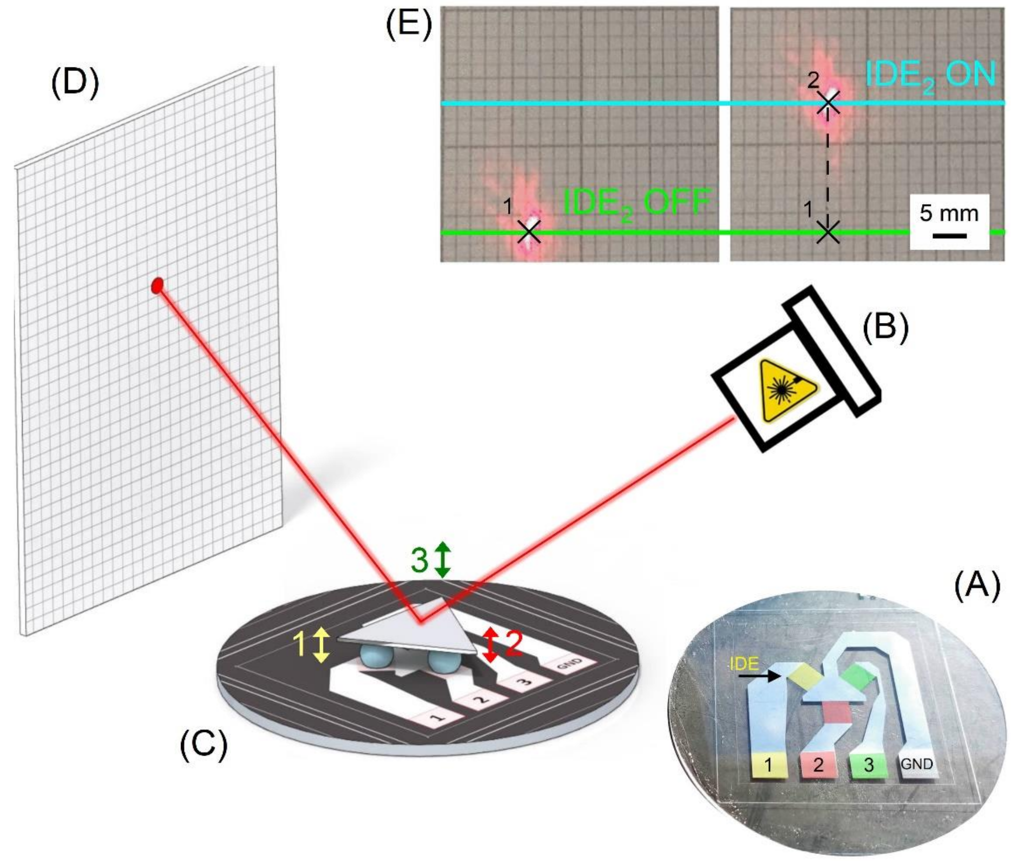

Figure 74 (A) Schematic of a device with three control electrodes (1, 2, and 3) and a common ground (GND). (B) Class-1 laser beam. (C) The conceptual design of the tilt mechanism with three droplets to control the surface orientation. (D) The projection screen to monitor the laser beam position. (E) The experimental results showing the beam steering when IDE (2) is activated.

Figure 75 A shows the device structure with three separate parts, the reflective cover plate, L-DEP device with three separate IDEs (4 mm × 4 mm) at a phase angle of 120°, and DI water droplets. Figure 75 B shows the top view of the IDEs electrode design with a gap distance of 20 µm. The fabrication process of the L-DEP device was identical to the device shown in Chapter 4. However, the insulating layer was aluminium oxide with a nominal thickness of 400 nm, deposited using atomic layer deposition (ALD) technique. Aluminium oxide was chosen because of its superb dielectric properties while also providing good chemical and mechanical protection. Figure 75 C shows the side view image of the device during operation.

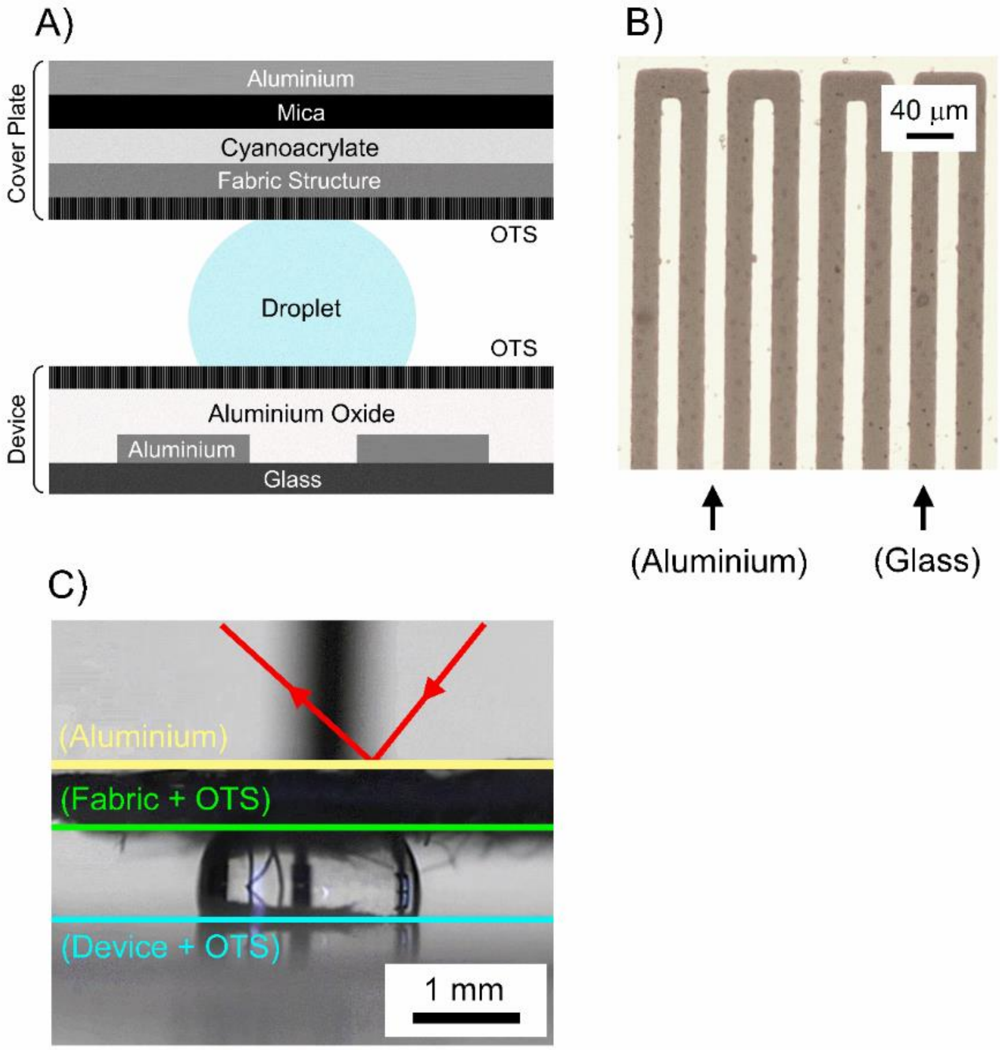

Figure 75 (A) Device structure with four main layers: glass, aluminium, SU-8, and OTS. The mirror plate consisted of an aluminium layer on a Mica substrate. Mica was attached to a fabric structure functionalised with SAM OTS using cyanoacrylate (adhesive material). (B) The side view image of a device (10 mm × 10 mm) during testing. (C) Superhydrophobic surface with contact angles exceeding 160°.

The base substrate (15 mm × 15mm) for the fabrication of the reflective cover plate was Mica with a nominal thickness of 0.1 mm. Mica sheets have many unique properties including, excellent dielectric properties, chemically stable, lightweight, optically reflective, flexible, and resilient. The sheets can be split into very thin layer, typically between 25 µm and 125 µm. Mica sheets are principally used in the electronic industry, for example, as an electrical insulator in electronic equipment.[259] Mica is also used in the production of ultra-flat/thin-film imaging substrates with applications in atomic force microscopy.[260, 261]

The samples were cut out in triangular or rectangular shapes, cleaned thoroughly with IPA, and dried with nitrogen gas. Subsequently, an aluminium layer with a thickness of 70 nm was deposited using the E-beam evaporator to act as a reflective top layer. The untreated mica substrate has a high surface energy with a low contact angle with water (hydrophilic). The beam steering range and resolution can be readily improved using a substrate with a higher contact angle to minimise the droplet compression effect.

SAM OTS was coated on a fabric structure (cleanroom wipes) to provide a lightweight and superhydrophobic reflective layer. A similar surface treatment was demonstrated for developing humidity-resistant fabric coating using SAM OTS for wearable triboelectric energy harvesting.[262] The texture and roughness (fibres networking on the surface) enabled contact angels in excess of 160 ° (Figure 76 A).

Figure 76 B - D shows SEM images with different magnification at 5.0 kV using Carl Zeiss Sigma VP 300 FEG-SEM. The samples were sputter coated with 20 nm of gold prior to SEM observations. The observed material consists of 45% polyester and 55% cellulose, with an entangled fabric structure (micro-scale), and a basis weight of 67 g/m^2. Figure 76 B shows a broad overview of the surface when it is treated with SAM OTS. Figure 76 C and D, show SEM images comparing the fabric features before and after the SAM OTS surface treatment, respectively. Note that the fibres are slightly swollen after the SAM OTS surface treatment. The changes in the fabric structure was because of the evaporating solvent. Moreover, SAM OTS was in the nano-scale, and the thickness of the layer was dwarfed by the fabric size, which was in the micro-scale.

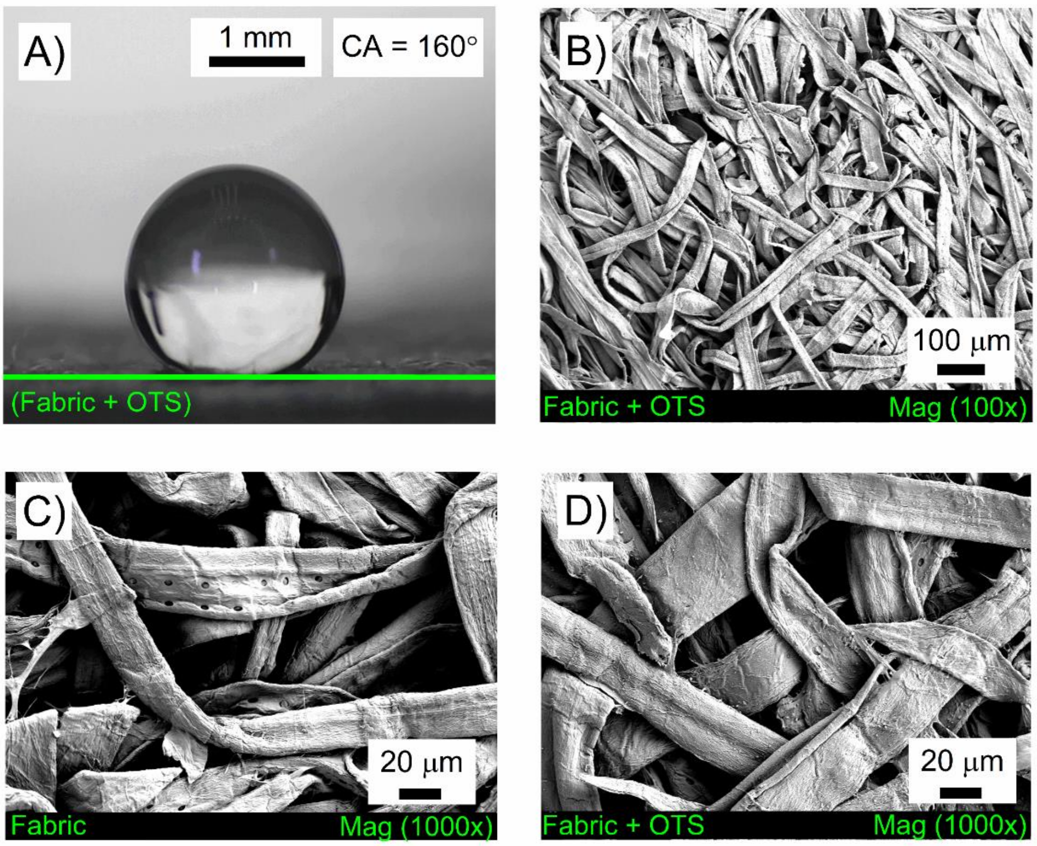

Figure 76 (A) Superhydrophobic surface with a contact angle exceeding 160°. (B) SEM image (Mag 100 ×) showing the micro-scale entangled fabric structures. (C) The fabric structure without SAM OTS treatment (Mag 1000 ×). (D) The fabric structure with SAM OTS surface treatment (Mag 1000 ×).

The micro-scale surface roughness (fibres networking on the surface) was the primary factor that explained the superhydrophobicity.[263] The droplet on a superhydrophobic surface rests on a patchwork of air and solid interface, and the low surface energy prevents the liquid interface from penetrating within the roughness, thus, producing a high contact angle (Cassie-Baxter model).

The experiments were carried out on an optical table, and a recording camera measured the changes in the position of the laser beam. Figure 77 shows the main experimental parameters. Initially, the laser beam was aligned to the centre of the mirror plate at an incident angle of 45°. Since the angle of incident I was constant, the angle of defection θ, in addition to the longitudinal deflection distance of the mirror plate δ, can be calculated by measuring the total distance the laser beam moves on the projection screen X_2. Additionally, the side view image of the device during testing can also validate the optical measurements.

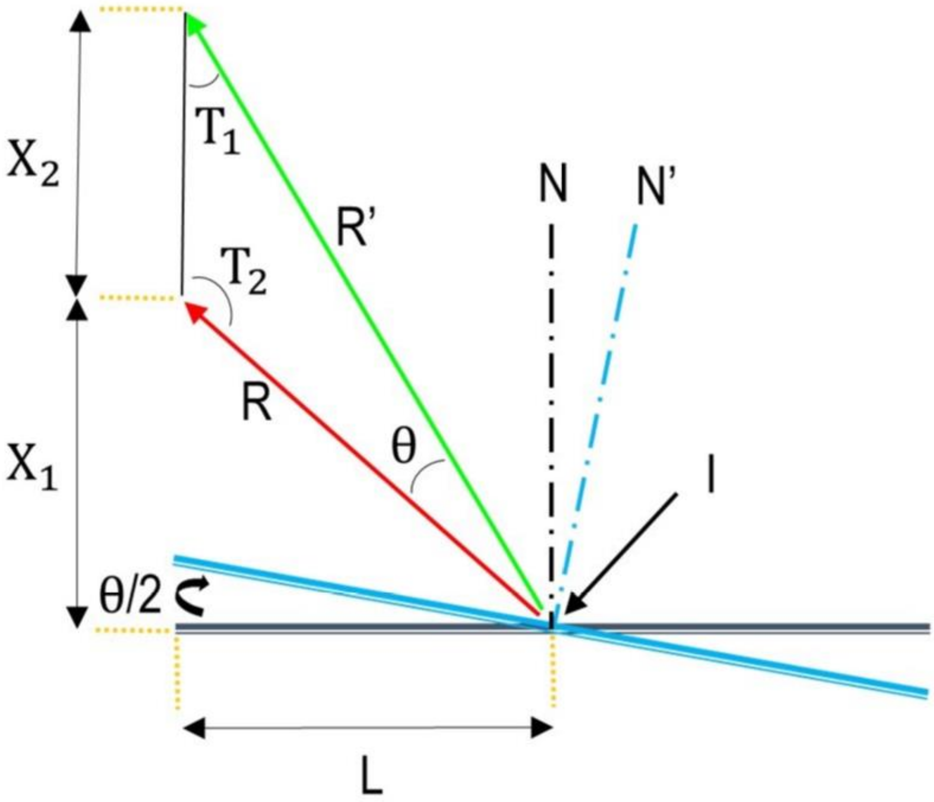

Figure 77 Schematic drawing showing the constant angle of incident I, and two angles of reflection for when the device is off and on R and R', respectively. N and N' are the normal angles for when the device is off and on, respectively. The angle of deflection θ is also shown here. X_1 is the distances away from ground. X_2 is the distance the laser beam moves on the observation panel. The schematic also shows the inner triangles formed when the position of the laser beam is changed, with two important angles of T_1 and T_2.

The calculations for θ and δ are shown here, where (X_1 = 0.89 m), and (L = 0.97 m).

$$T_1 = \tan^{-1}(L / (X_1 + X_2)) \tag{27}$$

$$T_2 = 180 - \tan^{-1}(L / X_1) \tag{28}$$

$$\theta = 180 - (T_1 + T_2) \tag{29}$$

$$\delta = 0.015\ (\tan(\theta/2) \tag{30}$$

Another application for the micromirror platform was studying L-DEP without measuring the droplet contact angle. Other characterising methods include contact angle measurements and a rise of liquid height between parallel plates (see Chapter 2). Figure 78 A shows the optical angle of deflection and deflection distance versus the drive voltage (up to 100 V) for a fixed signal frequency of 30 kHz. The experimental results verified that the actuation performance rises nonlinearly with the applied voltage. The dielectrophoretic force was dependent on the strength of electric field, and thus a larger applied voltage generates greater forces.

The voltage breakdown limit was the only limiting factor to generate higher forces, which also emphasised the need to use a good quality insulating layer. Furthermore, the alumina layer deposited using the ALD technique produced a superior dielectric layer with a long-lasting performance at high voltages (up to 100 V or more). However, the ALD deposition technique is expensive and time-consuming, with a limited application outside of the research laboratories.

Every liquid (e.g., propylene carbonate, water, and ethylene glycol) exhibits a distinctive frequency-dependent response. Figure 78 B shows the frequency-dependent testing results. The angular manipulation of the laser beam was carried out using a sine-wave AC signal with a frequency range between 100 Hz to 2 MHz for a fixed applied voltage of 65 V. Furthermore, the results confirmed that the optimum performance was between 20 kHz and 30 kHz. However, the actuation performance diminishes rapidly at higher frequencies (more than 500 kHz). Note that any variation in the electrical conductivity of the liquid can significantly shift the critical signal frequency.[190]

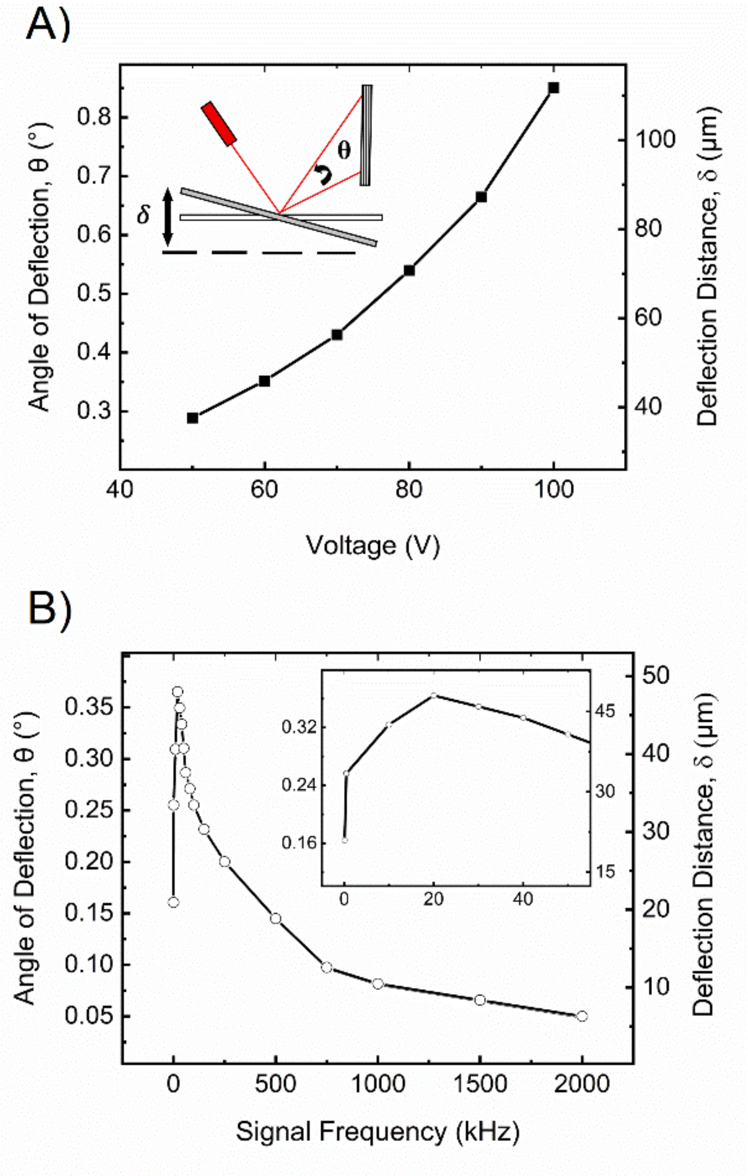

Figure 78 Experimental measurements using the micromirror platform. (A) The voltage-dependent study showing the L-DEP characteristics at a fixed signal frequency of 30 kHz. (B) Investigating the frequency-dependent L-DEP behaviour (100 Hz to 2 MHz) for a fixed applied voltage of 65 V. The inset is showing a zoom in of the peak region.

The tilting platform enabled angular coverage up to 0.9° (± 0.02°), with a maximum displacement of 120 µm. These values can be readily improved with a superhydrophobic coating on both the reflective cover plate and the device or using a higher applied voltage. Furthermore, the actuation resolution can be improved using smaller increments of applied voltage and signal frequency.

L-DEP is strongly dependent on the signal frequency, and the bulk effect is dominant when the applied frequency was more than 10 kHz and rapidly diminishes after 500 kHz. This is contrary to EWOD, which is dominant in the lower signal frequency spectrum (typically between 50 Hz and 1 kHz).[264] In EWOD-based platforms, large electrode pads (several millimetres) produces an electric double-layer effect, and thus, they are only compatible with conductive liquids.[265] L-DEP actuation was the dominant mechanism in our study because the electrode gap distance was 20 µm, generating a strong local non-uniform electric field.

The frequency-dependent analysis using the tilt platform also correlates with previous L-DEP studies using Pellat's experiments and contact angle measurements. Our data similarly confirms the theoretical and experimental approach that DI water experiences a DEP effect when the signal frequency is at least 10 kHz or more.[190] The thickness of the dielectric layer can also change the critical frequency. Previous investigations showed that the critical frequency could decrease from 60 kHz to 10 kHz when a dielectric thickness changes from 10 µm to 2 µm, respectively.[40]

The tilting platform has several advantages when compared to the conventional contact angle measurements,[191] or Pellat's experiment.[40] Primarily, it is simple to operate and has no requirement for a contact angle goniometer, which reduces the experimental costs. The collected data using a simple camera is equivalent to the contact angle measurements. Moreover, replacing the observable panel with a photo-diode would also significantly increase the resolution of the measurements.

Figure 79 shows the dynamic performance of the angle of deflection as a function of the switching frequency (modulated square-wave signal). Figure 79 A shows the dynamic performance for two modulated signal frequencies (10 Hz and 0.5 Hz), with a fixed sine-wave carrier signal of 20 kHz.

The droplet actuation behaviour on a typical IDEs exhibits a small degree of hysteresis,[266] related to the swapping from the advancing to receding contact angles. This effect was only detected in the first activation cycle (OFF-ON-OFF), as depicted in Figure 79 A with dotted lines. This will translate into inaccuracies (± 0.01°) in the position of the mirror. Therefore, this can be neglected in applications where there is a large variation in the angle of deflection. Additionally, regulating the applied voltage and signal frequency may reduce this hysteresis in the initial switching cycles at the expense of a more complex control system.

Figure 79 B shows the range in the angle of deflection (between ON and OFF state) with a fixed signal frequency of 20 kHz at various modulated signal frequencies between 0.5 Hz and 500 Hz. Previously, the hydrodynamic response was verified using a high-speed camera with a high-magnification lens.[267] Furthermore, the droplet spreading speed was approximately 33.3 mm s^{-1} and 5.8 mm s^{-1} when the device was turned ON and OFF, respectively. This is similar to the measured experimental data using a contact angle goniometer, which was also reported elsewhere.[267]

The droplet spreading time is critical when selecting an appropriate activation time for switching electrodes in a droplet actuating platform. Additionally, it is an important factor to consider for a beam steering application. The droplet spreading time was approximately 30 ms and 170 ms when the device was turned ON and OFF, respectively. Therefore, a modulated signal with a frequency larger than 2 Hz exceeds the hydrodynamic response of the droplet, as verified in Figure 79 B. Therefore, various factors influencing the hydrodynamic response should be considered depending on the application. Several examples are droplet volume, liquid viscosity, and temperature.[268-270]

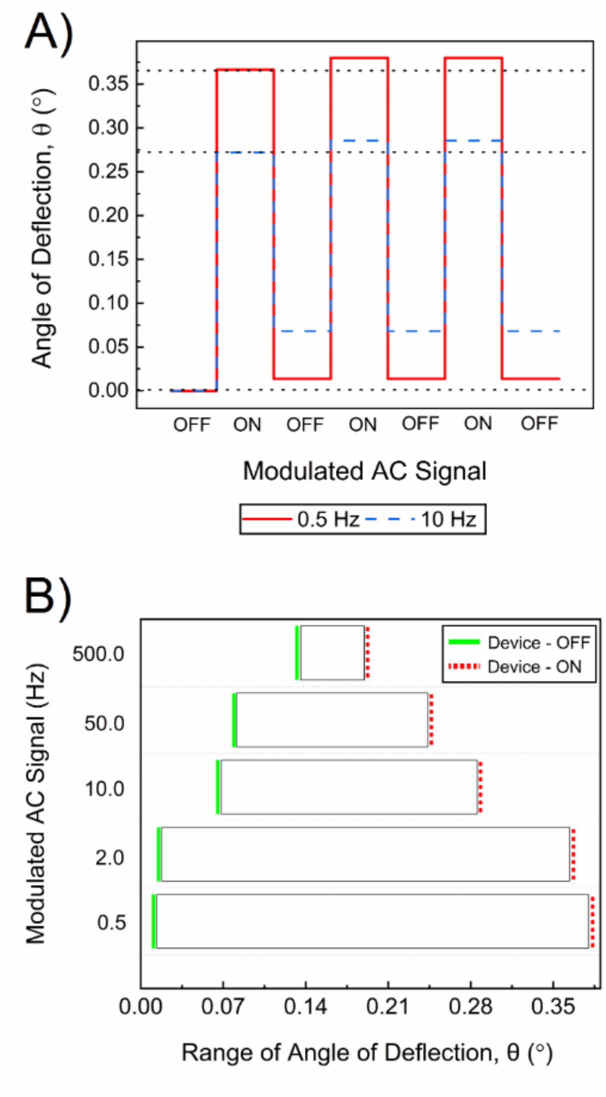

Figure 79 Testing results showing the optical angle of deflection with a fixed signal frequency of 10 kHz at different modulated signal frequencies (0.5 Hz to 500 Hz). Note that a modulated signal frequency greater than 2 Hz exceeds the hydrodynamic response of the droplet. Therefore, the laser beam fails to recover back to the original position.

The movement of the laser beam is critical in some optical MEMS applications.[271] Figure 80 shows the optical beam steering to create a triangular shape via switching between the three IDEs. The operating voltage was 70 V with a signal frequency of 10 kHz. The position of the laser beam can be precisely controlled by regulating the applied voltage or signal frequency. Furthermore, it is possible to generate other geometries (circles, polygons, quadrilaterals) by sequentially combining the IDEs. For example, activating the IDEs 1-2, then IDEs 2, then IDEs 2-3, and so on, to generate a hexagonal shape.

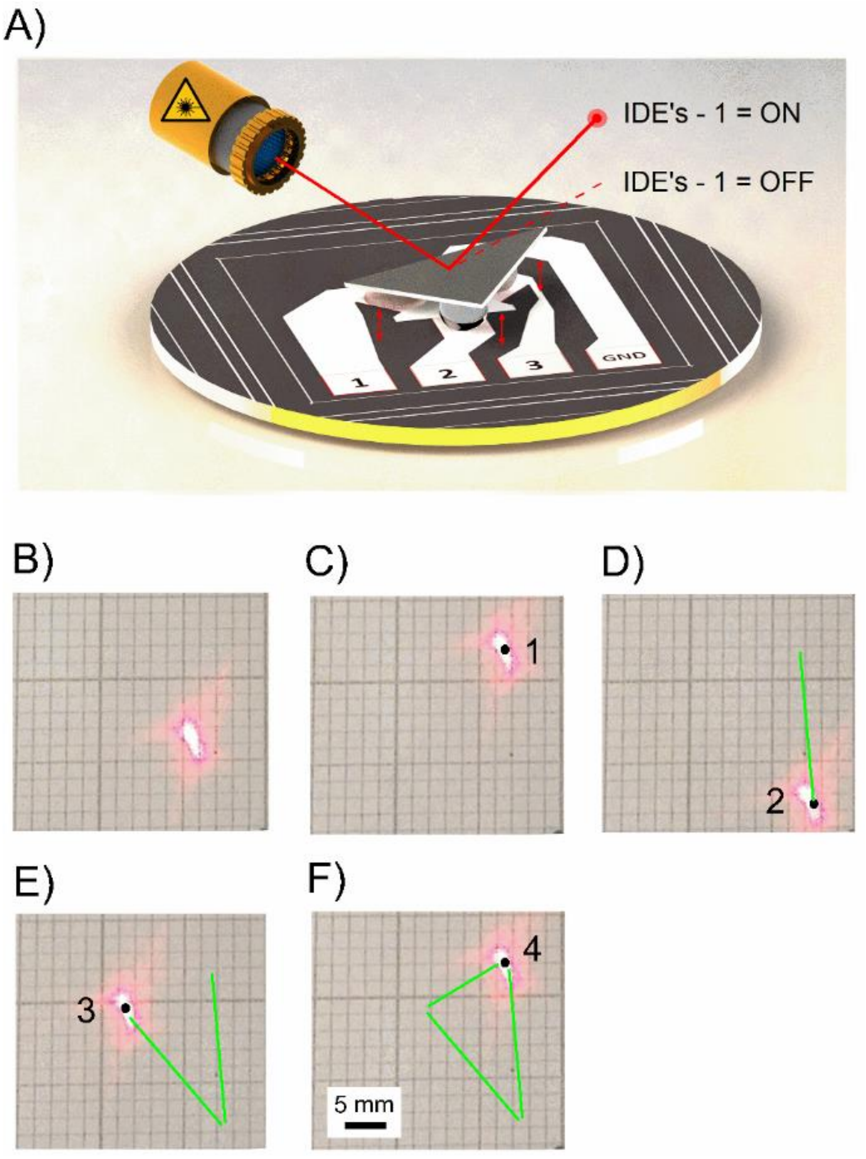

Figure 80 The beam steering operation using the micromirror platform with a three-axis tilt mechanism. (A) Schematic showing the platform during operation. (B - E) The laser beam steering operation to generate a triangular pattern. Note that the switching of the IDEs can be regulated to produce complex geometries such as hexagons and circles.

Any future study on this topic should also consider controlling the laser beam position using a feedback control system. In principle, accurattions are feasible down to the micro-scale, enabling various optical applications, such as lithography. The main objective of this study was to understand the effect of signal frequency and applied voltage to improve the performance. However, further analysis is needed to commercialise the tilting platform. Primarily, a temperature-dependent study is required to study the effect of droplet evaporation in different ambient conditions. Although the testing liquid was DI water, other dielectric liquids with a different evaporation rate are similarly compatible, such as oil-based solutions, propylene carbonate, ethylene glycol.

7.3 Electric microhydraulic actuator

Although the focus of this thesis was to study EWOD and L-DEP for a cleaning application, the technology is also applicable in other fields.[111, 115] The microhydraulic actuator presented here was based on electrowetting using the VIDEs configuration (see Figure 81). The actuator works by placing a cover plate on top of a droplet to create a moving platform structure to transport solid contaminants along the length of the electrode. There are several reported droplet-based moving platforms using electrowetting.[111, 272, 273] However, their operation is entirely different, and they typically lack the continuous droplet motion.

The actuation method opens new possibilities for positioning and manipulating particles and components. These could be hazardous medical materials or even radioactive substances, where direct contact should be avoided. Compared to similar mechanical platforms, the electrowetting-based design offers a unique combination of low-cost, low-voltage, and scalability, not easily achievable on the microscale. Furthermore, the actuator has no moving parts, and the disposable cover plate is ideal for one-time use applications.

The testing results are demonstrated in Figure 81, transporting two cover plates along the length of the electrode pad. These include a polyvinyl chloride plate, which is a biocompatible material that is also used for electrical insulation (see Figure 81 B - D), and a superhydrophobic filter paper similar to the concept shown in section 7.2 (see Figure 81 E - G).

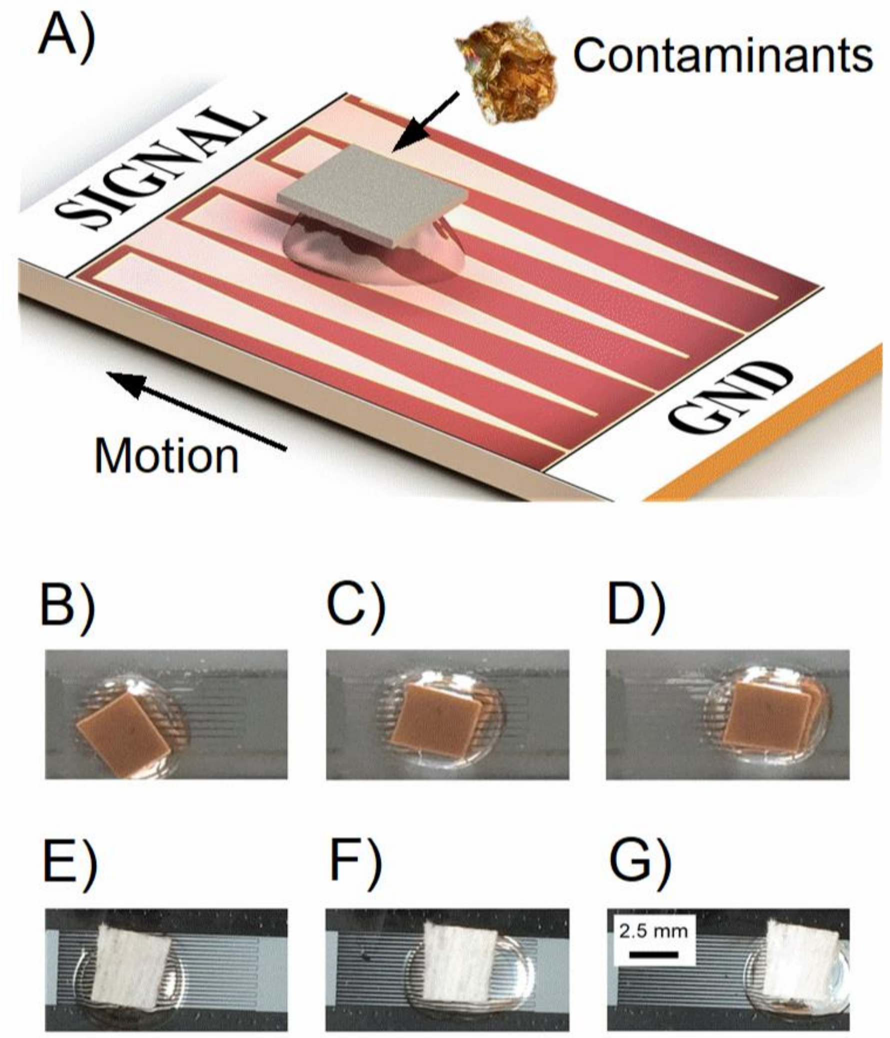

Figure 81 (A) Schematic model showing VIDEs functioning as a microhydraulic actuator to transport solid contaminants along the length of the electrode pad. Transporting solid contaminants has several microfluidic applications. (B - G) Testing results showing a droplet with a cover plate moving along the length of the electrode pad. (B - D) Polyvinyl chloride plate, and (E - G) a superhydrophobic cleanroom paper.

The primary limitation of the actuator was that only small samples (in the micro-scale) can be transported as the heavy samples would make the platform imbalanced. Even though the actuation was only demonstrated on a single electrode, the operation still remains practical using multiple electrode pads on a larger scale or using multiple droplets to transport a larger cover plate (i.e., four droplets to carry a larger pad), as illustrated in Figure 82. Furthermore, the 2D actuation of droplets using the VIDEs would be beneficial. For instance, a bidirectional actuation is feasible, having two sets of electrode patterns with an opposite variation of gap distance.

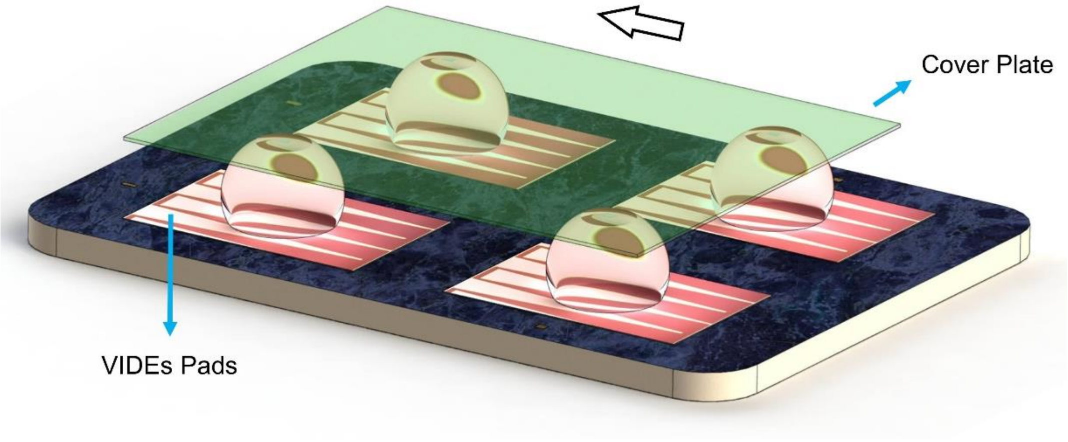

Figure 82 Schematic model for a conceptual device with multiple VIDEs functioning as a microhydraulic actuator to transport a large cover plate. A larger platform enables better stability as well as the transportation of heavier contaminants. An arrow shows the actuation direction of the cover plate.

7.4 Summary

This chapter explored different applications based on the electric manipulation of droplets using EWOD and L-DEP. The primary focus of the study was to investigate the performance of a self-cleaning cover lens based on the VIDEs design configuration. The cleaning platform was tested on the road by connecting it to the car battery. The performance was also evaluated in laboratory conditions. The testings verified that the actuation mechanism was effective under several operating conditions, maintaining a good visibility during rainfall. The cleaning platform effectively actuated a range of contaminants typically found on the road including, sand, dust, mud and rain.

The self-cleaning cover lens remained functional after long period of use (several weeks). Moreover, fabricating the device using a flexible substrate enabales large-scale manufacturing and low fabrication costs. The flexible substrates would enable device assembly on curved surfaces, which is an essential requirement for automotive applications (see section 8.2).

Additionally, we verified the defrosting and melting of ice droplets using electric fields. The defroster platform can also actuate droplets using multiple IDEs pads. Therefore, providing a multi-purpose cleaning platform with various functions. The device melted frost and ice layers in several seconds. The operation was energy-efficient, consuming far less power than the current systems based on resistive heating technology.

In this chapter, we presented a tilting micromirror platform with optical applications based on the L-DEP principle. The beam steering mechanism was also an alternative method to study L-DEP. The experimental results were similar and comparable to studies using parallel plate electrodes or a contact angle goniometer. The droplet manipulation produced a three-axis tilt mechanism via modifying the operating voltage or the signal frequency. The platform was simple and easy to set up, using low operating voltage (65 V or less), with a wide angle of deflection angle (up to 1°), and a high response (as low as 30 ms).

There is also a similar reported study of a tilting stage platform using a sandwich EWOD configuration.[274] There are several fundamental differences between an EWOD and L-DEP actuating platforms. Primarily, the electrode design is planar in L-DEP, meaning that the ground and signal electrodes are positioned on the same plane. Therefore, the electrode configuration enables simple modifications to improve the performance. For instance, using a superhydrophobic fabric layer on the reflective cover plate to minimise the droplet compression effect. Furthermore, lower voltages are feasible by scaling down the electrode dimensions to the micron scale with a thinner insulating layer. Moreover, dielectrophoresis is compatible with dielectric liquids. Therefore, the testing liquid can be oil-based solutions, organic compounds, and liquid crystals with a lower evaporation rate. Lastly, we evaluated the device performance using a beam-steering method, using minimum video processing and low experimental setup costs.

Operating the micromirror platform without a solid-solid contact overcomes the stiction limitation of the moving parts. The developments can also assist researchers in designing new actuating platforms based on the L-DEP principle. A notable configuration is an array of micromirrors, opening new avenues for developing digital micromirror devices and optical switches in next-generation sensor networks.

This chapter also introduced an electrowetting-based microhydraulic actuator using VIDEs for transporting solid samples. The cover plate transported solid contaminants along the length of the VIDEs. The contactless motion of the cover plate has several applications to move hazardous materials.

Chapter 8
Conclusion & Future Work

8.1 Summary of the findings

The primary focus of this thesis was to develop a self-cleaning platform for an automotive application, with a significant emphasis on scalability and design simplicity. L-DEP and EWOD were investigated through several methods by employing different electrode configurations. The voltage and frequency dependence of the actuation methods were studied using various techniques. They include contact angle measurements, droplet actuation speed, droplet elongation, and beam steering method using a tilting platform. Moreover, the droplet actuation force was also investigated using a frictionless tilting platform. The experiments provided adequate results to select various optimum operating conditions, such as signal frequency, operating voltage, and optimum electrode geometry.

An electronic control system with a relay module was developed to switch high voltages. The main advantages of the controller unit were hardware customisability, low costs, and accessibility. The modular design enabled large-scale experiments, and the electronic system was controlled using a single microcontroller unit. Additionally, the electronic design allowed the control of individual relay module boards using separate BNC connections. Thus, it provided up to four signal outputs from separate high voltage signal amplifiers.

The initial design adaptation was based on the IDEs configuration. IDEs are reliable and commonly used in various dielectrowetting studies. However, we introduced several design changes to improve it for a cleaning application. An iterative switching method was developed by combining microscale electrodes to realise larger arrays for actuating droplets with different volumes. Moreover, fabricating IDEs with a smaller gap distance (20 µm) and a thinner insulating and hydrophobic layer (less than a micrometre) lowered the operating voltages to 100 V from several hundred volts in previous studies.[132] Furthermore, the operating voltages were further reduced by introducing a lubricant layer (as low as 30 V). Additionally, a large-scale device based on the IDEs (5 inches) was also presented with an active area of 60 cm^2.

Interdigitated electrodes with a variable gap distance produced a continuous droplet motion. The novel approach enabled droplet manipulation with varying volumes. Furthermore, the actuation was independent of the droplet position, thus eliminating the requirement for a control system. Additionally, multiple large-scale devices (3 inches or more) based on the VIDEs configuration were fabricated and tested. An embedded electrode design enabled the switching of multiple groups of electrodes by connecting them in a spiral loop. The simple design adaptation was appropriate for a large-scale platform and minimised costs.

A series of analytical studies based on an RC circuit network model estimated the critical signal frequency. The equivalent RC models calculated the dielectric layer capacitance, liquid capacitance, and liquid conductance. The maximum electrostatic energy and force was estimated for various electrode geometries. Additionally, it was demonstrated that the frequency response was dependent on the droplet position. Therefore, the signal frequency response could also explain the continuous droplet motion on the VIDEs. COMSOL Multiphysics simulated the distribution and strength of the applied electric field for various electrode geometries. The strength of the electric field is also related to the magnitude of the applied electric force, and highlights the optimum design parameters.

The droplet actuation force was calculated experimentally using a frictionless surface on a tilted platform. The experimental approach estimated the actuation force of a droplet as a function of gravity on a slippery surface. The study verified the actuation behaviour as a function of signal frequency and applied voltage. The reported results were similar to the analysis based on the droplet actuation speed shown in the section 4.3. The experimental results were also comparable to the analytical analysis based on the RC circuit network model.

The frequency-dependent study highlighted the optimum operating condition and verified the critical signal frequency for various electrode geometries. The study concluded that higher signal frequencies (5 kHz or more) generated a dielectrophoretic response. On the other hand, it was electrowetting that dominated the droplet spreading behaviour at lower frequencies (5 kHz or less) for conductive liquids. Furthermore, a fixed signal frequency (500 Hz) minimised the droplet actuation complexity, and transported various liquids, including DI water, rainwater, mud rain, and KCl-water solutions.

In principle, IDEs with a small gap distance (20 μm) were more effective in the L-DEP spectrum when applied at a high signal frequency (40 kHz). In contrast, the optimum performance of the VIDEs was dominated by the electrowetting mechanism, typically employed at less than 5 kHz. Additionally, applying a higher voltage generated a proportionally stronger electric field to maximise the applied forces in both electrode designs.

SAM OTS hydrophobic and superhydrophobic surfaces presented an alternative method to maintain a surface clean. Droplets tend to roll off from a hydrophobic surface, carrying dirt and contaminants. Furthermore, their low surface energy improves the droplet actuation performance using electrostatic forces. The continuous droplet actuation was confirmed using a wettability gradient. We also proposed an integrated design for a future study that combined the wettability gradient with an electric switching method for a large-scale application.

Three applications are proposed in this thesis based on the L-DEP and EWOD mechanisms. The primary application was a self-cleaning cover lens based on the VIDEs without a control system. The cover lens was tested in the cleanroom under controlled conditions, and similarly, on the road by connecting it to the car battery via a power inverter. The cleaning platform demonstrated the actuation of standard dirt and other contaminants typically found on the road. The testing on the road concluded that the self-cleaning platform was effective when the car was moving at different speeds. Additionally, the self-cleaning cover lens was tested by placing it over a LiDAR sensor to produce a 3D scan of an office with furniture. The study concluded that high quality scans were achievable using a transparent device made with ITO electrodes.

The fabricated devices remained functional after long periods of use. The SU-8 insulating layer remained stable, assuming that the operating voltages were below the breakdown limit. The experimental results confirmed that the operation was reliable, actuating a variety of water-based solutions with different electrical conductivity, ice formations, mud rain, dust, and sand. We noted that the SAM OTS hydrophobic properties degraded over time, as do all hydrophobic coatings. However, a higher applied voltage can always compensate for any environmental degradation. We recommend a comprehensive study of the hydrophobic layer, considering alternative materials and fabrication methods.

We also explored other applications of L-DEP and EWOD actuations in this thesis. A new tilting micromirror platform based on the L-DEP was presented, to provide a three-axis tilt mechanism by electrically manipulating the droplets. The voltage and frequency dependant behaviour of L-DEP was investigated to confirm the optimum operating conditions. The proposed platform was considerably cheaper when compared to similar technologies (e.g., magnetic or piezoelectric). Additionally, the tilting platform was an effective instrument to study L-DEP without measuring the droplet contact angle. In principle, the optical tilting method can also estimate the dynamic droplet contact angle, assuming that the initial contact angle is known. The analysis was comparable to L-DEP studies using contact angle measurements, droplet actuation speed, and measuring rise of liquid height between two parallel electrodes.

A new electrowetting-based microhydraulic actuator was also presented for transporting solid particles. In this technique, the droplet movement on a typical VIDEs actuated a solid platform situated on top of a droplet. Therefore, the platform could act as a carrier to move other materials and contaminants. The microhydraulic actuator is contactless, and a particular interest would be to handle biological and radioactive materials.

In conclusion, this work presented a surface cleaning technology based on the EWOD and L-DEP actuation mechanisms. Furthermore, various design modifications enabled a scalable and simple operation, which was previously absent in the research field. The improvements presented in this thesis open many avenues for future innovative applications. A particular interest would be to develop a self-cleaning cover lens for an automotive application. We can also expect in the next decade to witness the utilisation of a similar platform for various droplet based microfluidic systems.

8.2 Future work

This chapter presents an outlook for the droplet actuation methods, and proposes several design improvements for a future study based on some initial experimental results. Initially, we explored several new electrode designs with irregular patterns to maximise the magnitude and non-uniformity of the electric field. Electrodes with an irregular pattern presented some unique actuation behaviours such as rapid droplet evaporation, lower operating voltage, asymmetric droplet spreading, and complete film formation. However, their performance was unreliable and demand a comprehensive study to fabricate a stable device. This is primarily because their irregular features are prone to fabrication defects. We also explored alternative materials and fabrication methods to improve existing designs in this thesis for a new application.

The size and shape of the electrode geometry changes the strength and distribution of the electric field based on the fundamental theory of electrostatic. Figure 83 shows an array of aluminium fishbone and triangular edge pattern IDEs. The irregular branched structures are intended to increase the strength of the electric field while reducing the input voltages. Four different gaps were considered (10 µm, 20 µm, 40 µm, and 80 µm). However, devices with an electrode gap distance smaller than 40 µm were predominantly neglected due to fabrication defects and device failure from a dielectric breakdown.

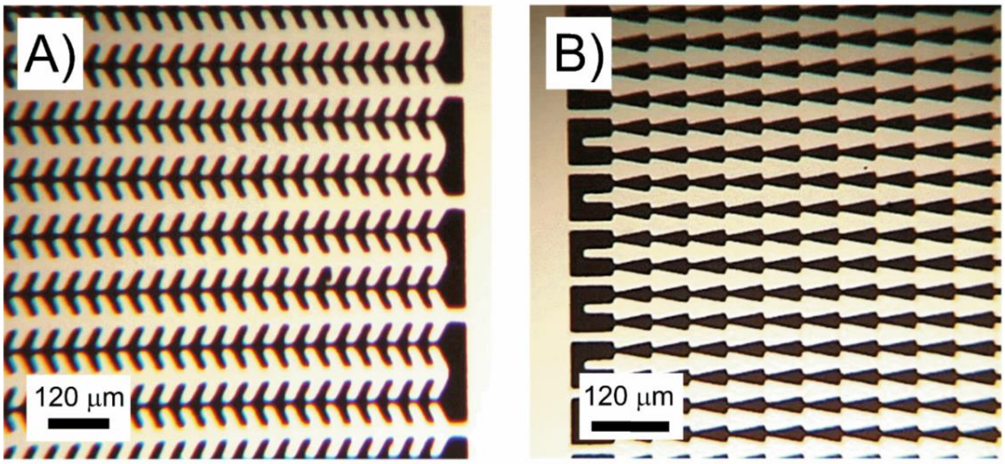

Figure 83 Microscopic images showing electrodes with irregular branched structures. (A) Fish-bone electrode designs for generating strong non-uniform electrical fields. (B) The triangular edge electrode design. The electrodes (shown as silver colour) are covered with a protective layer of SU-8 insulating material and a functionalised SAM OTS hydrophobic coating.

Figure 84 shows COMSOL Multiphysics simulation results for the electric field distribution across IDEs with a fishbone electrode pattern. The gap distance was 50 µm. The primary advantage of using IDEs with irregular patterns is to minimise the operating voltages. Fabricating IDEs with a small gap distance (20 µm or less) require a cleanroom with very high fabrication standards to minimise defects. Alternative fabrication methods such as electron-beam lithography can reduce fabrication defects for smaller structures at the expense of a higher fabrication cost.

Another recommendation is depositing a high-quality alumina film using the atomic layer deposition technique, similar to the device shown in section 5.3.

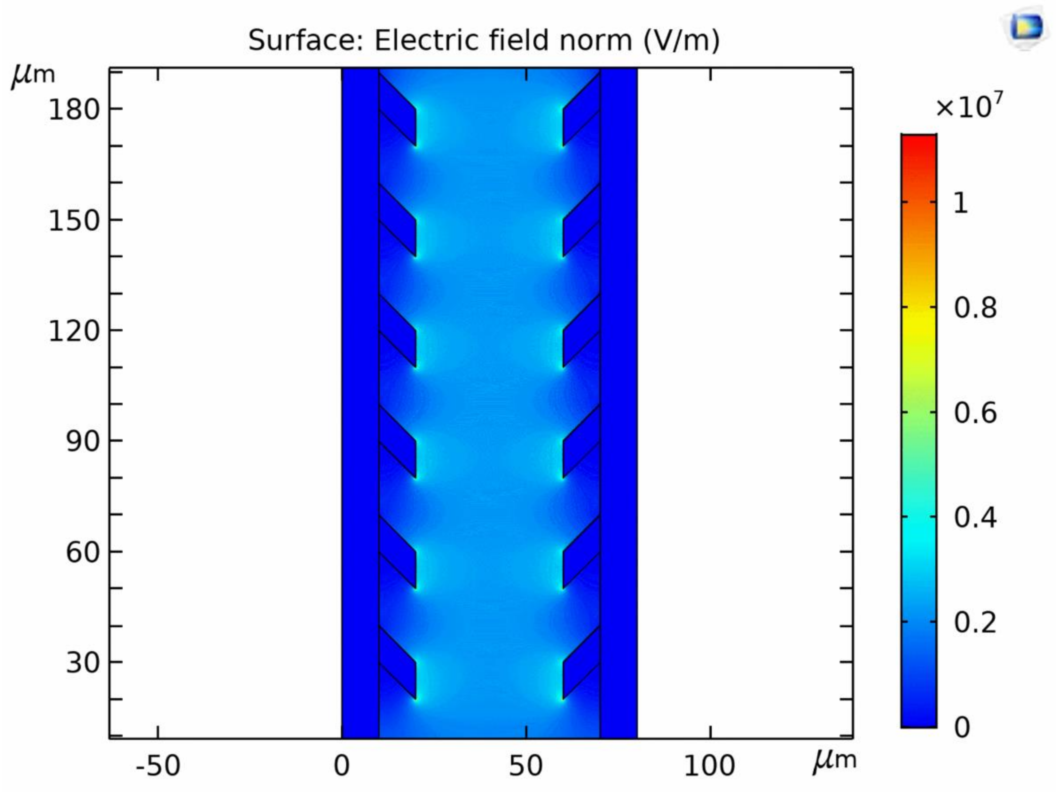

Figure 84 COMSOL Multiphysics simulation results showing a 2D colour electric field contour of a fish-bone electrode structure. Note that a strong electric field is generated near the irregular branched structures.

We recommend a comprehensively future study to investigate the irregular electrode designs to reduce the operating voltages. Various design features require investigating to improve the voltage breakdown limit. For instance, minimising sharp fabrication features, alternative composite insulating films, and the appropriate size of gap distance and insulating thickness. Figure 85 shows several recommended IDEs designs with irregular breached structures. A particularly unique electrode design is shown in Figure 85 A, with the highest electric fields intensity per unit area.

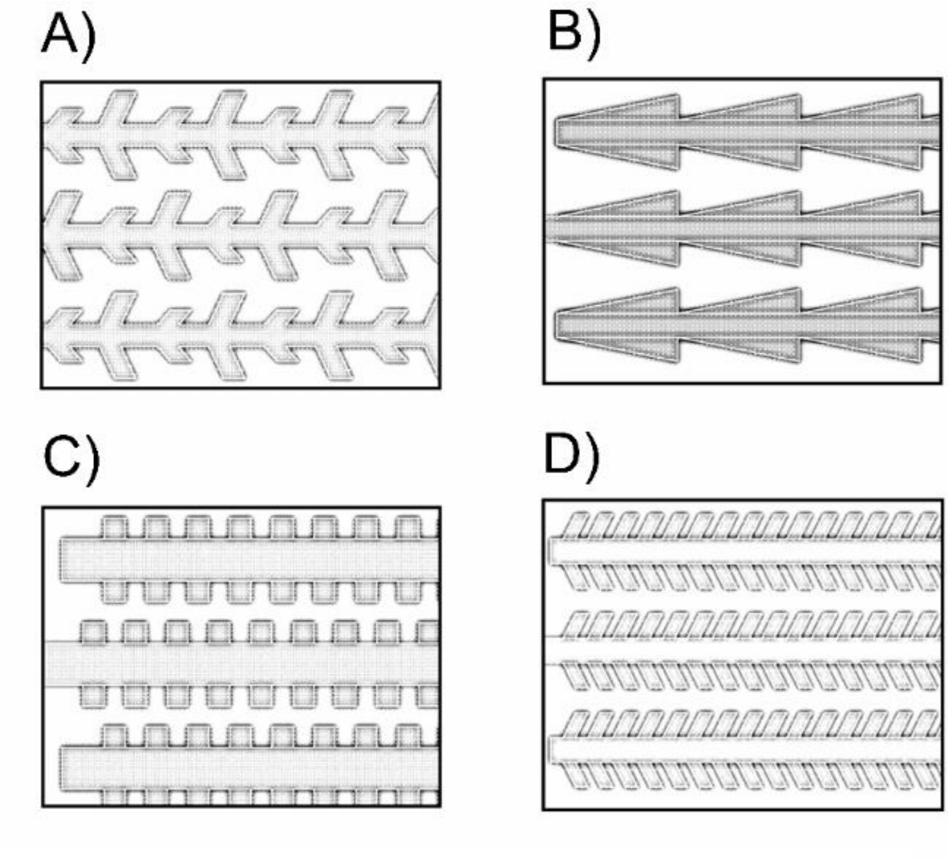

Figure 85 Schematic drawing showing different proposed electrode designs with irregular branched structures. The electrode designs should be included in a future study.

L-DEP is a bulk force acting on the dipoles of a dielectric liquid, and it is generally considered a localised effect. Therefore, the droplet spreading behaviour is determined by the interaction between the solid-liquid interface. The electrode fingers in a typical linear IDEs represent potential energy barriers to produce a non-axisymmetric spreading, as depicted in Figure 86 A, B. Additionally, the axisymmetric spreading has been reported elsewhere using a spiral IDEs design operating at several hundred volts.[275]

However, the fishbone IDEs may break the energy barriers and produce an axisymmetric spreading (see Figure 86 C, D). The L-DEP effect was achieved at 100 V or more with a signal frequency of 60 kHz using DI water. The axisymmetric spreading opens many avenues for future innovative applications, including 2D droplet motion and axisymmetric film formations.

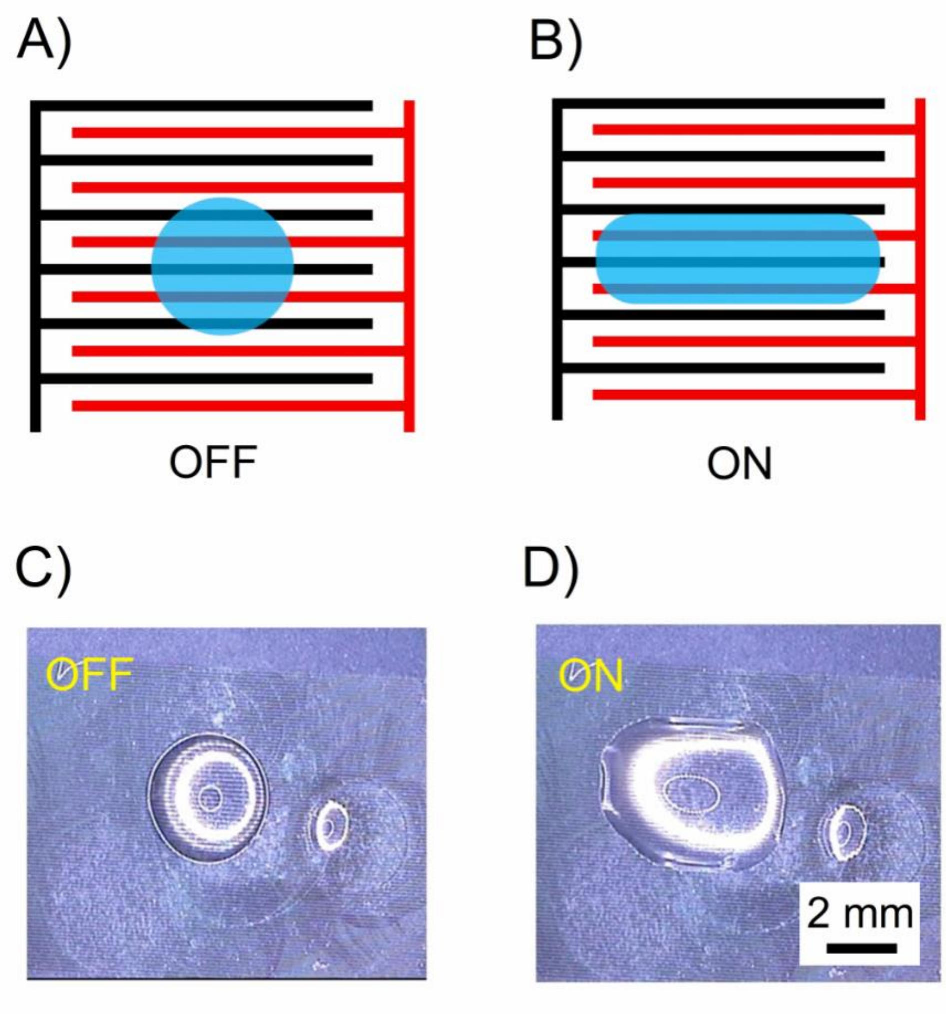

Figure 86 Axisymmetric spreading behaviour of DI water droplet. (A - B) Schematic drawing showing the non-axisymmetric spreading of a droplet using a typical IDEs. (C - D) The axisymmetric spreading of DI water droplet using the fishbone IDEs. The applied voltage was at least 100 V at 60 kHz.

Initial observations showed that the induced L-DEP wetting could even achieve a complete film formation over the entire electrode pad. Figure 87 shows the spreading behaviour, where a droplet of Hexane turned into a thin film using 100 V with a signal frequency of 10 kHz. The film formation has several applications, such as boundary lubrication, film coating, drug delivery, and self-cleaning platforms.

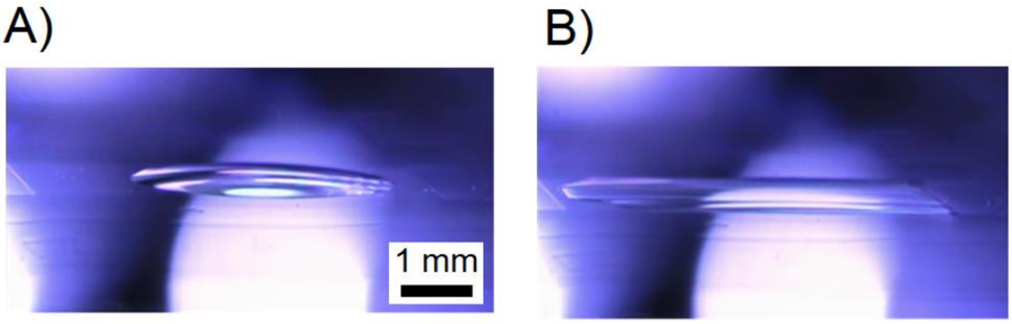

Figure 87 Experimental results showing a complete film formation of a droplet using the fishbone IDEs. (A) Hexane droplet without an applied voltage. (B) Hexane film formation after applying 100 V with a signal frequency of 10 kHz.

Figure 88 shows a transparent device fabricated on a glass substrate using ITO, SU-8, and OTS. Fabricating transparent devices enable various optical applications operating within the visible light spectrum.

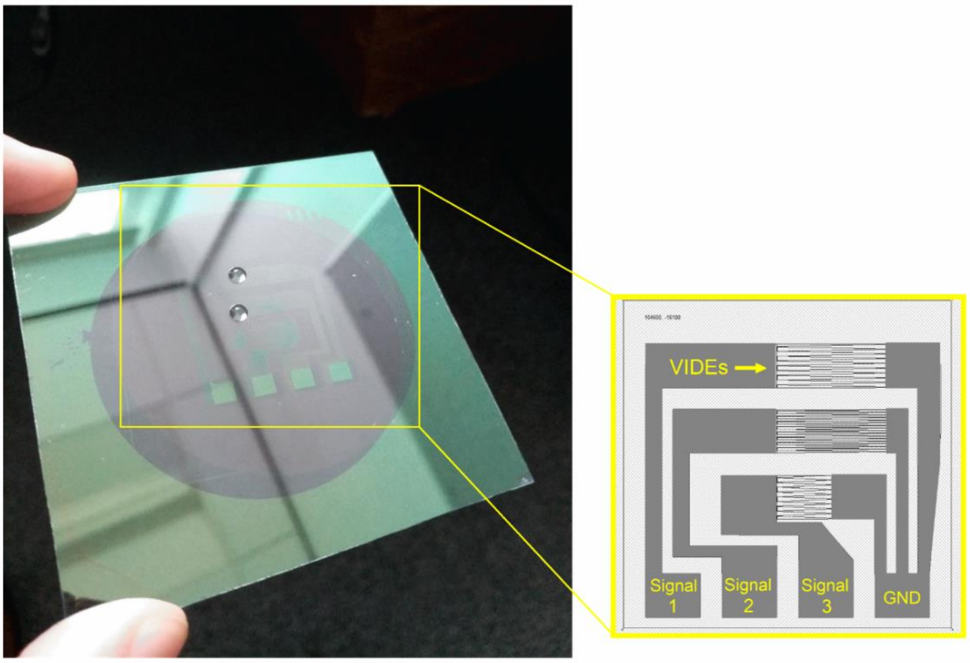

Figure 88 A transparent device fabricated on a glass substrate using ITO, SU-8, and SAM OTS. The electrode configuration is based on the VIDEs.

We recommend several alternative materials for a future study. An improved insulating layer can increase the device performance. For example, a composite metal oxide layer, or a combination of SU-8 with another metal oxide layer is recommended. Additionally, employing a different hydrophobic coating with a lower sliding angle or preferably a superhydrophobic coating would further reduce the operating voltages or generate a faster droplet motion. Fabricating devices on a flexible substrate would enable large-scale manufacturing at a low cost. Figure 89 A shows two fabricated flexible devices using ITO and aluminium electrode patterns

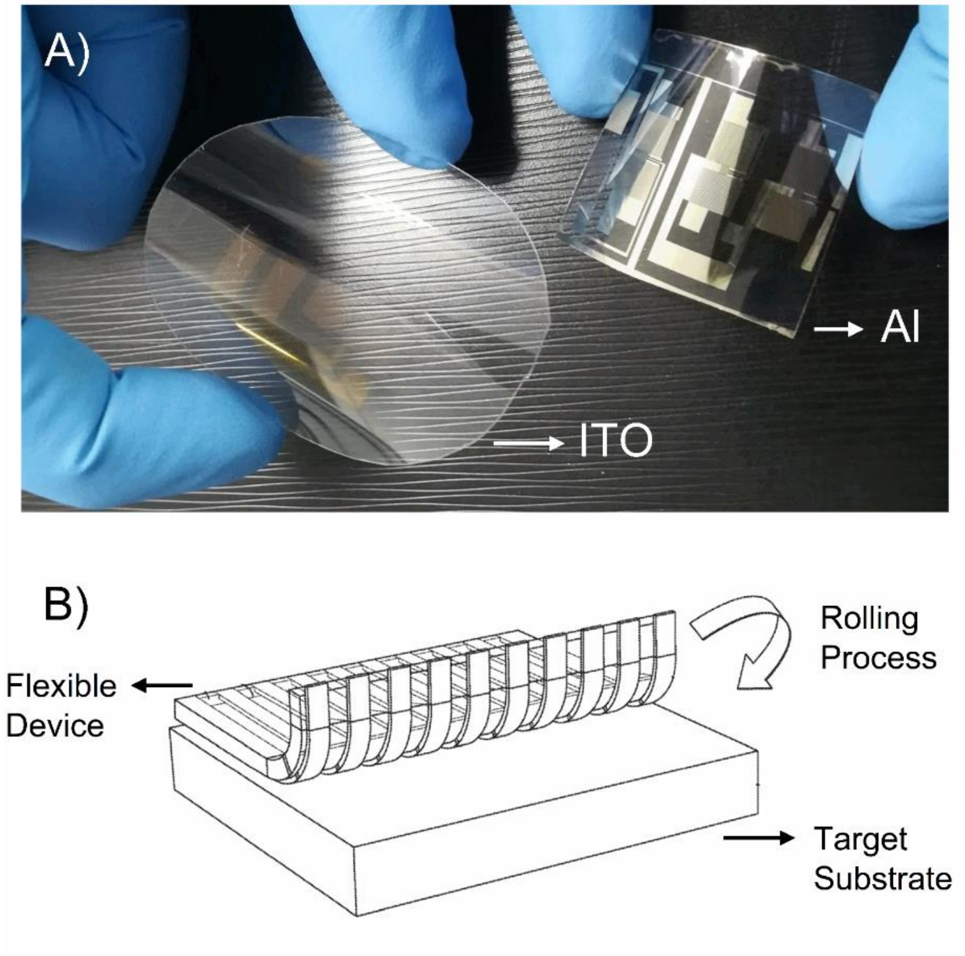

Figure 89 (A) A device based on the VIDEs configuration which was fabricated on a flexible PET substrate and ITO electrodes. Another flexible device was also fabricated using aluminium on a PET substrate. (B) The inverted device with a base flexible substrate acting as an insulator layer. The device is rolled over the target substrate. The transparent flexible device can be manufactured in larger numbers and can be easily mounted on a curved surface. The design of this device is particularly useful in the automotive industry.

The devices can be coated with an insulating layer (e.g., SU-8) and coated with a SAM OTS hydrophobic layer. However, the base flexible substrate can also be used as an insulator in an inverted design. Figure 89 B shows a rolling process to attach an inverted flexible device on a target substrate using an adhesive layer. Additionally, flexible substrates can easily be mounted on to curved surfaces. This is a critical design requirement for automotive applications.

VIDEs in paper electronics presents a new droplet actuation concept, combining a paper substrate as a functional part of the device (see Figure 90). The primary advantages are low fabrication costs, easily disposable, wide-scale availability, and recyclability. The paper-based droplet actuation has various applications in microfluidic and lab-on-chip devices. A notable application is a disposable device for biomedical applications to split, mix, and transport droplets (i.e., blood) for analysis.

Figure 90 A - F shows the fabrication process of electrodes on a device with a paper substrate. Initially, the paper substrate was cleaned with nitrogen gas, and 100 nm of an aluminium layer was deposited on the paper using an E-beam evaporator. The substrate was cut-out, and the four corners were folded to create a boat-like origami structure. The paper substrate had a protective plastic layer on one side (the side without an aluminium layer), but the folded corners allowed the substrate to float on liquid surfaces. We used the same technique during the photolithography and wet etching process to fabricate the electrode pattern shown in Figure 90 G.

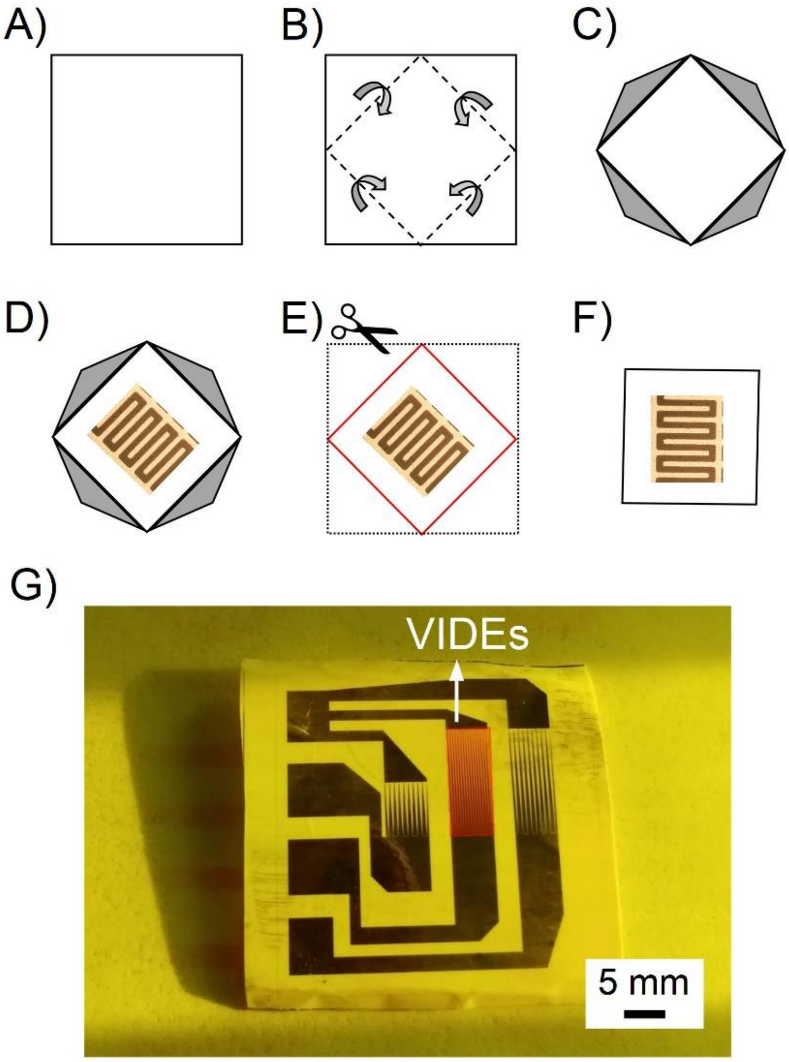

Figure 90 Fabrication process on a paper substrate. (A) Cut-out paper substrate. (B) Depositing a metal layer, spreading a photoresist, exposing the resist layer to UV light, and then folding the corners. (C) Making a boat-like origami. (D) Floating the substrate for developing and etching a pattern. The unique fabrication technique prevents etchants and developers from penetrating the paper substrate. (E) Cut the folded sides using a sharp blade. (F) Fabricated electrodes on paper. (G) An image showing the fabricated VIDEs on a paper substrate.

Appendix A Testing Materials

A.1 Testing Materials

Table 5 shows the testing liquids used in the experiments with the relevant chemical, physical, and electrical properties. The higher surface tension was important in both EWOD and L-DEP. The higher permittivity was crucial in the L-DEP actuation, whereas the larger electrical conductivity was more dominant in the EWOD actuation up to the saturation limit.

Table 5 List showing the key material properties of the testing liquids, including electrical conductivity, dielectric constant, surface tension, and liquid density.

Testing Liquids	**Permittivity**	**Surface Tension**	**Density**
Units	(F/m)	(mN/m)	(kg/m^3)
DI water	81	72.72	997
KCl-water (0.06 M)	78	72	997
KCl-water (saturated)	45	78.58	997
Rain water	80	72.72	997
Propylene carbonate	66.1	40.9	1200

Isopropyl alcohol	18.2	21.79	786
Hexane	1.89	18.43	655
Skimmed-milk	60	38	1027
Mineral oil	2.1	29.23	870

A.2 Electrode design

Table 6 shows the electrode geometries used in the thesis and associated control system requirements.

Table 6 The electrode geometries and control system requirements.

VIDEs Configuration	**Variable Gap Distance, (µm)**	**VIDEs Length (mm)**	**Control System Requirement**	**Utilized in Which Device**
Linear VIDEs 1.0	D_{min} = 20 D_{max} = 200	5	NA	Chapter 4.3.2 Chapter 4.3.3 Chapter 4.3.4 Chapter 5.3.0 Chapter 7.1.1 Chapter 7.1.2 Chapter 7.1.3 Chapter 7.3.0

Linear VIDEs 2.0	$D_{min} = 20$ $D_{max} = 200$	10	NA	Chapter 4.3.2 Chapter 5.3.0
Linear VIDEs Multiple	$D_{min} = 20$ $D_{max} = 200$	5.5	3 control signals	Chapter 6.2.0
Sunflower VIDEs	$D_{min} = 20$ $D_{max} = 200$	0.5, 1, 1.5, 2.5, 4, 6.5	3 control signals, but separate connections if there is a large variation in the droplet volume	Chapter 6.2.0
Bilateral-Symmetrical VIDEs	$D_{min} = 20$ $D_{max} = 600$	20	2 control signals	Chapter 6.2.0
Circular Symmetrical VIDEs	$D_{min} = 20$ $D_{max} = 150, 200$	3, 2, 1	NA	Chapter 7.1.1 Chapter 7.1.2
IDEs Configuration	**Gap Distance, (µm)**	**Pad Size (mm)**	**Control System Requirement**	**Utilized in Which Device**
Single IDEs	20 - 110	10 × 5	NA	Chapter 4.1.2 Chapter 7.1.4 Chapter 7.1.5 Chapter 7.2.0
Single IDEs with irregular features	20 - 80	10 × 5	NA	Chapter 8.2.0

36 IDEs	20	1 × 6	36 signals with a control system	Chapter 4.1.4
Large-scale IDEs	20	1 × 64	72 signals with a control system	Chapter 6.1.0

A.3 PCB design

Several attempts were made to design the control system and relay module PCBs. The initial designs were primarily for troubleshooting and identifying problems, such as voltage spikes and signal noise. Figure 91-92 shows the final PCB design used in the control system. Figure 93-94 shows the PCB design used in the relay module.

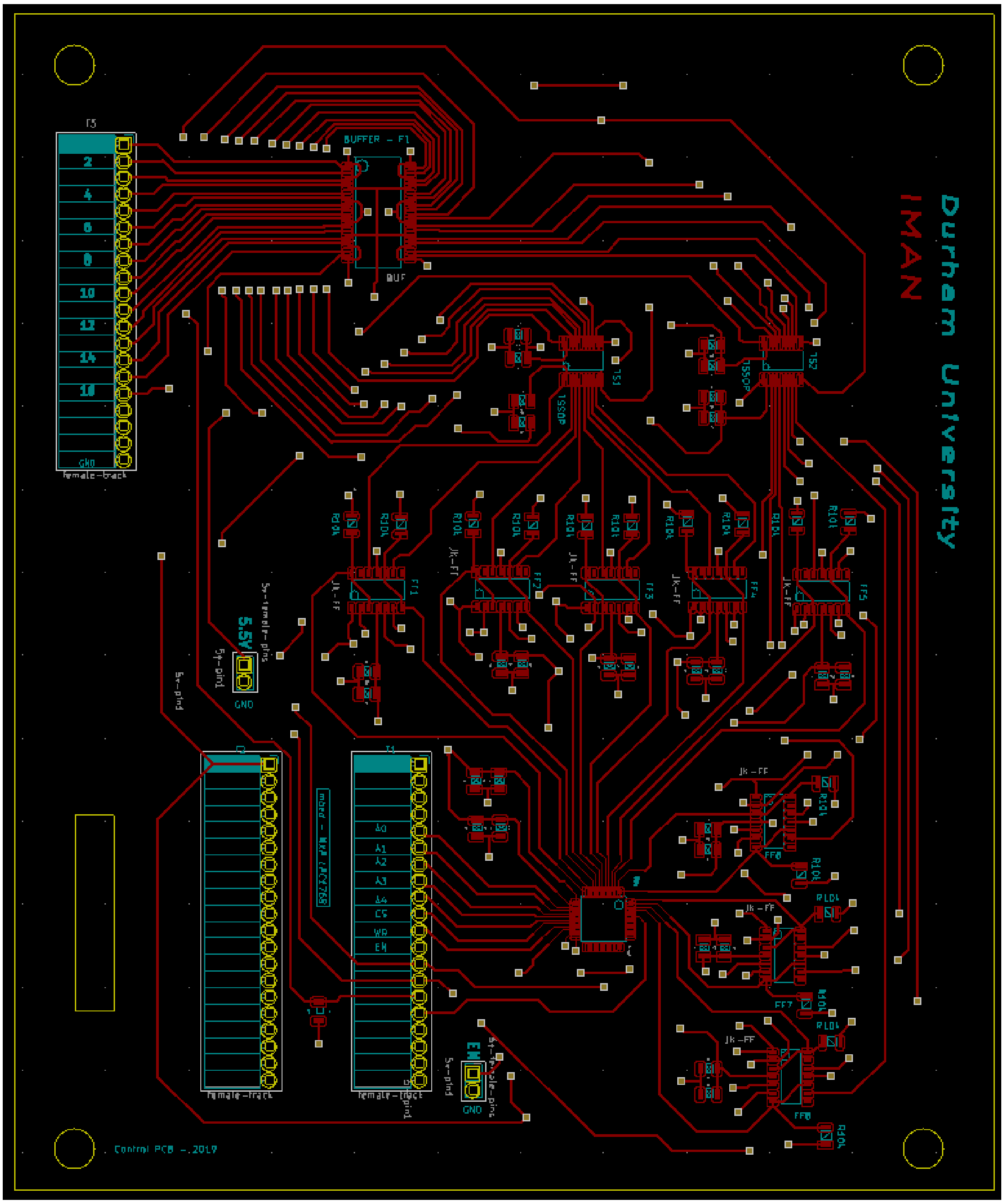

Figure 91 PCB design for the control system (front cover).

Figure 92 PCB design for the control system (back cover).

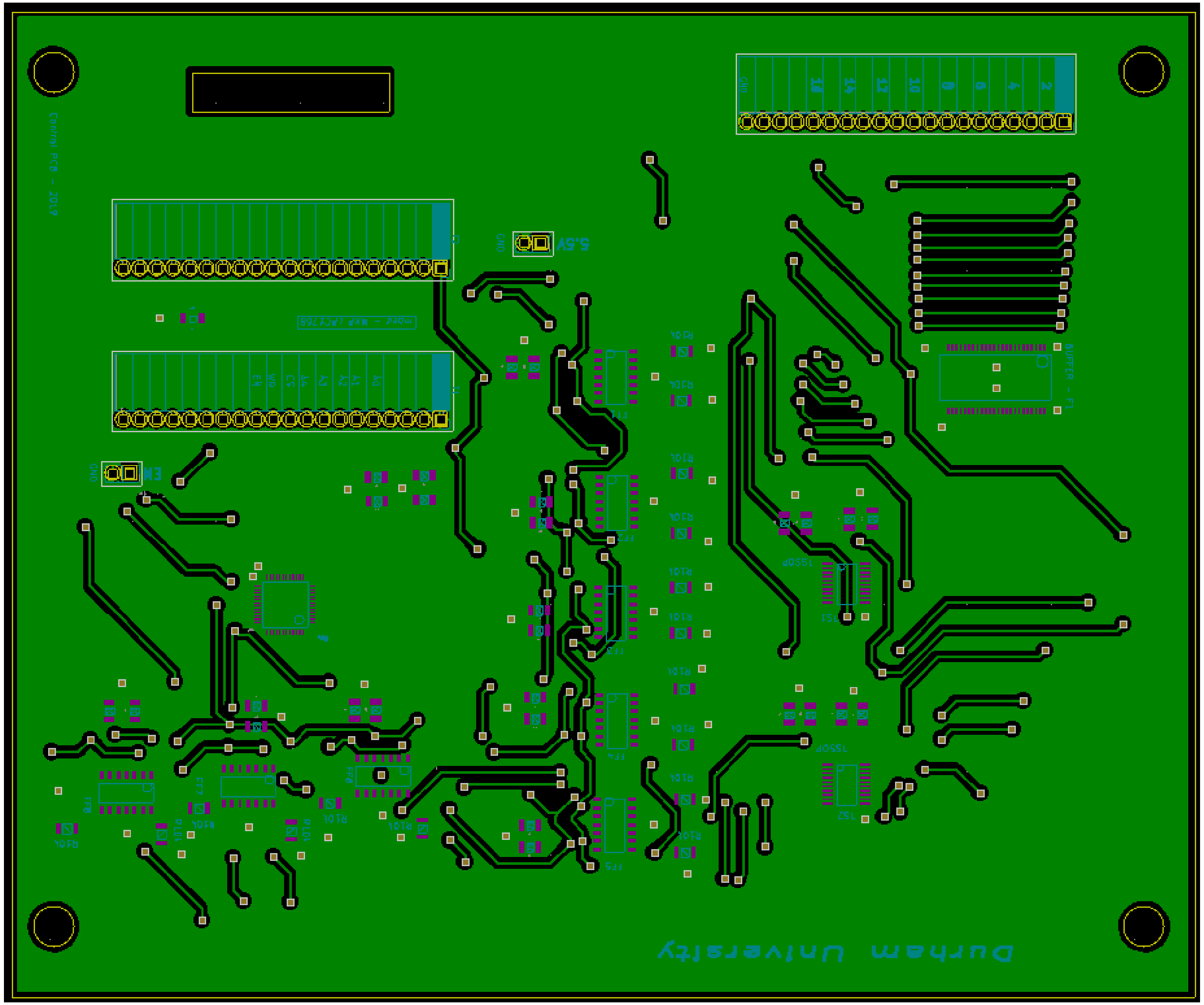

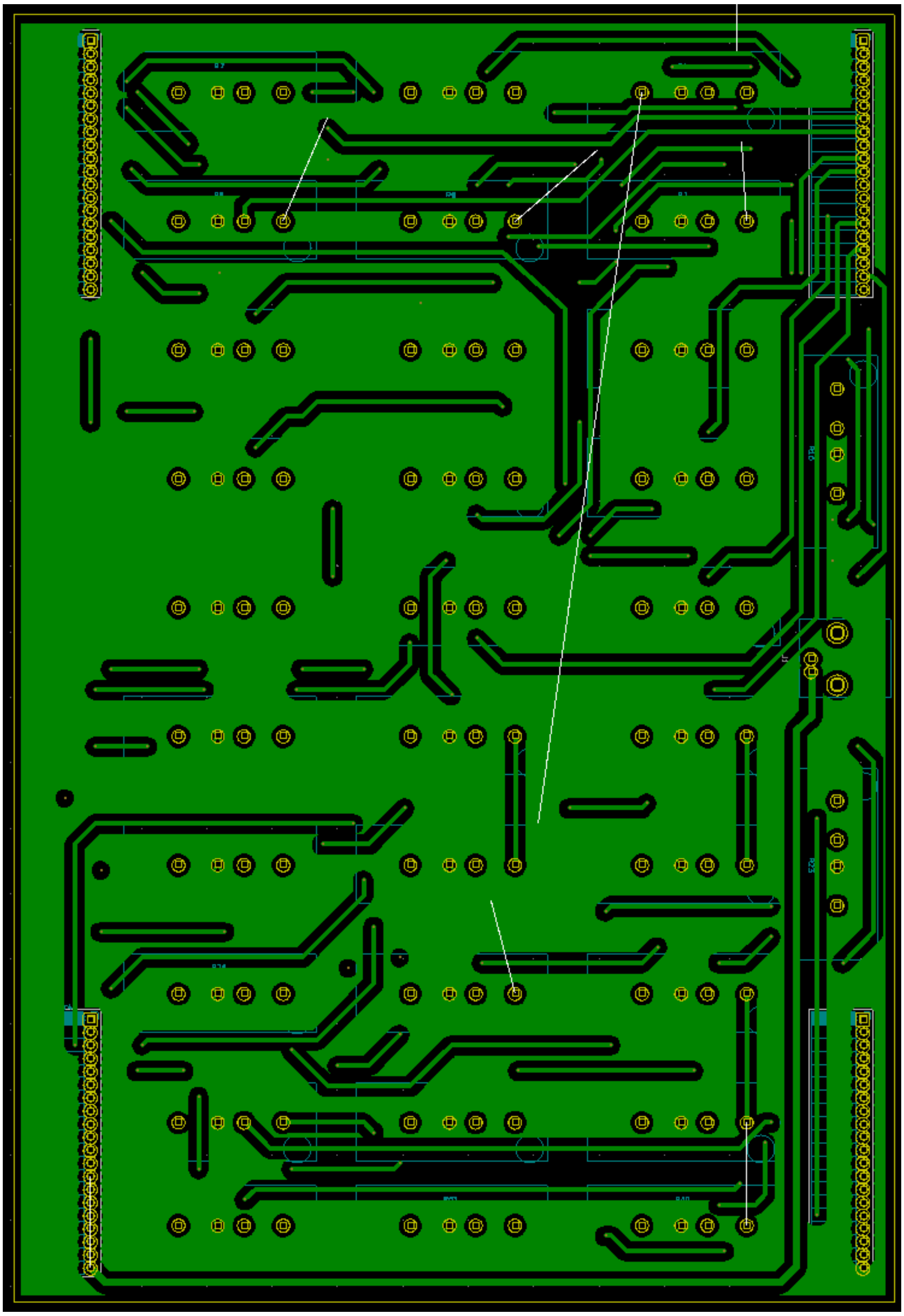

Figure 93 PCB design for the relay module (back cover).

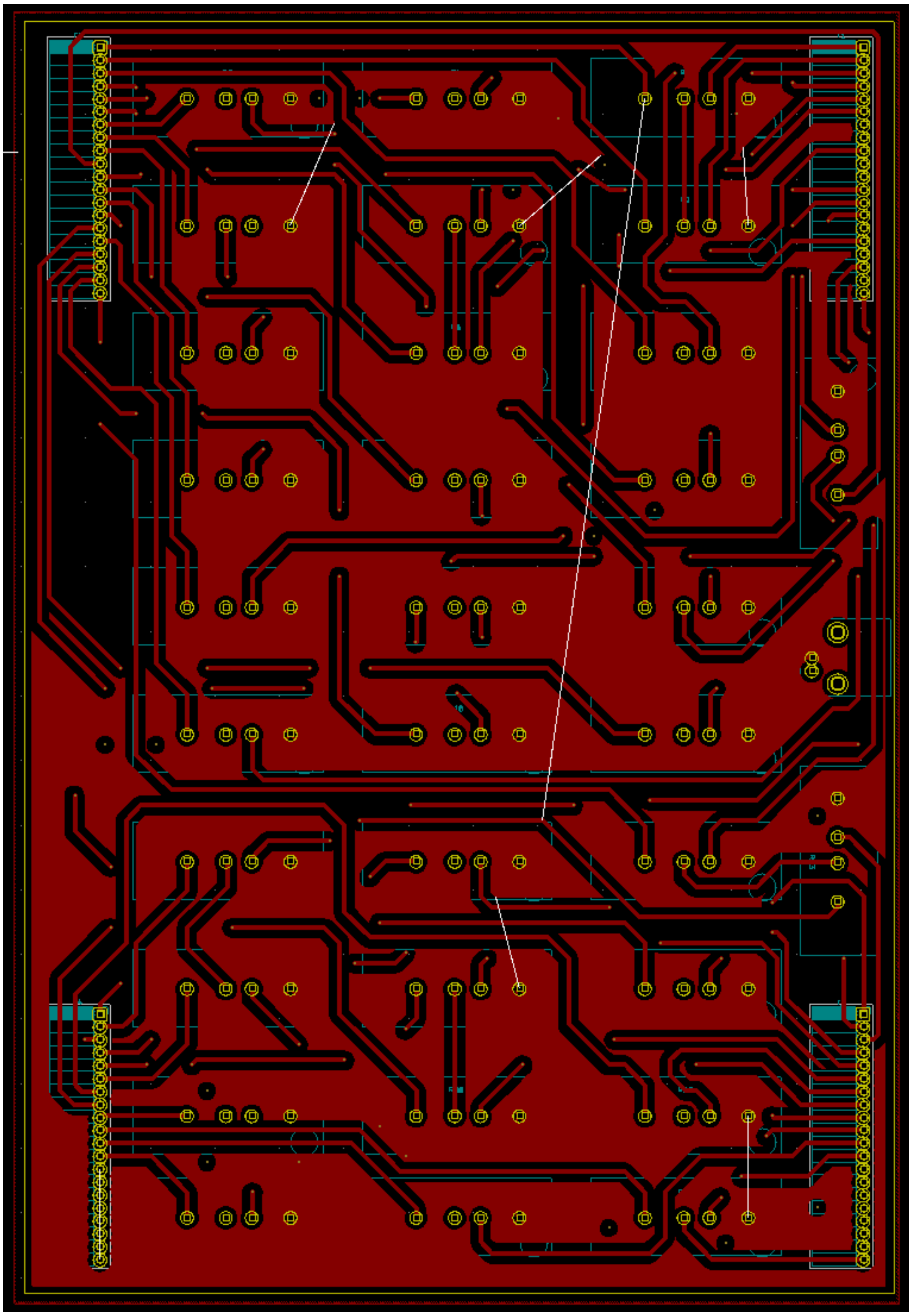

Figure 94 PCB design for the relay module (front cover).

Appendix B Algorithms and Computer codes

B.1 Mbed - C programming code

Computer code programmed on the Mbed compiler, accessed via the official online Web app. The C programming language shows the iterative switching of the IDEs used for a large-scale actuation of droplet with varying volumes.

```
 #include "mbed.h"

 #define T_DELAY 0.1
DigitalOut led1(LED1);

 // flip flops
DigitalOut JK_res(p14);
DigitalOut JK_clk(p13);

 // mux
DigitalOut MUX_a0(p5);
DigitalOut MUX_a1(p6);
DigitalOut MUX_a2(p7);
DigitalOut MUX_a3(p8);
DigitalOut MUX_a4(p9);
DigitalOut MUX_cs(p10);
DigitalOut MUX_wr(p11);
DigitalOut MUX_en(p12);
DigitalOut MUX_d(p16);
```

```
 // out
DigitalOut OUT_en(p15);
void select_FF(int f) {
    // select FF
    MUX_a0 = f & 0b00000001;
    MUX_a1 = (f & 0b00000010) >> 1;
    MUX_a2 = (f & 0b00000100) >> 2;
    MUX_a3 = (f & 0b00001000) >> 3;
    MUX_a4 = (f & 0b00010000) >> 4;
}
void clock_FF() {
    // do one clock cycle
    JK_clk = 1;
    wait(0.01);
    JK_clk = 0;
    wait(0.01);
}
int main() {
        uint8_t i, j;
    // disable outputs
    OUT_en = 0;
    // reset FFs
    JK_res = 0;
    wait(0.1);
    JK_res = 1;
    // enable mux
    MUX_cs = 0;
    MUX_en = 0;
    MUX_wr = 0; //unlatched
 // enable outputs
    OUT_en = 1;
    wait(0.1);
        // set toggle to 1
    MUX_d = 1;
    while(1) {
                // iteration #1
              if(led1==0)
            led1 = 1;
        else
```

```
            led1 = 0;
                // reset FFs
        JK_res = 0;
        wait(0.1);
        JK_res = 1;
        wait(0.1);

                // ----- 0 - 1 - 0 - 2 - 1 - 0 - 2 - 1 - 0 - 2
- 1 - 0 - 2
                for(i=0;i<30;i=i+3) {
            select_FF(i);
            clock_FF();
        }
        wait(T_DELAY);
                for(j=0;j<3;j++){
            for(i=1;i<30;i=i+3) {
                select_FF(i);
                clock_FF();
            }
            wait(T_DELAY);
            for(i=0;i<30;i=i+3) {
                select_FF(i);
                clock_FF();
            }
            wait(T_DELAY);
            for(i=2;i<30;i=i+3) {
                select_FF(i);
                clock_FF();
            }
            wait(T_DELAY);
        }
                // iteration #2

        if(led1==0)
            led1 = 1;
        else
            led1 = 0;
        // reset FFs
        JK_res = 0;
```

```
wait(0.1);
JK_res = 1;
wait(0.1);

        // ----- 01 - 23 - 01 - 45 - 23 ....
        for(i=0;i<29;i=i+3) {
    select_FF(i);
    clock_FF();
    select_FF(i+1);
    clock_FF();
}
wait(T_DELAY);
        for(j=0;j<3;j++){
    for(i=2;i<29;i=i+6) {
        select_FF(i);
        clock_FF();
        select_FF(i+1);
        clock_FF();
    }
    wait(T_DELAY);
                            for(i=0;i<29;i=i+3) {
        select_FF(i);
        clock_FF();
        select_FF(i+1);
        clock_FF();
    }
    wait(T_DELAY);
                for(i=4;i<29;i=i+3) {
        select_FF(i);
        clock_FF();
        select_FF(i+1);
        clock_FF();
    }
    wait(T_DELAY);
}
                // iteration #3
        if(led1==0)
    led1 = 1;
else
```

```
    led1 = 0;
// reset FFs
JK_res = 0;
wait(0.1);
JK_res = 1;
wait(0.1);

        // ----- 012 - 345 - 012 - 678 - 345 ....
       for(i=0;i<28;i=i+3) {
    select_FF(i);
    clock_FF();
    select_FF(i+1);
    clock_FF();
    select_FF(i+2);
    clock_FF();
}
wait(T_DELAY);
       for(j=0;j<3;j++){
    for(i=3;i<28;i=i+3) {
        select_FF(i);
        clock_FF();
        select_FF(i+1);
        clock_FF();
        select_FF(i+2);
        clock_FF();
    }
    wait(T_DELAY);
                for(i=0;i<28;i=i+3) {
        select_FF(i);
        clock_FF();
        select_FF(i+1);
        clock_FF();
        select_FF(i+2);
        clock_FF();
    }
    wait(T_DELAY);
                for(i=6;i<28;i=i+3) {
        select_FF(i);
        clock_FF();
```

```
                select_FF(i+1);
                clock_FF();
                select_FF(i+2);
                clock_FF();
            }
            wait(T_DELAY);
        }
                        // iteration #4
                if(led1==0)
            led1 = 1;
        else
            led1 = 0;
                      // reset FFs
        JK_res = 0;
        wait(0.1);
        JK_res = 1;
        wait(0.1);

                // ----- 01234 - 56789 - 01234 -
10,11,12,13,14 ....
        for(i=0;i<26;i=i+5) {
            select_FF(i);
            clock_FF();
            select_FF(i+1);
            clock_FF();
            select_FF(i+2);
            clock_FF();
            select_FF(i+3);
            clock_FF();
            select_FF(i+4);
            clock_FF();
        }
        wait(T_DELAY);
                for(j=0;j<3;j++){
            for(i=5;i<26;i=i+5) {
                select_FF(i);
                clock_FF();
                select_FF(i+1);
                clock_FF();
```

```
                select_FF(i+2);
                clock_FF();
            }
            wait(T_DELAY);
            for(i=0;i<26;i=i+5) {
                select_FF(i);
                clock_FF();
                select_FF(i+1);
                clock_FF();
                select_FF(i+2);
                clock_FF();
            }
            wait(T_DELAY);
            for(i=10;i<26;i=i+5) {
                select_FF(i);
                clock_FF();
                select_FF(i+1);
                clock_FF();
                select_FF(i+2);
                clock_FF();
            }
            wait(T_DELAY);
        }
// -----------------
    } // while
} // main
```

B.2 MATLAB – RC network model

This section shows MATLAB codes for solving the equivalent RC circuit network models to calculate the capacitance in the dielectric layer, capacitance in the liquid, and the liquid conductance. The critical signal frequency, electrostatic energy, and the electrostatic force was calculated.

```
clc
clear all

 % Finding x1 & x2 (depending on the p', also known as x')
 % Finding Area(Ax)
 % Finding Cd Cw Gw

  %% Independent Variables
Length = 5000e-6; % Length of electrode
D = 100e-6; % Half of Dmax

y1 = 10e-6; % Distance Y1 (Half of Dmin for half of the
design) - Fixed
R = 1500e-6; % Droplet radius

  %% Dependent Variables
L = Length - R; % Liquid-electrode interface Length - droplet
radius
d = D + y1; % Distance from the centre half of the electrode
to base line
y2 = d - 10e-6; % Distance Y2
l = 2*R; % Liquid length
p = linspace(R,L,100); % Distance x'

  %% Finding x1 and x2 @ varying d - VIDEs
x1 = p - sqrt((R^2) - (d^2)); % Distance @ x1
x2 = p + sqrt((R^2) - (d^2)); % Distance @ x2

  %% Find the area - VIDEs
```

```
Ax = (y1 - y2)*(x2.^2-x1.^2)/(2*L) + (d-y1).*(x2 - x1); % Area
of the strip

  %% -------------- Calculate Cd Cw Gw
  %% Variables
e0 = 8.85418782 * 10^-12; % Permittivity of free space
er = 3.2; % Permittivity of SU-8
DE = 0.5E-6; % SU-8 thickness

ew = 80; % Permittivity of water
T = 20e-6; % Conductivity of water (microsiemens per meter)

w0 =10e3; % Signal frequency
V = 70; % Applied voltage

  %% Find Cd
Cd = (e0*er*Ax)/DE; % Capacitance using two fingers

  %% Finding Gw
w = (y1-y2).*p/L + d-y1; % Electrode width - VIDEs
s = 2*(d-w); % Electrode gap - VIDEs

k = s./(s+(2.*w));
K = ellipke(k); % Elliptic integral of the first kind

Gw = (T*(K.*(1-k.^2))*l)./(2*K.*k.^2); % Conductance of liquid

  %% Find Cw
Cw = (e0*ew/T)*Gw; % Liquid capacitance


  %% Find critical frequency, electrostatic energy, and force
fidx = 1;

for w0=linspace(100,500e3,1000)


    %% Voltage across Cw
    Rw=1./Gw; % Resistance Rw
```

```
    Vw = V*Rw.*Cd/2*1i*w0./(1i*w0*Rw.*(Cd/2+Cw)+1); % Voltage
across liquid

    %% Voltage across Cd
    Vd = (V - Vw); % Voltage across insulator

    %% Energy
    E = ((Cd.*abs(Vd).^2)/4) + ((Cw.*abs(Vw).^2)/2); %
Electrostatic energy

    %% Critical Frequency
    Fc = (Gw./ ((2 * pi)*(((Cd)/2) + (Cw)))); % Natural
frequency

    %% Numerical value for force - VIDEs
    dEdp = - diff(E)./diff(p); % Total electric force for a
pair of strips


    %% end
    freq0(fidx) = w0/(2*pi);
    force(fidx) = max(dEdp); % Can also use max(E) to find the
maximum electrostatic energy
    fidx = fidx+1;
end

plot(freq0/1000,force*1e6) % Plotting the generated force
between a pair of strips


  %% End
disp("done")
```

B.3 RC network model

This section shows the calculations for the electrical impedance (Z) in the RC circuit network model, as depicted in Figure 96 to derive a term that defines the voltage drop across the liquid (V_w), and dielectric layer (V_D).

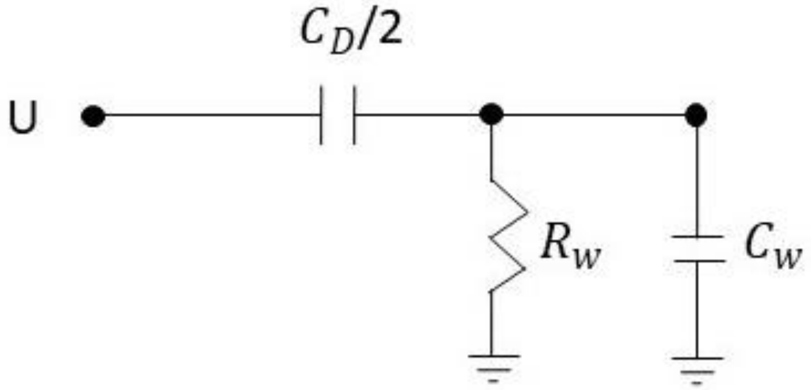

Figure 95 The schematic diagram showing the RC network circuit model of a droplet situated on a pair of electrodes (VIDEs) covered with an insulating layer.

$$V_W = \frac{Z_w}{Z_w + \frac{1}{i\omega C_D/2}} U$$

$$Z_W = \frac{R_w}{1 + i\omega R_w C_w}$$

$$V_W = \frac{\frac{R_w}{1+i\omega R_w C_w}}{\frac{R_w}{1+i\omega R_w C_w} + \frac{1}{i\omega(C_D/2)}} U$$

$$V_W = \frac{\frac{R_w}{1+i\omega R_w C_w}}{\frac{i\omega R_w(C_D/2) + 1 + i\omega R_w C_w}{i\omega(C_D/2)(1+i\omega R_w C_w)}} U$$

$$V_W = \frac{\frac{R_w}{1+i\omega R_w C_w}}{\frac{1 + i\omega R_w(C_D/2) + i\omega R_w C_w}{i\omega(C_D/2)(1+i\omega R_w C_w)}} U$$

$$V_W = \frac{i\omega(C_D/2)R_w}{1 + i\omega R_w(C_D/2) + i\omega R_w C_w} U$$

$$|V_W|^2 = \frac{\omega^2(C_D/2)^2 {R_w}^2}{1 + \omega^2 {R_w}^2 (C_D/2 + C_w)^2} |U|^2$$

$$|V_D|^2 \ = |U - V_W|^2$$

$$|V_D|^2 = \left|1 - \frac{i\omega(C_D/2)R_w}{1 + i\omega R_w(C_D/2 + C_w)}\right|^2 |U|^2$$

$$|V_D|^2 = \frac{1 + \omega^2 {C_w}^2 {R_w}^2}{1 + \omega^2 {R_w}^2 (C_D/2 + C_w)^2} |U|^2$$

Energy in C_w (w_w) and C_D (w_D):

$$w_w = \frac{1}{2}|V_W|^2 C_w$$

$$w_D = \frac{1}{4}|V_D|^2 C_D$$

References

1. Apple unveils new iPad Pro with breakthrough LiDAR Scanner and brings trackpad support to iPadOS. https://www.apple.com/uk/newsroom/2020/03/apple-unveils-new-ipad-pro-with-lidar-scanner-and-trackpad-support-in-ipados/ (accessed 2021).

2. datsvs White Jaguar XF 2 Car. https://purepng.com/photo/4884/transportation-cars-white-jaguar-xf-2-car (accessed 2021).

3. Morgan, H.; Green, N. G., *AC electrokinetics colloids and nanoparticles*. Research Studies Press ; Institute of Physics Pub. ; Distribution, North America, AIDC: Baldock, Hertfordshire, England; Philadelphia, Pa.; Williston, VT, 2003.

4. Jones, T. B.; Gunji, M.; Washizu, M.; Feldman, M. J., Dielectrophoretic liquid actuation and nanodroplet formation. *J. Appl. Phys.* **2001,** *89* (2), 1441-1448.

5. Jones, T. B.; Wang, K. L.; Yao, D. J., Frequency-dependent electromechanics of aqueous liquids: electrowetting and dielectrophoresis. *Langmuir* **2004,** *20* (7), 2813-8.

6. Latthe, S. S.; Terashima, C.; Nakata, K.; Fujishima, A., Superhydrophobic Surfaces Developed by Mimicking Hierarchical Surface Morphology of Lotus Leaf. *Mol.* **2014,** *19* (4), 4256-4283.

7. Percenta Lotus effect. https://percenta-nanoproducts.com/lotus-effect/ (accessed 2021).

8. Prestigia Sensor and camera cleaning. https://www.ficosa.com/products/underhood/sensor-and-camera-cleaning/ (accessed 2021).

9. Anderson, M. Window-cleaning device. US16212503A, 1903.

10. Berge, B., Electrocapilarity and wetting of insulator film by water. *C.R Acad. Sci. Paris Ser II.* **1993,** *317*, 157-163.

11. Kim, J.-H.; Lee, J.-H.; Mirzaei, A.; Kim, H. W.; Tan, B. T.; Wu, P.; Kim, S. S., Electrowetting-on-dielectric characteristics of ZnO nanorods. *Sci. Rep.* **2020,** *10* (1), 14194.

12. Liu, H.; Dharmatilleke, S.; Maurya, D. K.; Tay, A. A. O., Dielectric materials for electrowetting-on-dielectric actuation. *Microsyst. Technol.* **2009,** *16* (3), 449.

13. Batchelder, J. S., Dielectrophoretic manipulator. *Rev. Sci. Instrum.* **1983,** *54* (3), 300-302.

14. Hernandez, W. C. Surface to move a fluid via fringe electric fields. US20120211109A1, 2012.

15. Xi, H.-D.; Zheng, H.; Guo, W.; Gañán-Calvo, A. M.; Ai, Y.; Tsao, C.-W.; Zhou, J.; Li, W.; Huang, Y.; Nguyen, N.-T.; Tan, S. H., Active droplet sorting in microfluidics: a review. *Lab Chip* **2017,** *17* (5), 751-771.

16. Teh, S.-Y.; Lin, R.; Hung, L.-H.; Lee, A. P., Droplet microfluidics. *Lab Chip* **2008,** *8* (2), 198-220.

17. Sung Kwon, C.; Hyejin, M.; Chang-Jin, K., Creating, transporting, cutting, and merging liquid droplets by electrowetting-based actuation for digital microfluidic circuits. *J Microelectromech Syst* **2003,** *12* (1), 70-80.

18. Wheeler, A. R., Putting Electrowetting to Work. *Sci* **2008,** *322* (5901), 539.

19. Samiei, E.; Tabrizian, M.; Hoorfar, M., A review of digital microfluidics as portable platforms for lab-on a-chip applications. *Lab Chip* **2016,** *16* (13), 2376-2396.

20. Borcia, R.; Borcia, I. D.; Bestehorn, M., Can Vibrations Control Drop Motion? *Langmuir* **2014,** *30* (47), 14113-14117.

21. Lee, C.-E.; Kim, H.-K., Analysis of the Cross-Sectional Shape and Wiping Angle of a Wiper Blade. *SAE International Journal of Materials and Manufacturing* **2020,** *13* (2), 183-194.

22. Chen, Z.; Gu, Z.; Jiang, T., Research on transient aerodynamic characteristics of windshield wipers of vehicles. *INT J NUMER METHOD H* **2019,** *29* (8), 2870-2884.

23. Baudoin, M.; Brunet, P.; Matar, O. B.; Herth, E., Low power sessile droplets actuation via modulated surface acoustic waves. *Appl. Phys. Lett.* **2012,** *100* (15), 154102.

24. Mark, D.; Haeberle, S.; Roth, G.; von Stetten, F.; Zengerle, R., Microfluidic lab-on-a-chip platforms: requirements, characteristics and applications. *Chem. Soc. Rev.* **2010,** *39* (3), 1153-1182.

25. Watson, L. Is it time to wave goodbye to windscreen wipers? McLaren confirms it's developing new system to improve visibility in bad weather that's adapted from fighter jets. https://www.dailymail.co.uk/sciencetech/article-2524001/McLaren-confirms-developing-new-wiper-free-windscreens.html (accessed 2020).

26. Zhang, S. P.; Lata, J.; Chen, C.; Mai, J.; Guo, F.; Tian, Z.; Ren, L.; Mao, Z.; Huang, P.-H.; Li, P.; Yang, S.; Huang, T. J., Digital acoustofluidics enables contactless and programmable liquid handling. *Nat. Commun.* **2018,** *9* (1), 2928.

27. Yeo, L. Y.; Friend, J. R., Surface Acoustic Wave Microfluidics. *Annu. Rev. Fluid Mech.* **2014,** *46* (1), 379-406.

28. Yang, D.; Haworth, L.; Agrawal, P.; Tao, R.; McHale, G.; Torun, H.; Martin, J.; Luo, J.; Hou, X.; Fu, Y., Dynamic Mitigation Mechanisms of Rime Icing with Propagating Surface Acoustic Waves. *Langmuir* **2022**.

29. Shyam, S.; Asfer, M.; Mehta, B.; Mondal, P. K.; Almutairi, Z. A., Magnetic field driven actuation of sessile ferrofluid droplets in the presence of a time dependent magnetic field. *Colloids Surf. A Physicochem. Eng. Asp.* **2020,** *586*, 124116.

30. Fan, X.; Dong, X.; Karacakol, A. C.; Xie, H.; Sitti, M., Reconfigurable multifunctional ferrofluid droplet robots. *Proc. Natl. Acad. Sci.* **2020,** *117* (45), 27916-27926.

31. Khan, A.; Qian-PingLi; Xiao-DongNiu; Yu-QiaoWang; Ming-FuWen; De-CaiLi; HiroshiYamaguchi; JuanLi, Magnetic field based actuation and amalgamation of ferrofluid droplets on hydrophobic surface: An experimental and numerical study. *Phys. Fluids* **2020,** *32* (11), 112108.

32. Ikezoe, Y.; Hirota, N.; Nakagawa, J.; Kitazawa, K., Making water levitate. *Nature* **1998,** *393* (6687), 749-750.

33. Laumann, D., Even Liquids Are Magnetic: Observation of the Moses Effect and the Inverse Moses Effect. *Phys. Teach.* **2018,** *56* (6), 352-354.

34. Katsikis, G.; Breant, A.; Rinberg, A.; Prakash, M., Synchronous magnetic control of water droplets in bulk ferrofluid. *Soft Matter* **2018,** *14* (5), 681-692.

35. Yan, Z.; Jin, M.; Li, Z.; Zhou, G.; Shui, L., Droplet-Based Microfluidic Thermal Management Methods for High Performance Electronic Devices. *Micromachines (Basel)* **2019,** *10* (2), 89.

36. Zhang, K.; Ren, Y.; Tao, Y.; Deng, X.; Liu, W.; Jiang, T.; Jiang, H., Efficient particle and droplet manipulation utilizing the combined thermal buoyancy convection and temperature-enhanced rotating induced-charge electroosmotic flow. *Anal. Chim. Acta* **2020,** *1096*, 108-119.

37. Wang, Z.; Chen, R.; Zhu, X.; Liao, Q.; Ye, D.; Zhang, B.; He, X.; Li, W., Control of the droplet generation by an infrared laser. *AIP Adv.* **2018,** *8* (1), 015302.

38. Dodd, L. E.; Wood, D.; Geraldi, N. R.; Wells, G. G.; McHale, G.; Xu, B. B.; Stuart-Cole, S.; Martin, J.; Newton, M. I., Low Friction Droplet Transportation on a Substrate with a Selective Leidenfrost Effect. *ACS Appl Mater Interfaces* **2016,** *8* (34), 22658-63.

39. DAVIES, A. Tesla Has Found a Use for Lasers—Cleaning Glass. https://www.wired.com/story/tesla-use-lasers-clean-glass/ (accessed 2020).

40. Jones, T. B., On the Relationship of Dielectrophoresis and Electrowetting. *Langmuir* **2002,** *18* (11), 4437-4443.

41. Teng, P.; Tian, D.; Fu, H.; Wang, S., Recent progress of electrowetting for droplet manipulation: from wetting to superwetting systems. *Mater. Chem. Front.* **2020,** *4* (1), 140-154.

42. Mohammed, M.; Babadagli, T., Wettability alteration: A comprehensive review of materials/methods and testing the selected ones on heavy-oil containing oil-wet systems. *Adv. Colloid Interface Sci.* **2015,** *220*, 54-77.

43. Dey, T.; Naughton, D., Cleaning and anti-reflective (AR) hydrophobic coating of glass surface: a review from materials science perspective. *J Solgel Sci Technol* **2016,** *77* (1), 1-27.

44. Li, S.; Huang, J.; Chen, Z.; Chen, G.; Lai, Y., A review on special wettability textiles: theoretical models, fabrication technologies and multifunctional applications. *J. Mater. Chem.* **2017,** *5* (1), 31-55.

45. Good, R. J., Contact angle, wetting, and adhesion: a critical review. *J Adhes Sci Technol* **1992,** *6* (12), 1269-1302.

46. Vazirinasab, E.; Jafari, R.; Momen, G., Application of superhydrophobic coatings as a corrosion barrier: A review. *Surf. Coat. Technol* **2018,** *341*, 40-56.

47. Frankiewicz, C.; Attinger, D., Texture and wettability of metallic lotus leaves. *Nanoscale* **2016,** *8* (7), 3982-3990.

48. Otitoju, T. A.; Ahmad, A. L.; Ooi, B. S., Superhydrophilic (superwetting) surfaces: A review on fabrication and application. *J Ind Eng Chem* **2017,** *47*, 19-40.

49. Kaplan, W. D.; Chatain, D.; Wynblatt, P.; Carter, W. C., A review of wetting versus adsorption, complexions, and related phenomena: the rosetta stone of wetting. *J. Mater. Sci.* **2013,** *48* (17), 5681-5717.

50. Seo, K.; Kim, M.; Kim, D. H., Re-derivation of Young's Equation, Wenzel Equation, and Cassie-Baxter Equation Based on Energy Minimization. In *Surface Energy*, 2015.

51. He, B.; Yang, S.; Qin, Z.; Wen, B.; Zhang, C., The roles of wettability and surface tension in droplet formation during inkjet printing. *Sci. Rep.* **2017,** *7* (1), 11841.

52. Mugele, F.; Baret, J.-C., Electrowetting: from basics to applications. *J. Phys. Condens. Matter* **2005,** *17* (28), R705-R774.

53. Byun, D.; Hong, J.; Saputra; Ko, J. H.; Lee, Y. J.; Park, H. C.; Byun, B.-K.; Lukes, J. R., Wetting Characteristics of Insect Wing Surfaces. *J. Bionic Eng.* **2009,** *6* (1), 63-70.

54. Abraham, M.; Claudio, D. V.; Stefano, S.; Alidad, A.; W., D. J., Contact angles and wettability: towards common and accurate terminology. *Surf. Innov.* **2017,** *5* (1), 3-8.

55. Eral, H. B.; ’t Mannetje, D. J. C. M.; Oh, J. M., Contact angle hysteresis: a review of fundamentals and applications. *Colloid Polym Sci* **2013,** *291* (2), 247-260.

56. Ghannam, H.; Chahboun, A.; Turmine, M., Wettability of zinc oxide nanorod surfaces. *RSC Adv.* **2019,** *9* (65), 38289-38297.

57. Kuan, W.-F.; Chen, L.-J., The preparation of superhydrophobic surfaces of hierarchical silicon nanowire structures. *Nanotechnology* **2008,** *20* (3), 035605.

58. Wang, J.; Wu, Y.; Cao, Y.; Li, G.; Liao, Y., Influence of surface roughness on contact angle hysteresis and spreading work. *Colloid Polym Sci* **2020,** *298* (8), 1107-1112.

59. Erbil, H. Y.; Cansoy, C. E., Range of Applicability of the Wenzel and Cassie−Baxter Equations for Superhydrophobic Surfaces. *Langmuir* **2009,** *25* (24), 14135-14145.

60. Bell, M. S.; Borhan, A., A Volume-Corrected Wenzel Model. *ACS Omega* **2020,** *5* (15), 8875-8884.

61. Tran, H.-H.; Kim, Y.; Ternon, C.; Langlet, M.; Riassetto, D.; Lee, D., Lubricant Depletion-Resistant Slippery Liquid-Infused Porous Surfaces via Capillary Rise Lubrication of Nanowire Array. *Adv. Mater. Interfaces* **2021,** *8* (7), 2002058.

62. Torabi, S.; Li, L.; Grabau, J.; Sands, M.; Berron, B. J.; Xu, R.; Trinkle, C. A., Cassie-Baxter Surfaces for Reversible, Barrier-Free Integration of Microfluidics and 3D Cell Culture. *Langmuir : the ACS journal of surfaces and colloids* **2019,** *35* (32), 10299-10308.

63. Kota, A. K.; Kwon, G.; Tuteja, A., The design and applications of superomniphobic surfaces. *NPG Asia Mater.* **2014,** *6* (7), e109-e109.

64. Simpson, J. T.; Hunter, S. R.; Aytug, T., Superhydrophobic materials and coatings: a review. *Rep. Prog. Phys* **2015,** *78* (8), 086501.

65. Liu, C.; Zhan, H.; Yu, J.; Liu, R.; Zhang, Q.; Liu, Y.; Li, X., Design of superhydrophobic pillars with robustness. *Surf. Coat. Technol* **2019,** *361*, 342-348.

66. Erbil, H. Y., Practical Applications of Superhydrophobic Materials and Coatings: Problems and Perspectives. *Langmuir* **2020,** *36* (10), 2493-2509.

67. Akamatsu, Y.; Makita, K.; Inaba, H.; Minami, T., Water-repellent coating films on glass prepared from hydrolysis and polycondensation reactions of fluoroalkyltrialkoxylsilane. *Thin Solid Films* **2001,** *389* (1), 138-145.

68. Zhao, B.; MacMinn, C. W.; Juanes, R., Wettability control on multiphase flow in patterned microfluidics. *Proc. Natl. Acad. Sci.* **2016**, 201603387.

69. Liu, C.; Sun, J.; Li, J.; Xiang, C.; Che, L.; Wang, Z.; Zhou, X., Long-range spontaneous droplet self-propulsion on wettability gradient surfaces. *Sci. Rep.* **2017,** *7* (1), 7552.

70. Sadullah, M. S.; Launay, G.; Parle, J.; Ledesma-Aguilar, R.; Gizaw, Y.; McHale, G.; Wells, G. G.; Kusumaatmaja, H., Bidirectional motion of droplets on gradient liquid infused surfaces. *Commun. Phys.* **2020,** *3* (1), 166.

71. Hooda, A.; Goyat, M. S.; Pandey, J. K.; Kumar, A.; Gupta, R., A review on fundamentals, constraints and fabrication techniques of superhydrophobic coatings. *Prog. Org. Coat.* **2020,** *142*, 105557.

72. Bayer, I. S., Superhydrophobic Coatings from Ecofriendly Materials and Processes: A Review. *Adv. Mater. Interfaces* **2020,** *7* (13), 2000095.

73. Li, J.; Zhou, X.; Li, J.; Che, L.; Yao, J.; McHale, G.; Chaudhury, M. K.; Wang, Z., Topological liquid diode. *Sci. Adv.* **2017,** *3* (10), eaao3530.

74. Li, J.; Kim, C.-J. C., Current commercialization status of electrowetting-on-dielectric (EWOD) digital microfluidics. *Lab Chip* **2020,** *20* (10), 1705-1712.

75. Wheeler, A. R., Putting Electrowetting to Work. *Science* **2008,** *322* (5901), 539-540.

76. Edwards, A. M. J.; Brown, C. V.; Newton, M. I.; McHale, G., Dielectrowetting: The past, present and future. *Curr. Opin. Colloid Interface Sci.* **2018,** *36*, 28-36.

77. Jones, T. B., Liquid dielectrophoresis on the microscale. *J. Electrost.* **2001,** *51-52*, 290-299.

78. Garcí-Sánchez, P.; Mugele, F., Fundamentals of Electrowetting and Applications in Microsystems. In *Electrokinetics and Electrohydrodynamics in Microsystems*, Ramos, A., Ed. Springer Vienna: Vienna, 2011; pp 85-125.

79. Jones, T. B.; Fowler, J. D.; Chang, Y. S.; Kim, C.-J., Frequency-Based Relationship of Electrowetting and Dielectrophoretic Liquid Microactuation. *Langmuir* **2003,** *19* (18), 7646-7651.

80. Castle, G. S. P., Industrial applications of electrostatics:: the past, present and future. *J Electrostat* **2001,** *51-52*, 1-7.

81. Kim, J.-H.; Lee, J.-H.; Kim, J.-Y.; Mirzaei, A.; Wu, P.; Kim, H. W.; Kim, S. S., Electrowetting on dielectric (EWOD) properties of Teflon-coated electrosprayed silica layers in air and oil media and the influence of electric leakage. *J. Mater. Chem. C* **2018,** *6* (25), 6808-6815.

82. Dhindsa, M.; Heikenfeld, J.; Weekamp, W.; Kuiper, S., Electrowetting without Electrolysis on Self-Healing Dielectrics. *Langmuir* **2011,** *27* (9), 5665-5670.

83. Cooney, C. G.; Chen, C.-Y.; Emerling, M. R.; Nadim, A.; Sterling, J. D., Electrowetting droplet microfluidics on a single planar surface. *Microfluid. Nanofluidics* **2006,** *2* (5), 435-446.

84. Ma, H.; Hu, S.; Jie, Y.; Jin, K.; Su, Y., A floating top-electrode electrowetting-on-dielectric system. *RSC Adv* **2020,** *10* (9), 4899-4906.

85. Wang, Y.; Zhao, Y.-P., Electrowetting on curved surfaces. *Soft Matter* **2012,** *8* (9), 2599-2606.

86. Fiorini, G. S.; Chiu, D. T., Disposable microfluidic devices: fabrication, function, and application. *BioTechniques* **2005,** *38* (3), 429-446.

87. Tan, X. B.; Yang, J.; Zeng, P.; Kim, E. G. R.; Huard, C.; Cheng, M. M. C. In *Electrowetting on flexible, transparent and conducting single-layer graphene*, 2012 EEE Int. Conf. Micro Elec (MEMS), 29 Jan.-2 Feb. 2012; 2012; pp 1037-1040.

88. Zhou, R.; Fu, S.; Jiang, H.; Li, X.; Zhou, G., Thermal accelerated aging study of water/fluoropolymer/ITO contact in electrowetting display systems. *Results Phys.* **2019,** *15*, 102737.

89. Nelson, W. C.; Sen, P.; Kim, C.-J. C. J., Dynamic contact angles and hysteresis under electrowetting-on-dielectric. *Langmuir : the ACS journal of surfaces and colloids* **2011,** *27* (16), 10319-10326.

90. Peykov, V.; Quinn, A.; Ralston, J., Electrowetting: a model for contact-angle saturation. *Colloid Polym. Sci.* **2000,** *278* (8), 789-793.

91. Huh, D.; Tkaczyk, A. H.; Bahng, J. H.; Chang, Y.; Wei, H.-H.; Grotberg, J. B.; Kim, C.-J.; Kurabayashi, K.; Takayama, S., Reversible Switching of High-Speed Air−Liquid Two-Phase Flows Using Electrowetting-Assisted Flow-Pattern Change. *J. Am. Chem. Soc* **2003,** *125* (48), 14678-14679.

92. Beni, G.; Hackwood, S.; Jackel, J. L., Continuous electrowetting effect. *Appl. Phys. Lett.* **1982,** *40* (10), 912-914.

93. Lee, J.; Kim, C.-J., Surface-tension-driven microactuation based on continuous electrowetting. *J Microelectromech Syst* **2000,** *9*, 171-180.

94. Nelson, C. W.; Lynch, C. M.; Crane, N. B., Continuous electrowetting via electrochemical diodes. *Lab chip* **2011,** *11* (13), 2149-2152.

95. Ni, Q.; Capecci, D. E.; Schlafly, M.; Crane, N. B., Robust bidirectional continuous electrowetting based on metal–semiconductor (M–S) diodes. *Microfluid. Nanofluidics* **2016,** *20* (8), 122.

96. Crane, N. B.; Volinsky, A. A.; Mishra, P.; Rajgadkar, A.; Khodayari, M., Bidirectional electrowetting actuation with voltage polarity dependence. *Appl. Phys. Lett.* **2010,** *96* (10), 104103.

97. Yeo, L.; Friend, J., Electrowetting, Applications. In *Encyclopedia of Microfluidics and Nanofluidics*, Li, D., Ed. Springer US: Boston, MA, 2008; pp 606-615.

98. Krupenkin, T.; Taylor, J. A., Reverse electrowetting as a new approach to high-power energy harvesting. *Nat. Commun.* **2011,** *2* (1), 448.

99. Hayes, R. A.; Feenstra, B. J., Video-speed electronic paper based on electrowetting. *Nature* **2003,** *425* (6956), 383-385.

100. Hendriks, B. H. W.; Kuiper, S.; Van As, M. A. J.; Renders, C. A.; Tukker, T. W., Electrowetting-Based Variable-Focus Lens for Miniature Systems. *Optical Review* **2005,** *12* (3), 255-259.

101. Eral, H. B.; de Ruiter, J.; de Ruiter, R.; Oh, J. M.; Semprebon, C.; Brinkmann, M.; Mugele, F., Drops on functional fibers: from barrels to clamshells and back. *Soft Matter* **2011,** *7* (11), 5138-5143.

102. Iman, F.; Michael, C.; Zoltán, R.; Ian, B.; Vibin, A.; David, W.; Gallant, A. J.; Claudio, B., Programmable Droplet Actuating Platform Using Liquid-Dielectrophoresis. *J. Micromech. Microeng* **2021**.

103. Peng, C.; Zhang, Z.; Kim, C.-J. C.; Ju, Y. S., EWOD (electrowetting on dielectric) digital microfluidics powered by finger actuation. *Lab Chip* **2014,** *14* (6), 1117-1122.

104. Geng, H.; Feng, J.; Stabryla, L. M.; Cho, S. K. In *Droplet manipulations by dielectrowetting: Creating, transporting, splitting, and merging*, 2017 Proc. IEEE Int. Conf. Micro Elec (MEMS), 22-26 Jan. 2017; 2017; pp 113-116.

105. Chiang, C.-E.; Huang, H.-Y.; Lin, K.-T.; Alias, A. B.; Lu, P.-J.; Wang, Y.-W.; Wu, T.-H.; Jiang, P.-S.; Chen, C.-A.; Yao, D.-J., A medical innovation: a new and improved method of DNA extraction with electrowetting-on-dielectric of genetic testing in-vitro fertilization (IVF). *Microfluid. Nanofluidics* **2020,** *24* (7), 55.

106. Pollack, M. G.; Pamula, V. K.; Srinivasan, V.; Eckhardt, A. E., Applications of electrowetting-based digital microfluidics in clinical diagnostics. *Expert Rev Mol Diagn* **2011,** *11* (4), 393-407.

107. Jang, L. S.; Lin, G. H.; Lin, Y. L.; Hsu, C. Y.; Kan, W. H.; Chen, C. H., Simulation and experimentation of a microfluidic device based on electrowetting on dielectric. *Biomed. Microdevices* **2007,** *9* (6), 777-86.

108. Dhindsa, M.; Heikenfeld, J.; Kwon, S.; Park, J.; Rack, P. D.; Papautsky, I., Virtual electrowetting channels: electronic liquid transport with continuous channel functionality. *Lab Chip* **2010,** *10* (7), 832-836.

109. Feenstra, B. J.; Hayes, R. A.; Dijk, R. v.; Boom, R. G. H.; Wagemans, M. M. H.; Camps, I. G.; Giraldo, A.; Heijden, B. v. d. In *Electrowetting-Based Displays: Bringing Microfluidics Alive On-Screen*, 19th Proc. IEEE Int. Conf. Micro Elec (MEMS), 22-26 Jan. 2006; 2006; pp 48-53.

110. Feenstra, J., Video-Speed Electrowetting Display Technology. In *Handbook of Visual Display Technology*, Chen, J.; Cranton, W.; Fihn, M., Eds. Springer Berlin Heidelberg: Berlin, Heidelberg, 2012; pp 1731-1745.

111. Kedzierski, J.; Holihan, E., Linear and rotational microhydraulic actuators driven by electrowetting. *Sci. Robot.* **2018,** *3* (22), eaat5643.

112. Han, W. C.; Wang, D. S.; Xiang, L. P.; Wang, Y. D.; Huang, Z. Q.; Li, A. F., A Parametric Study of Microfluidic Power Generator Based on Reverse Electrowetting in a Microchannel Geometry. *Adv Mat Res* **2014,** *986-987*, 1159-1162.

113. Lifton, V. A.; Simon, S.; Frahm, R. E., Reserve battery architecture based on superhydrophobic nanostructured surfaces. *Bell Syst. Tech.* **2005,** *10* (3), 81-85.

114. Murade, C. U.; Oh, J. M.; van den Ende, D.; Mugele, F., Electrowetting driven optical switch and tunable aperture. *Opt. Express* **2011,** *19* (16), 15525-15531.

115. Cheng, W.; Liu, J.; Zheng, Z.; He, X.; Zheng, B.; Zhang, H.; Cui, H.; Zheng, X.; Zheng, T.; Gnade, B. E.; Cheng, J., Adaptive optical beam steering and tuning system based on electrowetting driven fluidic rotor. *Commun. Phys.* **2020,** *3* (1), 25.

116. Quinn, A.; Sedev, R.; Ralston, J., Influence of the Electrical Double Layer in Electrowetting. *J. Phys. Chem. B* . **2003,** *107* (5), 1163-1169.

117. Nili, H.; Green, N. G., AC Electrokinetics of Nanoparticles. In *Encyclopedia of Nanotechnology*, Bhushan, B., Ed. Springer Netherlands: Dordrecht, 2012; pp 18-25.

118. From Electric Double Layer Theory to Lippmann's Electrocapillary Equation. In *Electrowetting*, 2018; pp 113-131.

119. Lu, H. W.; Glasner, K.; Bertozzi, A. L.; Kim, C. J., A diffuse-interface model for electrowetting drops in a Hele-Shaw cell. *J. Fluid Mech.* **2007,** *590*, 411-435.

120. Nelson, W. C.; Kim, C.-J. C., Droplet Actuation by Electrowetting-on-Dielectric (EWOD): A Review. *J. Adhes. Sci. Technol* **2012,** *26* (12-17), 1747-1771.

121. Sondag-Huethorst, J. A. M.; Fokkink, L. G. J., Potential-Dependent Wetting of Electroactive Ferrocene-Terminated Alkanethiolate Monolayers on Gold. *Langmuir* **1994,** *10* (11), 4380-4387.

122. Welters, W. J. J.; Fokkink, L. G. J., Fast Electrically Switchable Capillary Effects. *Langmuir* **1998,** *14* (7), 1535-1538.

123. Mibus, M.; Jensen, C.; Hu, X.; Knospe, C.; Reed, M. L.; Zangari, G., Dielectric breakdown and failure of anodic aluminum oxide films for electrowetting systems. *J. Appl. Phys.* **2013,** *114* (1), 014901.

124. Papathanasiou, A. G.; Boudouvis, A. G., Manifestation of the connection between dielectric breakdown strength and contact angle saturation in electrowetting. *Appl. Phys. Lett.* **2005,** *86* (16), 164102.

125. Jones, T. B.; Perry, M. P.; Melcher, J. R., Dielectric Siphons. *Science* **1971,** *174* (4015), 1232-1233.

126. McHale, G.; Brown, C.; Newton, M.; Wells, G.; Sampara, N., *Developing interface localized liquid dielectrophoresis for optical applications*. SPIE: 2012; Vol. 8557.

127. Cheng, C.-C.; Alex Chang, C.; Andrew Yeh, J., Variable focus dielectric liquid droplet lens. *Opt. Express* **2006,** *14* (9), 4101-4106.

128. McHale, G.; Brown, C. V.; Sampara, N., Voltage-induced spreading and superspreading of liquids. *Nat. Commun.* **2013,** *4* (1), 1605.

129. Brown, C. V.; Wells, G. G.; Newton, M. I.; McHale, G., Voltage-programmable liquid optical interface. *Nat. Photonics* **2009,** *3* (7), 403-405.

130. Pile, D., Programmable liquid optical interfaces. *Nat. Photonics* **2009,** *3* (7), 420-420.

131. Fair, R. B., Digital microfluidics: is a true lab-on-a-chip possible? *Microfluid. Nanofluidics* **2007,** *3* (3), 245-281.

132. Geng, H.; Feng, J.; Stabryla, L. M.; Cho, S. K., Dielectrowetting manipulation for digital microfluidics: creating, transporting, splitting, and merging of droplets. *Lab Chip* **2017,** *17* (6), 1060-1068.

133. Geng, H.; Cho, S. K., Antifouling digital microfluidics using lubricant infused porous film. *Lab Chip* **2019,** *19* (13), 2275-2283.

134. Xu, S.; Ren, H.; Wu, S.-T., Dielectrophoretically tunable optofluidic devices. *J. Phys. D: Appl. Phys* **2013,** *46* (48), 483001.

135. Ren, H.; Xu, S.; Wu, S.-T., Voltage-expandable liquid crystal surface. *Lab Chip* **2011,** *11* (20), 3426-3430.

136. Xu, S.; Ren, H.; Liu, Y.; Wu, S., Color Displays Based on Voltage-Stretchable Liquid Crystal Droplet. *J DISP TECHNOL Journal* **2012,** *8* (6), 336-340.

137. Wells, G. G.; Sampara, N.; Kriezis, E. E.; Fyson, J.; Brown, C. V., Diffraction grating with suppressed zero order fabricated using dielectric forces. *Opt. Lett.* **2011,** *36* (22), 4404-4406.

138. Bikos, D. A.; Mason, T. G., Band-collision gel electrophoresis. *Nat. Commun.* **2019,** *10* (1), 3631.

139. Biscombe, C. J. C., The Discovery of Electrokinetic Phenomena: Setting the Record Straight. *Angew. Chem. Int. Ed.* **2017,** *56* (29), 8338-8340.

140. Jones, T. B., *Electromechanics of Particles*. CAMBRIDGE UNIVERSITY PRESS: 2005.

141. Torkkeli, A. Droplet microfluidics on a planar surface. Thesis (Doctoral) 2003.

142. Aghdaei, S. Electrodynamic droplet actuation for lab on a chip system. Thesis (Doctoral), 2011.

143. Ruiz-Gutiérrez, É.; Edwards, A. M. J.; McHale, G.; Newton, M. I.; Wells, G. G.; Brown, C. V.; Ledesma-Aguilar, R., Lattice Boltzmann Simulations of Multiphase Dielectric Fluids. *Langmuir* **2021,** *37* (24), 7328-7340.

144. Dielectrowetting for Digital Microfluidics: Principle and Application. Int J Adhes Adhes, 2018; pp 253-285.

145. Brown, C. V.; Al-Shabib, W.; Wells, G. G.; McHale, G.; Newton, M. I., Amplitude scaling of a static wrinkle at an oil-air interface created by dielectrophoresis forces. *Appl. Phys. Lett.* **2010,** *97* (24), 242904.

146. Barman, J.; Shao, W.; Tang, B.; Yuan, D.; Groenewold, J.; Zhou, G., Wettability Manipulation by Interface-Localized Liquid Dielectrophoresis: Fundamentals and Applications. *MICROMACHINES-BASEL* **2019,** *10* (5), 329.

147. Margulies, S., Force on a dielectric slab inserted into a parallel-plate capacitor. *Am. J. Phys.* **1984,** *52* (6), 515-518.

148. Paris, D. T. H. F. K., *Basic electromagnetic theory*. McGraw-Hill: New York, 1969.

149. Young, P. M.; Mohseni, K., Calculation of DEP and EWOD Forces for Application in Digital Microfluidics. *J. Fluids Eng.* **2008,** *130* (8).

150. Baird, E.; Young, P.; Mohseni, K., Electrostatic force calculation for an EWOD-actuated droplet. *Microfluidics Nanofluidics* **2007,** *3* (6), 635-644.

151. Jones, T. B., Hydrostatics and steady dynamics of spatially varying electromechanical flow structures. *J. Appl. Phys.* **1974,** *45* (4), 1487-1491.

152. Jones, T. B., An electromechanical interpretation of electrowetting. *Journal of Micromechanics Microengineering* **2005,** *15* (6), 1184-1187.

153. Mugele, F.; Klingner, A.; Buehrle, J.; Steinhauser, D.; Herminghaus, S., Electrowetting: a convenient way to switchable wettability patterns. *J. Condens. Matter Phys* **2005,** *17* (9), S559-S576.

154. Jones, T. B.; Wang, K. L.; Yao, D. J., Frequency-dependent electromechanics of aqueous liquids: electrowetting and dielectrophoresis. *Langmuir : the ACS journal of surfaces and colloids* **2004,** *20* (7), 2813-2818.

155. Gruzintsev, A. N.; Volkov, V. T.; Matveeva, L. N., ZnO Films Deposited by Electron-Beam Evaporation: The Effect of Ion Bombardment. *Russ. Microelectron* **2002,** *31* (3), 193-199.

156. Electron Beam Evaporation Deposition. In *Advanced Nano Deposition Methods*, 2016; pp 33-58.

157. Nadkarni, V. S.; Samant, S. D., Spin coating technique for the preparation of thin nitrocellulose films for solid state nuclear track detection. *Radiat. Meas.* **1997,** *27* (3), 505-510.

158. Hanaor, D. A. H.; Triani, G.; Sorrell, C. C., Morphology and photocatalytic activity of highly oriented mixed phase titanium dioxide thin films. *Surf. Coat. Technol* **2011,** *205* (12), 3658-3664.

159. Ceyssens, F.; Puers, R., SU-8 Photoresist. In *Encyclopedia of Nanotechnology*, Bhushan, B., Ed. Springer Netherlands: Dordrecht, 2012; pp 2530-2543.

160. Keller, S.; Blagoi, G.; Lillemose, M.; Haefliger, D.; Boisen, A., Processing of thin SU-8 films. *J. Micromech. Microeng.* **2008,** *18* (12), 125020.

161. Ramli, N. A.; Arslan, T.; Haridas, N.; Zhou, W., Design, simulation and analysis of a digital RF MEMS varactor using thick SU-8 polymer. *Microsystem Technologies* **2018,** *24* (1), 473-482.

162. Shelly, M.; Lee, S.-I.; Suarato, G.; Meng, Y.; Pautot, S., Photolithography-Based Substrate Microfabrication for Patterning Semaphorin 3A to Study Neuronal Development. *Methods Mol Biol* **2017,** *1493*, 321-343.

163. Heuberger, A., X-ray lithography. *Microelectron. Eng.* **1986,** *5* (1), 3-38.

164. Melngailis, J.; Mondelli, A. A.; III, I. L. B.; Mohondro, R., A review of ion projection lithography. *J Vac Sci Technol B Microelectron Nanometer Struct Process Meas Phenom* **1998,** *16* (3), 927-957.

165. Chen, Y., Nanofabrication by electron beam lithography and its applications: A review. *Microelectron. Eng.* **2015,** *135*, 57-72.

166. Bazargan, A. M.; Sharif, F.; Mazinani, S.; Naderi, N., A high quality ITO/PET electrode for flexible and transparent optoelectronic devices. *J. Mater. Sci. Mater.* **2017,** *28* (3), 2962-2969.

167. Melai, J.; Salm, C.; Smits, S.; Visschers, J.; Schmitz, J., The electrical conduction and dielectric strength of SU-8. *J. Micromech. Microeng* **2009,** *19* (6), 065012.

168. Greener, J.; Li, W.; Ren, J.; Voicu, D.; Pakharenko, V.; Tang, T.; Kumacheva, E., Rapid, cost-efficient fabrication of microfluidic reactors in thermoplastic polymers by combining photolithography and hot embossing. *Lab Chip* **2010,** *10* (4), 522-524.

169. Matarèse, B. F. E.; Feyen, P. L. C.; Falco, A.; Benfenati, F.; Lugli, P.; deMello, J. C., Use of SU8 as a stable and biocompatible adhesion layer for gold bioelectrodes. *Sci. Rep.* **2018,** *8* (1), 5560.

170. Arscott, S., SU-8 as a material for lab-on-a-chip-based mass spectrometry. *Lab Chip* **2014,** *14* (19), 3668-3689.

171. Jin, J.; Wang, L.; Zheng, Z.; Zhang, J.; Hu, X.; Lu, J. R.; Etor, D.; Pearson, C.; Song, A.; Wood, D.; Gallant, A. J.; Balocco, C., Metal-insulator-metal diodes based on alkyltrichlorosilane self-assembled monolayers. *AIP Adv.* **2019,** *9* (6), 065017.

172. Wang, Y.; Lieberman, M., Growth of Ultrasmooth Octadecyltrichlorosilane Self-Assembled Monolayers on SiO2. *Langmuir* **2003,** *19* (4), 1159-1167.

173. Kumar, V.; Sharma, N. N., Synthesis of hydrophilic to superhydrophobic SU8 surfaces. *J. Appl. Polym. Sci.* **2015,** *132* (18).

174. Le, C. V.; Ly, N. G.; Stevens, M. G., Measuring the Contact Angles of Liquid Droplets on Wool Fibers and Determining Surface Energy Components. *Text. Res. J.* **1996,** *66* (6), 389-397.

175. Huhtamäki, T.; Tian, X.; Korhonen, J. T.; Ras, R. H. A., Surface-wetting characterization using contact-angle measurements. *Nat. Protoc.* **2018,** *13* (7), 1521-1538.

176. Launay, G. DROP SHAPE ANALYSIS USING PYTHON. https://gabylaunay.github.io/Python-cookbook/image-analysis/ (accessed 2021).

177. Electronics, S., SHV Reed Relay Data Sheet. Electronics, S., Ed. Standex Electronics Standex Electronics 2021.

178. 64 Channel USB Relay Module. https://numato.com/product/64-channel-usb-relay-module/ (accessed 2021).

179. Wang, X.; Yue, H.; Liu, G.; Zhao, Z., The Application of COMSOL Multiphysics in Direct Current Method Forward Modeling. *Prog. Earth Planet. Sci.* **2011,** *3*, 266-272.

180. Trauth, M. H., Introduction to MATLAB. In *MATLAB® Recipes for Earth Sciences*, Springer Berlin Heidelberg: Berlin, Heidelberg, 2015; pp 11-55.

181. Knowles, N. C., Finite element analysis. *Comput Aided Des* **1984,** *16* (3), 134-140.

182. Fairclough, C. Efficiently Mesh Your Model Geometry with Meshing Sequences. https://uk.comsol.com/blogs/efficiently-mesh-your-model-geometry-with-meshing-sequences/ (accessed 2020).

183. Electrostatics Theory. https://www.comsol.nl/multiphysics/electrostatics-theory?parent=electromagnetics-072-162 (accessed 2021).

184. Fuchs, N.; Petrjanoff, I., Microscopic Examination of Fog-, Cloud-and Rain-Droplets. *Nature* **1937,** *139* (3507), 111-112.

185. Time Series Viewer. http://data.ecn.ac.uk/tsv/results.asp (accessed 2020).

186. Junge, C. E.; Werby, R. T., THE CONCENTRATION OF CHLORIDE, SODIUM, POTASSIUM, CALCIUM, AND SULFATE IN RAIN WATER OVER THE UNITED STATES. *J. Meteorol.* **1958,** *15* (5), 417-425.

187. Gorham, E., On the acidity and salinity of rain. *Geochimica et Cosmochimica Acta* **1955,** *7* (5), 231-239.

188. . Melai, C. S., S. Smits, J. Visschers and J. Schmitz, The electrical conduction and dielectric strength of SU-8. *J. Micromech. Microeng* **2009,** *19* (65012).

189. Yang, Y.; Bittner, A. M.; Baldelli, S.; Kern, K., Study of self-assembled triethoxysilane thin films made by casting neat reagents in ambient atmosphere. *Thin Solid Films* **2008,** *516* (12), 3948-3956.

190. Ahmad, I.; Pathak, M.; Khan, M. K., Electrowetting induced microdroplet oscillation over interdigitated electrodes for hotspot cooling applications. *Exp. Therm. Fluid Sci.* **2021,** *125*, 110372.

191. McHale, G.; Orme, B. V.; Wells, G. G.; Ledesma-Aguilar, R., Apparent Contact Angles on Lubricant-Impregnated Surfaces/SLIPS: From Superhydrophobicity to Electrowetting. *Langmuir* **2019,** *35* (11), 4197-4204.

192. Barman, J.; Pant, R.; Nagarajan, A. K.; Khare, K., Electrowetting on dielectrics on lubricating fluid-infused smooth/rough surfaces with negligible hysteresis. *J Adhes Sci Technol* **2017,** *31* (2), 159-170.

193. Ogihara, H.; Xie, J.; Okagaki, J.; Saji, T., Simple Method for Preparing Superhydrophobic Paper: Spray-Deposited Hydrophobic Silica Nanoparticle Coatings Exhibit High Water-Repellency and Transparency. *Langmuir* **2012,** *28* (10), 4605-4608.

194. Jeevahan, J.; Chandrasekaran, M.; Britto Joseph, G.; Durairaj, R. B.; Mageshwaran, G., Superhydrophobic surfaces: a review on fundamentals, applications, and challenges. *J. Coat. Technol. Res.* **2018,** *15* (2), 231-250.

195. Ryu, J.; Kim, K.; Park, J.; Hwang, B. G.; Ko, Y.; Kim, H.; Han, J.; Seo, E.; Park, Y.; Lee, S. J., Nearly Perfect Durable Superhydrophobic Surfaces Fabricated by a Simple One-Step Plasma Treatment. *Sci. Rep.* **2017,** *7* (1), 1981.

196. Yong, J.; Chen, F.; Yang, Q.; Farooq, U.; Hou, X., Photoinduced switchable underwater superoleophobicity–superoleophilicity on laser modified titanium surfaces. *J. Mater. Chem. A.* **2015,** *3* (20), 10703-10709.

197. Yun, X.; Xiong, Z.; He, Y.; Wang, X., Superhydrophobic lotus-leaf-like surface made from reduced graphene oxide through soft-lithographic duplication. *RSC Adv* **2020,** *10* (9), 5478-5486.

198. Self-Assembly of Organic Molecules into Nanostructures. In *Soft Matter Nanotechnology*, 2015; pp 21-94.

199. Kumar, V.; Maheshwari, N.; Sharma, N. N., Self Assembled Monolayer Modified SU8 Surface for Electrowetting Application. *Macromol Symp* **2015,** *357* (1), 18-22.

200. Dong, J.; Wang, A.; Ng, K. Y. S.; Mao, G., Self-assembly of octadecyltrichlorosilane monolayers on silicon-based substrates by chemical vapor deposition. *Thin Solid Films* **2006,** *515* (4), 2116-2122.

201. Lee, S.; Ishizaki, T.; Saito, N.; Takai, O., Effect of Reaction Temperature on Growth of Organosilane Self-Assembled Monolayers. *JJAP* **2008,** *47* (8), 6442-6447.

202. Rozlosnik, N.; Gerstenberg, M. C.; Larsen, N. B., Effect of Solvents and Concentration on the Formation of a Self-Assembled Monolayer of Octadecylsiloxane on Silicon (001). *Langmuir* **2003,** *19* (4), 1182-1188.

203. Saner, C. K.; Lusker, K. L.; LeJeune, Z. M.; Serem, W. K.; Garno, J. C., Self-assembly of octadecyltrichlorosilane: Surface structures formed using different protocols of particle lithography. *Beilstein J. Nanotechnol.* **2012,** *3*, 114-122.

204. Papadopoulos, P.; Pinchasik, B.-E.; Tress, M.; Vollmer, D.; Kappl, M.; Butt, H.-J., Wetting of soft superhydrophobic micropillar arrays. *Soft Matter* **2018,** *14* (36), 7429-7434.

205. Ennaceri, H.; Wang, L.; Erfurt, D.; Riedel, W.; Mangalgiri, G.; Khaldoun, A.; El Kenz, A.; Benyoussef, A.; Ennaoui, A., Water-resistant surfaces using zinc oxide structured nanorod arrays with switchable wetting property. *Surf. Coat. Technol.* **2016,** *299*, 169-176.

206. Ding, X.; Lin, K.; Li, Y.; Dang, M.; Jiang, L., Synthesis of Biocompatible Zinc Oxide (ZnO) Nanoparticles and Their Neuroprotective Effect of 6-OHDA Induced Neural Damage in SH-SY 5Y Cells. *J. Clust. Sci.* **2020,** *31* (6), 1315-1328.

207. Coleman, V. A.; Bradby, J. E.; Jagadish, C.; Munroe, P.; Heo, Y. W.; Pearton, S. J.; Norton, D. P.; Inoue, M.; Yano, M., Mechanical properties of ZnO epitaxial layers grown on a- and c-axis sapphire. *Appl. Phys. Lett.* **2005,** *86* (20), 203105.

208. Zhang, S.; Huang, J.; Chen, Z.; Yang, S.; Lai, Y., Liquid mobility on superwettable surfaces for applications in energy and the environment. *J. Mater. Chem. A* **2019,** *7* (1), 38-63.

209. Launay, G.; Sadullah, M. S.; McHale, G.; Ledesma-Aguilar, R.; Kusumaatmaja, H.; Wells, G. G., Self-propelled droplet transport on shaped-liquid surfaces. *Sci. Rep.* **2020,** *10* (1), 14987.

210. Yasuda, T.; Harada, S.; Daimon, K., Microfluidic Dispensing Device Using Wettability Gradient and Electrowetting. *IEEJ Trans. Sens. Micromachines* **2008,** *128* (3), 75-79.

211. Stamatopoulos, C.; Milionis, A.; Ackerl, N.; Donati, M.; Leudet de la Vallée, P.; Rudolf von Rohr, P.; Poulikakos, D., Droplet Self-Propulsion on Superhydrophobic Microtracks. *ACS Nano* **2020,** *14* (10), 12895-12904.

212. Frozanpoor, I.; Cooke, M. D.; Ambukan, V.; Gallant, A. J.; Balocco, C., Continuous Droplet-Actuating Platforms via an Electric Field Gradient: Electrowetting and Liquid Dielectrophoresis. *Langmuir* **2021,** *37* (21), 6414-6422.

213. Hong, F.; Bai, F.; Cheng, P., A parametric study of electrothermal flow inside an AC EWOD droplet. *Int. Commun. Heat Mass Transf.* **2014,** *55*, 63-70.

214. Sun, D.; Böhringer, K. F., Directional Droplet Transport and Fog Removal on Textured Surfaces Using Liquid Dielectrophoresis. *J. Microelectromechanical Syst* **2020,** *29* (5), 1002-1007.

215. Lee, C.-P.; Fang, B.-Y.; Wei, Z.-H., Influence of electrolytes on contact angles of droplets under electric field. *Analyst* **2013,** *138* (8), 2372-2377.

216. Zhang, K.; Wang, W.; Li, C.; Riaud, A.; Zhou, J., 2D large-scale EWOD devices with honeycomb electrodes for multiplexed multidirectional driving of micro-droplets. *AIP Adv* **2020,** *10* (5), 055227.

217. Armani, M.; Chaudhary, S.; Probst, R.; Walker, S.; Shapiro, B., Control of microfluidic systems: two examples, results, and challenges. *Int. J. Robust Nonlinear Control.* **2005,** *15* (16), 785-803.

218. Schwartz, J. A.; Vykoukal, J. V.; Gascoyne, P. R. C., Droplet-based chemistry on a programmable micro-chip. *Lab Chip* **2004,** *4* (1), 11-17.

219. Isgor, P. K.; Marcali, M.; Keser, M.; Elbuken, C., Microfluidic droplet content detection using integrated capacitive sensors. *Sens. Actuators B Chem.* **2015,** *210*, 669-675.

220. Sadeghi, S.; Ding, H.; Shah, G. J.; Chen, S.; Keng, P. Y.; Kim, C.-J. C.; van Dam, R. M., On Chip Droplet Characterization: A Practical, High-Sensitivity Measurement of Droplet Impedance in Digital Microfluidics. *Anal. Chem.* **2012,** *84* (4), 1915-1923.

221. Shirinkami, H.; Kim, J.; Lee, C.; Kim, H. C.; Chun, H., Improvement of droplet speed and stability in electrowetting on dielectric devices by surface polishing. *Biochip J.* **2017,** *11* (4), 316-321.

222. Colaço, A. F.; Molin, J. P.; Rosell-Polo, J. R.; Escolà, A., Application of light detection and ranging and ultrasonic sensors to high-throughput phenotyping and precision horticulture: current status and challenges. *Hortic. Res.* **2018,** *5* (1), 35.

223. Krupenkin, T.; Taylor, J. A., Reverse electrowetting as a new approach to high-power energy harvesting. *Nat. Commun.* **2011,** *2*, 448-448.

224. Yang, H.; Hong, S.; Koo, B.; Lee, D.; Kim, Y.-B., High-performance reverse electrowetting energy harvesting using atomic-layer-deposited dielectric film. *Nano Energy* **2017,** *31*, 450-455.

225. Mampallil, D.; Eral, H. B., A review on suppression and utilization of the coffee-ring effect. *Adv. Colloid Interface Sci.* **2018,** *252*, 38-54.

226. Mobility motor prices. https://www.monsterscooterparts.com/mobility/mobility-categories/mobilitymotor (accessed 2021).

227. Esposito, A.; Montello, A. D.; Guezennec, Y. G.; Pianese, C., Experimental investigation of water droplet–air flow interaction in a non-reacting PEM fuel cell channel. *J. Power Sources* **2010,** *195* (9), 2691-2699.

228. Schillberg, C. H.; Kandlikar, S. G. In *A Review of Models for Water Droplet Detachment From the Gas Diffusion Layer-Gas Flow Channel Interface in PEMFCs*, ASME 2007 5th International Conference on Nanochannels, Microchannels, and Minichannels, 2007; pp 299-310.

229. Fan, J.; Wilson, M. C. T.; Kapur, N., Displacement of liquid droplets on a surface by a shearing air flow. *J. Colloid Interface Sci* **2011,** *356* (1), 286-292.

230. Monjo, R., Measure of rainfall time structure using the dimensionless n-index. *Climate Research* **2016,** *67*, 71-86.

231. Williams, C. R.; Bringi, V. N.; Carey, L. D.; Chandrasekar, V.; Gatlin, P. N.; Haddad, Z. S.; Meneghini, R.; Joseph Munchak, S.; Nesbitt, S. W.; Petersen, W. A.; Tanelli, S.; Tokay, A.; Wilson, A.; Wolff, D. B., Describing the Shape of Raindrop Size Distributions Using Uncorrelated Raindrop Mass Spectrum Parameters. *J. Appl. Meteorol. Climatol.* **2014,** *53* (5), 1282-1296.

232. Gaylard, A. P.; Kirwan, K.; Lockerby, D. A., Surface contamination of cars: A review. *Proceedings of the Institution of Mechanical Engineers, Part D: Int. J. Automot. Eng.* **2017,** *231* (9), 1160-1176.

233. GORHAM, E., Factors Influencing Supply of Major Ions to Inland Waters, with Special Reference to the Atmosphere. *GSA Bulletin* **1961,** *72* (6), 795-840.

234. Atkins, W. R. G., Electrical Conductivity of River, Rain and Snow Water. *Nature* **1947,** *159* (4046), 674-674.

235. Sarma, V. V. J.; Rao, C. S., Electrical conductivity of rain water at Visakhapatnam, India. *J. Geophys. Res. (1896-1977)* **1972,** *77* (12), 2197-2200.

236. ECN Data Centre Summary Database. http://data.ecn.ac.uk/tsv/ECNdB.asp (accessed 2021).

237. Zhang, G.; Liu, D.; He, X.; Yu, D.; Pu, M., Acid rain in Jiangsu province, eastern China: Tempo-spatial variations features and analysis. *Atmos. Pollut. Res.* **2017,** *8* (6), 1031-1043.

238. Loÿe-Pilot, M. D.; Martin, J. M.; Morelli, J., Influence of Saharan dust on the rain acidity and atmospheric input to the Mediterranean. *Nature* **1986,** *321* (6068), 427-428.

239. Li, L.; Hu, H.; Lin, H.; Ye, D. T., Electrowetting of the blood droplet on the hydrophobic film of the EWOD chips. *Conf Proc IEEE Eng Med Biol Soc* **2005,** *2005*, 1941-4.

240. Kwak, T. J.; Hossen, I.; Bashir, R.; Chang, W.-J.; Lee, C. H., Localized Dielectric Loss Heating in Dielectrophoresis Devices. *Sci. Rep.* **2019,** *9* (1), 18977.

241. Sridharan, S.; Zhu, J.; Hu, G.; Xuan, X., Joule heating effects on electroosmotic flow in insulator-based dielectrophoresis. *ELECTROPHORESIS* **2011,** *32* (17), 2274-2281.

242. Cohen, A.; Klassen, S.; Evans, D., Ethics in Archaeological Lidar. *Digit. Appl. Archaeol.* **2020,** *3* (1), 76-91.

243. Wulder, M. A.; White, J. C.; Nelson, R. F.; Næsset, E.; Ørka, H. O.; Coops, N. C.; Hilker, T.; Bater, C. W.; Gobakken, T., Lidar sampling for large-area forest characterization: A review. *Remote Sens. Environ.* **2012,** *121*, 196-209.

244. Yan, W. Y.; Shaker, A.; El-Ashmawy, N., Urban land cover classification using airborne LiDAR data: A review. *Remote Sens. Environ.* **2015,** *158*, 295-310.

245. Yeong, D. J.; Velasco-Hernandez, G.; Barry, J.; Walsh, J., Sensor and Sensor Fusion Technology in Autonomous Vehicles: A Review. *Sensors* **2021,** *21* (6), 2140.

246. Holmström, S. T. S.; Baran, U.; Urey, H., MEMS Laser Scanners: A Review. *J Microelectromech Syst* **2014,** *23* (2), 259-275.

247. Oh, C. W.; Cao, Z.; Tangdiongga, E.; Koonen, T., Free-space transmission with passive 2D beam steering for multi-gigabit-per-second per-beam indoor optical wireless networks. *Opt. Express* **2016,** *24* (17), 19211-19227.

248. Pollock, C.; Morrison, J.; Imboden, M.; Little, T. D. C.; Bishop, D. J., Beam shaping with tip-tilt varifocal mirror for indoor optical wireless communication. *Opt. Express* **2017,** *25* (17), 20274-20285.

249. Liu, A. Q.; Zhang, X. M., A review of MEMS external-cavity tunable lasers. *J. Micromech. Microeng.* **2006,** *17* (1), R1-R13.

250. Wang, D.; Watkins, C.; Xie, H., MEMS Mirrors for LiDAR: A Review. *Micromachines (Basel)* **2020,** *11* (5), 456.

251. Pengwang, E.; Rabenorosoa, K.; Rakotondrabe, M.; Andreff, N., Scanning Micromirror Platform Based on MEMS Technology for Medical Application. *Micromachines (Basel)* **2016,** *7* (2), 24.

252. Ji, C.-H.; Kim, Y.-K. In *Fabrication and Experiments on Electromagnetic Micromirror Array with Bulk Silicon Mirror Plate and Aluminum Spring*, Transducers '01 Eurosensors XV, Berlin, Heidelberg, 2001//; Obermeier, E., Ed. Springer Berlin Heidelberg: Berlin, Heidelberg, 2001; pp 1292-1295.

253. Sadhukhan, D.; Singh, G. P., Study of electrostatic actuated MEMS biaxial scanning micro-mirror with comb structure. *AIP Conf Proc* **2020,** *2269* (1), 030019.

254. Mu, X.; Sun, W.; Feng, H.; Yu, A.; Chen, K. W. S.; Fu, C. Y.; Olivo, M., MEMS micromirror integrated endoscopic probe for optical coherence tomography bioimaging. *Sens. Actuator A Phys.* **2011,** *168* (1), 202-212.

255. Eltagoury, Y. M.; Soliman, M.; Sabry, Y. M.; Alotaibi, M. J.; Khalil, D., Electrostatic Comb-Drive Actuator with High In-Plane Translational Velocity. *Micromachines (Basel)* **2016,** *7* (10).

256. Kim, K. H.; Park, B. H.; Maguluri, G. N.; Lee, T. W.; Rogomentich, F. J.; Bancu, M. G.; Bouma, B. E.; de Boer, J. F.; Bernstein, J. J., Two-axis magnetically-driven MEMS scanning catheter for endoscopic high-speed optical coherence tomography. *Opt. Express* **2007,** *15* (26), 18130-18140.

257. Aljasem, K.; Werber, A.; Seifert, A.; Zappe, H., Fiber optic tunable probe for endoscopic optical coherence tomography. *J. Opt.* **2008,** *10* (4), 044012.

258. Frozanpoor, I.; Cooke, M.; Alvarez-Ruiz, D.; Ambukan, V.; Gallant, A.; Balocco, C., Tilting micromirror platform based on liquid dielectrophoresis. *Sens. Actuator A Phys.* **2021**, 113177.

259. Zhao, Y.; Dang, W.; Lu, Z.; Wang, L.; Si, L.; Zhang, M., A novel mica-based composite with hybrid aramid fibers for electrical insulating applications: largely improved mechanical properties and moisture resistance. *Polym. Int.* **2018,** *67* (2), 204-211.

260. Weisenhorn, A. L.; Henriksen, P. N.; Chu, H. T.; Ramsier, R. D.; Reneker, D. H., Atomically resolved images of bismuth films on mica with an atomic force microscope. *J. Vac. Sci. Technol. B:Nanotechnol. Microelectron.* **1991,** *9* (2), 1333-1335.

261. Richter, R. P.; Brisson, A. R., Following the Formation of Supported Lipid Bilayers on Mica: A Study Combining AFM, QCM-D, and Ellipsometry. *Biophys. J.* **2005,** *88* (5), 3422-3433.

262. Kim, M.-O.; Pyo, S.; Song, G.; Kim, W.; Oh, Y.; Park, C.; Park, C.; Kim, J., Humidity-Resistant, Fabric-Based, Wearable Triboelectric Energy Harvester by Treatment of Hydrophobic Self-Assembled Monolayers. *Adv. Mater. Technol.* **2018,** *3* (7), 1800048.

263. Parvate, S.; Dixit, P.; Chattopadhyay, S., Superhydrophobic Surfaces: Insights from Theory and Experiment. *J. Phys. Chem. B* **2020,** *124* (8), 1323-1360.

264. Li, Y.-J.; Cahill, B. P., Frequency Dependence of Low-Voltage Electrowetting Investigated by Impedance Spectroscopy. *Langmuir* **2017,** *33* (45), 13139-13147.

265. Karuwan, C.; Sukthang, K.; Wisitsoraat, A.; Phokharatkul, D.; Patthanasettakul, V.; Wechsatol, W.; Tuantranont, A., Electrochemical detection on electrowetting-on-dielectric digital microfluidic chip. *Talanta* **2011,** *84* (5), 1384-1389.

266. Zhao, R.; Liu, Q.-C.; Wang, P.; Liang, Z.-C., Contact angle hysteresis in electrowetting on dielectric. *Chin. Phys. B* **2015,** *24* (8), 086801.

267. Edwards, A. M. J.; Ledesma-Aguilar, R.; Newton, M. I.; Brown, C. V.; McHale, G., Electrostatic control of dewetting dynamics. *Appl. Phys. Lett.* **2020,** *116* (25), 253703.

268. Vo, Q.; Su, H.; Tran, T., Universal Transient Dynamics of Electrowetting Droplets. *Sci. Rep.* **2018,** *8* (1), 836.

269. Ren, X.; Wei, S.; Qu, X.; Liu, F., Electrohydrodynamic analysis of electrowetting-on-dielectric (EWOD)-Induced transport of a microdroplet based on the lattice Boltzmann method. *AIP Adv* **2019,** *9* (5), 055021.

270. García-Sánchez, P.; Ramos, A.; Mugele, F., Electrothermally driven flows in ac electrowetting. *Phys. Rev. E* **2010,** *81* (1), 015303.

271. Wolter, A.; Hsu, S.-T.; Schenk, H.; Lakner, H., *Applications and requirements for MEMS scanner mirrors*. SPIE: 2005; Vol. 5719.

272. Kedzierski, J.; Chea, H., Multilayer microhydraulic actuators with speed and force configurations. *Microsyst. Nanoeng.* **2021,** *7* (1), 22.

273. Kedzierski, J.; Holihan, E.; Cabrera, R.; Weaver, I., Re-engineering artificial muscle with microhydraulics. *Microsyst. Nanoeng.* **2017,** *3* (1), 17016.

274. Preston, D. J.; Anders, A.; Barabadi, B.; Tio, E.; Zhu, Y.; Dai, D. A.; Wang, E. N., Electrowetting-on-dielectric actuation of a vertical translation and angular manipulation stage. *Appl. Phys. Lett.* **2016,** *109* (24), 244102.

275. Brabcova, Z.; McHale, G.; Wells, G. G.; Brown, C. V.; Newton, M. I.; Edwards, A. M. J., Near Axisymmetric Partial Wetting Using Interface-Localized Liquid Dielectrophoresis. *Langmuir* **2016,** *32* (42), 10844-10850.